3D and 2D Microrheology of Soft Matter Systems Consisting of Particles

Dissertation

Zur Erlangung des Grades

Doktor der Naturwissenschaften

im Promotionsfach Physikalische Chemie

am Fachbereich Chemie, Pharmazie und Geowissenschaften

der Johannes Gutenberg-Universität Mainz

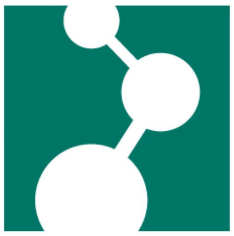

von

Shilin Huang

geboren in Guangdong, China

Mainz, December 2016

Die vorliegende Arbeit wurde in der Zeit von September 2013 bis Dezember 2016 unter der Betreuung von [In der elektronischen Fassung aus Datenschutzgründen entfernt] am Max-Planck-Institut für Polymerforschung in Mainz angefertigt.

Tag der Prüfung: 13. Februar 2017
Dekan: [In der elektronischen Fassung aus Datenschutzgründen entfernt]
1. Berichterstatter: [In der elektronischen Fassung aus Datenschutzgründen entfernt]
2. Berichterstatter: [In der elektronischen Fassung aus Datenschutzgründen entfernt]
Dissertation an der Universität Mainz (D77)

Table of Contents

Abstract

Soft matter systems consist of a large range of materials, including polymers, emulsions, foams, granular materials, etc. Cells, tissues and organisms also belong to the category of soft matter systems. All these systems play an important role in our daily life and in industrial applications. Because soft matter systems are sensitive to external applied forces and stimuli, they can be used to fabricate stimulus-responsive materials, such as actuators and sensors. The rheological properties of soft matter systems determine how they deform under forces.

Understanding the rheological properties of soft matter systems on different length scales can help to design the stimulus-responsive materials. Depending on the probed length scale, rheology can be divided into bulk rheology, microrheology and nanorheology. Among these methods, microrheology probes the rheological properties of soft matter systems on the micrometer scale. It gives essential information on the interactions between the building blocks of the systems. In this thesis, the microrheological properties of two soft matter systems are studied.

The first studied systems are the magneto-responsive hybrid gels (MRGs). A MRG consists of a polymer network swollen in a good solvent, and embedded micro-sized magnetic particles. MRGs have potential applications as soft actuators, artificial muscles, and sensors, etc. It is well known that the magnetic responsibility of the MRGs arises from the magnetic interactions between the embedded magnetic particles. However, the details about how the magnetic particles couple to the surrounding polymer network on a microscopic scale are still not clear. In this thesis, an experimental model system for MRGs is developed. It consists of paramagnetic particle chains inside the soft gels. Using laser scanning confocal microscopy, the 3D rearrangement of the magnetic particles in the soft gels under a homogeneous magnetic field is studied. Under an applied magnetic field, the magnetic interactions between the magnetic particles tend to align the magnetic particle chains along the field direction. However, this is impeded by the cross-linked polymer network. In the experiments, I find that the interplay between these two effects leads to rich morphological changes (e.g., buckling) of the paramagnetic particle chains under the magnetic field. Together with theorists from Heinrich-Heine-Universität Düsseldorf and Universität Stuttgart, we develop a simplified theoretical model and perform simulations to understand this magnetic-field-induced buckling behavior. In addition, in order to understand how the magnetic particles interact with each other in the gel matrix, theorists from Heinrich-Heine-Universität Düsseldorf propose a theory which can calculate the effective interactions between particles in the elastic matrix analytically. To confirm the theory, I perform experiments on small groups of paramagnetic particles embedded in a soft gel matrix. Applying an external magnetic field induces magnetic forces between the

particles. Rotating the magnetic field tunes these forces. In this thesis, it will be shown that the theory can correctly predict the change of positions of the magnetic particles embedded in the gel under the magnetic field.

The second studied systems consist of microgels at the water/oil interface. Microgels have been used to prepared emulsions which are responsive to temperature or pH value. However, it is still not clear how the microgels interact at the interface, and how these interactions influence the rheological properties of the microgel-laden interfaces. In this thesis, the rheological properties of the microgel monolayers at the water/oil interface are studied on the single-microgel level. It is observed that driven by the capillary interactions, the microgels at the water/oil interface tend to aggregate. At low surface coverage, the aggregated microgels form open networks which show dominating elasticity. Passive microrheology is used to determine the elasticity of these microgel networks at the interface. At high surface coverage, when the microgels become closely packed at the water/oil interface, the elasticity of the microgel monolayers is dominated by the overlapping of the microgels. Their elasticity can be measured using the active microrheology with the magnetic dimers as probes. The advantage of using microrheology is that the structure of the microgel monolayers can be well observed during the rheological measurements.

Zusammenfassung

Weiche Materie Systeme bestehen aus einer Vielzahl von Materialien, darunter Polymere, Emulsionen, Schäume, granulare Materialien etc. Zellen, Stoffe und Organismen gehören auch in die Kategorie der weichen Materie. Alle diese Materialien spielen eine wichtige Rolle in unserem täglichen Leben ebenso wie in industriellen Anwendungen. Da sie empfindlich auf externe Kräfte und Reize reagieren, können sie zur Herstellung stimulussensitiver Materialien verwendet werden, zum Beispiel für Aktuatoren und Sensoren. Die rheologischen Eigenschaften von weicher Materie bestimmen das Verhalten unter dynamischer Krafteinwirkung.

Das Verständnis der rheologischen Eigenschaften von weicher Materie Systemen auf unterschiedlichen Längenskalen kann dazu beitragen, solche stimulus-sensitive Materialien zu entwerfen. Abhängig von der untersuchten Längenskala kann die Rheologie in Makrorheologie, Mikrorheologie und Nanorheologie unterteilt werden. Unter diesen Methoden untersucht die Mikrorheologie die rheologischen Eigenschaften von Weichstoffsystemen auf der Mikrometerskala und liefert wesentliche Informationen über die Wechselwirkungen zwischen den Bausteinen der Systeme. In dieser Arbeit werden die mikrorheologischen Eigenschaften zweier weicher Stoffsysteme untersucht.

Das erste untersuchte System ist ein magnetisch-responsives Hybridgel (MRG). Das MRG besteht aus einem Polymernetzwerk, das mit einem angepasstem Lösungsmittel gequollen ist, und eingebettete magnetische Mikropartikel enthält. MRGs haben potenzielle Anwendungen als weiche Aktuatoren, künstliche Muskeln, Sensoren etc. Obwohl bekannt ist, dass die magnetische Reaktion der MRGs aus den magnetischen Wechselwirkungen zwischen den eingebetteten magnetischen Partikeln entsteht, sind die Details darüber, wie die magnetischen Partikel auf mikroskopischer Ebene an das umgebenden Polymernetzwerk koppeln noch nicht bekannt. In dieser Arbeit wird ein experimentelles Modellsystem für MRG entwickelt, welches aus paramagnetische Partikelketten besteht, die in weichen Gelen eingebettet werden. Unter Verwendung von konfokaler Laserscanning Mikroskopie wird die 3D-Umlagerung der magnetischen Partikel in den weichen Gelen unter dem Einfluss eines homogenen Magnetfeldes untersucht. Unter dem magnetischen Feld neigen die magnetischen Partikel aufgrund magnetischer Wechselwirkungen dazu, die magnetischen Partikelketten entlang der Feldrichtung auszurichten. Dies wird jedoch durch das vernetzte Polymernetzwerk behindert. In meinen Experimenten finde ich, dass das Zusammenspiel dieser beiden Effekten führt zu morphologischen Veränderungen der paramagnetischen Partikelketten unter dem Einfluss des Magnetfeld (z.B. Undulationen der Partikelketten). Zusammen mit Theoretikern der Heinrich-Heine-Universität Düsseldorf und der Universiät Stuttgart entwickelte ich ein vereinfachtes theoretisches Modell und erarbeitete Simulationen, um dieses magnetfeldinduzierte Undu-

lationsverhalten zu verstehen. Um zu verstehen, wie die magnetischen Teilchen in der Gelmatrix miteinander interagieren, schlagen Theoretiker der Heinrich-Heine-Universität Düsseldorf eine Theorie vor, mithilfe derer die analytisch wirksamen Wechselwirkungen zwischen den Teilchen in der elastischen Matrix berechnen können. Um die Theorie zu bestätigen, experimentiere ich mit kleinen Gruppen paramagnetischer Partikel, welche in einer weichen Gelmatrix eingebettet sind. Das Anlegen eines externen Magnetfelds induziert magnetische Kräfte zwischen den Teilchen. Durch Drehen des Magnetfeldes werden diese Kräfte eingestellt. In dieser Arbeit zeige ich auch, daß diese Theorie die Lageänderung der in dem Gel unter Magnetfeld eingebetteten magnetischen Teilchen korrekt vorhersagen kann.

Das zweite untersuchte System besteht aus Mikrogelen an der Wasser / Öl-Grenzfläche. Es wurden Mikrogele verwendet, um Emulsionen herzustellen, die auf Temperatur oder pH-Wert ansprechen. Es ist jedoch noch nicht klar, wie die Mikrogele an der Grenzfläche wechselwirken und wie diese Wechselwirkungen die rheologischen Eigenschaften der mikrogelbeladen Grenzflächen beeinflussen. In dieser Arbeit werden die rhelologischen Eigenschaften einer Mikrogel-Monoschicht an der Wasser / Öl-Grenzfläche auf Einzelmikrogel-Ebene untersucht. Ich beobachte, dass die Mikrogele an der Wasser / Öl-Grenzfläche, die durch Kapillarwechselwirkungen angetrieben werden, dazu neigen zu aggregieren. Bei niedriger Oberflächenkonzentration bilden die aggregierten Mikrogele offene Netzwerke aus, die dominierende Elastizität zeigen. Zur Bestimmung der Elastizität der Mikrogelnetze an der Grenzfläche wird die passive Mikrorheologie verwendet. Bei hoher Oberflächenkonzentration, wenn die Mikrogele an der Wasser / Öl-Grenzfläche dicht gepackt sind, wird die Elastizität der Mikrogelmonoschichten durch die Überlappung der Mikrogele dominiert. Ihre Elastizität kann mit der aktiven Mikrorheologie mit den magnetischen Dimeren als Sonden gemessen werden. Der Vorteil der Mikrorheologie liegt darin, dass die Struktur der Mikrogelmonoschichten während der rheologischen Messungen gut beobachtet werden kann.

1. Introduction and Motivation

1.1 Soft matter

Simple solids show small deformations under an external force, while simple liquids flow under the same force. Many materials are neither simple solids nor simple liquids. For example, a toothpaste acts as a solid under a small force (e.g., under the gravity), while it starts to flow (like a liquid) if we squeeze it. There are many materials showing mechanical properties between solids and liquids, including polymers, emulsions, foams, granular materials, surfactants and liquid crystals, etc. They are all soft matter.[1,2] Cells, tissues and organisms are also in the category of soft matter.[3]

Even though soft matter systems cover a large range of materials, they have some common characteristics:[2,3]

(i) Soft matter show large responses to weak forces. For example, a gel can show a large elongation under a tensile force. Typically, the large response of soft matter cannot be described using a linear relation between the stress and strain. Instead, nonlinear effects should be taken into account.

(ii) The building blocks of soft matter are much larger than atoms. For example, the building blocks for the polymer materials are the polymer chains. A polymer chain may consist of thousands of monomer units. Fig. 1.1 shows the length scales of the building blocks for the typical soft matter systems.

(iii) When the building blocks of soft matter show collective motions, the resulting dynamics of soft matter is slow. Owing to the slow relaxation, soft matter cannot easily reach the equilibrium state. The non-equilibrium properties are important for soft matter systems.

1.2 Viscoelasticity of soft matter

Soft matter are usually viscoelastic. That is, they have both elastic and viscous properties. The viscoelastic properties of soft matter play an important role in their processing and applications. To quantify the viscoelasticity of a soft material, let's first consider a cubical element inside the material. The stress, i.e., the force per unit area acting on the face of the cubical element, is in fact a tensor with different components as shown in Fig. 1.2a. In a pure shear experiment, the strain tensor (γ_{ij}) and the stress tensor (σ_{ij}) can be written as[4]

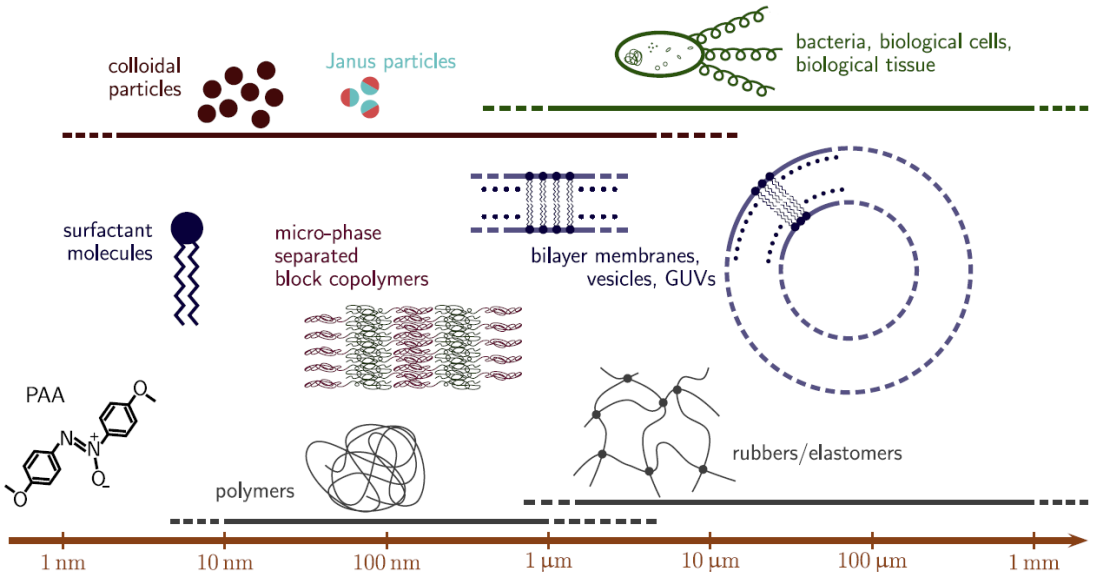

Figure 1.1 Typical examples of soft matter systems and their characteristic sizes of the building blocks. Reprinted from Ref. 3 with permission.

$$\gamma_{ij} = \begin{bmatrix} 0 & \gamma & 0 \\ \gamma & 0 & 0 \\ 0 & 0 & 0 \end{bmatrix}, \qquad \sigma_{ij} = \begin{bmatrix} -P & \sigma_s & 0 \\ \sigma_s & -P & 0 \\ 0 & 0 & -P \end{bmatrix}, \tag{1.1}$$

where P is an isotropic pressure. The non-zero shear components and the resulting shear deformation are shown in Fig. 1.2b. For an isotropic elastic material under infinitesimal (pure) shear deformation, the Hooke's law can be simplified as:

$$\sigma_s = G\gamma, \tag{1.2}$$

where G is the shear modulus. For an isotropic viscous liquid under slow flow, instead, the shear stress is related to the shear velocity ($\dot{\gamma} = \partial\gamma/\partial t$) following the Newton's law:

$$\sigma_s = \eta\dot{\gamma}, \tag{1.3}$$

where η is the viscosity.

The deformation of an ideal elastic solid under a force does not depend on how long the force is applied, while an ideal viscous liquid has no memory about its deformation history. For most soft matter systems, however, their rheological properties are time-dependent and have a memory effect (i.e., they are viscoelastic). For example, a polymer can creep under a constant force. Its deformation depends on the time when the force is applied. According to Boltzmann superposition principle, the effects of mechanical history are linearly additive. The stress can be described as a function of rate of strain history (see Eq. (1.4)), or alternatively the strain can be described as a function of the history of rate of change of stress (see Eq. (1.5)):[4]

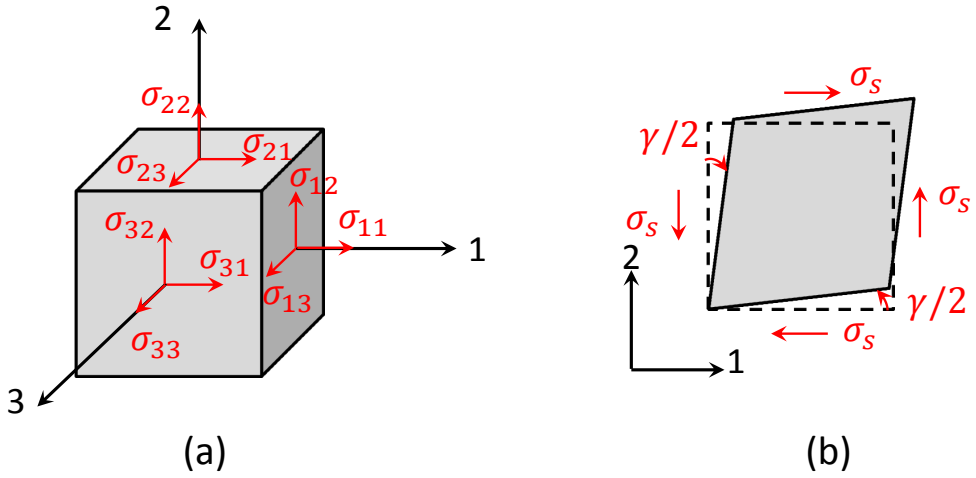

Figure 1.2 (a) Stress tensor (σ_{ij}) and the components. (b) Pure shear deformation. The dashed square represents the plane before deformation. The shear stress is σ_s and the resulting strain is γ.

$$\sigma_s(t) = \int_{-\infty}^{t} G(t-\tau)\dot{\gamma}(\tau)\,d\tau, \tag{1.4}$$

$$\gamma(t) = \int_{-\infty}^{t} J(t-\tau)\dot{\sigma}_s(\tau)\,d\tau. \tag{1.5}$$

Here, $G(t)$ is the relaxation modulus at time t. In general, the ratio of a stress to the corresponding strain is called a modulus, and for a perfectly elastic solid the equilibrium shear modulus G is defined as σ_s/γ. $J(t)$ is called the creep compliance, which has the dimension of reciprocal modulus. It is a monotonically non-decreasing function of time. $J(t)$ and $G(t)$ are correlated by:[4]

$$\int_0^t G(\tau)J(t-\tau)\,d\tau = t, \tag{1.6}$$

$$\int_0^t J(\tau)G(t-\tau)\,d\tau = t. \tag{1.7}$$

Thus $J(t)G(t) \leq 1$ (for a perfectly elastic solid, $J(t)G(t) = 1$). $J(t)$ and $G(t)$ can be obtained from creep experiments and relaxation experiments. Alternatively, oscillatory shear experiments are widely used to characterize the rheological properties of soft matter systems over a wide range of frequencies. The dynamic moduli are correlated with the relaxation modulus following:

$$G'(\omega) = G_e + \omega\int_0^\infty [G(t)-G_e]\sin(\omega t)\,dt, \tag{1.8}$$

$$G''(\omega) = \omega\int_0^\infty [G(t)-G_e]\cos(\omega t)\,dt, \tag{1.9}$$

where $G'(\omega)$ is the storage modulus, $G''(\omega)$ is the loss modulus, G_e is the equilibrium modulus at infinite time, and ω is the angular frequency. $G'(\omega)$ and $G''(\omega)$ quantify the

elastic and viscous properties of the soft matter systems, respectively. They are correlated to each other by the Kronig-Kramers relation:[5]

$$G'(\omega) = G_e + \frac{2}{\pi}\int_0^\infty \frac{\omega^2 G''(\beta)}{\beta(\omega^2-\beta^2)}\,d\beta, \tag{1.10}$$

$$G''(\omega) = \frac{2}{\pi}\int_0^\infty \frac{\omega[G'(\beta)-G_e]}{\beta^2-\omega^2}\,d\beta. \tag{1.11}$$

The rheological properties of soft matter systems can be measured using different methods. Depending on the probed length scale, these methods can be divided into bulk rheology, microrheology and nanorheology.[6] In the following section, I will give a brief introduction to these methods, and mainly discuss about microrheology, which is the main topic of this thesis.

1.3 Microrheology of soft matter

Bulk rheology probes an overall mechanical response of a sample on a macroscopic scale. It may fail to study the rheological properties of a sample under some processing and application conditions, e.g., under strong confinement. It is also unable to measure the heterogeneity of the sample, which can be significant in soft matter systems. In addition, simutaneous observation of the internal structure of the sample is normally not accessible in bulk rheology. This makes it difficult to use bulk rheology to study the rheology-structure relationship in soft matter systems.

There is a need to probe the rheological properties of soft matter systems on shorter length scales. "Nanorheology" is the technique that probes the rheological properties of a sample on the nanometer scale. For example, atomic force microscopy (AFM), nanoindentation and the surface force apparatus (SFA) are the typical techniques for nanorheology. They are able to study the rheology at a single-molecular level.[6]

In other cases, it is important to probe the rheological properties of soft matter systems on the micrometer scale, e.g., for cells or soft matter systems in microchannels. Microrheology, which focuses on the rheology on micrometer scale (100 nm$-$100 μm), close the gap between bulk rheology and nanorheology. It provides the possibility to observe the structure and the intrinsic heterogeneity of the sample when the rheological properties are probed.[7] The microrheology also has the advantage of being non-destructive (suitable to probe the viscoelastic properties of living cells),[8–10] requiring only a small sample volume, having an extended frequency range and large shear strain range. In the following the principles for different techniques of microrheology will be illustrated.

1.3.1 Passive microrheology

Passive microrheology is the technique that can be used to obtain the rheological properties of the soft matter systems, via the measurement of the thermal fluctuation of embedded micro-sized tracers. It is called “passive” microrheology because no external forces are required. Its development is based on the generalized Stokes-Einstein relation.

1.3.1.1 Generalized Stokes-Einstein relation

A spherical particle moving in a viscous fluid with a velocity of $\mathbf{v}$ feels a frictional force $\mathbf{F_d}$, called “Stokes’ drag". It acts on the interface between the fluid and the particle:[11]

$$\mathbf{F_d} = -\xi \mathbf{v} \tag{1.12}$$

The friction coefficient ξ, first derived by Stokes for small Reynolds numbers (e.g., for small particles moving in highly viscous liquid), is related to the radius of the particle (R) and the dynamic viscosity of the liquid (η):

$$\xi = 6\pi\eta R. \tag{1.13}$$

Small spherical particles in a purely viscous liquid undergo Brownian motion driven by the thermal energy k_BT, where k_B is the Boltzmann constant and T is the temperature. As the thermal forces are stochastic, the resulting mean displacement of the diffusing particles over time is zero, while the mean-squared displacement MSD ($\langle|\Delta\mathbf{x}(t)|^2\rangle$) changes over time ($t$):[7]

$$\langle|\Delta\mathbf{x}(t)|^2\rangle = \langle|\mathbf{x}(t)-\mathbf{x}(0)|^2\rangle = 2dDt \tag{1.14}$$

where $\mathbf{x}(t)$ is the position of the particle at time t, D is the diffusion coefficient, d is the dimensionality, and $\langle\bullet\rangle$ denotes time-average and/or ensemble-average. The diffusion coefficient can be obtained by the Einstein relation (or Einstein–Smoluchowski relation):[12–14]

$$D = k_BTb_T = \frac{k_BT}{\xi}. \tag{1.15}$$

Here b_T (i.e., $1/\xi$) is the translational mobility of the spherical particles in the liquid. Combining Eqs. (1.13-1.15) results in the Stokes–Einstein equation:

$$\langle|\Delta\mathbf{x}(t)|^2\rangle = \frac{d}{3}\frac{k_BT}{\pi\eta R}\,t. \tag{1.16}$$

According to the Stokes-Einstein equation, one can measure the viscosity of a liquid by measuring $\langle|\Delta\mathbf{x}(t)|^2\rangle$ of the diffusing particles inside the liquid. This is the basic idea of passive microrheology. However, the Stokes-Einstein equation is only valid for ideal viscous liquids. In another extreme when the spherical particles are in an ideal elastic matrix, the particles cannot diffuse. They can only fluctuate around their mean positions

driven by thermal forces.[15] In three-dimensional (3D) systems, the resulting $\langle|\Delta\mathbf{x}(t)|^2\rangle$ follows

$$\langle|\Delta\mathbf{x}(t)|^2\rangle = \frac{k_B T}{\pi R G}, \tag{1.17}$$

where G is the shear modulus of the elastic matrix.

For the particles in a viscoelastic matrix, one would expect that $\langle|\Delta\mathbf{x}(t)|^2\rangle$ has a time dependence between $\langle|\Delta\mathbf{x}(t)|^2\rangle \propto t^1$ and $\langle|\Delta\mathbf{x}(t)|^2\rangle \propto t^0$. In fact, the complex shear modulus ($G^* = G' + iG''$) of a viscoelastic matrix is related to $\langle|\Delta\mathbf{x}(t)|^2\rangle$ through the generalized Stokes-Einstein relation (GSER), which was firstly introduced by Mason and co-workers:[16,17]

$$G^*(\omega) = \frac{k_B T}{i\omega\pi R\mathscr{F}_u\{\langle|\Delta\mathbf{x}(t)|^2\rangle\}}, \tag{1.18}$$

where $\mathscr{F}_u$ denotes the unilateral Fourier Transform $\mathscr{F}_u\{f(t)\} = \int_0^\infty e^{-i\omega\tau} f(\tau)\, d\tau$. The GSER can be derived based on the Langevin equation, energy equipartition and fluctuation-dissipation theorem.[17] It is valid when the inertial effects of the probed particles and the probed matrix, as well as the longitudinal compression mode in the probed matrix can all be neglected. As a result, it can be predicted that the frequency range over which the GSER can be used with good accuracy is $10 - 10^5$ Hz.[7,18] In practice GSER can be used for an even broader frequency range ($10^{-2} - 10^6$ Hz).

1.3.1.2 Techniques of passive microrheology

A typical passive microrheology measurement has two steps. Firstly, $\langle|\Delta\mathbf{x}(t)|^2\rangle$ of the embedded tracer particles is measured. Secondly, the GSER is used to obtain the viscoelastic moduli of the soft matter systems based on the measured $\langle|\Delta\mathbf{x}(t)|^2\rangle$. Passive microrheology can be realized using different techniques, such as particle tracking, two-point microrheology, and light scattering techniques.

1.3.1.2.1 Particle tracking

Particle tracking microrheology uses digital microscopy to detect the motions of the particles. Image-based particle tracking routines can be used to locate the particles. The Brownian trajectories are constructed from the videos, and $\langle|\Delta\mathbf{x}(t)|^2\rangle$ can be directly obtained from the trajectories; see Fig. 1.3. As suggested by Mason, the Fourier Transform of $\langle|\Delta\mathbf{x}(t)|^2\rangle$ in Eq. (1.18) can be estimated algebraically by describing $\langle|\Delta\mathbf{x}(t)|^2\rangle$ as a local power law.[17] Compared to performing fast Fourier Transform, this method can reduce the errors of the moduli near the frequency extremes. Finally, the moduli of the probed

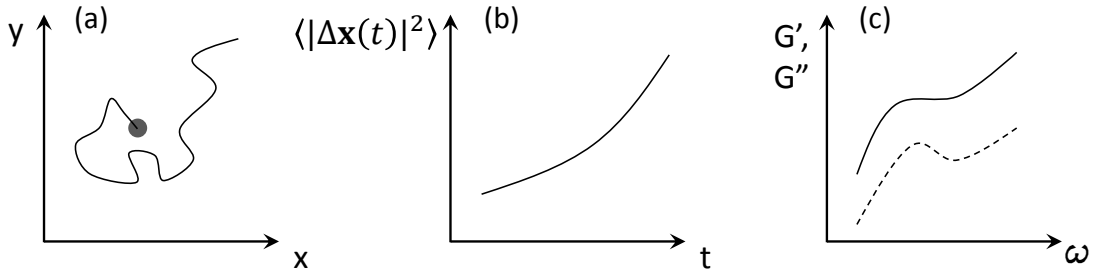

Figure 1.3 Particle tracking microrheology for determining the shear moduli of soft matter. (a) The trajectories of the tracer particles are measured. (b) The mean squared displacement ($\langle|\Delta\mathbf{x}(t)|^2\rangle$) is deduced from the trajectories. (c) The shear moduli are obtained from $\langle|\Delta\mathbf{x}(t)|^2\rangle$ based on the GSER.[7]

samples can be calculated using the following equations:[17]

$$G'(\omega) = |G^*(\omega)|\cos(\pi\alpha(\omega)/2), \tag{1.19a}$$

$$G''(\omega) = |G^*(\omega)|\sin(\pi\alpha(\omega)/2), \tag{1.19b}$$

$$|G^*(\omega)| \approx \frac{k_B T}{\pi R\langle|\Delta\mathbf{x}(1/\omega)|^2\rangle\Gamma[1+\alpha(\omega)]}, \tag{1.19c}$$

where Γ refers to the gamma function. $\alpha(\omega)$ is the power law exponent describing the logarithmic slope of $\langle|\Delta\mathbf{x}(t)|^2\rangle$ at $t = 1/\omega$. It can be obtained by: $\alpha(\omega) = \frac{\mathrm{d}\ln\langle|\Delta\mathbf{x}(t)|^2\rangle}{\mathrm{d}\ln t}|_{t=1/\omega}$.

If the ensemble-average $\langle|\Delta\mathbf{x}(t)|^2\rangle$ is measured, Eq. (1.19) results in the bulk rheology of the sample (when the tracers are much larger than the building blocks of the sample). Alternatively, when $\langle|\Delta\mathbf{x}(t)|^2\rangle$ for each particle is measured, the particle tracking method can be used to study the heterogeneity of the sample.[19]

1.3.1.2.2 Two-point microrheology

Direct use of Eq. (1.18) requires that the tracers are embedded in a homogeneous material and the tracers are strongly bond to the material. The tracers must have a "no-slip" boundary condition at their surfaces. If these conditions are not fulfilled, the particle tracking method can lead to incorrect results. For example, if the material has a porous structure, the tracers can diffuse (or hop) through the pores. Consequently, a softer and more fluid-like behavior is observed. If the small tracers are strongly adhesive to the segments of the porous material, the results from particle tracking are smaller compared to those from bulk rheology, although the correct frequency dependence can be obtained.[9] Thus, the "gold standard" to obtain the correct moduli of the sample using passive microrheology is that the size of the tracers should be larger than the size of the pores.[20] In order to decrease the uncertainties related to the interaction between the tracers and sample (i.e., the boundary conditions on the tracer surfaces), two-point microrheology has been developed.[21] The basic principle of two-point microrheology is that the Brownian motions of the tracers

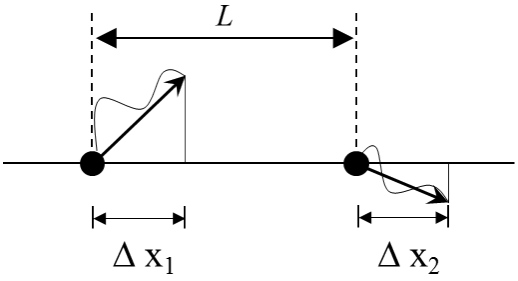

Figure 1.4 Schematic of displacements used to compute the two-point MSD.[9]

in the soft materials are statistically correlated. Two-point microrheology considers the tracers' cross-correlated motions. The cross correlation function for two particles along their connecting line (see Fig. 1.4) is:

$$C_{rr}(L,t) = \langle \Delta x_1(t) \Delta x_2(t) \rangle. \tag{1.20}$$

This cross correlation function is related to the shear modulus of the soft material following:

$$\mathscr{L}\{C_{rr}(L,t)\} = \frac{k_B T}{2\pi s L \mathscr{L}\{G(t)\}} \tag{1.21}$$

where $\mathscr{L}$ means the unilateral Laplace transform, $\mathscr{L}[f(t)] = \int_0^\infty e^{-s\tau} f(\tau)\, d\tau$, s is the complex number frequency and L means the separation between two particles (see Fig. 1.4). The two-point MSD can be calculated by:

$$\langle |\Delta \mathbf{x}(t)|^2 \rangle_2 = \frac{2L}{R} C_{rr}. \tag{1.22}$$

Substituting the two-point MSD in Eq. (1.18), the moduli of the probed samples can be obtained. The two-point MSD and one-point MSD (Eq. (1.14)) will be equal if the probed sample satisfies the following conditions: (a) homogeneous and isotropic on length scales significantly smaller than the size of the tracers, (b) incompressible, and (c) connected to the tracers by no-slip boundary conditions over their entire surfaces. If these boundary and homogeneity conditions are not satisfied, the two-point MSD and one-point MSD will be unequal. In this case, using the two-point MSD in the GSER will yield the bulk rheology of the sample (on the long length scale). Yet, using the one-point MSD results in the rheology that is a complex superposition of the bulk rheology and the rheology of the material at the tracer boundary.[9,22] Therefore, for samples with heterogeneous structures or with large pore sizes, the two-point microrheology has the merit to probe the correct bulk rheology.

1.3.1.2.3 DLS/DWS

The ensemble-average MSD of the tracer particles in the sample can also be measured using dynamic light scattering (DLS, also called photon correlation spectroscopy or quasi-

elastic light scattering). The basic idea of DLS is that the particles with a different reflective index with the medium can scatter the incident lights. The correlation function of the electric field of the scattered light $g^1(t)$ is related to $\langle|\Delta\mathbf{x}(t)|^2\rangle$ by:[23–27]

$$g^1(t) = \exp[-q^2\langle|\Delta\mathbf{x}(t)|^2\rangle/6], \tag{1.23}$$

where q is the magnitude of the scattering vector given as $q = (4\pi n/\lambda)\sin(\theta_s/2)$. Here n is the refractive index of the medium, and λ is the wave length of the light. θ_s is the angle between the incident light and the detector measuring the scattered intensity. $g^1(t)$ cannot be measured directly, but the intensity autocorrelation function, $g^2(t)$, can be measured from DLS. $g^1(t)$ and $g^2(t)$ are correlated through the Siegert relation:

$$g^2(t) = \frac{\langle I(q,0)I(q,t)\rangle}{\langle I(q)\rangle^2} = 1 + g^1(t)^2. \tag{1.24}$$

where I is the intensity of the detected scattered light. Thus, in DLS we measure $g^2(t)$, from which $g^1(t)$ and MSD can be obtained. After knowing MSD, the rheological properties of the sample can be deduced using Eqs. (1.18-1.19). Alternatively, following the same principle, DLS has been widely used to measure the size of the particles in a liquid with a known viscosity.

When a sample has a relatively high concentration of particles, photons are scattered multiple times before being detected, thus the elastic scattering condition is not fulfilled. In the limit of strong multiple scattering, diffusing wave spectroscopy (DWS) is able to use the multiple scattering signal to obtain the viscoelatiscity of the sample. DWS can probe the viscoelasticity at high frequencies (up to 1 MHz); see Table 1.1.[7,25,28]

Table 1.1 Accessible frequency and shear modulus in different microrheological techniques.[7]

Technique	Frequency range (Hz)	Modulus range (Pa)
Particle tracking	$10^{-2} - 10$	$10^{-5} - 1$
Dynamic light scattering[25,27]	$10^{-2} - 10$	$10^{-5} - 10^{1}$
Diffusing wave spectroscopy	$10^{-1} - 10^{6}$	$10^{-3} - 10^{3}$
Optical tweezer	$10^{-2} - 10^{4}$	$10^{-3} - 10^{2}$
Magnetic tweezer	$10^{-2} - 10^{3}$	$10^{-3} - 10^{4}$
Rotational magnetic chains[29]	$10^{-3} - 10^{2}$	$10^{-2} - 10^{3}$

1.3.2 Active microrheology

1.3.2.1 Optical tweezer and magnetic tweezer

In active microrheology one applies external forces to the embedded particles in the samples in order to measure the rheological properties. Optical tweezers are most widely used.

They trap and manipulate individual dielectric microspheres with diameter of the order of 1 μm. In an optical tweezer, a tightly focused laser beam is used to trap the particles. The resulting optical force can be between 0.1 pN to 100 pN. By modeling the optical trap as a linear spring (with a spring constant of k), the small displacement of the trapped particle from the center of the trap gives the information of the force acting on the particle. The stiffness of the trap depends on the following factors: the refractive indices of the particle and the surrounding medium, the size of the particle, the wavelength of the trapping light, the dimensions and photon flux in the trap focus. These factors are independent of the viscosity of the sample, making it possible to use optical tweezers for active microrheology.[30] For example, considering a single particle with a mass of M trapped in a stationary optical tweezer, the GSER can be written as[31]

$$\mathscr{L}\{G(t)\} = s\mathscr{L}\{\eta(t)\} = \frac{s}{6\pi R}\left[\frac{2dk_BT}{s^2\mathscr{L}\{\langle|\Delta\mathbf{x}(t)|^2\rangle\}} - Ms - \frac{k}{s}\right]. \tag{1.25}$$

In the brackets of Eq. (1.25), the first term is related to the thermal fluctuation of the trapped particle which reflects the viscoelasticity of the sample. The second term gives the inertial contribution of the particle. For micro-sized particles, this term is typically much smaller compared to the first term, thus it is negligible for low frequencies ($s \ll 10^6$). The third term gives the contribution from the optical trap. If $k/s \to 0$, e.g., for vanishing trap strength or at high frequencies, Eq. (1.25) recalls the GESR in Eq. (1.18). If $k/s \to \infty$, e.g., for infinitely strong trap or at extremely low frequencies, Eq. (1.25) describes a bead connected to an elastic spring with a stiffness of k. When $0 < k/s < \infty$, the third term only influences the real part of the complex modulus. Therefore, its contribution can be subtracted from the observed storage modulus.

Optical tweezers are noninvasive and allow the study of local viscoelastic properties of soft matter systems. They can measure relatively high moduli (up to 100 Pa). The highest detectable frequency of optical tweezers is $\sim$10 kHz, which is not accessible using particle tracking methods (typically limited to 10 Hz);[7] see Table 1.1.

Different to optical tweezers, magnetic tweezers use a magnetic field (gradient) to apply force on the magnetic particles. Relatively large forces (up to $\sim$2000 pN) can be applied in magnetic tweezers.[7] Compared to passive microrheology, optical and magnetic tweezers have higher measurable moduli (see Table 1.1).

1.3.2.2 Rotational-magnetic-chain microrheology

Magnetic particle chains can also be used as rheological probes in active microrheology. Different to magnetic tweezers which trigger the translation motion of the individual magnetic particles, the rotational-magnetic-chain microrheology focuses on the rotations of the chains of magnetic particles.

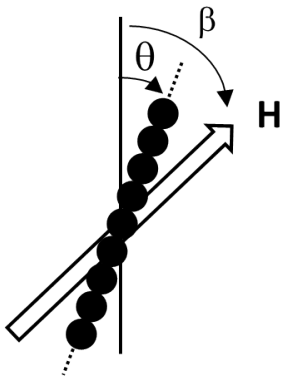

Figure 1.5 Sketch of a magnetic chain consisting of 9 paramagnetic particles. The arrow indicates the direction of the magnetic field **H**. θ is the angle relative to its initial orientation, and β is the angle of **H**.[32]

The chains of magnetic particles inside the probed sample are manipulated by a sinusoidally oscillating magnetic field **H**; see Fig. 1.5. The magnetic torque applied to a chain of N particles is[10,29,32]

$$\Gamma_m = \Gamma_0 \frac{\sin[2(\beta-\theta)]}{2}, \tag{1.26}$$

where $\Gamma_0 = \frac{3\mu_0 m^2}{8\pi}\frac{N}{(2R)^3}$, μ_0 is the permeability of vacuum, m is the magnetic moment, and $2R$ is the particle diameter. The angles β and θ are shown in Fig. 1.5. The mechanical torque acting on the particle chain is

$$\Gamma_{ve} = \kappa V G \theta, \tag{1.27}$$

where κ is the geometrical factor (determined by the number of particles in the chain) and V is the volume of the magnetic chain. Once an oscillating magnetic field with an oscillating amplitude of β_0 is applied to the magnetic chain, the chain is driven to oscillate with an amplitude of θ_0. In a viscoelastic sample, the magnetic chain oscillates with a phase lag (ϕ) behind the magnetic field. For small magnetic particles the inertial effects are negligible, leading to $\Gamma_m = \Gamma_{ve}$. Consequently, the shear moduli of the sample can be obtained based on the measured β_0, θ_0 and ϕ using the following equations:[10]

$$G' = \frac{\Gamma_0}{\kappa V}\left[\frac{\beta_0}{\theta_0}\cos\phi - 1\right], \tag{1.28a}$$

$$G'' = \frac{\Gamma_0}{\kappa V}\frac{\beta_0}{\theta_0}\sin\phi. \tag{1.28b}$$

1.3.3 Non-optical microrheology

In the above-mentioned microrheological methods, micro-sized particles are embedded into the samples, and optical techniques are used to measure the displacements of the particles under forces (external forces or thermal forces). There are also some non-optical

techniques for microrheology. The principle is similar to the conventional bulk rheometry. However, the gap of the geometry is set to be in the micrometer range. It can be realized by adapting the conventional rotational rheometer, or by using the sliding plate rheometry on the micrometer scale.[6,33] Microfluids, piezo vibrators, and radial channel flows can also be used for non-optical microrheology.[6]

1.4 Rheology at 2D

In the previous section, the rheology of 3D soft matter systems and the relating rheological techniques were introduced. Here let's decrease the dimensionality, and focus on the rheology (especially the microrheology) in two-dimensional (2D) soft matter systems.

1.4.1 Dilatational rheology

The change of interfacial tension (σ) due to the introduction of molecules or particles at the interface is called surface pressure, $\Pi = \sigma_0 - \sigma$, where σ_0 is the interfacial tension of the neat water/oil interface. The surface pressure is related to the compression state of the interfacial layer consisting of molecules or particles. For viscoelastic interfaces, Π is not only dependent on the relative change of the area of the interface $u(t)= \frac{\delta A(t)}{A_0}$ (where A represents the area and A_0 the initial area), but also on the rate of the area change $\frac{\partial u(t)}{\partial t}$. The rate-dependent contribution can be quantified by the dilatational viscosity, η_d. Under a small-amplitude oscillation ($\delta A(t) \sim e^{i\omega t}$) with an angular frequency of ω, the relationship between the surface pressure and the deformation is:[34]

$$-d\Pi(t) = \left[E'(\omega) + \eta_d(\omega)\frac{\partial}{\partial t}\right] \cdot u(t) = E^*(\omega) \cdot u(t), \tag{1.29}$$

where $E'(\omega)$ is the interfacial storage dilatational modulus and $E^*(\omega)$ is the interfacial dynamic dilatational modulus: $E^*(\omega) = -\frac{\partial \Pi(t)}{\partial A(t)/A}$. $E^*(\omega)$ is a complex number which depends on frequency. It can be written as: $E^*(\omega) = E'(\omega) + iE''(\omega)$, with $E''(\omega)$ the interfacial loss dilatational modulus ($E''(\omega) = \eta_d\omega$). For insoluble films at equilibrium or for quasi-static compression (expansion), the viscous contribution on the dilatational viscoelasticity can be neglected, thus the storage modulus equals the compression modulus (E_0), which can be deduced from the equilibrium isotherm:

$$E^*(\omega \to 0) = E_0 = -A\left(\frac{\partial \Pi}{\partial A}\right)_T. \tag{1.30}$$

Different methods have been used to study the dilatational rheology of the interface, including surface wave experiments, Langmuir trough with oscillatory barrier, and pendant drop or sessile bubble methods.[34] It should be mentioned that under the uniaxial in-plane compression in Langmuir trough, both strain and stress have the dilatational and in-plane

shear components (although for liquid interfaces the shear component is small). For elastic interfaces, a nonuniform deformation is present in conventional Langmuir troughs. Using circular barriers or vertically moving ring devices, an isotropic deformation can be produced, and the shear component can be avoided or reduced.[34,35]

1.4.2 Interfacial shear rheology

Even though the shear rheology of interface is less studied compared to the dilatational rheology, it is important because of a wide range of technical aspects such as foaming, emulsification, oil recovery and coating fabrication.[34] The dilatational rheology is related to the composition of the interfacial layers, while the shear rheology reflects essentially the structures formed at the interface.[36] A shear rheological probe at the interface not only deforms the interface, but also deforms the subphase. The dimensionless ratio between the drag from the interface and the drag from the subphase, is called Boussinesq number B_0:

$$B_0 = \frac{\text{interface drag}}{\text{subphase drag}} = \frac{\eta_\mathrm{s}(\mathrm{V_e}/L_\mathrm{c}^{\text{interface}})\mathrm{P_c}}{\eta_\mathrm{b}(\mathrm{V_e}/L_\mathrm{c}^{\text{subphase}})\mathrm{A_c}} \tag{1.31}$$

Here η_s is the surface viscosity, η_b is the bulk viscosity for the subphase, $\mathrm{V_e}$ is a characteristic velocity, $L_\mathrm{c}^{\text{interface}}$ and $L_\mathrm{c}^{\text{subphase}}$ are the characteristic length scales for the velocity decay in the interface and subphase, respectively. $\mathrm{P_c}$ is the contact perimeter and $\mathrm{A_c}$ is the contact area of the probe. When $B_0 \gg 1$, the subphase drag is negligible. When $B_0 \ll 1$, it is difficult to measure the interfacial viscosity. For the intermediate B_0, both interface and the subphase contribute to the drag on the probe. The Boussinesq number can be simplified as $B_0 = \eta_\mathrm{s}/(\eta_\mathrm{b}L)$ with L the length scale relating to the geometry of the measurement.[35] For interfacial shear rheometers, B_0 determines the sensitivity.

For the in-plane deformation of the interface, the shear modes and compression modes are decoupled (their amplitude and time evolution are independent). This makes it possible to define the interfacial shear modulus: $G_s = \sigma_{xy}/\gamma_{xy}$, where σ_{xy} is the 2D shear stress and γ_{xy} the 2D shear strain.[34] For a liquid interface, the interfacial viscosity is: $\eta_s = \sigma_{xy}/\dot{\gamma}_{xy}$, with $\dot{\gamma}_{xy}$ as the shear strain rate.

Similar to the 3D analog, the interface can be viscoelastic. Therefore, under an oscillatory shear deformation, the ratio between the 2D shear stress and the 2D shear strain $G_s^* = \sigma_{xy}(t)/\gamma_{xy}(t)$ is a complex number (called interfacial complex shear modulus):

$$G_s^*(\omega) = G_s'(\omega) + iG_s''(\omega), \tag{1.32}$$

where G_s' is the interfacial shear storage modulus and G_s'' is the interfacial shear loss modulus. For the viscoelastic interface, the Boussinesq number has the following complex form:[34,35]

$$B_0(\omega) = \frac{G_s''(\omega) - iG_s'(\omega)}{\omega L \eta_b}. \tag{1.33}$$

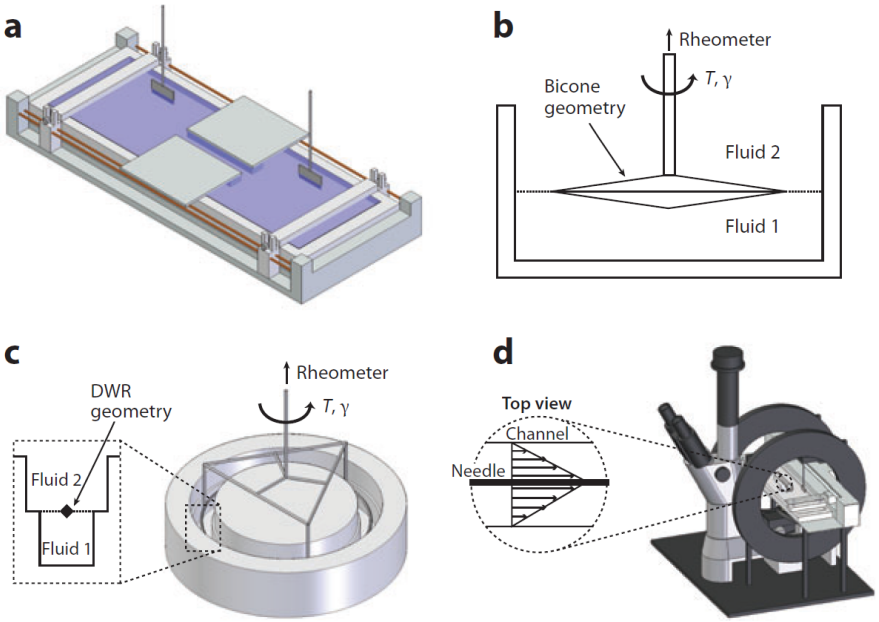

Figure 1.6 Interfacial shear rheometers: (a) surface channel rheometer, (b) bicone rheometer, (c) double-wall ring (DWR) geometry rheometer, and (d) interfacial magnetic rod stress rheometer. Reprinted from Ref. 35 with permission.

Fig. 1.6 shows several experimental setups for measuring the interfacial shear moduli. Compared to the surface channel rheometer in Fig. 1.6a, the rotational geometry (Fig. 1.6b, c) is more flexible, because it can be used in commercial rheometer to perform different types of rheological tests. According to Eq. (1.31), the ratio P_c/A_c directly influences B_0. B_0 can be increased by using thin-ring or sharp-edge geometry (Fig. 1.6c), instead of using flat or biconical disc (Fig. 1.6b).[35,37] In addition, the magnetic rod stress rheometer has been developed. It can measure the interfacial moduli from 5×10^{-6} N/m to 5×10^{-2} N/m.[38]

1.4.3 Microrheology at 2D

The macroscopic interfacial rheometer has an lower detection limit (for viscosity) of about 10^{-6} Ns/m. For many systems (e.g., polymers or proteins laden interfaces), however, the interfacial shear viscosity can be lower than this limit. Decreasing the Boussinesq number can help to decrease this measurement limit. It can be realized by using smaller probes at the interface, for example, using micro-sized particles or nanorods. 2D microrheology can measure interfacial shear viscosity as low as 10^{-10} Ns/m.[39]

1.4.3.1 Passive microrheology at 2D

The Brownian motion of the particles at the interface can be described by the 2D MSD,

$$\langle |\Delta \mathbf{x}(t)|^2 \rangle = 2dDt = 4Dt, \tag{1.34}$$

where D is the diffusion coefficient and t is the lag time. Sometimes the relative MSD ($\langle|\Delta\mathbf{x}_{rel}(t)|^2\rangle$) is used in order to get rid of the collective motion of the fluid arising from thermal gradients or sample drift:[39]

$$\langle|\Delta\mathbf{x}_{rel}(t)|^2\rangle = \langle|\Delta\vec{\mathbf{x}}_i(t) - \Delta\vec{\mathbf{x}}_j(t)|^2\rangle = 8Dt. \tag{1.35}$$

Here, i and j indicate two particles, and $\Delta\vec{\mathbf{x}}_i(t)$ is the displacement vector for particle i. The Einstein's equation, $D = k_B T b_T$ (b_T–translational mobility) is still valid in 2D systems, but the Stocks' law for the viscous drag on the particle (Eq. (1.12)) does not apply for the particles moving at the interface. Different models have been proposed to obtain the friction coefficient of particles at the interface. For example, Saffman and Delbrück modeled a cylindrical object of radius R embedded in a membrane of thickness h and a viscosity of η_m.[40] Here, η_m is the 3D viscosity of the membrane material. It is related to the interfacial viscosity by $\eta_s = \eta_m h$. The both sides of the membrane are in contact with the adjacent liquid phases with a viscosity of η_b. Using the hydrodynamic description and the non-slip boundary condition around the cylinder, different solutions can be found based on different assumptions. If the membrane has a finite size, the cylinder at the center of a circular membrane of radius R_m ($R_m \gg R$) has a translational mobility as

$$b_T = \frac{1}{4\pi\eta_{\mathrm{m}}h}(\ln\frac{R_m}{R} - \frac{1}{2}). \tag{1.36}$$

If the viscosity of the subphases is taken into account, then

$$b_T = \frac{1}{4\pi\eta_{\mathrm{m}}h}(\ln\frac{\eta_{\mathrm{m}}h}{\eta_{\mathrm{b}}R} - 0.5772). \tag{1.37}$$

This equation is still valid if the cylinder protrudes from the membrane. More generally, Hughes et al. extended this expression into[41]

$$b_T = \frac{1}{4\pi\eta_{\mathrm{m}}h}[\ln(2/\varepsilon) - 0.5772 + \frac{4}{\pi}\varepsilon - \frac{1}{2}\varepsilon^2\ln(2/\varepsilon) + \mathrm{o}(\varepsilon^2)], \tag{1.38}$$

where $\varepsilon = R(\eta_1 + \eta_2)/(\eta_{\mathrm{m}}h)$, with η_1 and η_2 the viscosities of the subphases on both sides of the interface. In addition, some theoretical models also take into account the finite thickness of the subphases.[42,43]

These models have been used to explain the experimental results. For example, Eremin et al. studied the 2D microrheology of freely suspended liquid crystal membranes. In the membrane where the Saffman length ($l_S = \eta_m h/2\eta_b$) is comparable or larger than the membrane width, the confinement effect (finite size of the membrane) governs the motion of the small inclusion (i.e., $R \ll l_S$). For the Saffmann length which is smaller than the membrane size, the coupling between the inclusion and the subphase determines the motion of the inclusion.[44]

Saffman and Delbrück's model considers a thin cylinder in the membrane. For the microrheological methods, however, spherical colloidal particles are typically used. Danov

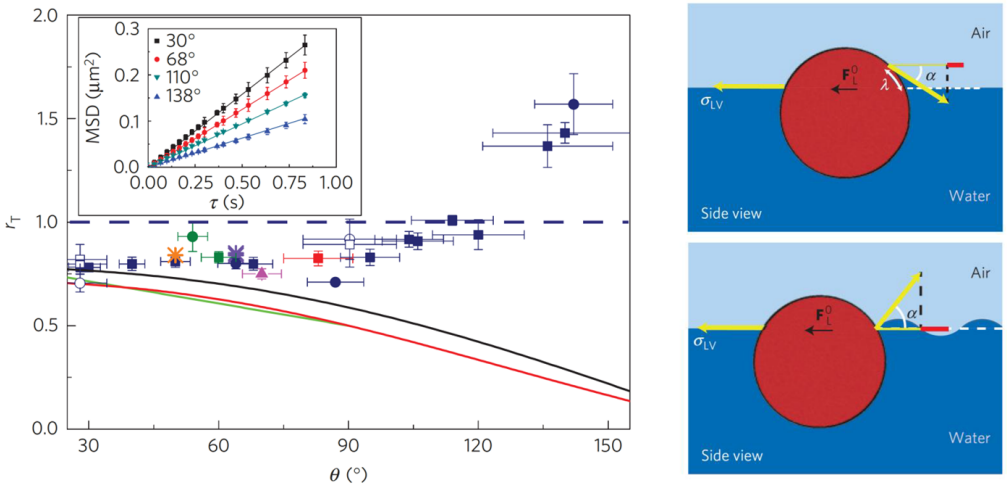

Figure 1.7 The ratio of the translational viscous drags at the interface and in the bulk r_T of spherical particles at a fluid interface versus contact angle. The data points are from experiments while the solid curves are from existing theoretical models. The deviation between experiments and theories becomes more obvious for larger contact angles. The inset shows MSDs for silica particles at the interface with different contact angles. The right sketches show the two mechanisms for the fluctuation of the triple line. Top: moving contact line on the particle surface; bottom: capillary wave at the interface. Reprinted from Ref. 47 with permission.

et al. study the motion of a spherical particle partially immersed in a viscous fluid (i.e., the particle is at the liquid-gas interface) in the frame of low Reynolds number hydrodynamics. Their results reveal that the drag and torque exerted on the floating particle depend heavily on the surface viscosity as well as the contact angle.[45]

As an extension of Saffman and Delbrück,[40] Hughes et al.[41] and Stone and Ajdari,[43] Fischer et al. incorporated Marangoni forces into the treatment of a sphere immersed in a membrane by solving the equations for an incompressible interface.[46] The Marangoni stress is a tangential surface stress due to the gradients in surface tension (e.g., due to gradients in surface density of surfactants). In the limit of vanishing surface compressibility, the Marangoni effect can be simply incorporated into theoretical description by approximating the interface as incompressible. Fischer et al. showed that the Marangoni effect in the membrane can strongly influence the drag on the sphere immersed in the membrane. In addition, the effect of protrusion of the sphere into the subphase is more important when the surface viscosity of the membrane is low.

Recently, Boniello et al. showed experimentally that a particle straddling an water/air interface felt a viscous drag that was unexpectedly larger than that in the bulk.[47] The ratio of the translational viscous drags (friction coefficients) at the interface and in the bulk r_T is plotted as a function of contact angle of particles at the interface in Fig. 1.7. The deviation from the theories (based on the hydrodynamics) became more significant when the particles were modified to be more hydrophobic (larger contact angle). Ruling

out the possible causes by the contamination and additional hydrodynamic effects such as wedge flow, the authors concluded that a new theoretical paradigm beyond hydrodynamics should be proposed to understand this deviation. They suggested that the thermally activated fluctuation of the triple line could give rise to extra random forces on the particles, which led to the additional viscous drag (diffusion slowing down). The thermally activated deformations of the interface could have two mechanisms. First, in the limit of the moving contact line around the particle, it was due to the thermally activated jumps of water molecules between hydrophilic sites at the particle surface. By hydrophobization, the spacing between hydrophilic sides increased, leading to larger fluctuation at the triple line. The second mechanism assumed that the three phase contact line was pinned at the particle surface, and the thermal fluctuation of the interface came from the capillary waves at the interface (with a correlation length of about 1 nm). Based on these experimental observations, it can be concluded that so far, not everything is well understood for the viscous drag of a colloidal particle moving at the interface.

Even though there are still fundamental issues on determining the drag coefficient of the particles at the interfaces, microrheology has been used to study the rheological properties of the interfaces. For example, based on Eq. (1.37), Prasad et al. used two-particle microrheology to study a quasi-2D system (human serum albumin protein at air-water interface).[48] They observed a transition of the particle motion from interface-dominated (at high η_s) to subphase-dependent (at low η_s). This two-particle-microrheology technique can provide accurate measurement of the surface viscosity even when the interface shows heterogeneity. The upper limit of detection for passive microrheology at 2D is $\eta_s \sim 10^{-6}$ Ns/m.[49]

1.4.3.2 Active microrheology at 2D

The upper limit of detection for microrheology in 2D systems can be increased using active microrheology. The active microrheology can also be used to study the force/velocity dependence of the 2D rheological properties. One of the most widely used active microrheological techniques at 2D is the optical tweezer. For example, Park et al. used the oscillating optical tweezer to probe the shear moduli of the lipid monolayers and the polyelectrolyte/insoluble lipid composite monolayers with a wide range of frequency (sub-Hz to $\sim$ 2000 Hz).[50,51]

The magnetically driven micro-/nano-sized probes can also be used for the active microrheology at 2D. Dhar et al. used the nanorod viscometer (300 nm in diameter) to study the surface viscosity of albumin at an air-water interface.[49] They found that even though the surface pressure saturated in short times (in minutes), the surface viscosity increased from 10^{-9} to 10^{-5} Ns/m over 2 h. Their results implied that during annealing, a more densely packed film with changes in the inter-protein interactions formed, leading to the increase of shear resistance. These changes could not be reflected by the surface pressure.

The nanorod active microrheology provides the same sensitivity as passive microrheology, but it can measure higher viscosity compared to passive microrheology. The measurable range of the interfacial viscosity using micro-/nano-sized probes is $10^{-9} - 10^{-3}$ Ns/m.[52]

It is also possible to perform active interfacial microrheology using the ferromagnetic microbutton (or microdisk) probes.[53–55] These ferromagnetic microbutton probes are fabricated using photolithography. They are coated with ferromagnetic materials (e.g., nickel). The "buttonholes" in the microdisks make them orientationally anisotropic and their rotation trackable. Their size can be as small as several microns, thus simutaneous structural and rheological measurements are feasible. They can measure interfacial shear moduli in the range of $10^{-8} - 10^{-3}$ N/m.

In addition, because of the complex physics of the triple lines around the particles at the interface (e.g., the thermal fluctuation of the triple line, as discussed above), some researchers have explored some non-contact microrheological techniques to study the interfacial properties. For example, Boatwright et al. used optical tweezer to locate the probed particle at a short distance below the air/water interface. Through the in-plane fluctuations of the particle, they were able to measure the rheological properties of the interface.[56]

1.5 Interactions between colloidal particles

The rheological properties of soft matter systems are controlled by the interactions between their building blocks. For example, in soft matter systems consisting of particles (e.g., colloidal suspensions and gels), the interactions between the colloidal particles in the suspending liquids determine the rheological properties. In the following I will give a brief overview of the typical interactions between colloidal particles in 3D and 2D systems.

1.5.1 Colloidal particles in 3D systems

1.5.1.1 Van der Waals Forces

The van der Waals forces between molecules include three types: (i) the Keesom interaction which is the interaction between dipoles; (ii) the Debye interaction which is the interaction between permanent and induced dipoles; and (iii) the London dispersion interaction which is caused by fluctuative interactions between neutral atoms or molecules with no permanent dipoles. The interaction energies of these forces scale as $1/L^6$, with L the intermolecular distance.[57]

Although the van der Waals interactions between molecules decay quickly with increasing the intermolecular distance, the summation (pairwise additivity) of all the forces

between molecules inside the colloidal particles leads to long-range van der Waals interactions. The van der Waals interaction energy for two particles with radii of R_1 and R_2 and a center-center distance of L in vacuum is:

$$U_{vdW} = -\frac{A_{12}}{6}\left[\frac{2R_1R_2}{L^2-(R_1+R_2)^2}+\frac{2R_1R_2}{L^2-(R_1-R_2)^2}+\ln\frac{L^2-(R_1+R_2)^2}{L^2-(R_1-R_2)^2}\right], \quad (1.39)$$

where A_{12} is the Hamaker constant, which is typically in the range of $(0.4-4)\times10^{-19}$ J. This means that for two particles with radius of 0.5 μm, using $A_{12} \approx 1\times10^{-19}$ J, U_{vdW} becomes comparable to the thermal energy k_BT (or 10 k_BT) when the surface-surface distance is 220 nm (or 60 nm). The van der Waals force between two particles in vacuum will always be attractive.[57]

In Eq. (1.39), U_{vdW} is obtained using simple pairwise additivity, ignoring the influence of neighboring molecules on the interactions between pairs of molecules. This is only valid in rarefied media (gases). For particles interacting through a medium, simple pairwise additivity does not apply. To solve this problem, Lifshitz theory treats the particles as continuous media and express the interaction between the particles in terms of bulk properties (dielectric constants and refractive indices). The structure of Eq. (1.39) still holds, but one needs to replace the Hamaker constant with the effective Hamaker constant (A). In a medium, A depends on the dielectric constants of the medium (ε_m) and the particles (ε_p, assuming that the particles consist of the same material), as well as on their refractive indices n_m and n_p:

$$A = \frac{3}{4}k_BT\left(\frac{\varepsilon_p-\varepsilon_m}{\varepsilon_p+\varepsilon_m}\right)^2+\frac{3h\nu_e}{16\sqrt{2}}\frac{(n_p^2-n_m^2)^2}{(n_p^2+n_m^2)^{3/2}} \quad (1.40)$$

where h is the Planck constant and ν_e is the main electronic absorption frequency in the UV (typically around 3×10^{15} s^{-1}).[58] Eq. (1.40) reveals that the van der Waals force between two identical particles in a medium is always attractive (if the particles in the medium have different dielectric constants, the van der Waals force between them may be repulsive).

1.5.1.2 Electrical double layer forces

Because of the van der Waals force, dispersed colloidal particles have a tendency to aggregate. In water (or any liquid of high dielectric constant), however, charged particles can produce long-range repulsive forces which prevail over the van der Waals forces, preventing the aggregation.[59,60] The charges at the surface of the particles can come from the ionization or dissociation of the surface groups, or from adsorption (binding) of ions from solution onto the surface. The surface charges produce an electric field which attracts counter ions from the solution. The surface charge layer and the counter ion layer near the surface form the "electrical double layer".[60] The electric potential decreases exponentially from the surface to the solution, with an characteristic decay length (κ^{-1}),

called Debye length. When two like-charged colloidal particles of radius R in water approach each other, the overlapping of the double layer can lead to an repulsive interaction potential:[58,59]

$$U_r = \frac{64\pi R\rho_\infty k_B T}{\kappa^2}\gamma_p{}^2\exp(-\kappa h), \tag{1.41}$$

where h is the surface-surface separation between the particles, and ρ_∞ is the bulk density of ions. γ_p is the reduced surface potential: $\gamma_\mathrm{p} = \tanh[ze\psi/(4k_BT)]$, where z is the ion valency, e is the elementary charge, and ψ is the electrical potential.

In the DLVO theory (named after Derjaguin, Landau,Verwey and Overbeek),[61,62] the van der Waals force and the electrical repulsive force are combined to describe the interaction between charged particles in water. In a particle suspension, the other inter-particle interaction forces may also exist. These forces include the solvation forces, hydrophobic forces, steric forces, depletion forces, etc.[59] In the following, I will mainly introduce the field-induced forces, because they are most related to the rheological properties of the stimulus-responsive soft matter systems, which are the main focus of this thesis.

1.5.1.3 Field-induced forces

It is possible to control the interactions between colloidal particles using external fields (e.g., electric or magnetic fields). This field-responsive property is important for designing intelligent materials and devices. For example, magnetorheological (MR) fluids find their applications as dampers, brakes, clutches, valves, artificial joints, precision polishing, and sensors, etc.[63] Under a magnetic field, the magnetic particles in the MR fluids are polarized, acting as magnetic dipoles and aligning into chains and columns. Consequently, the MR fluids change into a solid state under a magnetic field (i.e., the apparent viscosity increases for several order of magnitudes when the magnetic field is switched on).

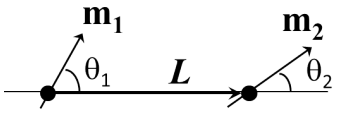

Figure 1.8 Configuration of two magnetic dipoles, $\mathbf{m_1}$ and $\mathbf{m_2}$, separated with an inter-particle distance of L.

The magnetorheological effect of the MR fluids arises from the magnetic-field-induced polarization of the magnetic particles. For MR fluids, micro-sized carbonyl iron particles are most widely used as the magnetic particles because of their high saturation magnetization and low remanence.[63] The magnetic interaction potential between two magnetized particles is[64]

$$U_{dd} = \frac{\mu_0}{4\pi}\frac{1}{L^3}[\mathbf{m_1}\cdot\mathbf{m_2} - 3(\mathbf{m_1}\cdot\hat{\boldsymbol{L}})(\mathbf{m_2}\cdot\hat{\boldsymbol{L}})], \tag{1.42}$$

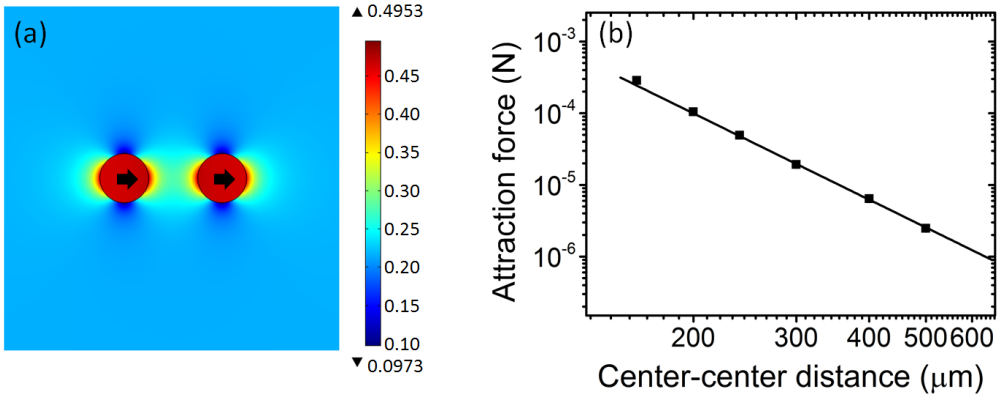

Figure 1.9 (a) The magnetic flux density around two Nickel particles in a homogeneous magnetic field, simulated using Comsol Multiphysics software. The arrows at the centers of the particles indicate the direction of magnetization. The colormap gives the flux density of the magnetic field (unit Tesla). The radius of the particles is 75 μm and their center-center distance is 150 μm. The external applied field is 216 mT along horizontal direction. The input magnetization curve for simulation is obtained by measuring a commercial Nickel powder sample (Alfa Aesar, $-100+325$ mesh, purity 99.8%). (b) The simulated force between the two Nickel particles as a function of the center-center distance. The data points are from simulation, and the solid line is obtained based on Eq. (1.42).

where μ_0 is the permeability of vacuum, $\mathbf{m_1}$ and $\mathbf{m_2}$ are the vectorial magnetic moments, $\boldsymbol{L}$ is the vector connecting the two magnetic moments (with a length of L and a normalized vector of $\hat{\boldsymbol{L}}$), and θ_1 (or θ_2) is the angle between $\mathbf{m_1}$ (or $\mathbf{m_2}$) and $\boldsymbol{L}$, see Fig. 1.8. Two identical paramagnetic particles in a homogeneous magnetic field are polarized along the same direction, thus $\theta_1 = \theta_2 = \theta_m$. The resulting interaction is attractive when θ_m is smaller than the so-called magic angle (54.7°).

The dipole moment of a paramagnetic particle in a homogeneous magnetic field is related to the magnetization property of the material: $|\mathbf{m}| = VM_m$, where V is the volume of the particle and M_m is the magnetization of the material. The magnetization can be deduced by $M_m = \chi_s H_i$, where χ_s is the susceptibility and H_i is the magnetic field inside the particle. In typical systems, we know the external applied magnetic field H_a instead of H_i. These two fields are different because of the demagnetization effect: $H_i = H_a - N_d M_m$ with N_d the demagnetization factor ($N_d = 1/3$ for spherical particles).[65] At low fields (linear magnetization), the magnetization of a spherical particle is

$$M_m = \chi_s H_i = \frac{\chi_s}{1+\chi_s/3} H_a. \tag{1.43}$$

At high fields where the linear magnetization is not fulfilled, we need to use the magnetization curve $M_m(H_i)$ for the material to obtain $M_m(H_a)$. Briefly, knowing the $M_m(H_i)$ we can deduce $M_m(H_a)$ based on $H_a = H_i + 1/3M_m$. This is the inverse process of using the vibrating sample magnetometer (VSM) to measure the magnetization curve $M_m(H_i)$: in a VSM measurement, the magnetic moment of the sample with a defined shape is mea-

sured at different external magnetic fields (i.e., $M_m(H_a)$ is originally measured), and the magnetization curve $M_m(H_i)$ is obtained after correcting the demagnetization effect.

Fig. 1.9 shows the magnetic flux density around two Nickel particles under a homogeneous magnetic field (along the horizontal direction). The magnetic force between the two particles can be well described using Eq. (1.42) (attraction force $= dU/dr$) .

1.5.2 Colloidal particles at interfaces

1.5.2.1 Repulsive forces

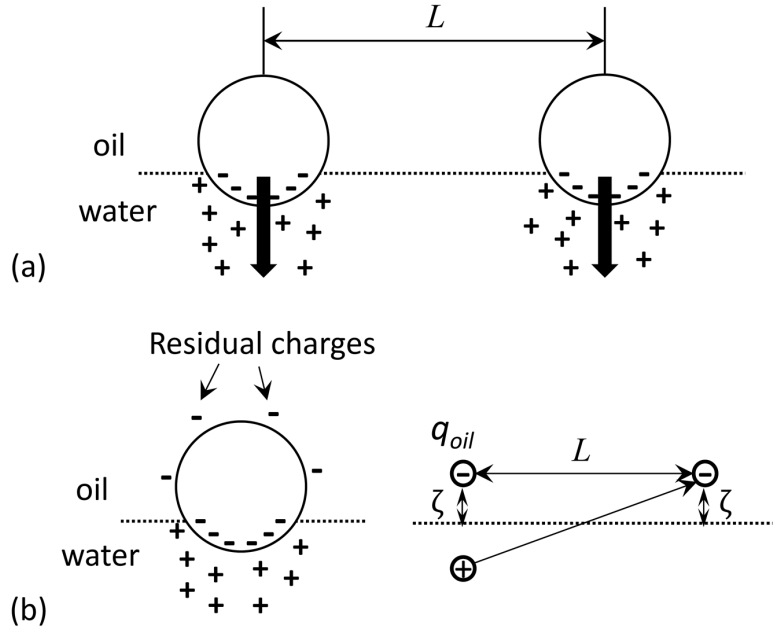

Figure 1.10 (a) Schematic of the dipolar interaction between two charged particles at the interface. The arrows indicate the resulting dipoles due to the asymmetric distribution of the charges.[66] (b) At the oil side, there may be some residual charges on the surface of the particle. These redidual charges are treated as a point charge q_{oil} located above the water/oil interface with a distance of ζ. At short distance the interaction between the particles is dominated by the charge-charge interaction through the oil, while at long distance, the dipole-charge interaction dominates because of the influence of the image charge.[67]

Charged colloidal particles at the water/oil (or water/air) interface tend to form highly ordered structures because of the electrostatic repulsion forces.[66] Compared to the electrostatic forces in water, the repulsive forces between the colloidal particles at the interface can be significantly enhanced.[68] One reason for this enhanced repulsion force is the asymmetry of the ionic cloud around the particles at the water/oil interface; see Fig. 1.10a. On the water side the particles are charged and have the electrical double layers, while on the oil side the particles are uncharged. This gives the particles at the interface a dipolar structure, leading to the long-range dipole-dipole repulsions between the particles. The

resulting dipole-dipole interaction force is[69]

$$f_{\text{inter}} \approx \frac{3\varepsilon_{\text{oil}} q_{\text{water}}^2}{2\pi\varepsilon_0 \varepsilon_{\text{water}}^2 \kappa^2 L^4}, \tag{1.44}$$

where L is the inter-particle distance L, ε_0 is the permittivity of free space and ε_{oil} and $\varepsilon_{\text{water}}$ are the relative dielectric constants of oil and water, respectively. κ^{-1} is the Debye screening length. q_{water} is the charge in the water-immersed part. It can be obtained by: $q_{\text{water}} = 2\pi R^2(1+\cos\theta_w)C_{water}$ for $\kappa R \ll 1$; for $\kappa R \gg 1$, $q_{\text{water}} = 2\pi R \sin\theta_w \kappa^{-1} C_{water}$, where R is the radius of the particle, C_{water} is the surface charge density on the water side, and θ_w is the contact angle of the particles at the interface measured from the water side.[69]

In some experimental systems, it is found that the repulsion force described by Eq. (1.44) is too small to explain the experimental results. As suggested by Aveyard et al., the repulsive force between charged colloidal particles at the interface can be mainly due to the residual charges at the particle-oil interface; see Fig. 1.10b.[67,69] The charges are presented as a point charge q_{oil} located at a distance ζ above the oil-water interface ($\zeta = R(3+\cos\theta_w)/2$). With this consideration, the interaction force between the particles is

$$f_{\text{inter}} \approx \frac{q_{\text{oil}}^2}{4\pi\varepsilon_{\text{oil}}\varepsilon_0}\left[\frac{1}{L^2} - \frac{L}{(4\zeta^2+L^2)^{3/2}}\right]. \tag{1.45}$$

The first term represents the Coulombic force between two identical point charges. The second term represents the force between the point charge and the image charge of another particle (image charge appears due to the oil/water interface). For large separations ($(\zeta/L)^2 \ll 1$), the interaction between the colloidal particles has the asymptotic form:

$$f_{\text{inter}} \approx \frac{6q_{\text{oil}}^2\zeta^2}{4\pi\varepsilon_{\text{oil}}\varepsilon_0 L^4}. \tag{1.46}$$

The decay of the repulsive force between charged particles at the interface as L^{-4} has been measured using optical tweezer.[69–71]

1.5.2.2 Attractive forces

Apart from the repulsive forces for charged colloidal particles at the interface, it has been widely reported that the particles at the interface can show long-range attractions. For macroscopic particles on the interface, the gravity acting on the particles can cause the deformation of the interface, leading to a long-range attraction force (capillary force) between the particles. For micro-sized colloidal particles, their weight is too small to deform the interface. However, since the colloidal particles have a certain degree of surface roughness and chemical inhomogeneity, the three-phase contact lines surrounding the particles are in fact undulated; see Fig. 1.11a. As a result, the interface around the

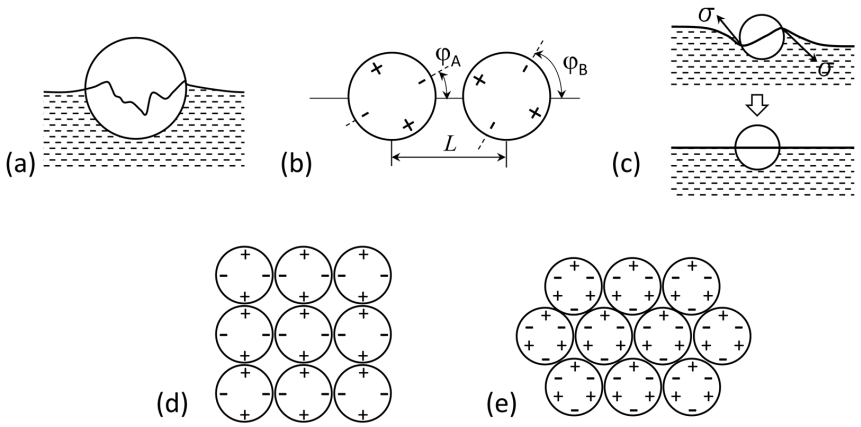

Figure 1.11 (a) Undulation of the contact line at the particle surface. (b) Sketch of two capillary quadrupoles. The signs "+" and "-" denote positive and negative "capillary charges", i.e., convex and concave at the interface. Orientations of the quadrupoles are presented by φ_A and φ_B. (c) Capillary dipole does not exist for micro-sized spherical particles because the particle can rotate to the equilibrium position. (d) Square array of capillary quadrupoles. (e) Hexagonal array of capillary hexapoles.[72,73]

particle is deformed. The deformed interface leads to the capillary interactions between the micro-sized colloidal particles at the water/oil interface. The height of the contact line around a particle can be decomposed into multipoles using

$$h(r_c,\phi) = \sum_{k=2}^{\infty} H_k \cos[k(\varphi - \varphi_{k,0})], \tag{1.47}$$

where H_k is the amplitude of the undulation (for mode k) of the contact line whose average radius is r_c. φ is the orientation angle (see Fig. 1.11b) and $\varphi_{k,0}$ is the phase angle. The monopole ($k = 0$) is not present because the normal force (e.g., the gravity) acting on the micro-sized particle is negligible. The dipole ($k = 1$) is also not present because it can be automatically canceled by self rotation (see Fig. 1.11c). Thus the quadrupolar term ($k = 2$) is the leading term in the multipole expansion.[72]

Considering two particles A and B with the same size and the same undulation of the contact line, the interaction potential for the quadrupoles is

$$U_{qq}(L) \approx -12\pi\sigma H_2^2 \cos[2(\varphi_A - \varphi_B)]\frac{r_c^4}{L^4} \quad (\text{for } L \gg 2r_c), \tag{1.48}$$

where σ is the interfacial tension, H_2 is the undulation amplitude of the contact line for quadrupole, and $\varphi_A - \varphi_B$ is the relative (in-plane) orientation angle (see Fig. 1.11b). For example, assuming $\sigma \sim$70 mN/m, $H_2 \sim 20$ nm and $r_c/L \sim 0.3$, the resulting attraction energy reaches up to 2080 k_BT.[72,73]

The interactions between the capillary multipoles depend on the mutual orientations of the particles. As a result, quadrupoles tend to form square lattice or chains, while

hexapoles tend to form hexagonal lattice (see Fig. 1.11d, e). The particles at the interface interacting through the capillary multipoles are expected to behave as 2D elastic solids. For a square array of close-contact quadrupoles, the shear storage modulus is $G_s' = 23\sigma(H_2/r_c)^2$. For a hexagonal array of close-contact hexapoles, the shear storage modulus is $G_s' = 255.46\sigma(H_3/2r_c)^2$. For example, using $\sigma \sim$70 mN/m and $H_k/r_c \sim 0.1$, the resulting shear moduli are 16 mN/m and 45 mN/m for the square and hexagonal arrays, respectively (the other interactions between particles in close contacts are neglected for this simple estimation).[73,74]

1.6 Pickering-Ramsden emulsions

The soft matter systems consisting of colloidal particles at the interface, for example, Pickering-Ramsden emulsions, have many relevant industrial applications. In the following, I will introduce the Pickering-Ramsden emulsions and the rheological properties of colloidal monolayers at the interface. It will be shown that the rheological properties of the colloidal monolayers are strongly correlated with the interactions between the colloidal particles at the interface.

1.6.1 Introduction to Pickering-Ramsden emulsions

About 110 years ago, Pickering and Ramsden discovered that solid particles can be used to stabilize the emulsions.[75,76] The major benefit of Pickering-Ramsden emulsions is that they have a high resistance to coalescence, and they can be used in application fields which require "surfactant-free" products (surfactants may show adverse effects, e.g., irritancy or hemolytic behavior).[77]

At equilibrium, the solid particles can be located at the water/oil (or water/air) interface if they can be partially wetted by water and oil. This is controlled by the following interfacial tensions between different phases: σ_{sw} (solid-water), σ_{so} (solid-oil) and σ_{wo} (water-oil). A particle locating at an interface in Fig. 1.12a should fulfill the Young's law:[77]

$$\cos(\theta_w) = \frac{\sigma_{so} - \sigma_{sw}}{\sigma_{wo}}, \tag{1.49}$$

$$\cos(\theta_o) = \frac{\sigma_{sw} - \sigma_{so}}{\sigma_{wo}}. \tag{1.50}$$

The particle will be totally immersed in water if $\sigma_{so} > \sigma_{wo} + \sigma_{sw}$, and totally immersed in oil if $\sigma_{sw} > \sigma_{wo} + \sigma_{so}$; when $\sigma_{so} = \sigma_{sw}$, $\theta_w = 90°$. For hydrophilic particles, $\theta_w < 90°$, the larger parts of the particles are located on the water side. This adsorption state facilitates the formation of oil-in-water emulsions (Fig. 1.12b). On the contrary, for the hydrophobic particles, $\theta_w > 90°$, the larger parts of the particles are located in the oil phase. This adsorption state facilitates the formation of water-in-oil emulsions (Fig. 1.12c).

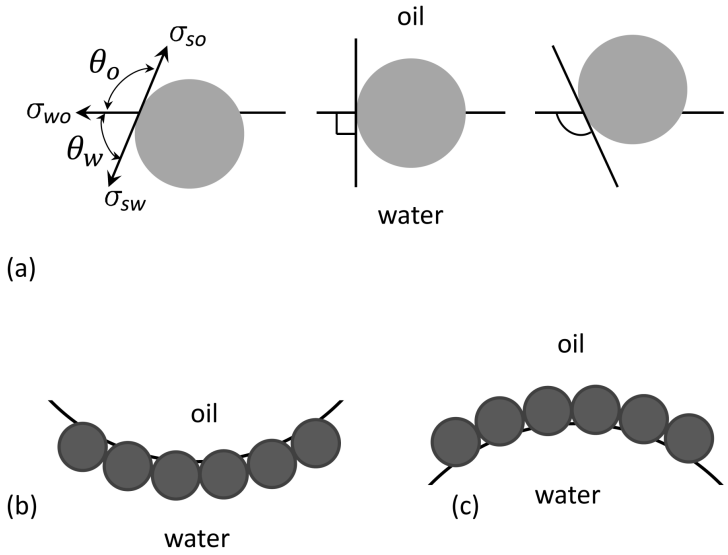

Figure 1.12 (a) Position of solid colloids at the water/oil interface for a contact angle (θ_w, measured on the water side) smaller than 90°, equal to 90°, and larger than 90°. For $\theta_w < 90°$, solid-stabilized oil-in-water emulsions may form (b); while for $\theta_w > 90°$, solid-stabilized water-in-oil emulsions may form (c).[78]

For low-molecular-weight surfactants at the water/oil interface, the adsorption and desorption take place on a relatively fast timescale. However, for colloidal particles at the interface, thanks to the fact that the detachment energy is much larger compared to thermal energy, they are strongly bond to the interface. The detachment energy U_d for a colloidal particle with a radius of R at the water/oil interface can be obtained by:

$$U_d = \pi R^2 \sigma_{wo} [1 \pm \cos(\theta_w)]^2. \tag{1.51}$$

The sign in the bracket is negative (or positive) if the particle is moved from the interface to the water (or oil) phase. For a particle with a diameter of 1 μm, a θ_w of 90°, and a σ_{wo} of 43 mN/m (i.e., for a water/polydimethylsiloxane interface), U_d is $\sim 8 \times 10^6\ k_B T$. This large detachment energy ensures that the particle sticks at the interface irreversibly.

1.6.2 Surface activity of solid colloids at interface

The adsorption of the solid colloids onto the interface leads to the decrease of entropy (from 3-dimensionality to 2-dimensionality). However, as shown by Eq. (1.51), the surface energy can be significantly decreased by adsorption of particles onto the interface. Thus, from a thermodynamic point of view, the partially wetted particles tend to locate at the interface. From a kinetic point of view, as the neat water/oil (or water/air) interface is negatively charged, the negatively charged particles can hardly adsorb at the interface without any mechanical energy input. In contrast, the positively charged particles can be

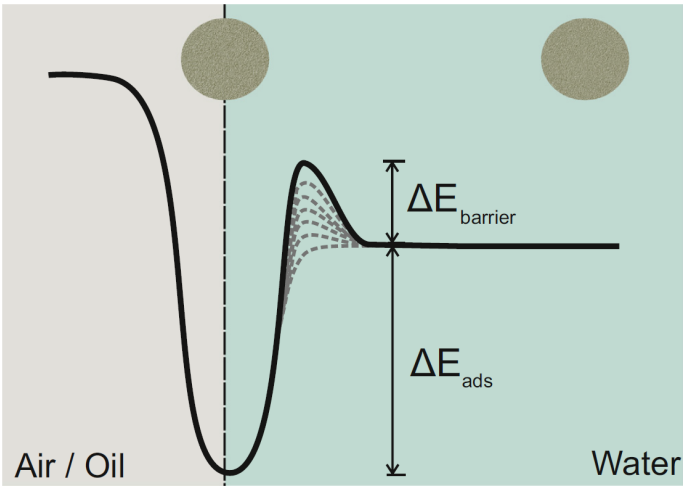

Figure 1.13 Schematic illustration of the energy landscape at the water/air (or water/oil) interface. The energy barrier $\Delta E_{barrier}$ increases as the surface coverage of particles increases. Reprinted from Ref. 79 with permission.

easily adsorbed.[79] The energy barrier for adsorption of a particle onto the interface also increases when the water/oil interface is covered with particles (Fig. 1.13).[79]

The charged particles at the interface can produce a repulsive potential between neighboring particles, leading to a 2D osmotic pressure inside the particle monolayer. The surface pressure, i.e., the decrease of surface tension, shows an increasing tendency under compression. The repulsive monolayer collapses by folding (buckling) when the surface pressure equal to the surface tension of the neat water/oil interface.[80] Even though it is reported that the repulsive particles can be used to produce stable emulsions with a low surface coverage, in an industrial process, their resistance to strong flow and external forces is challenged. The emulsions with aggregated particle networks at the water/oil interfaces are more stable.[81]

1.6.3 Rheology of solid particle monolayers at interface

The stability of an emulsion is strongly correlated with the rheological property of the particle monolayers at the water/oil interface, because the deformation during the droplet collisions produces shear and compression stresses in the interfacial layers.[82] A mechanically rigid network at the interface can hinder the coalescence of the droplets. Once coalescence occurs, the interfacial area decreases, leading to an increase of the particle density at the interface. Further coalescence can be prevented when the particles become closely packed at the interface; see Fig. 1.14 for the experimental observation of the coalescence process of particle-covered droplets.[83]

The rheological properties of the particle monolayers depend on their structures. The monolayers with crystalline structures behavior like elastic solids.[68,84] They show a divergence of the storage modulus near close packing. The monolayers with aggregated

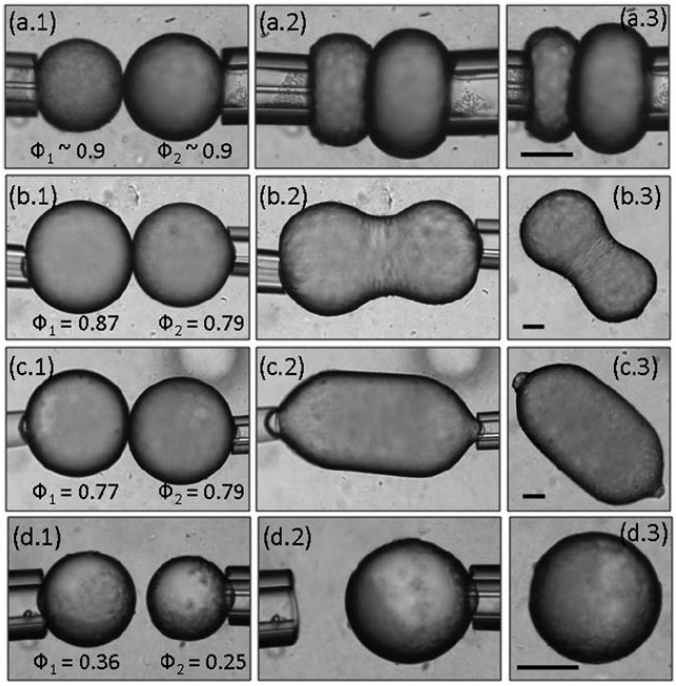

Figure 1.14 Coalescence behavior influenced by the droplet surface coverage (ϕ). (a) At high surface coverage, the two droplets are stable. (b, c) At intermediate surface coverage, arrested coalescence is observed. (d) Complete coalescence of the droplets occurs when the surface coverage is low. The scale bars represent 50 μm. Reprinted from Ref. 83 with permission.

structures behave similar to their 3D counterparts. For example, they have higher storage moduli compared to loss moduli, their rheological properties are sensitive to shear strain, and the storage moduli increase with increasing the surface coverage following a power law. The structural and rheological properties of the particle monolayers can be tuned by changing the inter-particle interactions.

Bykov et al. reported the dilatational elasticity of monolayers consisting of polystyrene microparticles at the water/air interface (0.01 M NaCl solution as the aqueous phase). They found that the whole range of the surface pressure isotherm had 3 regimes: at low compression, the electrostatic interactions between particles dominated the dilatational elasticity (< 50 mNm^{-1}); in the second region, the hydrophobic interactions between the particles led to the high dilatational elasticity (~ 500 mNm^{-1}). At high compression, however, the monolayer collapsed and the dilatational elasticity was almost zero. In another work by Safouane et al., it was found that by increasing the particle hydrophobicity, the dilatational/shear storage moduli of the particle monolayers increased.[82] This phenomenon was interpreted by the fact that with increasing hydrophobicity, the particle surfaces became more heterogeneous. As a result, the capillary interactions between particles became stronger, leading to larger storage moduli of the particle monolayers.

1.7 Microgels at interface

In the previous sections, the interactions and the rheological properties of solid colloids at the water/oil interface were discussed. Compared to the systems with solid colloids at the interface, the systems with soft colloids at the interfaces are less studied. In recent years, soft colloids at the interfaces have obtained great attentions because they can be used to fabricate stimulus-responsive emulsions. In this section, I will introduce the most widely studied soft colloids, called microgels, and their surface activity as well as their 2D rheological properties.

1.7.1 Introduction of microgels

Microgels are cross-linked colloidal particles which are swollen by their good solvents (when their size in the swollen state is smaller than 50 nm, the cross-linked particles are called nanogels). Different cross-linked polymers can be used to fabricate micorgels, including polystyrene, poly(methacrylic acid), etc. Among these polymers, poly(N-isopropylacrylamide) (PNIPAM) is most widely used. The PNIPAM-based microgels can be swollen by water. They contain 80–99% water in the swollen state.[85] PNIPAM based microgels can incorporate some acidic or basic co-monomers (such as the acrylic acid, methacrylic acid or N-(3-aminopropyl)methacrylamide hydrochloride), rendering the microgels pH sensitivity.[86–89]

At room temperature the PNIPAM-based microgels are swollen in water, while they collapse at temperatures higher than the lower critical solution temperature (LCST). This is because the constituting polymer PNIPAM has a LCST ($\sim 32°$), above which it deswells in water. At room temperature, water is a good solvent for PNIPAM, because water can interact with PNIPAM by the hydrogen bonding with the amide groups. The hydrogen bonding is disrupted when the temperature is increased, and water becomes the poor solvent, leading to the collapse of the polymer chains. In the collapsed state, the inter- and intra-polymer hydrogen bonding and polymer-polymer hydrophobic interactions dominate the interactions between PNIPAM chains.[85]

The swollen microgels in water contain a high volume fraction of water, thus the dielectric constant and the refractive index of the swollen microgels are very close to those of water. According to Eq. (1.40), therefore, the effective Hamaker constant for swollen microgels in water is close to zero, meaning that the van der Waals forces between swollen microgels are not significant. The main interactions between the microgels in water are the steric and electrostatic forces, both of which are repulsive when the microgels are in close contact. This is the reason why microgels form relatively stable dispension in water. At high temperature, the microgels are deswollen and thus larger van der Waals forces between the collapsed microgels are expected. However, the collapsed microgels do not aggregate, because they are stabilized by the electrostatic repulsions from the sur-

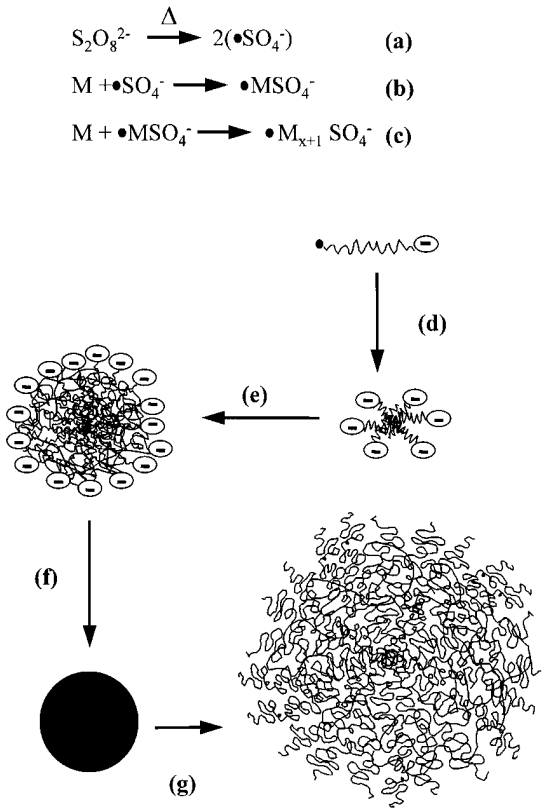

Figure 1.15 Using surfactant free emulsion polymerization to fabricate the PNIPAM-based microgels. The steps represent decomposition of the initiator (a), initiation of the monomer (b), propagation (c), particle nucleation (d), particle aggregation (e), particle growth (in a poor solvent, i.e., in water at high temperature) (f) and particle swelling in water at room temperature (g). The charges in steps (f) and (g) are not shown for clarity. M represents the vinyl monomer. Reprinted from Ref. 85 with permission.

face charges.[85] These charges are introduced into the microgels during synthesis; see Fig. 1.15.

Flory and Rehner's swelling theory can be used to describe the swelling behavior of a homogeneous microgel in water:[85,90,91]

$$\phi_2 = [\frac{X v_1}{V_c(1/2 - \chi_{12})}]^{3/5}. \tag{1.52}$$

Here, the subscripts 1 and 2 represent the solvent (water) and the microgel, respectively. ϕ_2 is the polymer volume fraction at equilibrium. X is the number of cross-links in the collapsed microgel whose volume is V_c. χ_{12} is the Flory solvent-polymer interaction parameter, and v_1 is the molar volume of water. This equation implies that a microgel with lower cross-linking density can be swollen more in water.

For typical microgels fabricated by surfactant free emulsion polymerization, however, the cross-linking density is not homogeneous for the entire microgels. Instead, the cross-linking density is higher at the center and decreases toward the periphery. The high propor-

tion of the cross-links at the center of the microgels is incorporated during initial growth of the microgels during synthesis; see Fig. 1.15.[85,89]

Note that for ionized microgels, Eq. (1.52) also does not account for the effect of charges: firstly, the charges in the polymer network show Coulombic repulsions which tend to expand the polymer network; secondly, the concentration of counterion is different inside and outside the microgels, leading to an extra osmotic pressure (Donnan effect) which also tends to expand the network.[92]

Because of the unique properties of microgels, e.g., the temperature and pH sensitivity, they have been used for templated synthesis of inorganic nanoparticles, drug delivery, sensing, fabrication of photonic crystals, and separation and purification technologies.[93] They are also used as model systems for studying fundamental physical phenomena, such as the glass transition,[94] vibration modes of glasses and crystals,[95] and shear thinning behavior.[96] In addition, microgels have been used to fabricate stimulus-responsive emulsions. This is owing to their surface activity which will be discussed in the following section.

1.7.2 Surface activity of microgels

Linear PNIPAM is surface active: it decreases the surface tension of water to about 42 mN/m which is not very dependent on temperature.[97–99] The PNIPAM based microgels are also surface active. They decrease the surface tension of water to a similar value.[99] The cross-linking property of the microgels does not influence the steady-state surface tension, but a higher cross-linking density increases the time required to achieve the steady state. The adsorption of the microgels to the interface has two steps: first, the microgels diffuse from the subphase (water) to the interface; second, the PNIPAM tails and loops on the surface of the microgels unfold and spread at the interface.[97]

1.7.3 Morphology of microgels at interface

PNIPAM-based microgels tend to spread (flatten) along the interface in order to decrease the unfavorable contacts between water and oil.[103] However, the flattening is restricted by the cross-links in the microgels. Consequently, the microgels at the interface adopt the "fried-egg" like structure. The dense cores of the microgels at the interface appear similar to the egg yolk, and the spreading layers of polymer surrounding the cores appear similar to egg white. This core-shell structure for microgels at the interface can be captured in experiments using AFM or cryo-SEM (Cryo-electron microscopy); see Fig. 1.16a/b.[100,101] A similar morphology is also observed in simulations.[101,103,104] In simulation, it is found that the free dangling chains inside the microgels facilitate the formation of shells.[104]

Recent studies using neutron reflectivity reveal that the microgels at the interface have a three-layer structure; see Fig. 1.16c. The interfacial polymer layer in direct contact with

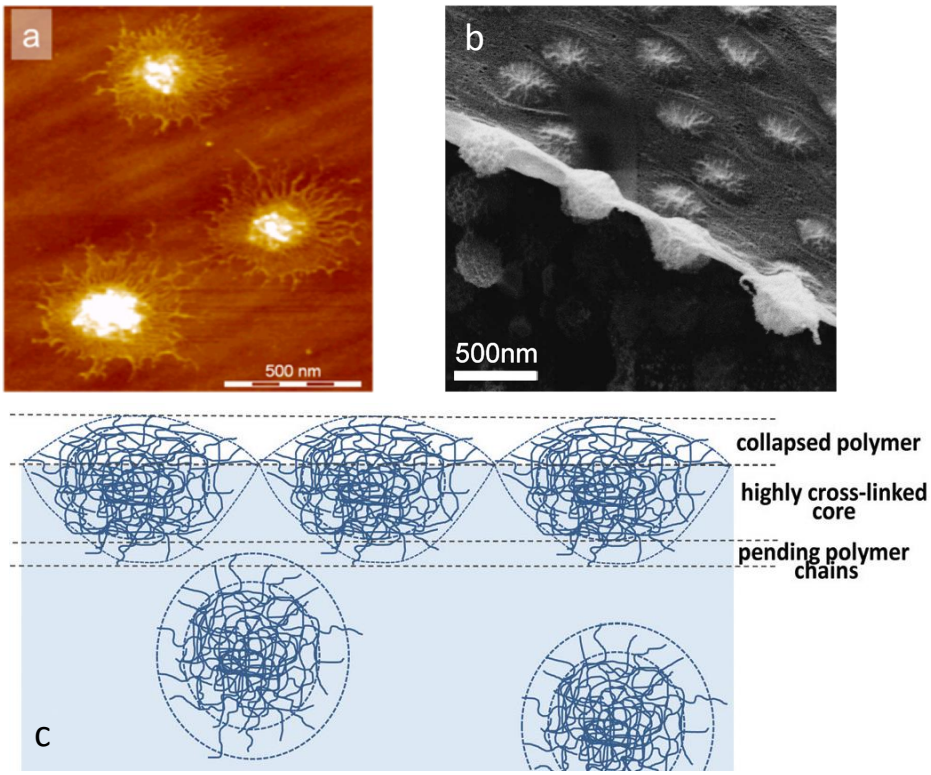

Figure 1.16 "Fried-egg" like structure of microgels at the interface. (a) AFM image of the microgels at the solid substrate. Reprinted from Ref. 100 with permission. (b) Cryo-SEM image of the side view of PNIPAM microgels at the oil-water interface. The bottom side is the water phase. Reprinted from Ref. 101 with permission. (c) The three-layer structure of microgels at the interface studied using neutron reflectivity. Reprinted from Ref. 102 with permission.

the non-polar phase (oil or air) is partially dehydrated (collapsed).[102] The collapsed polymer layer is also present for linear PNIPAM at the water/air interface. It has a thickness of about 1 nm, and the water content is less than 10% for linear PNIPAM.[102,105] For microgels (cross-linked PNIPAM), the water content in the collapsed polymer layer increases with increasing the cross-linking density.

1.7.4 Emulsions stabilized by microgels

Microgels are used as stabilizers in order to fabricate the stimulus-responsive emulsions, which can be responsive to temperature or pH value. These features are useful in some applications. For example, in biocatalysis, in order to improve the reaction between the enzymes in water and the substrate in oil, large water/oil contact area is required. Microgels can be used as stabilizer to produce the emulsions with small droplet size to ensure the large interfacial area.[106] Moreover, the microgels adsorbed at the interface can locate the enzymes (immobile inside microgels) in close proximity to the oil phase without direct contact. This guarantees that the enzymes are still in the water phase without losing biocatalysis activity. In this biocatalysis system, the products can be easily extracted

by breaking the emulsion through increasing temperature; moreover, the enzymes and microgels can be recycled.

The most important factor influencing the stability of the microgel-stabilized emulsions is the softness of the microgels.[107] The softer the microgels are, the easier they can spread and flatten at the water/oil interface. Therefore, softer microgels have a higher emulsifier efficiency. In contrast, charges in the microgels play a minor and indirect role.[86]

Because of the deformability of the microgels, the properties of the microgel-stabilized emulsions depend strongly on the emulsification process. High shear rates cause strong flattening of the microgels at the water/oil interface, resulting in emulsions with bridged droplets. On the contrary, low shear rates ensure the formation of dense microgel monolayers at the water/oil interface, resulting in well dispersed emulsions.[108] The size of the microgels also plays a role. Microgels with a larger size are easier to form bridged emulsions. This is attributed to the fact that larger microgels have a more heterogeneous internal structure, which makes them difficult to form uniform dense layers at the water/oil interface.[109]

1.7.5 Rheology of microgels at the interface

Because of the soft nature and the specific structure of the microgels at the interface, they have characteristic rheological properties. For example, the microgel monolayers show complex responses under lateral compression; see Fig. 1.17 for a typical isothermal compression of microgels at the interface.[110] In the first regime, the diluted microgels behave as non-interacting particles, resulting in the constant surface pressure. In the second regime the surface pressure shows a quick increase because of the overlapping of the shells. In the third regime, the increase of surface pressure is not obvious, because the microgels deform perpendicularly to the interface; see Fig. 1.17f. This perpendicular deformation represents (i) desorption of the polymer segments from the interface, and (ii) vertical deformation of the microgels due to lateral compression.[110] In the fourth regime, when the cores of the microgels overlap, the surface pressure increases. At high compression, i.e., in the fifth regime, another plateau for the surface pressure is observed. This is caused by the desorption, multilayer formation or buckling of the microgel monolayers.

The shear rheological properties of the microgel monolayers at the interface are determined by the inter-microgel interactions. In fact, even at low surface coverage, the microgels at the interface have a strong tendency to aggregate. This is probably driven by the capillary forces due to undulation of the contact line surrounding the microgels.[112] When the microgel shells or cores at the interface overlap, steric repulsive forces are also present. Under compression, the shear modulus of the microgel monolayer increases in the second and fourth regimes, while it decreases in the third regime; see Fig. 1.17h.[111]

For microgel-stabilized emulsions, the emulsion stability is strongly correlated with the rheological properties of the microgel-laden interfaces. For example, Brugger et al.

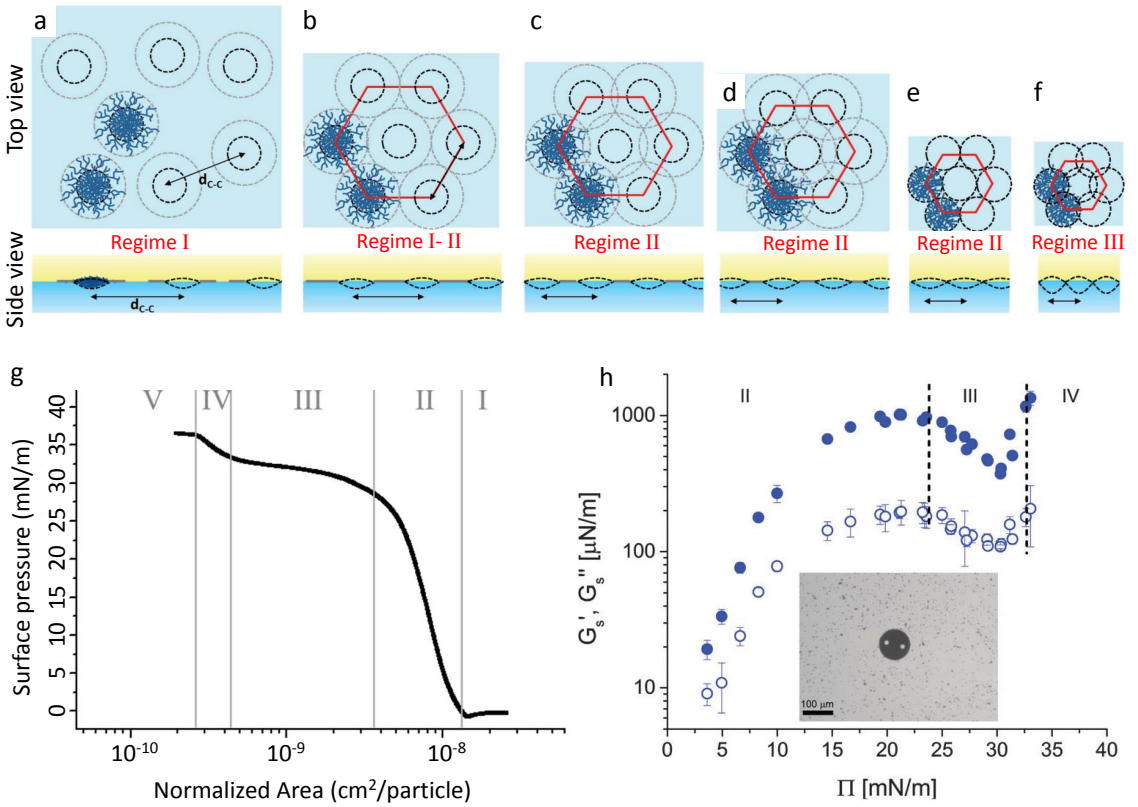

Figure 1.17 (a-f) Schematic illustration of microgels at the interface under isothermal compression. (g) Surface pressure of microgels at a water/oil interface plotted as a function of normalized area (cm^2/particle). (h) Interfacial shear moduli (G_s': storage modulus, G_s'': loss modulus) of the microgels at a water/air interface plotted as functions of surface pressure (Π). The inset shows the experimental setup: a microbutton (microdisk) at the interface. (a-g) Reprinted from Ref. 110 with permission. (h) Reprinted from Ref. 111 with permission.

studied the pH-sensitive poly-(N-isopropylacrylamide-co-methacrylicacid) (PNIPAM-co-MAA) microgels. They found that at high pH when the microgels were charged, the microgels formed elastic interfaces. The resulting emulsions were stable. However, at low pH when the microgels were uncharged, they formed brittle interfaces. Correspondingly, the resulting emulsions were unstable.[113]

1.8 Objectives and perspectives of the present work

1.8.1 Objectives

Microrheology is a powerful tool in characterizing the rheological properties of the soft matter systems, especially for the systems with small sizes and with spatial inhomogeneity. For instance, it is widely used to explore the mechanics of living cells.[8–10] Soft matter systems are sensitive to external applied forces and stimuli, thus they are widely used to

fabricate stimulus-responsive materials. Under stimulation, the materials undergo certain microstructural changes and show correspondingly the macroscopic responses. For example, the magneto-responsive hybrid gels (MRGs) can change their elasticity, swelling property and shape under a magnetic field. MRGs have potential applications as soft actuators, artificial muscles, and sensors, etc. Understanding the magnetic responses of MRGs on different length scales can help to guide the bottom-up design of these materials. Thus, theoretical models on different levels have been proposed, including the macroscopic continuum mechanics models,[114,115] mesoscopic models,[116–119] and microscopic models.[120–122] From a microscopic point of view, the most important question for MRGs is how the magnetic particles interact with each other through the gel matrix under a magnetic field. More specifically, this includes (i) how the magnetic field induces interactions between the magnetic particles, (ii) how the particles couple with the gel matrix, and (iii) how the gel matrix responses to the forces from the particles. In order to answer these questions, in this thesis, different experimental model systems for MRGs will be developed. Using microrheology, these questions will be explored on a single-particle level.

Compared to rheology of the bulk, rheology at the interface is more difficult to probe. Conventional interfacial rheometers (CIRs) face some typical problems. For example, relatively large interfacial layers are probed in CIRs. If the interfacial layers are not homogeneous over the entire area, the measured rheological properties may mainly reflect the mesoscopic structure of the interfaces.[123] Furthermore, the lower limit of detection for CIRs is not low enough for some interfaces (due to the relatively high Boussinesq number for CIRs). These problems may be partially solved by in-situ observation of the structure of the interface, and by improving the design of CIRs. Yet, for some specific systems, e.g., for the cell membrane, CIRs cannot be used. In this case, microrheology should be applied. As discussed above, microrheology at the interface still has some fundamental issues, especially concerning the difficulty in evaluating the interfacial drag on the probed particles. This difficulty is mainly caused by the drag coupling between the interface and the subphase, and by the thermal fluctuation of the contact lines on the particles. So far, it is still a challenging task to develop a complete theoretical description of microrheology at interfaces. From an experimental point of view, it is helpful to study the microrheology of 2D model systems, whose structures and inter-particle interactions can be well probed.

In this thesis, a 2D system (microgel monolayer on the water/oil interface) will be studied. This system is related to the micorgel-stabilized emulsions, which become popular because of their responsibility to temperature or pH value. To date, the stimulus responsibility of microgel-stabilized emulsions is still not well understood. Some fundamental questions are still open, such as (i) how the microgels interact with each other at the interface, (ii) what controls the rheological property of microgel monolayers at the interface, and (iii) what mechanism dominates the sensitivity of microgel-laden interface to temper-

ature and pH value. Here, these questions will be explored using microrheology. With the merit of being able to resolve single microgels, microrheology provides a way to study the interaction-structure-rheology relationship for microgel monolayers at the interface.

1.8.2 Framework of the present work

In Chapter 2 of this thesis, the microrheology of a model system of MRGs will be studied. It consists of a soft gel matrix with embedded paramagnetic particle chains. Using the laser scanning confocal microscopy (LSCM), the 3D morphology of the paramagnetic particle chains in the soft gels is observed. A homogeneous magnetic field is realized by building a Halbach magnetic array near the sample stage of LSCM. Under the magnetic field, the magnetic interactions between the paramagnetic particles tend to align the paramagnetic particle chains along the field direction. However, this tendency is impeded by the cross-linked polymer network. In the experiment, I find that the interplay between these two effects leads to rich morphological changes (e.g., buckling) of the paramagnetic particle chains under the magnetic field. Together with theorists from Heinrich-Heine-Universität Düsseldorf and Universität Stuttgart, we develop a simplified theoretical model and perform simulations to understand this magnetic-field-induced buckling behavior. Our results help to understand the magneto-elastic coupling effect of MRGs.

One of the most essential questions for MRGs is how the magnetic particles interact with each other in the gel matrix. To answer this question, theorists from Heinrich-Heine-Universität Düsseldorf develop a theory which can calculate the effective interactions between spherical particles in the elastic matrix analytically. In Chapter 3, to confirm this theory, I perform experiments on small groups of paramagnetic particles embedded in a soft gel matrix. Applying an external magnetic field induces magnetic forces between the particles. Rotating the magnetic field tunes these forces. It will be shown that the theory can correctly predict the change of positions of the paramagnetic particles embedded in the gel.

In Chapter 4, the PNIPAM-based microgels at the water/oil interface are studied. Fluorescently-labled poly(N-isopropylacrylamide) microgels were provided by colleagues from the Technische Universität Berlin. I use LSCM to study the single microgel behavior at the water/oil interface. It is observed that the microgels at the water/oil interface have a long-range attraction potential. When the microgels are adsorbed onto the interface, they deform and spread along the interface. The complete spreading is not allowed when the concentration of the microgels at the interface is high. This leads to a decrease of inter-microgel distance at high surface coverage. Moreover, the inter-microgel distance for microgels at the interface decreases over time, implying a slow ageing process. Magnetic particles are used to laterally compress the microgel aggregates at the interface. Under the lateral compression, the microgel aggregates show a layer-by-layer thinning behavior.

In Chapter 5 of this thesis, as a continuation of the work in Chapter 4, the rheological

properties of the microgel monolayers at the water/oil interface are studied using passive and active microrheological methods. For active microrheology, a few magnetic dimers in the microgel monolayers are used as the mechanical probes, which are driven to oscillate under an oscillating magnetic field. Thanks to the small size of the probes (diameter $\sim$4.4 μm for each magnetic particle), the arrangement of microgels around the probes can be observed simultaneously during the rheological tests. According to our knowledge, this is the first in-situ study of the rheological and structural properties of microgels at an interface. The correlation between the inter-microgel interactions and the rheological properties of the microgel monolayers is explored. At low concentrations, the microgels form aggregated networks with dominating elasticity, which is owing to the interaction between the capillary multipoles. At high concentrations when the microgels become densely packed at the interface, the elasticity of the microgel monolayers arises from the overlapping of the microgels. It is also observed that under compression the microgel monolayers behave similar to soft glassy materials.

1.8.3 Perspectives

1.8.3.1 Microrheology of MRGs

(i) As shown in Chapter 2, there exist relatively stiff polymer layers surrounding the paramagnetic particles in the soft gels. Their contribution to the buckling of the paramagnetic particle chains in the soft gels under the magnetic field has not been quantified. These stiff polymer layers exist, probably due to the adsorption of polymer chains on the particle surfaces. A follow-up study can focus on modifying the surface of the paramagnetic particles in order to change the amount of adsorbed polymer chains. This may provide a way to change the stiffness of the polymer layers on the paramagnetic particles.

(ii) Inspired by the significant change of morphology for the paramagnetic particle chains in the soft gels under the magnetic field, some magneto-responsive materials/devices may be designed. For example, under a perpendicular magnetic field, the linear magnetic chains in the soft gels become buckled. This should also change the optical opacity of the material (soft gels with magnetic chains) under the magnetic field. This effect could be used to design some magneto-optics devices.

(iii) To better understand the magnetic response of MRGs, it is important to study the effect of particle rotation on the matrix-mediated interactions between the magnetic particles (some magnetic particles can show magnetic anisotropy due to the non-spherical shape or anisotropy magnetization).

(iv) It is also interesting to extend the investigations in Chapter 3 to dynamic situations. In this case the viscoelastic properties of the matrix will play a role.

1.8.3.2 Microrheology of microgel monolayers

(i) A follow-up study could focus on the change of rheological property of the microgel monolayers under the external stimuli (e.g., changes of temperature or pH value).

(ii) It is important to study how the softness (the cross-linking density) and chemical details of the microgels at the interface influence the inter-microgel interactions and the interfacial rheology.

(iii) In preliminary experiments I observed that the dense microgel monolayers show shear thinning (or yielding). For a final conclusion, however, further study along this direction is necessary.

(iv) In addition, microgel monolayer at the interface can serve as an experimental model system to study 2D soft glassy dynamics, which is widely observed in soft matter systems.

(v) From a technical point of view, the active microrheological method used in Chapter 5 requires that the magnetic particles form short chains (e.g., dimers, trimers, etc.) at the water/oil interface. In the present work, these structures are not well controlled. In the future study, it will be helpful to link the magnetic particles into dimers or trimers before use. This can be realized by synthesizing Janus magnetic particles, or by linking the spherical magnetic particles with silica shells or polymer layers. In addition, in the present work the oscillating magnetic field setup only has two well calibrated field strengths (52.7 mT and 28.8 mT). The system woks like a stress-controlled rheometer. In the future, it may be useful to develop a strain-controlled setup, which requires a feedback control system.

Bibliography

[1] Coussot, P. *Rheophysics, Soft and Biological Matter*; Springer International Publishing Switzerland, 2014.

[2] Doi, M. *Soft Matter Physics*; Oxford University Press, 2013.

[3] Menzel, A. M. Tuned, driven, and active soft matter. *Phys. Rep.* **2015**, *554*, 1–45.

[4] Ferry, J. D. *Viscoelastic properties of polymers*; John Wiley & Sons, 1980.

[5] Tschoegl, N. W. *The phenomenological theory of linear viscoelastic behavior an introduction*; Springer-Verlag Berlin Heidelberg, 1989.

[6] Vleminckx, G.; Clasen, C. The dark side of microrheology: Non-optical techniques. *Curr. Opin. Colloid Interface Sci.* **2014**, *19*, 503–513.

[7] Waigh, T. A. Microrheology of complex fluids. *Rep. Prog. Phys.* **2005**, *68*, 685.

[8] Guo, M.; Ehrlicher, A. J.; Jensen, M. H.; Renz, M.; Moore, J. R.; Goldman, R. D.; Lippincott-Schwartz, J.; Mackintosh, F. C.; Weitz, D. A. Probing the stochastic, motor-driven properties of the cytoplasm using force spectrum microscopy. *Cell* **2014**, *158*, 822–832.

[9] Crocker, J. C.; Hoffman, B. D. Multiple-Particle Tracking and Two-Point Microrheology in Cells. *Methods Cell Biol.* **2007**, *83*, 141–178.

[10] Wilhelm, C. Out-of-Equilibrium Microrheology inside Living Cells. *Phys. Rev. Lett.* **2008**, *101*, 028101.

[11] Stokes, G. G. *On the effect of the internal friction of fluids on the motion of pendulums*; Pitt Press, 1851; Vol. 9; p 38.

[12] Einstein, A. Über die von der Molekularkinetischen Theorie der Wärme Geforderte Bewegung von in Ruhenden Flüssigkeiten Suspendierten Teilchen. *Ann. Phys.* **1905**, *4*, 549–560.

[13] Von Smoluchowski, M. Zur kinetischen Theorie der Brownschen Molekularbewegung und der Suspensionen. *Ann. phys.* **1906**, *326*, 756–780.

[14] Sutherland, W. LXXV. A dynamical theory of diffusion for non-electrolytes and the molecular mass of albumin. *The London, Edinburgh, and Dublin Philosophical Magazine and Journal of Science* **1905**, *9*, 781–785.

[15] Moschakis, T. Microrheology and particle tracking in food gels and emulsions. *Curr. Opin. Colloid Interface Sci.* **2013**, *18*, 311–323.

[16] Mason, T. G.; Weitz, D. Optical measurements of frequency-dependent linear viscoelastic moduli of complex fluids. *Phys. Rev. Lett.* **1995**, *74*, 1250.

[17] Mason, T. G. Estimating the viscoelastic moduli of complex fluids using the generalized Stokes–Einstein equation. *Rheol. Acta* **2000**, *39*, 371–378.

[18] Levine, A. J.; Lubensky, T. C. One-and two-particle microrheology. *Phys. Rev. Lett.* **2000**, *85*, 1774.

[19] Lee, C. H.; Crosby, A. J.; Emrick, T.; Hayward, R. C. Characterization of heterogeneous polyacrylamide hydrogels by tracking of single quantum dots. *Macromolecules* **2014**, *47*, 741–749.

[20] Wong, L. H.; Kurniawan, N. A.; Too, H.-P.; Rajagopalan, R. Spatially resolved microrheology of heterogeneous biopolymer hydrogels using covalently bound microspheres. *Biomechanics and modeling in mechanobiology* **2014**, *13*, 839–849.

[21] Crocker, J. C.; Valentine, M. T.; Weeks, E. R.; Gisler, T.; Kaplan, P. D.; Yodh, A. G.; Weitz, D. A. Two-point microrheology of inhomogeneous soft materials. *Phys. Rev. Lett.* **2000**, *85*, 888.

[22] Levine, A. J.; Lubensky, T. Response function of a sphere in a viscoelastic two-fluid medium. *Physical Review E* **2001**, *63*, 041510.

[23] Hassan, P. A.; Rana, S.; Verma, G. Making sense of brownian motion: colloid characterization by dynamic light scattering. *Langmuir* **2014**, *31*, 3–12.

[24] Berne, B. J.; Pecora, R. *Dynamic light scattering: with applications to chemistry, biology, and physics*; Courier Corporation, 1976.

[25] Dasgupta, B. R.; Tee, S.-Y.; Crocker, J. C.; Frisken, B.; Weitz, D. Microrheology of polyethylene oxide using diffusing wave spectroscopy and single scattering. *Physical Review E* **2002**, *65*, 051505.

[26] Popescu, G.; Dogariu, A.; Rajagopalan, R. Spatially resolved microrheology using localized coherence volumes. *Physical Review E* **2002**, *65*, 041504.

[27] Gardel, M. L.; Valentine, M. T.; Weitz, D. A. *Microscale diagnostic techniques*; Springer, 2005; pp 1–49.

[28] Mason, T. G.; Weitz, D. Optical measurements of frequency-dependent linear viscoelastic moduli of complex fluids. *Physical review letters* **1995**, *74*, 1250.

[29] Wilhelm, C.; Browaeys, J.; Ponton, A.; Bacri, J. C. Rotational magnetic particles microrheology: the Maxwellian case. *Phys. Rev. E* **2003**, *67*, 011504.

[30] Brau, R. R.; Ferrer, J. M.; Lee, H.; Castro, C. E.; Tam, B. K.; Tarsa, P. B.; Matsudaira, P.; Boyce, M. C.; Kamm, R. D.; Lang, M. J. Passive and active microrheology with optical tweezers. *J. Opt. A: Pure Appl. Opt.* **2007**, *9*, S103.

[31] Yao, A.; Tassieri, M.; Padgett, M.; Cooper, J. Microrheology with optical tweezers. *Lab Chip* **2009**, *9*, 2568–2575.

[32] Wilhelm, C.; Gazeau, F.; Bacri, J. C. Rotational magnetic endosome microrheology: viscoelastic architecture inside living cells. *Phys. Rev. E* **2003**, *67*, 061908.

[33] Roth, M.; D'Acunzi, M.; Vollmer, D.; Auernhammer, G. K. Viscoelastic rheology of colloid-liquid crystal composites. *The Journal of chemical physics* **2010**, *132*, 124702.

[34] Mendoza, A. J.; Guzmán, E.; Martínez-Pedrero, F.; Ritacco, H.; Rubio, R. G.; Ortega, F.; Starov, V. M.; Miller, R. Particle laden fluid interfaces: dynamics and interfacial rheology. *Advances in colloid and interface science* **2014**, *206*, 303–319.

[35] Fuller, G. G.; Vermant, J. Complex fluid-fluid interfaces: rheology and structure. *Annual review of chemical and biomolecular engineering* **2012**, *3*, 519–543.

[36] Miller, R.; Ferri, J. K.; Javadi, A.; Krägel, J.; Mucic, N.; Wüstneck, R. Rheology of interfacial layers. *Colloid and Polymer Science* **2010**, *288*, 937–950.

[37] Krägel, J.; Derkatch, S.; Miller, R. Interfacial shear rheology of protein–surfactant layers. *Advances in colloid and interface science* **2008**, *144*, 38–53.

[38] Reynaert, S.; Brooks, C. F.; Moldenaers, P.; Vermant, J.; Fuller, G. G. Analysis of the magnetic rod interfacial stress rheometer. *Journal of Rheology* **2008**, *52*.

[39] Ortega, F.; Ritacco, H.; Rubio, R. G. Interfacial microrheology: particle tracking and related techniques. *Current Opinion in Colloid & Interface Science* **2010**, *15*, 237–245.

[40] Saffman, P.; Delbrück, M. Brownian motion in biological membranes. *Proceedings of the National Academy of Sciences* **1975**, *72*, 3111–3113.

[41] Hughes, B.; Pailthorpe, B.; White, L. The translational and rotational drag on a cylinder moving in a membrane. *Journal of Fluid Mechanics* **1981**, *110*, 349–372.

[42] Evans, E.; Sackmann, E. Translational and rotational drag coefficients for a disk moving in a liquid membrane associated with a rigid substrate. *Journal of Fluid Mechanics* **1988**, *194*, 553–561.

[43] Stone, H. A.; Ajdari, A. Hydrodynamics of particles embedded in a flat surfactant layer overlying a subphase of finite depth. *Journal of Fluid Mechanics* **1998**, *369*, 151–173.

[44] Eremin, A.; Baumgarten, S.; Harth, K.; Stannarius, R.; Nguyen, Z.; Goldfain, A.; Park, C.; Maclennan, J.; Glaser, M.; Clark, N. Two-dimensional microrheology of freely suspended liquid crystal films. *Physical review letters* **2011**, *107*, 268301.

[45] Danov, K.; Aust, R.; Durst, F.; Lange, U. Influence of the surface viscosity on the hydrodynamic resistance and surface diffusivity of a large Brownian particle. *Journal of colloid and interface science* **1995**, *175*, 36–45.

[46] Fischer, T. M.; Dhar, P.; Heinig, P. The viscous drag of spheres and filaments moving in membranes or monolayers. *Journal of Fluid Mechanics* **2006**, *558*, 451–475.

[47] Boniello, G.; Blanc, C.; Fedorenko, D.; Medfai, M.; Mbarek, N. B.; In, M.; Gross, M.; Stocco, A.; Nobili, M. Brownian diffusion of a partially wetted colloid. *Nature materials* **2015**, *14*, 908–911.

[48] Prasad, V.; Koehler, S.; Weeks, E. R. Two-particle microrheology of quasi-2D viscous systems. *Physical review letters* **2006**, *97*, 176001.

[49] Dhar, P.; Cao, Y.; Fischer, T. M.; Zasadzinski, J. A. Active interfacial shear microrheology of aging protein films. *Physical review letters* **2010**, *104*, 016001.

[50] Park, C. Y.; Ou-Yang, H. D.; Kim, M. W. Interface shear microrheometer with an optically driven oscillating probe particle. *Review of Scientific Instruments* **2011**, *82*, 094702.

[51] Park, C. Y.; Kim, M. W. Dynamic Mechanical Properties of a Polyelectrolyte Adsorbed Insoluble Lipid Monolayer at the Air–Water Interface. *The Journal of Physical Chemistry B* **2015**, *119*, 5315–5320.

[52] Tajuelo, J.; Pastor, J.; Rubio, M. A magnetic rod interfacial shear rheometer driven by a mobile magnetic trap. *Journal of Rheology (1978-present)* **2016**, *60*, 1095–1113.

[53] Zell, Z. A.; Nowbahar, A.; Mansard, V.; Leal, L. G.; Deshmukh, S. S.; Mecca, J. M.; Tucker, C. J.; Squires, T. M. Surface shear inviscidity of soluble surfactants. *Proceedings of the National Academy of Sciences* **2014**, *111*, 3677–3682.

[54] Zell, Z. A.; Mansard, V.; Wright, J.; Kim, K.; Choi, S. Q.; Squires, T. M. Linear and nonlinear microrheometry of small samples and interfaces using microfabricated probes. *Journal of Rheology (1978-present)* **2016**, *60*, 141–159.

[55] Choi, S.; Steltenkamp, S.; Zasadzinski, J.; Squires, T. Active microrheology and simultaneous visualization of sheared phospholipid monolayers. *Nature communications* **2011**, *2*, 312.

[56] Boatwright, T.; Dennin, M.; Shlomovitz, R.; Evans, A. A.; Levine, A. J. Probing interfacial dynamics and mechanics using submerged particle microrheology. II. Experiment. *Physics of Fluids (1994-present)* **2014**, *26*, 071904.

[57] Kleman, M.; Lavrentovich, O. D. *Soft matter physics: an introduction*; Springer Science & Business Media, 2007.

[58] Israelachvili, J. N. *Intermolecular and surface forces: revised third edition*; Academic press, 2011.

[59] Liang, Y.; Hilal, N.; Langston, P.; Starov, V. Interaction forces between colloidal particles in liquid: Theory and experiment. *Advances in colloid and interface science* **2007**, *134*, 151–166.

[60] Butt, H.-J.; Graf, K.; Kappl, M. *Physics and chemistry of interfaces*; John Wiley & Sons, 2003.

[61] Derjaguin, B.; Landau, L. Theory of the stability of strongly charged lyophobic sols and of the adhesion of strongly charged particles in solutions of electrolytes. *Acta physicochim. URSS* **1941**, *14*, 633–662.

[62] Verwey, E. J. W.; Overbeek, J. T. G. *Theory of the stability of lyophobic colloids*; Courier Corporation, 1999.

[63] de Vicente, J.; Klingenberg, D. J.; Hidalgo-Alvarez, R. Magnetorheological fluids: a review. *Soft Matter* **2011**, *7*, 3701–3710.

[64] Griffiths, D. J. *Introduction to Electrodynamics*, 3rd ed.; Prentice-Hall, Upper Saddle River, NJ,, 1999; p 282.

[65] Cullity, B. D.; Graham, C. D. *Introduction to magnetic materials*; John Wiley & Sons, 2011.

[66] Pieranski, P. Two-dimensional interfacial colloidal crystals. *Physical Review Letters* **1980**, *45*, 569.

[67] Aveyard, R.; Clint, J. H.; Nees, D.; Paunov, V. N. Compression and structure of monolayers of charged latex particles at air/water and octane/water interfaces. *Langmuir* **2000**, *16*, 1969–1979.

[68] Reynaert, S.; Moldenaers, P.; Vermant, J. Control over colloidal aggregation in monolayers of latex particles at the oil-water interface. *Langmuir* **2006**, *22*, 4936–4945.

[69] Aveyard, R.; Binks, B. P.; Clint, J. H.; Fletcher, P. D. I.; Horozov, T. S.; Neumann, B.; Paunov, V. N.; Annesley, J.; Botchway, S. W.; Nees, D.; Parker, A. W.; Ward, A. D.; Burgess, A. N. Measurement of long-range repulsive forces between charged particles at an oil-water interface. *Physical review letters* **2002**, *88*, 246102.

[70] Park, B. J.; Pantina, J. P.; Furst, E. M.; Oettel, M.; Reynaert, S.; Vermant, J. Direct measurements of the effects of salt and surfactant on interaction forces between colloidal particles at water-oil interfaces. *Langmuir* **2008**, *24*, 1686–1694.

[71] Park, B. J.; Furst, E. M. Attractive interactions between colloids at the oil–water interface. *Soft Matter* **2011**, *7*, 7676–7682.

[72] Stamou, D.; Duschl, C.; Johannsmann, D. Long-range attraction between colloidal spheres at the air-water interface: The consequence of an irregular meniscus. *Physical Review E* **2000**, *62*, 5263.

[73] Danov, K. D.; Kralchevsky, P. A.; Naydenov, B. N.; Brenn, G. Interactions between particles with an undulated contact line at a fluid interface: Capillary multipoles of arbitrary order. *Journal of colloid and interface science* **2005**, *287*, 121–134.

[74] Kralchevsky, P. A.; Denkov, N. D.; Danov, K. D. Particles with an undulated contact line at a fluid interface: interaction between capillary quadrupoles and rheology of particulate monolayers. *Langmuir* **2001**, *17*, 7694–7705.

[75] Pickering, S. U. CXCVI.-emulsions. *Journal of the Chemical Society, Transactions* **1907**, *91*, 2001–2021.

[76] Ramsden, W. Separation of Solids in the Surface-Layers of Solutions and 'Suspensions' (Observations on Surface-Membranes, Bubbles, Emulsions, and Mechanical Coagulation).–Preliminary Account. *Proceedings of the royal Society of London* **1903**, *72*, 156–164.

[77] Chevalier, Y.; Bolzinger, M.-A. Emulsions stabilized with solid nanoparticles: Pickering emulsions. *Colloids and Surfaces A: Physicochemical and Engineering Aspects* **2013**, *439*, 23–34.

[78] Aveyard, R.; Binks, B. P.; Clint, J. H. Emulsions stabilised solely by colloidal particles. *Advances in Colloid and Interface Science* **2003**, *100*, 503–546.

[79] Deshmukh, O. S.; van den Ende, D.; Stuart, M. C.; Mugele, F.; Duits, M. H. Hard and soft colloids at fluid interfaces: Adsorption, interactions, assembly & rheology. *Advances in colloid and interface science* **2015**, *222*, 215–227.

[80] Aveyard, R.; Clint, J. H.; Nees, D.; Quirke, N. Structure and collapse of particle monolayers under lateral pressure at the octane/aqueous surfactant solution interface. *Langmuir* **2000**, *16*, 8820–8828.

[81] Leal-Calderon, F.; Schmitt, V. Solid-stabilized emulsions. *Current Opinion in Colloid & Interface Science* **2008**, *13*, 217–227.

[82] Safouane, M.; Langevin, D.; Binks, B. Effect of particle hydrophobicity on the properties of silica particle layers at the air-water interface. *Langmuir* **2007**, *23*, 11546–11553.

[83] Pawar, A. B.; Caggioni, M.; Ergun, R.; Hartel, R. W.; Spicer, P. T. Arrested coalescence in Pickering emulsions. *Soft Matter* **2011**, *7*, 7710–7716.

[84] Reynaert, S.; Moldenaers, P.; Vermant, J. Interfacial rheology of stable and weakly aggregated two-dimensional suspensions. *Physical Chemistry Chemical Physics* **2007**, *9*, 6463–6475.

[85] Saunders, B. R.; Vincent, B. Microgel particles as model colloids: theory, properties and applications. *Advances in colloid and interface science* **1999**, *80*, 1–25.

[86] Geisel, K.; Isa, L.; Richtering, W. The Compressibility of pH-Sensitive Microgels at the Oil–Water Interface: Higher Charge Leads to Less Repulsion. *Angew. Chem.* **2014**, *126*, 5005–5009.

[87] Hu, X.; Tong, Z.; Lyon, L. A. Synthesis and physicochemical properties of cationic microgels based on poly (N-isopropylmethacrylamide). *Colloid and polymer science* **2011**, *289*, 333–339.

[88] Jones, C. D.; Lyon, L. A. Synthesis and characterization of multiresponsive core-shell microgels. *Macromolecules* **2000**, *33*, 8301–8306.

[89] Richtering, W. Responsive Emulsions Stabilized by Stimuli-Sensitive Microgels: Emulsions with Special Non-Pickering Properties. *Langmuir* **2012**, *28*, 17218–17229.

[90] Flory, P. J. *Principles of polymer chemistry*; Cornell University Press, 1953.

[91] Flory, P. J.; Rehner, J. Statistical Mechanics of Cross-Linked Polymer Networks II. Swelling. *The Journal of Chemical Physics* **1943**, *11*.

[92] Fernandez-Nieves, A.; Fernandez-Barbero, A.; Vincent, B.; De las Nieves, F. Charge controlled swelling of microgel particles. *Macromolecules* **2000**, *33*, 2114–2118.

[93] Das, M.; Zhang, H.; Kumacheva, E. Microgels: old materials with new applications. *Annu. Rev. Mater. Res.* **2006**, *36*, 117–142.

[94] Purnomo, E. H.; van den Ende, D.; Vanapalli, S. A.; Mugele, F. Glass transition and aging in dense suspensions of thermosensitive microgel particles. *Physical review letters* **2008**, *101*, 238301.

[95] Kaya, D.; Green, N.; Maloney, C.; Islam, M. Normal modes and density of states of disordered colloidal solids. *Science* **2010**, *329*, 656–658.

[96] Carrier, V.; Petekidis, G. Nonlinear rheology of colloidal glasses of soft thermosensitive microgel particles. *Journal of Rheology (1978-present)* **2009**, *53*, 245–273.

[97] Zhang, J.; Pelton, R. Poly (N-isopropylacrylamide) microgels at the air-water interface. *Langmuir* **1999**, *15*, 8032–8036.

[98] Zhang, J.; Pelton, R. The dynamic behavior of poly (N-isopropylacrylamide) at the air/water interface. *Colloids and Surfaces A: Physicochemical and Engineering Aspects* **1999**, *156*, 111–122.

[99] Pelton, R. Temperature-sensitive aqueous microgels. *Advances in colloid and interface science* **2000**, *85*, 1–33.

[100] Mourran, A.; Wu, Y.; Gumerov, R. A.; Rudov, A. A.; Potemkin, I. I.; Pich, A.; Möller, M. When colloidal particles become polymer coils. *Langmuir* **2016**, *32*, 723–730.

[101] Style, R. W.; Isa, L.; Dufresne, E. R. Adsorption of soft particles at fluid interfaces. *Soft matter* **2015**, *11*, 7412–7419.

[102] Zielińska, K.; Sun, H.; Campbell, R. A.; Zarbakhsh, A.; Resmini, M. Smart nanogels at the air/water interface: structural studies by neutron reflectivity. *Nanoscale* **2016**, *8*, 4951–4960.

[103] Rumyantsev, A. M.; Gumerov, R. A.; Potemkin, I. I. A polymer microgel at a liquid–liquid interface: theory vs. computer simulations. *Soft Matter* **2016**, *12*, 6799–6811.

[104] Mehrabian, H.; Harting, J.; Snoeijer, J. H. Soft particles at a fluid interface. *Soft matter* **2016**, *12*, 1062–1073.

[105] Richardson, R. M.; Pelton, R.; Cosgrove, T.; Zhang, J. A neutron reflectivity study of poly (N-isopropylacrylamide) at the air-water interface with and without sodium dodecyl sulfate. *Macromolecules* **2000**, *33*, 6269–6274.

[106] Wiese, S.; Spiess, A. C.; Richtering, W. Microgel-Stabilized Smart Emulsions for Biocatalysis. *Angewandte Chemie* **2013**, *125*, 604–607.

[107] Destribats, M.; Lapeyre, V.; Wolfs, M.; Sellier, E.; Leal-Calderon, F.; Ravaine, V.; Schmitt, V. Soft Microgels as Pickering Emulsion Stabilisers: Role of Particle Deformability. *Soft Matter* **2011**, *7*, 7689–7698.

[108] Destribats, M.; Wolfs, M.; Pinaud, F.; Lapeyre, V.; Sellier, E.; Schmitt, V.; Ravaine, V. Pickering emulsions stabilized by soft microgels: influence of the emulsification process on particle interfacial organization and emulsion properties. *Langmuir* **2013**, *29*, 12367–12374.

[109] Destribats, M.; Eyharts, M.; Lapeyre, V.; Sellier, E.; Varga, I.; Ravaine, V.; Schmitt, V. Impact of PNIPAM Microgel Size on Its Ability to Stabilize Pickering Emulsions. *Langmuir* **2014**, *30*, 1768–1777.

[110] Pinaud, F.; Geisel, K.; Massé, P.; Catargi, B.; Isa, L.; Richtering, W.; Ravaine, V.; Schmitt, V. Adsorption of microgels at an oil–water interface: correlation between packing and 2D elasticity. *Soft Matter* **2014**, *10*, 6963–6974.

[111] Rey, M.; Fernández-Rodríguez, M. Á.; Steinacher, M.; Scheidegger, L.; Geisel, K.; Richtering, W.; Squires, T. M.; Isa, L. Isostructural solid–solid phase transition in monolayers of soft core–shell particles at fluid interfaces: structure and mechanics. *Soft matter* **2016**, *12*, 3545–3557.

[112] Cohin, Y.; Fisson, M.; Jourde, K.; Fuller, G. G.; Sanson, N.; Talini, L.; Monteux, C. Tracking the Interfacial Dynamics of PNiPAM Soft Microgels Particles Adsorbed at the Air-Water Interface and in Thin Liquid Films. *Rheol. Acta* **2013**, *52*, 445–454.

[113] Brugger, B.; Vermant, J.; Richtering, W. Interfacial layers of stimuli-responsive poly-(N-isopropylacrylamide-co-methacrylicacid)(PNIPAM-co-MAA) microgels characterized by interfacial rheology and compression isotherms. *Physical Chemistry Chemical Physics* **2010**, *12*, 14573–14578.

[114] Jarkova, E.; Pleiner, H.; Müller, H.-W.; Brand, H. R. Hydrodynamics of isotropic ferrogels. *Phys. Rev. E* **2003**, *68*, 041706.

[115] Bohlius, S.; Brand, H. R.; Pleiner, H. Macroscopic dynamics of uniaxial magnetic gels. *Phys. Rev. E* **2004**, *70*, 061411.

[116] Wood, D. S.; Camp, P. J. Modeling the properties of ferrogels in uniform magnetic fields. *Phys. Rev. E* **2011**, *83*, 011402.

[117] Ivaneyko, D.; Toshchevikov, V.; Saphiannikova, M.; Heinrich, G. Effects of particle distribution on mechanical properties of magneto-sensitive elastomers in a homogeneous magnetic field. *Condens. Matter Phys.* **2012**, *15*, 33601.

[118] Han, Y.; Hong, W.; Faidley, L. E. Field-stiffening effect of magneto-rheological elastomers. *Int. J. Solids Struct.* **2013**, *50*, 2281–2288.

[119] Pessot, G.; Cremer, P.; Borin, D. Y.; Odenbach, S.; Lowen, H.; Menzel, A. M. Structural control of elastic moduli in ferrogels and the importance of non-affine deformations. *J. Chem. Phys.* **2014**, *141*, 124904.

[120] Weeber, R.; Kantorovich, S.; Holm, C. Deformation mechanisms in 2D magnetic gels studied by computer simulations. *Soft Matter* **2012**, *8*, 9923–9932.

[121] Weeber, R.; Kantorovich, S.; Holm, C. Ferrogels cross-linked by magnetic nanoparticles – Deformation mechanisms in two and three dimensions studied by means of computer simulations. *J. Magn. Magn. Mater.* **(in press) 2015**,

[122] Ryzhkov, A. V.; Melenev, P. V.; Holm, C.; Raikher, Y. L. Coarse-grained molecular dynamics simulation of small ferrogel objects. *J. Magn. Magn. Mater.* **2015**, *383*, 277.

[123] Barman, S.; Christopher, G. F. Role of capillarity and microstructure on interfacial viscoelasticity of particle laden interfaces. *Journal of Rheology (1978-present)* **2016**, *60*, 35–45.

2. Buckling of paramagnetic chains in soft gels

Shilin Huang,[a] Giorgio Pessot,[b] Peet Cremer,[b] Rudolf Weeber,[c] Christian Holm,[c] Johannes Nowak,[d] Stefan Odenbach,[d] Andreas M. Menzel,[b] and Günter K. Auernhammer*[a]

[a] Max Planck Institute for Polymer Research, Ackermannweg 10, 55128 Mainz, Germany.

[b] Institut für Theoretische Physik II: Weiche Materie, Heinrich-Heine-Universität Düsseldorf, 40225 Düsseldorf, Germany.

[c] Institute for Computational Physics, Universität Stuttgart, 70569 Stuttgart, Germany.

[d] Chair of Magnetofluiddynamics, Measuring and Automation Technology, Institute of Fluid Mechanics, Technische Universität Dresden, 01069 Dresden, Germany.

* Corresponding author. E-mail: auhammer@mpip-mainz.mpg.de

Reprinted with permission from Soft Matter 2016, 12, 228–237. Published by The Royal Society of Chemistry.

Statement of Contribution

In this paper, Shilin Huang contributes mainly to the experiments. In more details, the contribution includes the following aspects:

(1) The design of the Halbach magnetic setup which is used to apply the homogeneous magnetic field (Fig. 2.1a, Fig. 2.15, Fig. 2.16).

(2) The preparation of the magneto-responsive gels with the embedded paramagnetic particle chains.

(3) The experimental observation and analysis of the paramagnetic particle chains in the soft gels under the magnetic field (Fig. 2.1, Fig. 2.2, Fig. 2.3, Fig. 2.4a, Fig. 2.4b, Fig. 2.18, Fig. 2.19, the experimental data points in Fig. 2.8).

(4) Characterization of the size (Fig. 2.11a) and the magnetic properties (Fig. 2.12) of the paramagnetic particles.

(5) Rheological tests of the soft gels (Fig. 2.13, Fig. 2.14).

(6) Providing experimental evidence for the existence of adsorbed polymer layers on the surface of the particles (Fig. 2.17, Fig. 2.18).

In addition, Shilin Huang contributed partially to writing the paper.

Abstract

We study the magneto-elastic coupling behavior of paramagnetic chains in soft polymer gels exposed to external magnetic fields. To this end, a laser scanning confocal microscope is used to observe the morphology of the paramagnetic chains together with the deformation field of the surrounding gel network. The paramagnetic chains in soft polymer gels show rich morphological shape changes under oblique magnetic fields, in particular a pronounced buckling deformation. The details of the resulting morphological shapes depend on the length of the chain, the strength of the external magnetic field, and the modulus of the gel. Based on the observation that the magnetic chains are strongly coupled to the surrounding polymer network, a simplified model is developed to describe their buckling behavior. A coarse-grained molecular dynamics simulation model featuring an increased matrix stiffness on the surfaces of the particles leads to morphologies in agreement with the experimentally observed buckling effects.

2.1 Introduction

Magneto-responsive hybrid gels (MRGs) have been attracting great attention due to their tunable elasticity, swelling properties and shape that can be remotely controlled by a magnetic field. They have potential applications as soft actuators, artificial muscles, as well as sensors[1–3] and can serve as model systems to study the heat transfer in hyperthermal cancer treatment.[4] Compared to other stimuli-responsive gels, MRGs have the advantage of fast response, controlled mechanical properties and reversible deformabilities.[5–7] A typical MRG consists of a chemically cross-linked polymer network, swollen in a good solvent, and embedded magnetic particles.[5,8] The size of the magnetic particles can range from ~ 10 nm to several μm.[7]

The origin of the magneto-responsive behavior of MRGs is the magnetic interaction between the magnetic filler particles as well as their interaction with external magnetic fields.[9,10] In a uniform magnetic field, paramagnetic particles can be polarized and act as approximate magnetic dipoles. Depending on their mutual azimuthal configuration, the dipolar interactions can be either attractive or repulsive. In a liquid carrier, the dipolar interaction drives the magnetic particles to form chains and columns[11–14] aligning in the direction of the magnetic field. However, in a polymer gel, the particles cannot change their position freely. Instead, relative displacements of the particles, induced e.g. by changes in the magnetic interactions, lead to opposing deformations of the polymer network. As a result, the magnetic interactions can induce changes in the modulus of the gel.[7,15] This magneto-elastic effect is well known to be related to the spatial distribution of the magnetic particles.[16–21] For example, the modulus of anisotropic materials that contain aligned chain-like aggregates of magnetic filler particles[15,22–24] can be sig-

nificantly enhanced when an external magnetic field is applied along the chain direction.[7] The anisotropic arrangement of particles also dominates the anisotropic magnetostriction effects.[25–27]

Different theoretical routes have been pursued to investigate the magneto-elastic effects of MRGs: macroscopic continuum mechanics approaches,[28,29] mesoscopic modeling,[16–19] and more microscopic approaches[30–32] that resolve individual polymer chains. Theoretical routes to connect and unify these different levels of description have recently been proposed.[33–35] The authors of Ref. 34 show how the interplay between the mesoscopic particle distribution and the macroscopic shape of the sample affects the magneto-elastic effect. In addition to these factors, recent experiments and computer simulations also point out that a direct coupling between the magnetic particles and attached polymer chains can play another important role.[1,30,31,36–39]

An experimental model system showing a well-defined particle distribution and a measurable magneto-elastic effect can help to understand the magneto-elastic behavior of MRGs at different length scales. Projected into a two-dimensional plane, the distribution of magnetic particles in thin diluted MRGs can be detected using optical microscopy or light scattering methods.[15,40] By combining these techniques with magnetic or mechanical devices, it is possible to observe the particle rearrangement when the MRG sample is exposed to a magnetic field or mechanical stimuli.[15,41] For three-dimensional (3D) characterization, X-ray micro-tomography has been used.[23] Here we introduce another 3D imaging technique – laser scanning confocal microscopy (LSCM). Compared to normal optical microscopy, LSCM is able to observe 3D structures and it has a better resolution.[42] Compared to X-ray micro-tomography, LSCM is faster in obtaining a 3D image and easier to combine with other techniques for real-time investigation.[43,44]

We use LSCM to study the magneto-elastic effects of paramagnetic chains in soft gels. As a result, we find that the paramagnetic chains in soft gels (elastic modulus < 2 Pa) under an oblique magnetic field show rich morphologies. Depending on the length of the chain, modulus of the gel and strength of an external magnetic field, the chains can rotate, bend, and buckle. The deformation field in the polymer network around the deformed paramagnetic chains can also be tracked. The result confirms that the chains are strongly coupled to the polymer network. A simplified model is developed to understand the magnetically induced buckling behavior of the paramagnetic chains in soft gels. In addition to serving as a model experimental system for studying the magneto-elastic effect of MRGs, our approach may also provide a new microrheological technique to probe the mechanical property of a soft gel.[45] Furthermore, our results may be interesting to biological scientists who study how magnetosome chains interact with the surrounding cytoskeletal network in magnetotactic bacteria.[46]

2.2 Materials and Methods

The elastic network was obtained by hydrosilation of a difunctional vinyl-terminated polydimethylsiloxane (vinyl-terminated PDMS, DMS-V25, Gelest Inc.) prepolymer with a SiH-containing cross-linker (PDMS, HMS-151, Gelest Inc.). Platinum(0)-1,3-divinyl-1,1,3,3-tetramethyldisiloxane complex (Alfa Aesar) was used as a catalyst. A low-molecular-weight trimethylsiloxy-terminated PDMS (770 g/mol, Alfa Aesar GmbH & Co. KG, in the following "PDMS 770") served as a solvent that carried the polymer network and the paramagnetic particles. The paramagnetic particles were purchased from microParticles GmbH. They were labeled with fluorophores (visible in LSCM). The materials consist of porous polystyrene spheres. Within the pores, nanoparticulate iron oxide was distributed rendering the particles superparamagnetic. To prevent iron oxide leaching, the particles had a polymeric sealing that also held the fluorophores. The particles had a diameter of 1.48 ± 0.13 μm (Supplementary Information, Fig. 2.11a). We measured the magnetization curve (Supplementary Information, Fig. 2.11b) of the paramagnetic particles by a vibrating sample magnetometer (VSM, Lake Shore 7407). We found about 20% deviations in the magnetic properties of the magnetic particles (e.g., magnetic moment, see Supplementary Information, Fig. 2.12). In order to observe the deformation field in the polymer network, we used fluorescently labeled silica particles as tracers. They had a diameter of 830 ± 50 nm and the surface was modified with N,N-dimethyl-N-octadel-3-amino-propyltrimethoxysilylchloride.

After drying under vacuum at room temperature overnight, the paramagnetic particles were dispersed into PDMS 770. In some samples, tracer particles (3 wt%) were also dispersed into PDMS 770 in this step. The prepolymer mixture was prepared with 9.1 wt% vinyl-terminated PDMS and 90.9 wt% SiH-containing cross-linker. The prepolymer mixture (2.86 wt%) was dissolved in PDMS 770, which contained the paramagnetic particles. Finally, by adding PDMS 770, which carried the catalyst, the concentration of the prepolymer mixture in the sol solution was carefully adjusted in the range from 2.74 wt% to 2.78 wt%. This concentration range guaranteed the formation of soft gels with an elastic modulus lower than 10 Pa (see Supplementary Information, Fig. 2.13). In the sol solution, the catalyst concentration was 0.17 wt%, and the concentration of magnetic particles was 0.09 wt%. The sol solution was agitated at 2500 r/min with a Reax Control (Heidolph, Schwabach, Germany) for 2 min for homogenization, followed by ultrasonication (2 min, Transsonic 460/H, Elma) to disperse the magnetic particles. Then the sol solution was introduced into a thin sample cell (~ 160 μm thick and ~ 1 cm wide) by capillary forces. The sample cells consisted of two No. 1 standard coverslips, separated by ~ 160 μm spacers. After sealing with two-component glue, the cells that contained the sol were exposed to a 100.8 ± 0.5 mT magnetic field. The paramagnetic particles aligned into chains along the direction of the applied magnetic field while the prepolymer was crosslinking. A visible reaction of the prepolymer occurred within 10 min, and the rheological mea-

surements showed that it took about 40 min to form a gel. Due to the low concentration of magnetic particles, the magnetic chains in the gel were well separated ($> 30\ \mu$m). The length of the chains varied from a single particle up to about 170 particles. We stored the samples at ambient temperature for at least two weeks before testing. The modulus of the gels in the sample cells was characterized using microrheological techniques (see Supplementary Information, Fig. 2.14).[47]

A home-built LSCM setup was used to observe the chain structure in the gel.[43,44] We were able to analyze a sample of thickness of about 150 μm. A homogeneous magnetic field was attained by building Halbach magnetic arrays near the sample stage of the LSCM.[48] A 32-magnet array (Fig. 2.1a) was used to change the field direction while keeping the field strength constant (216.4 ± 1.1 mT, see Supplementary Information, Fig. 2.15). Another 4-magnet Halbach array (see Supplementary Information, Fig. 2.16) was used to change the field strength (up to 100.8 ± 0.5 mT). The magnetic field was measured by a Lake Shore Model 425 Gaussmeter with a transverse probe.

To study the deformation of the PDMS gel around the magnetic chain, the magnetic field strength was increased from 0 mT to 60.2 ± 0.3 mT in 8 steps ($\sim$ 30 min/step). 3D images of the sample with randomly distributed tracer particles were recorded in every step. One isolated magnetic chain was chosen for further analysis. Thus, from the 3D images we extracted a time series of 2D images that focused on this magnetic chain. From these 2D images, the trajectories of the embedded tracer particles were determined using the Particle Tracker plug-in developed on ImageJ software.[49] The corresponding displacements of the tracers were deduced from the trajectories. Naturally, the tracer particles were stochastically distributed over the sample. We divided the images into a grid of small rectangles ($7.0 \times 5.5\ \mu$m^2, containing, on average, $\sim$ 3.5 tracer particles) and determined the average displacement in each cell.

2.3 Results

In the absence of a magnetic field, the paramagnetic chains in a soft gel kept the aligned morphologies (Supplementary Information, Section 2.8.1, Movie S2-1). When a magnetic field (216.4 ± 1.1 mT) was applied in the direction parallel to the chains (Fig. 2.1c, images for 0°), the paramagnetic chains still aligned with the original chain direction (horizontal). We changed the direction of the magnetic field step-by-step (5° steps) in the clockwise direction ($\sim$1 min between steps, quasi-static). We also define the orientation of the magnetic field $\boldsymbol{B}$ as the angle included between the magnetic field and the initial chain direction (see Fig. 2.1b). The left images of Fig. 2.1c show a short chain with 15 particles in a gel of elastic modulus G' of 0.25 ± 0.06 Pa. The chain rotated to follow the magnetic field. However, the rotation angle of the chain was smaller than the orientation angle of the magnetic field (Fig. 2.1b). This difference increased until the orientation of

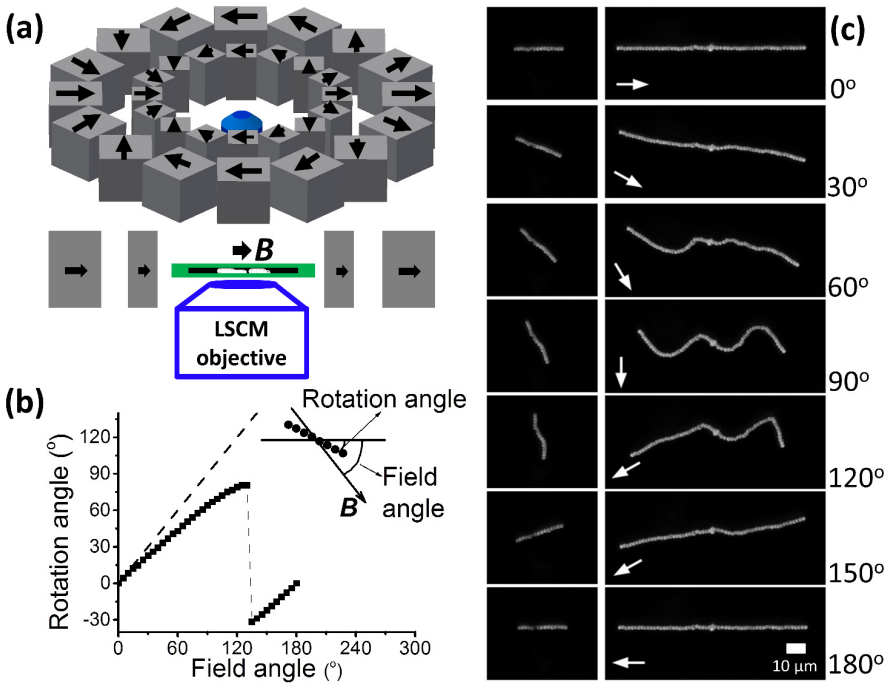

Figure 2.1 (a) Laser scanning confocal microscopy (LSCM) was used to observe the morphologies of the paramagnetic chains in the soft gels. The Halbach magnetic array provided a homogeneous magnetic field (here $B = 216.4 \pm 1.1$ mT). This array could be rotated to change the orientation of the magnetic field. (b) The orientation of the magnetic field $\boldsymbol{B}$ was successively increased from 0° to 180° in 36 steps (square points). A magnetic chain of 15 particles rotated to follow the magnetic field, but the rotation angle was smaller than the orientation angle of $\boldsymbol{B}$ (dashed line). (c) Morphologies of magnetic chains in a soft gel changed when the orientation angle of $\boldsymbol{B}$ increased. The scale bar is 10 μm. The gel in (b) and (c) had an elastic modulus G' of 0.25 ± 0.06 Pa.

$\boldsymbol{B}$ reached 135°, where the chain flipped backward and had a negative angle. The chain again became parallel to the field when the orientation of $\boldsymbol{B}$ increased to 180°. The morphology of the chain was the same at orientations of the magnetic field of 0° and 180° because of the superparamagnetic nature of the particles. Note that the chain was not straight at the intermediate angles (e.g., images for 60°, 90° and 120°). Instead it bended.

The images on the right-hand side of Fig. 2.1c show a longer chain with 59 particles in the same gel. When the orientation of $\boldsymbol{B}$ was 30°, the chain rotated and bended, with its two ends tending to point in the direction of the magnetic field. When the orientation of $\boldsymbol{B}$ was 60°, the chain wrinkled and started to buckle. A sinusoidal-shape buckling morphology was observed when the magnetic field was perpendicular to the original chain (orientation of the magnetic field of 90°, see Supplementary Information, Section 2.8.1, Movie S2-2). When the orientation of $\boldsymbol{B}$ increased from 90° to 120°, the left part of the chain flipped downward in order to follow the magnetic field. The right part flipped upward when the orientation of $\boldsymbol{B}$ increased from 120° to 150°. Finally, when the field direction was again parallel to the original chain direction (orientation of the magnetic

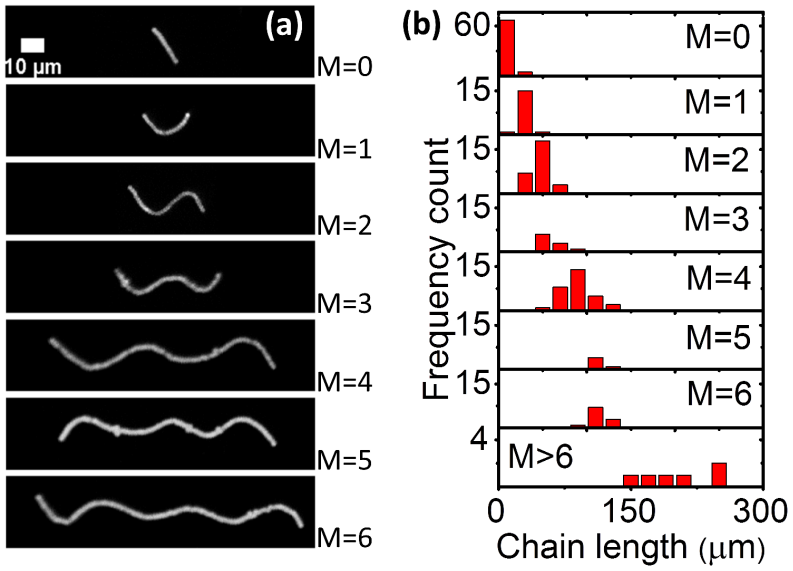

Figure 2.2 (a) Different morphologies of paramagnetic chains in a soft gel ($G' = 0.25 \pm 0.06$ Pa) under a perpendicular magnetic field (100.8 ± 0.5 mT). The original chain direction was horizontal, and the applied magnetic field was vertical. The scale bar is 10 μm. (b) Frequency count of different buckling morphologies in the same sample. M is the number of half waves.

field of 180°), the chain became straight. The same rotation/buckling morphologies as in Fig. 2.1c could be observed when increasing the orientation of $\boldsymbol{B}$ from 180° to 360°.

We also directly applied a perpendicular magnetic field to the paramagnetic chains in the soft gels. The paramagnetic chains showed different buckling morphologies (Fig. 2.2a) depending on the chain length. Fig. 2.2b gives frequency counts of the different morphologies in the same sample ($G' = 0.25 \pm 0.06$ Pa) under a magnetic field of 100.8 ± 0.5 mT. In total 180 chains were observed. Longer chains tended to buckle with a higher number of half waves. Moreover, the distributions overlapped, implying that paramagnetic chains of identical length could have different morphologies under the perpendicular magnetic field.

These buckling morphologies are reminiscent of the buckling of paramagnetic chains in a liquid medium under a perpendicular magnetic field.[50,51] The most stable morphology in the latter system was a straight chain aligning along the magnetic field direction. However, in our system this morphology was not observed. Even the short chains showed a rotation angle smaller than the orientation of the magnetic field (e.g., Fig. 2.1b). The major difference between our experiments and Refs. 50 and 51 was the nature of the surrounding medium. In our system, the polymer network around the paramagnetic chains impeded the rotation of the chains into the magnetic field direction (a more detailed discussion will be given below).

We used ImageJ software (NIH[52]) to extract the skeletons of the chains that have 2 half waves (S-shaped). The amplitude of deflection or deformation of different chains was quantified by the square root of the mean square displacement, i.e. Amplitude =

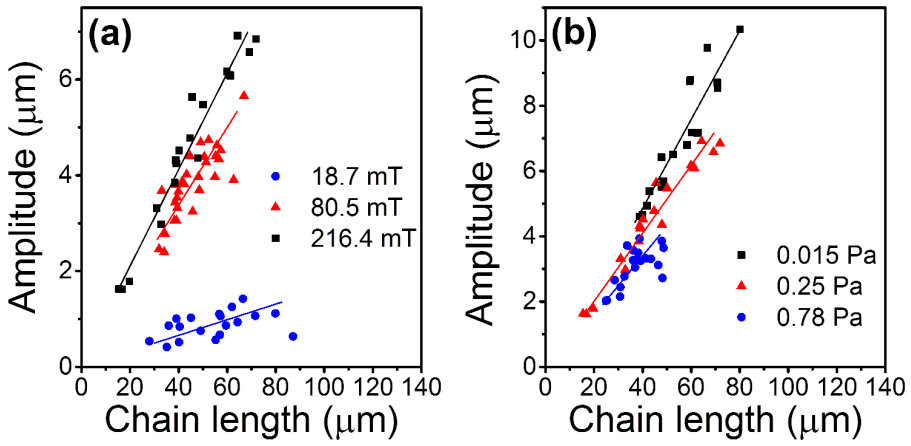

Figure 2.3 Influence of chain length, strength of magnetic field and elastic modulus of the gel matrix on the amplitude of the S-shaped chains, observed when the magnetic field is applied perpendicularly to the initial chain orientation. (a) The elastic modulus of the gel was 0.25 ± 0.06 Pa, and the magnetic field strengths were 216.4 ± 1.1 mT (black squares), 80.5 ± 0.4 mT (red triangles), and 18.7 ± 0.1 mT (blue circles), respectively. (b) The magnetic field strength was 216.4 ± 1.1 mT and the elastic moduli of the gel were 0.015 ± 0.005 Pa (black squares), 0.25 ± 0.06 Pa (red triangles), and 0.78 ± 0.22 Pa (blue circles), respectively. The solid lines are guides to the eye.

$(\langle y^2 \rangle - \langle y \rangle^2)^{1/2}$, where y measures the particle displacement along the field direction. The results are shown in Fig. 2.3. The amplitude increased with increasing chain length. At the same chain length, the amplitude tends to increase with increasing magnetic field strength (Fig. 2.3a; an example is also given in Fig. 2.4a) or with decreasing gel modulus (Fig. 2.3b).

The modulus dependence of the amplitude demonstrated that the polymer network around the paramagnetic chains impeded the chain deformations. Therefore, the deformation field within the polymer network plays an important role to understand the buckling of the chains. We thus added tracer particles into the gel matrix, and used their trajectories to record the deformation field around the paramagnetic chains. As shown in Fig. 2.4a, a linear paramagnetic chain buckled and formed an S shape in a perpendicular magnetic field. The amplitude increased with increasing field strength, while the contour length of the chain remained constant. The chain extension decreased along the original chain direction (horizontal direction) and increased along the perpendicular direction. Simultaneously, the polymer network around the chain followed the deformation (Fig. 2.4b) of the paramagnetic chain, both in the transverse and longitudinal directions. This confirmed that the paramagnetic chain is strongly coupled to the polymer network. Within our experimental resolution, the chain seemed to have a rigid non-slip contact to the surrounding network.

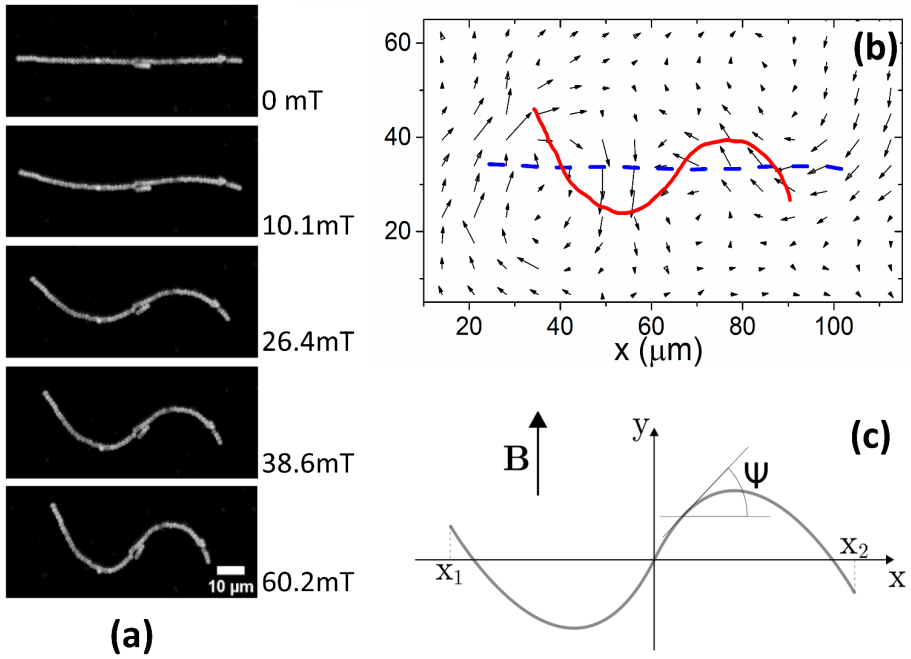

Figure 2.4 (a) Influence of the magnetic field strength on a buckling chain. From top to bottom, the magnetic field strengths were 0 mT, 10.1 ± 0.1 mT, 26.4 ± 0.1 mT, 38.6 ± 0.2 mT and 60.2 ± 0.3 mT, respectively. The modulus of this gel was about 0.01 Pa. (b) Tracer particles were inserted into the gel matrix of the sample. Tracking these embedded tracer particles, the deformation field in the gel matrix was determined. The red solid line represents the skeleton of the magnetic chain shown in (a) for a field strength of 60.2 ± 0.3 mT, and the dashed blue line indicates the original chain shape. (c) We modeled the paramagnetic chain in the elastic gel as a continuous object uniformly carrying dipolar magnetic moments. Without the magnetic field, the straight chain was oriented along the x-axis. Under a perpendicular magnetic field $\boldsymbol{B}$ (oriented along the y-axis), the magnetic chain deformed. The surrounding polymer network impeded the chain deformation.

2.4 Modeling

We now turn to a qualitative description of the situation in the framework of a reduced minimal model. Theoretically capturing in its full breadth the problem of displacing rigid magnetic inclusions in an elastic matrix is a task of high complexity and enormous computational effort.[53] We do not pursue this route in the following. Instead, we reduce our characterization to a phenomenological description in terms of the shape of the magnetic chain only. This is possible if the dominant modes of deformation of the surrounding matrix are reflected by the deformational modes of the magnetic chain.

Below, we assume that the chain is composed of identical spherical particles. In its undeformed state, the straight chain is located on the x-axis of our coordinate frame. The contour line of the deformed chain running through the particle centers is parameterized as $y(x)$, see Fig. 2.4c.

2.4.1 Magnetic Energy

First, concerning the magnetic energy along the chain, we assume dipolar magnetic interactions between the particles. In the perpendicular geometry (Fig. 2.4c), the external magnetic field approximately aligns all dipoles along the y-axis. For simplicity, we only include nearest-neighbor magnetic interactions. In an infinite straight chain, this would result in an error given by a factor of $\zeta(3) \approx 1.2$, where ζ is the Riemann zeta function.[33,54,55] Within our qualitative approach this represents a tolerable error. Replacing the magnetic interaction energy between the discrete magnetic particles by a continuous line integral and shifting the path of integration from the contour line of the chain to the x-axis, we obtain the magnetic interaction energy (see Supplementary Information, Section 2.8.3.1)

$$E_{magn} = W \int_{x_1}^{x_2} \frac{1}{\sqrt{1+y'(x)^2}}\, dx, \tag{2.1}$$

where x_1 and x_2 label the end points of the chain. The prefactor W has the dimension of energy per unit length and is given by (see Supplementary Information, Section 2.8.3.1)

$$W \approx \frac{3\mu_0 m^2}{4\pi d^4}, \tag{2.2}$$

where μ_0 is the vacuum magnetic permeability, m the magnetic moment of a single particle, and d its diameter.

2.4.2 Elastic Bending Energy

Next, we need to include terms that provide a measure for the magnitude of the elastic deformation energy. To estimate the importance of different modes of the elastic matrix deformation, we analyze the experimentally determined displacement field around the distorted chain shown in Fig. 2.4b. For this purpose, we model the continuous matrix by a discretized spring network.[19,56] Network nodes are set at the positions where the displacement field was tracked experimentally. The nodes are then connected by elastic springs. After that, we determine the normal modes of deformation of this network.[56] Finally, we can decompose the experimentally observed deformation field in Fig. 2.4b into these normal modes. Occupation numbers ϕ_n give the contribution of the nth mode to the overall deformation.

The four most occupied modes are shown in Fig. 2.5. We find a major contribution of "oscillatory" modes, i.e. alternating up and down displacements along the central horizontal axis. Such oscillatory displacements of the matrix are connected to corresponding oscillatory displacements of the chain, see Fig. 2.4b. A bending term of the form (see Supplementary Information, Section 2.8.3.2)

$$E_{bend} = C_b \int_{x_1}^{x_2} \frac{[y''(x)]^2}{[1+y'(x)^2]^{5/2}}\, dx \tag{2.3}$$

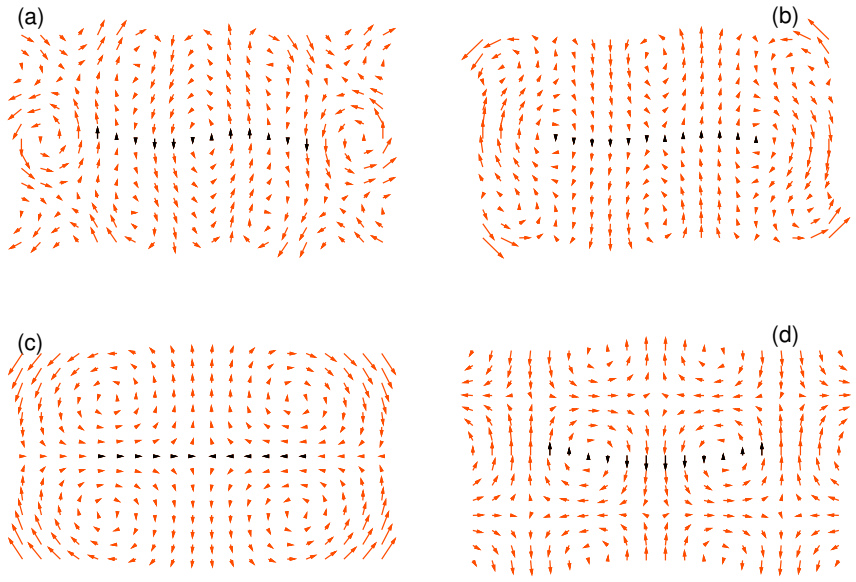

Figure 2.5 The four most occupied normal modes of the deformation field in Fig. 2.4b after projection to an elastic spring network, ordered by decreasing magnitude of contribution to the overall deformation. The normal modes (a), (b) and (d) are of an "oscillatory" type, whereas mode (c) represents a longitudinal contraction. Corresponding relative weights of the modes are $\phi^2_{(a)} = 0.095$, $\phi^2_{(b)} = 0.057$, $\phi^2_{(c)} = 0.055$, and $\phi^2_{(d)} = 0.051$, where we normalized the sum of the weights over all modes to unity. For better visualization, the overall amplitudes are rescaled as against the actual weights. The matrix region in close vicinity of the chain is indicated by black arrows.

becomes nonzero when such deformational modes occur and is therefore taken as a measure for their energetic contribution. In addition to that, we have experimental evidence that the chain itself shows a certain amount of bending rigidity (see Supplementary Information, Fig. 2.17), possibly due to the adsorption of polymer chains on the surfaces of the magnetic particles. Similar indication follows from two-dimensional model simulations, see below.

2.4.3 Elastic Displacement Energy

The bending term does not energetically penalize rotations of a straight chain, see Fig. 2.2a for $M = 0$. Yet, such rotations cost energy. Boundaries of the block of material are fixed, therefore any displacement of an inclusion induces a distortion of the surrounding gel matrix. We model this effect by a contribution (see Supplementary Information, Section 2.8.3.3)

$$E_{displ} = C_d \int_{x_1}^{x_2} [y(x)]^2 \left[1 + y'(x)^2\right]^{3/2} dx. \tag{2.4}$$

This term increasingly disfavors the rotations of longer straight chains, which reflects the experimental observations (see Supplementary Information, Fig. 2.19).

Moreover, in Fig. 2.5c the third dominating mode of the matrix deformation corresponds to a contraction along the chain direction and an expansion perpendicular to it. We conjecture that this should be the dominating mode in the deformational far-field, yet this hypothesis needs further investigation. It is induced by chain deflections in y-direction, which imply a matrix contraction in x-direction (experimentally we observe that the chain length is conserved under deformations and that the individual magnetic particles remain in close contact). We simultaneously use E_{displ} to represent the energetic contribution of this type of underlying matrix deformation.

2.4.4 Energetic Evaluation

We now consider the resulting phenomenological model energy $E_{tot} = E_{magn} + E_{bend} + E_{displ}$. A standard procedure would consist of minimizing E_{tot} with respect to the functional form of $y(x)$. Corresponding calculations and results are listed in the Supplementary Information, Section 2.8.3.4. There are, however, severe limitations to this route in the present case. In contrast to several previous approaches in different contexts,[57–61] our magnetic chains are of finite length and show significant displacements at their end points, see Fig. 2.2. Detailed knowledge of the boundary conditions of the deflection $y(x)$ and its derivatives at the end points of the chain would be necessary to determine the chain shape. Indeed the solutions become very sensitive to additional conditions (see Supplementary Information, Section 2.8.3.4). In our case, the necessary additional boundary conditions depend on the interaction with the matrix. They are not accessible in the present reduced framework.

Therefore, we proceed in a different way. We use as an input for our calculations the experimental observations. The experimentally found chain shapes can to good approximation be represented by a polynomial form

$$y(x) = S \prod_{m=0}^{M-1} (x - mb) \qquad \text{for } x_1 \leq x \leq x_2, \tag{2.5}$$

where M is again the number of half-waves, the prefactor S sets the strength or amount of chain deformation and deflection, b is the spacing between the nodes, and the interval $[x_1, x_2]$ follows from the experimental result of preserved chain length L,

$$\int_{x_1}^{x_2} \sqrt{1 + [y'(x)]^2}\, dx = L. \tag{2.6}$$

We prefer the polynomial form of Eq. (2.5) to, for instance, a sinusoidal ansatz because it better reproduces the deformations of our finite-sized chain objects. In particular, the pronounced displacements of the chain ends, see e.g. Fig. 2.2a, are well captured by polynomial forms. Likewise, an experimentally observed tendency to smaller oscillation amplitudes inside longer chains is covered. Furthermore, rotations of short straight chains are readily included in this way.

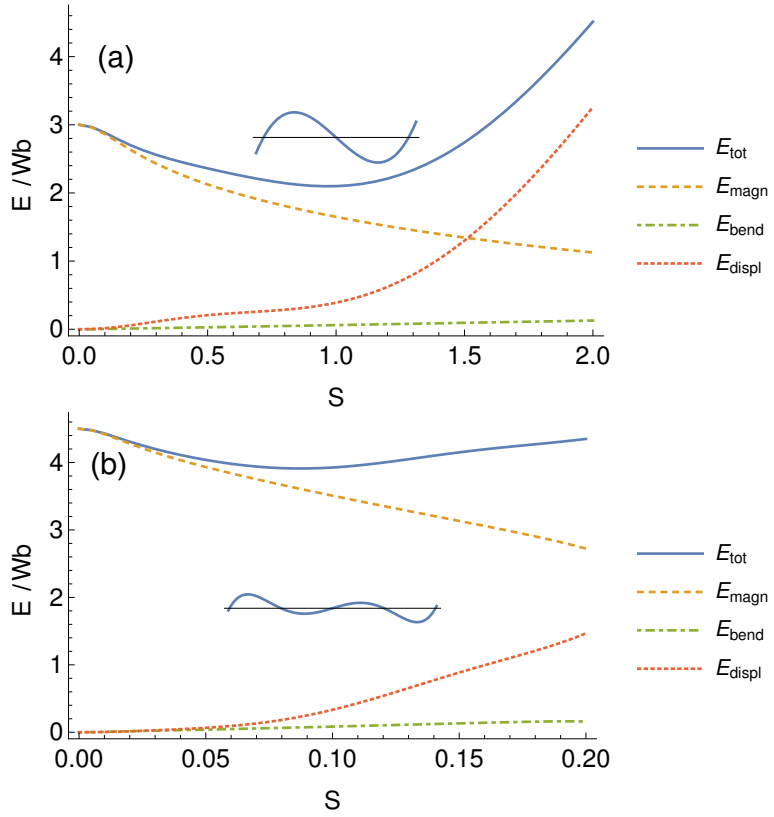

Figure 2.6 Contributions to the total energy as a function of the amount S of deformation and minimized with respect to x_1 and x_2 for a chain of the shape given by Eq. (2.5). Here we show the cases (a) $M = 2$, $L = 3b$ and (b) $M = 4$, $L = 4.5b$. The total energy E_{tot} has a global minimum as a function of S, which corresponds to the most stable chain shape. We always observed the global minimum for symmetric shapes.

Next, we insert Eq. (2.5) into the above expressions for the energy and minimize with respect to S, x_1, and x_2 for a given M, with the constraint of constant length L, see Eq. (2.6). The minimization was performed using Wolfram Mathematica minimization routines.[62] Parameter values of the coefficients C_b and C_d are found by matching the resulting shapes to the corresponding experimental profiles (chain deformations for $G' = 0.25$ Pa and magnetic field $B = 100.8$ mT as in Fig. 2.2a, $M = 2$, are used for this purpose). We obtain $C_b \approx 0.01 W b^2$ and $C_d \approx 2W/b^2$.

To illustrate how the energetic contributions vary under increasing preset deformation, we plot in Fig. 2.6 the energies for increasing S for two fixed combinations of M and L. The total energy E_{tot} shows a global minimum in both panels, which we always observed for symmetric chain deformations. As expected, with increasing S the magnetic energy decreases, whereas the deformation energies increase.

Next, we determine the minimal total energy as a function of chain length L for different numbers of half-oscillations M, see Fig. 2.7. With increasing chain length L the shapes that minimize the energy show an increasing number of half-waves M in good agreement with the experimental data in Fig. 2.2b.

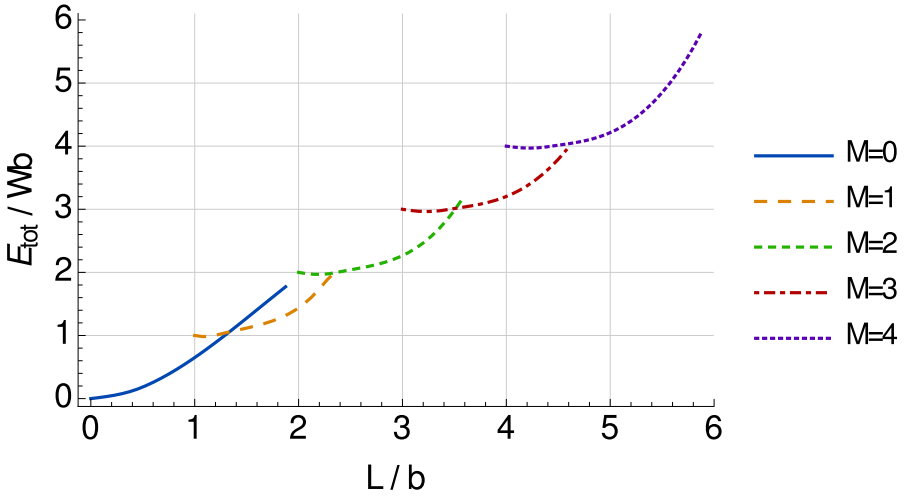

Figure 2.7 Energies E_{tot} of chain deformations of the shape given by Eq. (2.5), minimized with respect to S, x_1, and x_2, as a function of chain length L and number of half-oscillations M. Each curve describes a shape of M half-waves with a minimum total length of $(M-1)b$. The resulting curves show crossing points from where the total energy for an increasing L is lowered by bending one extra time (jumping to a higher M) rather than conserving the same shape.

Moreover, we quantify the amplitude of the chain deflection or deformation by

$$\text{Amplitude} = \sqrt{\langle y^2 \rangle - \langle y \rangle^2}, \qquad \langle \cdot \rangle = \frac{\int_{x_1}^{x_2} \cdot \, dx}{x_2 - x_1}. \tag{2.7}$$

Resulting values are plotted in Fig. 2.8. As mentioned above, we optimized the model parameters with respect to the experimental data for a magnetic field intensity of $B = 100.8$ mT. We demonstrate in Fig. 2.8 that moderate variations of the magnetic field intensity only slightly affect our results: the brighter curves are obtained when multiplying the magnetic energy scale W by a factor ~ 1.42, corresponding to an increased magnetic field intensity of approximately $B \sim 216$ mT (see Supplementary Information, Fig. 2.11b). This is in agreement with the experimental observations. We include in Fig. 2.8 the experimentally determined values for $B = 80.5$ mT and $B = 216.4$ mT. Only a slight trend of increasing deflection amplitudes is found for this increase of magnetic field intensity.

Together, although the curves for $M = 2$ in Fig. 2.8 slightly overshoot the data points, Figs. 2.7 and 2.8 are in good agreement with the experimental results. The amplitude of deflection and deformation is not observed to unboundedly increase with chain length L in the experiments. Likewise, our model predicts that longer chains prefer to bend one extra time (switching to higher-M shape) rather than to show too large deflection amplitudes.

2.5 Coarse-grained molecular dynamics simulation

We also studied the buckling of the chain using two-dimensional coarse-grained molecular dynamics simulations by means of the ESPResSo software.[63,64] A simple model was

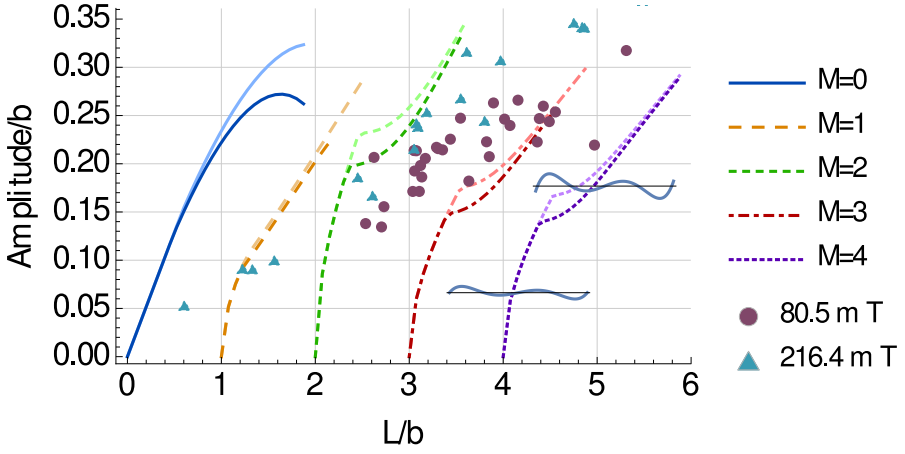

Figure 2.8 Resulting deflection amplitudes of the chain deformation, calculated according to Eq. (2.7). Darker curves represent the model parameters optimized with respect to the experimental shapes for a magnetic field intensity $B = 100.8$ mT. Brighter curves were obtained by increasing the magnetic energy scale W by a factor ~ 1.42, which corresponds to an increased magnetic field intensity of $B \sim 216$ mT (see Supplementary Information. Fig. 2.11b), comparable with the triangular experimental data points. Both, model curves and included experimental data points, demonstrate that moderate variations of the magnetic field intensities only slightly affect the observed deflection and deformation amplitudes. The value of b necessary to perform the analysis was determined from the $M = 2$ experimental data as $b = 12.6$ μm. For $M \geq 2$ "kinks" appear in the curves, which arise from a change in the type of solution as illustrated by the insets: for each $M \geq 2$ curve, left of the kink the chain deformation shows nodes at the end points of the chain, i.e. $y(x_1) \simeq y(x_2) \simeq 0$ (lower left inset); right from the kink, these outer nodes are shifted to the inside of the chain (upper right inset). As seen from Fig. 2.7, the solutions left of the kinks are not energetically preferred.

developed that allowed us to analyze the influence of particular interactions and material properties on the buckling effect. Here, we focus on the elasticity of the polymer matrix in the immediate vicinity of the magnetic particles.

By choosing the coarse-grained scale for our model, we ignore any chemical details but rather describe the system in terms of the magnetic particles as well as small pieces of polymer gel. As the buckling effect appears to be two-dimensional, and as the ground states for systems of dipolar particles have also been found to be two-dimensional,[55] we use this dimensionality for our simulations. We study a chain of 100 magnetic particles with a significant amount of surrounding elastic matrix.

As in the analytical approach, the gel matrix is modeled by a network of springs. Here, however, we use a regular hexagonal mesh as a basis. To mimic the non-linear elastic behavior of polymers, we use a finitely extensible non-linear elastic spring potential (FENE-potential[65]) for the springs along the edges of the mesh. As a simple implementation of the finite compressibility, we introduce FENE-like angular potentials on the angles at the mesh points, with a divergence at 0° and 180° (see Supplementary Information, Sec-

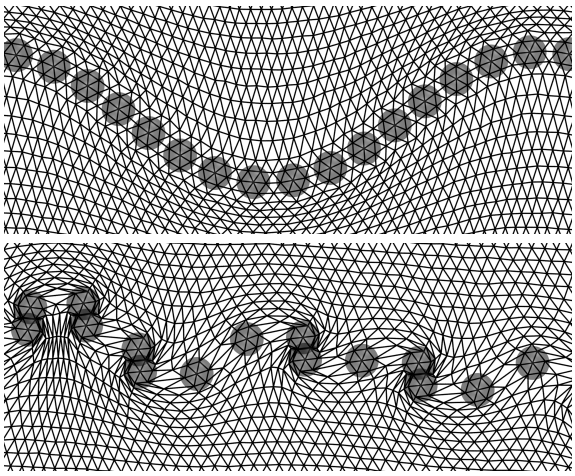

Figure 2.9 Detailed view of the local deformations in the polymer mesh around the magnetic particles with a layer of increased stiffness (top) and without one (bottom) in the immediate vicinity of the particle surfaces. The external magnetic field of strength 216 mT is applied in the vertical direction. When the boundary layer is assumed to be stiffer than the bulk (top), the buckling effect, as observed in the experiments, occurs. When the layer around the particles is soft (bottom), neighboring particles either form tight columns parallel to the field, or separate in the direction perpendicular to the field.

tion 2.8.4.2). The magnetic particles are modeled as rigid spheres interacting by a truncated, purely repulsive Lennard-Jones potential, the so-called Weeks-Chandler-Andersen potential (see Supplementary Information, Section 2.8.4.1).[66] Their magnetic moment is assumed to be determined purely by the external magnetic field and to be constant throughout the simulation. I.e. we assume that the external field is significantly stronger than the field created by the particles. The magnetic moments are taken parallel to the external field and with a magnitude given by the experimentally observed magnetization curve. The coupling between the particles and the mesh is introduced in such a way, that under the volume occupied by a particle, the mesh does not deform, but rigidly follows the translational and rotational motion of the particle (see Supplementary Information, Section 2.8.4.3). A local shear strain on the matrix can rotate a magnetic particle, but not its magnetic moment.

An important point is the elasticity of the polymer matrix in the immediate vicinity of the magnetic particles and, in particular, between two magnetic particles. We study two situations here, the first one including a stiffer region in the immediate vicinity of the particles, the second one without such a stiffer layer and directly jumping to the bulk elasticity. The stiffer layer, if imposed, is created using a spring constant larger by three orders of magnitude on those springs which originate from mesh sites within the particle volumes (see Supplementary Information, Section 2.8.4.3). The angular potentials are unchanged.

A comparison between the cases with and without a stiffer layer of gel around the magnetic particles can be seen in Fig. 2.9. The images show a small part of the resulting configuration of magnetic particles and the surrounding mesh for a field applied perpendicular to the initial chain direction. Thus the magnetic moments of the particles are oriented perpendicular to the undistorted chain direction. This results in an energetically unfavorable parallel side-by-side configuration for the dipole moments. The energy can be reduced either by increasing the distance between the dipoles along the initial chain direction, or by moving dipoles perpendicularly to the initial chain direction so that they approach the energetically most favorable head-to-tail configuration. If the matrix is made stiffer immediately around the particles, and thus the contour length of the chain cannot change significantly, the re-positioning towards the head-to-tail configuration causes the buckling effect observed in the experiments (Fig. 2.9). When one assumes the matrix immediately around the magnetic particles to be as soft as in the bulk of the material, neighboring particles can move apart and the chain breaks up into individual particles or small columns perpendicular to the original chain direction. Additionally, a layer of increased stiffness also introduces a bending rigidity of the chain. In Fig. 2.10, the full chain and the surrounding matrix is shown for an external field of magnitude 216 mT, which from the experimental magnetization measurements corresponds to a magnetic moment of about $4.5 \cdot 10^{-14}$ Am^2 (see Supplementary Information, Fig. 2.11b). Due to the different dimensionalities, the elastic modulus of the surrounding matrix could not be directly matched to the experimental system.

Actually, the amplitude of the chain oscillation increases when the external field is higher and induces larger dipole moments in the particles. This increases the tendency of the magnetic moments to approach the head-to-tail configuration, which in turn leads to a stronger deformation of the matrix. We note that the relative amplitude of the buckling along the chain is similar in the simulations (Fig. 2.9) and experiments (Fig. 2.2). The matrix surrounding the chain follows the chain oscillation with an amplitude that decreases over distance from the chain. Deviations may be expected from the deformational far-field in the experimental system due to the different dimensionalities of the systems.

In the Supplementary Information (Fig. 2.17) we show an experimental evidence for the existence of a stiff polymer layer around the magnetic particles. The sample was prepared at a concentration of prepolymer mixture well below the percolation threshold, i.e., some cross-linking of the polymer took place in the sample but no macroscopic gel was formed. When this cross-linking was done under an applied magnetic field, the particle chains stayed intact even after removal of the magnetic field (Fig. 2.17a). Hairpin or "S"-shape morphologies were observed when these chains were exposed to a magnetic field (Fig. 2.17b), indicating that they have a bending rigidity.[50,51] Our interpretation of this behavior is that a stiff gel layer connects the particles and stabilizes the particle chains, even though no bulk gel is formed. As the magnetic particles have a good affinity for

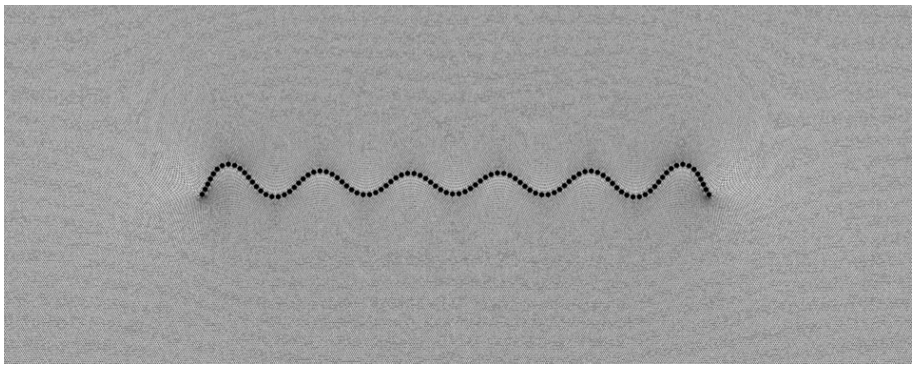

Figure 2.10 Buckling chain of magnetic particles and the surrounding polymer mesh for an external field of magnitude 216 mT pointing along the vertical direction. In this image, roughly one quarter of the full simulation area is shown. The surrounding matrix follows the chain oscillation with an amplitude that decreases over distance from the chain.

PDMS (e.g., the magnetic particles can be easily dispersed into PDMS), we conjecture that there is an adsorbed layer of polymer (i.e., PDMS prepolymer or cross-linker) on the surface of the magnetic particles.[67] Therefore, the gel layer on the particles is denser and thus stiffer than in the bulk. Further study of the stiff polymer layer and its effect on the buckling behavior is under way.

Moreover, in Fig. 2.18 (Supplementary Information) we show that the buckling behavior of the magnetic chains can still be observed in the gel when we increase the elastic modulus to 170 Pa (for this purpose, carbonyl iron particles are used as magnetic filler particles). Our studies on that stiffer sample provide further evidence that the interaction between the magnetic particles and the polymer matrix in their close vicinity can play an important role in the magneto-elastic response of soft MRGs.

2.6 Conclusions

We have shown that paramagnetic chains in a soft polymer gel can buckle in a perpendicular magnetic field. The buckling morphology depends on the length of the chain, the strength of the magnetic field and the modulus of the gel. Longer chains form buckling structures with a higher number of half waves. Higher strengths of the magnetic field and a lower modulus of the gel matrix can lead to higher deformation amplitudes. The deformation field in the surrounding gel matrix confirms that the embedding polymer network is strongly coupled to the paramagnetic chain. A minimal magneto-elastic coupling model is developed to describe the morphological behavior of the paramagnetic chains in the soft gel under a perpendicular magnetic field. It shows that the chains deform in order to decrease the magnetic energy. This is hindered by the simultaneous deformation of the gel matrix, which costs elastic energy. Additionally, we have introduced a coarse-grained

molecular dynamics simulation model, which covers both, the magnetic particles and the surrounding polymer mesh. In this model, the buckling of the chains can only be observed when the surface layer around the particles is assumed to be stiffer than the bulk of the gel. This prevents the chains from breaking up into columns oriented perpendicular to the initial chain direction or into isolated particles. These findings support the picture that the embedded magnetic chains themselves feature a certain bending rigidity, possibly due to the existence of a stiff polymer layer on the particle surfaces.

Since the magneto-elastic effect demonstrated and analyzed in this paper is pronounced, reversible, and controllable, it may be useful for designing micro-devices, e.g. microvalves and pumps for microfluidic control.[68] As the morphologies of the buckling paramagnetic chains are correlated with the modulus of the gel matrix, we may use them as mechanical probes for soft gels (similarly to active microrheology techniques).[45] Moreover, our study may help to understand the physical interactions between the magnetic chains and the surrounding cytoskeleton network in magnetotactic bacteria.[46] In our future study we will focus on how the interfacial coupling between the magnetic particles and the polymer network influences the local magneto-elastic coupling effect.

2.7 Acknowledgements

The authors acknowledge support by the Deutsche Forschungsgemeinschaft (DFG) through the SPP 1681 (SH and GKA acknowledge the project AU321/3-1; GP, PC and AMM acknowledge the project LO418/16-1; RW and CH acknowledge the project HO 1108/23-1; JN and SO acknowledge the project OD18/21). RW and CH acknowledge funding through the cluster of excellence EXC 310, SimTech at the University of Stuttgart. We thank Dr. Peter Blümler for inspiring discussions on designing the Halbach magnetic arrays.

Bibliography

[1] P. Ilg, *Soft Matter*, 2013, **9**, 3465–3468.

[2] R. L. Snyder, V. Q. Nguyen and R. V. Ramanujan, *Smart Mater. Struct.*, 2010, **19**, 055017.

[3] K. Zimmermann, V. A. Naletova, I. Zeidis, V. Böhm and E. Kolev, *J. Phys.: Condens. Matter*, 2006, **18**, S2973–S2983.

[4] R. Hergt, S. Dutz, R. Müller and M. Zeisberger, *J. Phys.: Condens. Matter*, 2006, **18**, S2919–S2934.

[5] D. Szabó, G. Szeghy and M. Zrínyi, *Macromolecules*, 1998, **31**, 6541–6548.

[6] S. S. Abramchuk, D. A. Grishin, E. Y. Kramarenko, G. V. Stepanov and A. R. Khokhlov, *Polym. Sci. Ser. A*, 2006, **48**, 138–145.

[7] G. Filipcsei, I. Csetneki, A. Szilágyi and M. Zrínyi, *Adv. Polym. Sci.*, 2007, **206**, 137–189.

[8] D. Collin, G. K. Auernhammer, O. Gavat, P. Martinoty and H. R. Brand, *Macromol. Rapid Comm.*, 2003, **24**, 737–741.

[9] J. Faraudo, J. S. Andreu and J. Camacho, *Soft Matter*, 2013, **9**, 6654–6664.

[10] D. J. Griffiths, *Introduction to Electrodynamics*, Prentice-Hall, Upper Saddle River, NJ, 3rd edn, 1999, p. 282.

[11] S. H. L. Klapp and M. Schoen, *J. Chem. Phys.*, 2002, **117**, 8050–8062.

[12] S. H. L. Klapp, *J. Phys.: Condens. Matter*, 2005, **17**, R525–R550.

[13] G. P. Gajula, M. T. Neves-Petersen and S. B. Petersen, *Appl. Phys. Lett.*, 2010, **97**, 103103.

[14] J. de Vicente, D. J. Klingenberg and R. Hidalgo-Alvarez, *Soft Matter*, 2011, **7**, 3701–3710.

[15] G. K. Auernhammer, D. Collin and P. Martinoty, *J. Chem. Phys.*, 2006, **124**, 204907.

[16] D. S. Wood and P. J. Camp, *Phys. Rev. E*, 2011, **83**, 011402.

[17] D. Ivaneyko, V. Toshchevikov, M. Saphiannikova and G. Heinrich, *Condens. Matter Phys.*, 2012, **15**, 33601.

[18] Y. Han, W. Hong and L. E. Faidley, *Int. J. Solids Struct.*, 2013, **50**, 2281–2288.

[19] G. Pessot, P. Cremer, D. Y. Borin, S. Odenbach, H. Löwen and A. M. Menzel, *J. Chem. Phys.*, 2014, **141**, 124904.

[20] A. M. Menzel, *Phys. Rep.*, 2015, **554**, 1–46.

[21] O. V. Stolbov, Y. L. Raikher and M. Balasoiu, *Soft Matter*, 2011, **7**, 8484–8487.

[22] G. Filipcsei, I. Csetneki, A. Szilágyi and M. Zrínyi, in *Magnetic Field-Responsive Smart Polymer Composites*, Springer Berlin Heidelberg, 2007, vol. 206, pp. 137–189.

[23] D. Günther, D. Y. Borin, S. Günther and S. Odenbach, *Smart Mater. Struct.*, 2012, **21**, 015005.

[24] T. Borbáth, S. Günther, D. Y. Borin, T. Gundermann and S. Odenbach, *Smart Mater. Struct.*, 2012, **21**, 105018.

[25] X. C. Guan, X. F. Dong and J. P. Ou, *J. Magn. Magn. Mater.*, 2008, **320**, 158–163.

[26] K. Danas, S. V. Kankanala and N. Triantafyllidis, *J. Mech. Phys. Solids*, 2012, **60**, 120–138.

[27] A. Y. Zubarev, *Soft Matter*, 2013, **9**, 4985–4992.

[28] E. Jarkova, H. Pleiner, H. W. Müller and H. R. Brand, *Phys. Rev. E*, 2003, **68**, 041706.

[29] S. Bohlius, H. R. Brand and H. Pleiner, *Phys. Rev. E*, 2004, **70**, 061411.

[30] R. Weeber, S. Kantorovich and C. Holm, *Soft Matter*, 2012, **8**, 9923–9932.

[31] R. Weeber, S. Kantorovich and C. Holm, *J. Magn. Magn. Mater.*, 2015, **383**, 262.

[32] A. V. Ryzhkov, P. V. Melenev, C. Holm and Y. L. Raikher, *J. Magn. Magn. Mater.*, 2015, **383**, 277.

[33] A. M. Menzel, *J. Chem. Phys.*, 2014, **141**, 194907.

[34] D. Ivaneyko, V. Toshchevikov, M. Saphiannikova and G. Heinrich, *Soft Matter*, 2014, **10**, 2213–2225.

[35] G. Pessot, R. Weeber, C. Holm, H. Löwen and A. M. Menzel, *J. Phys.: Condens. Matter*, 2015, **27**, 325105.

[36] L. Roeder, M. Reckenthäler, L. Belkoura, S. Roitsch, R. Strey and A. M. Schmidt, *Macromolecules*, 2014, **47**, 7200–7207.

[37] N. Frickel, R. Messing, T. Gelbrich and A. M. Schmidt, *Langmuir*, 2009, **26**, 2839–2846.

[38] N. Frickel, R. Messing and A. M. Schmidt, *J. Mater. Chem.*, 2011, **21**, 8466–8474.

[39] R. Messing, N. Frickel, L. Belkoura, R. Strey, H. Rahn, S. Odenbach and A. M. Schmidt, *Macromolecules*, 2011, **44**, 2990–2999.

[40] I. Csetneki, G. Filipcsei and M. Zrínyi, *Macromolecules*, 2006, **39**, 1939–1942.

[41] H. N. An, J. Groenewold, S. J. Picken and E. Mendes, *Soft Matter*, 2014, **10**, 997–1005.

[42] M. Minsky, *Scanning*, 1988, **10**, 128–138.

[43] M. Roth, M. Franzmann, M. D'Acunzi, M. Kreiter and G. K. Auernhammer, *arXiv preprint, arXiv:1106.3623*, 2011.

[44] M. Roth, C. Schilde, P. Lellig, A. Kwade and G. K. Auernhammer, *Eur. Phys. J. E.*, 2012, **35**, 124.

[45] C. Wilhelm, *Phys. Rev. Lett.*, 2008, **101**, 028101.

[46] A. Körnig, J. Dong, M. Bennet, M. Widdrat, J. Andert, F. D. Müller, D. Schüler, S. Klumpp and D. Faivre, *Nano Lett.*, 2014, **14**, 4653–4659.

[47] T. G. Mason, T. Gisler, K. Kroy, E. Frey and D. A. Weitz, *J. Rheol.*, 2000, **44**, 917–928.

[48] H. Raich and P. Blümler, *Concept. Magn. Reson. B*, 2004, **23**, 16–25.

[49] I. F. Sbalzarini and P. Koumoutsakos, *J. Struct. Biol.*, 2005, **151**, 182–195.

[50] C. Goubault, P. Jop, M. Fermigier, J. Baudry, E. Bertrand and J. Bibette, *Phys. Rev. Lett.*, 2003, **91**, 260802.

[51] V. P. Shcherbakov and M. Winklhofer, *Phys. Rev. E*, 2004, **70**, 061803.

[52] http://imagej.nih.gov/ij/.

[53] C. Spieler, M. Kästner, J. Goldmann, J. Brummund and V. Ulbricht, *Acta Mech.*, 2013, **224**, 2453–2469.

[54] M. A. Annunziata, A. M. Menzel and H. Löwen, *J. Chem. Phys.*, 2013, **138**, 204906.

[55] T. Prokopieva, V. Danilov, S. Kantorovich and C. Holm, *Phys. Rev. E*, 2009, **80**, 031404.

[56] M. Tarama, P. Cremer, D. Y. Borin, S. Odenbach, H. Löwen and A. M. Menzel, *Phys. Rev. E*, 2014, **90**, 042311.

[57] I. Gelfand and S. Fomin, *Calculus of variations*, Prentice-Hall Inc., Englewood Cliffs, NJ, 1963.

[58] G. W. Hunt, M. Wadee and N. Shiacolas, *J. Appl. Mech.*, 1993, **60**, 1033–1038.

[59] B. Audoly, *Phys. Rev. E*, 2011, **84**, 011605.

[60] H. Diamant and T. A. Witten, *arXiv preprint arXiv:1009.2487*, 2010.

[61] H. Diamant and T. A. Witten, *Phys. Rev. Lett.*, 2011, **107**, 164302.

[62] Wolfram Research, *Mathematica 10.0*, 2014.

[63] H. J. Limbach, A. Arnold, B. A. Mann and C. Holm, *Comp. Phys. Comm.*, 2006, **174**, 704–727.

[64] A. Arnold, O. Lenz, S. Kesselheim, R. Weeber, F. Fahrenberger, D. Röhm, P. Košovan and C. Holm, Meshfree Methods for Partial Differential Equations VI, 2013, pp. 1–23.

[65] H. R. Warner, *Ind. Eng. Chem. Fundam.*, 1972, **11**, 379–387.

[66] J. D. Weeks, D. Chandler and H. C. Andersen, *J. Chem. Phys.*, 1971, **54**, 5237.

[67] L. Cohen-Tannoudji, E. Bertrand, L. Bressy, C. Goubault, J. Baudry, J. Klein, J.-F. Joanny and J. Bibette, *Phys. Rev. Lett.*, 2005, **94**, 038301.

[68] E. K. Fleischmann, H. L. Liang, N. Kapernaum, F. Giesselmann, J. Lagerwall and R. Zentel, *Nature Commun.*, 2012, **3**, 1178.

2.8 Supplementary information

2.8.1 Supplementary movies

Movie S2-1 Typical 3D morphology of paramagnetic chains in a soft gel in the absence of a magnetic field. The elastic modulus of the gel is 0.78 ± 0.22 Pa and the scale bar is 300 μm.

Movie S2-2 Typical 3D morphology of paramagnetic chains in a soft gel under a perpendicular magnetic field ($B = 216.4 \pm 1.1$ mT). The elastic modulus of the gel is 0.78 ± 0.22 Pa and the scale bar is 300 μm.

2.8.2 Supplementary information for experiments

2.8.2.1 Paramagnetic particles

According to the manufacturer (microParticles GmbH), the paramagnetic particles were fabricated based on porous polystyrene particles. Within the pores of the polystyrene particles, nanoparticulate iron oxide was distributed, rendering the particles superparamagnetic. To prevent iron oxide leaching, the paramagnetic particles were covered with thin polymer layers which also held the fluorophores. The diameter of the paramagnetic particles from the scanning electron microscopy (SEM) images (see Fig. 2.11a) is 1.4 ± 0.2 μm. We also measured the length of linear particle chains in polydimethylsiloxane using laser scanning confocal microscopy (LSCM). Dividing the length of the chains by the number of particles in the chains we got a diameter of 1.48 ± 0.13 μm (average for 20 chains). We used the latter value for calibration and calculation in this paper.

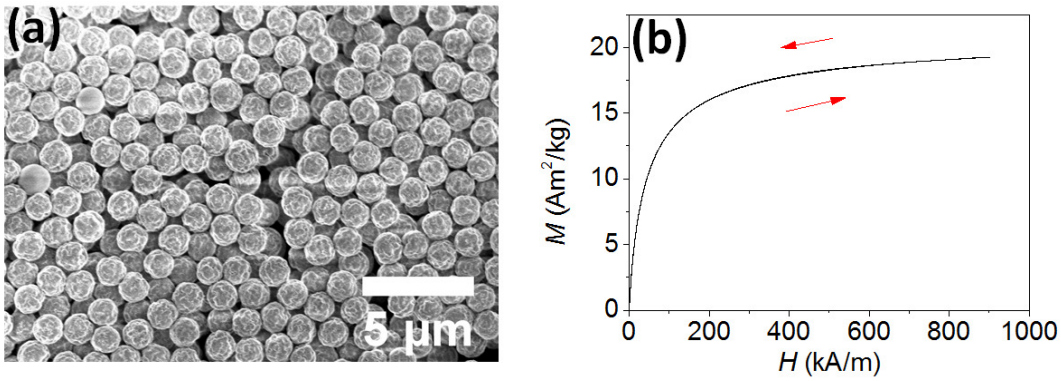

Figure 2.11 (a) Scanning electron microscopy (SEM) image of the paramagnetic particles. The scale bar is 5 μm. (b) Magnetization curve of the paramagnetic particles. The magnetic field H was increased from 0 kA/m to 900 kA/m and then decreased to 0 kA/m, and the magnetization M showed no hysteresis, as indicated by the red arrows.

The magnetization curve of the paramagnetic particles was measured by a vibrating sample magnetometer (VSM, Lake Shore 7407). The magnetization of the particles

showed no hysteresis when the external magnetic field was increased and decreased, demonstrating the superparamagnetic property (Fig. 2.11b).

2.8.2.2 Calibrating the magnetic properties of the paramagnetic particles

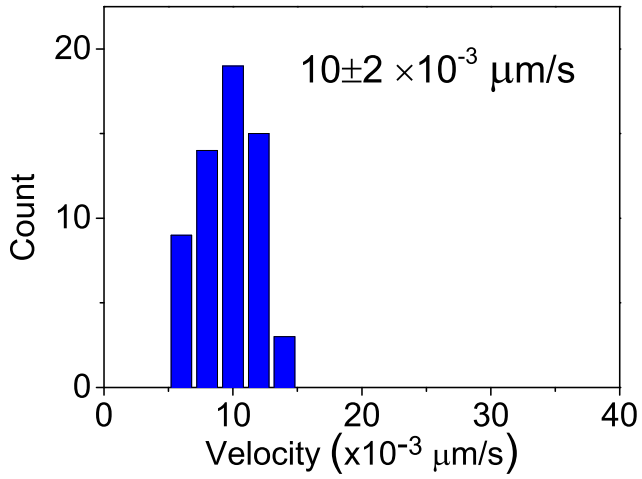

Figure 2.12 Histogram of velocity of paramagnetic particles moving in a viscous liquid. The viscosity of the liquid is 0.61 ± 0.02 Pa s. The magnetic field strength is 32.7 ± 0.2 mT and the magnetic gradient is $3.63 \pm 0.02 \times 10^{-5}$ mT/μm. Using a density of 1.7 g/cm^3, the movement of the particles, the magnetic gradient, and the magnetization curve can be correlated.[1,2]

A spherical colloidal particle moving in a viscous fluid with a relative velocity $\mathbf{v}$ is subject to a frictional force (Stokes' drag)

$$\mathbf{F}_d = -6\pi\eta R\mathbf{v}, \tag{2.8}$$

where R is the radius of the particle and η is the dynamic viscosity of the fluid.

Under a magnetic field $\mathbf{B}$, the magnetic particles move along the magnetic field gradient. The magnetic force $\mathbf{F}_m$ acting on a paramagnetic particle is[1,2]

$$\mathbf{F}_m = \mathbf{m} \cdot \nabla\mathbf{B}, \tag{2.9}$$

where $\mathbf{m}$ is the induced magnetic dipole moment of the paramagnetic particle. In the steady state, the magnetic force is balanced by Stokes' drag, thus

$$6\pi\eta R\mathbf{v} = \mathbf{m} \cdot \nabla\mathbf{B}. \tag{2.10}$$

From experiments, the left-hand side of Eq. (2.10) and $\nabla\mathbf{B}$ can be measured directly. We dispersed the paramagnetic particles into a viscous liquid with a viscosity of 0.61 ± 0.02 Pa s. The dispersion was added into a sample cell with a thickness of 160 μm. Then the sample cell was carefully sealed in order to avoid drift due to large-scale flow of

the liquid. We used a magnetic field of 32.7 ± 0.2 mT with a gradient of $3.63 \pm 0.02 \times 10^{-5}$ mT/μm to induce flow of the paramagnetic particles. The magnetic field was measured by a Lake Shore Model 425 Gaussmeter with a transverse probe. The movement of the particles (far from the walls of the sample cell) was recorded using LSCM. The magnitude of the magnetic moment m can be calculated via $m = 4\pi R^3 \rho M/3$, where M can be obtained from the magnetization curve (Fig. 2.11b) and ρ is the density of the paramagnetic particles. Using $\rho = 1.7$ g/cm^3, we find that Eq. (2.10) is satisfied. This density value is in agreement with the one provided by the manufacturer (1.5–2 g/cm^3).

In our study the paramagnetic particles are not ideally monodispersed and the induced magnetic moment is not ideally identical for every particle. For example, the velocity of the paramagnetic particles moving in a viscous liquid under a magnetic gradient has a distribution with $\sim 20\%$ deviation (Fig. 2.12). According to Eq. (2.10), the magnetic moment of the particles should have a similar distribution. For simplification, we do not consider this distribution in the modeling and simulation.

2.8.2.3 Determining the elastic modulus of the soft gels

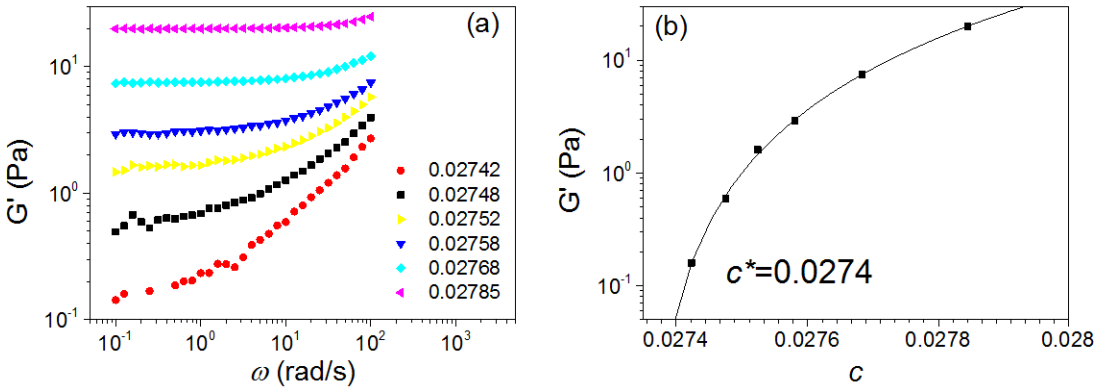

Figure 2.13 (a) Shear elastic modulus (G') of the gels as a function of angular frequency. The gels were fabricated with different concentrations (c) of the prepolymer mixture as indicated for the different sets of data points. (b) The low-frequency G' of the gels plotted as a function of c. The solid curve is the best fit of Eq. (2.11) to the experimental data.

The rheological experiments were performed in a strain-controlled rheometer (ARES-LS, Rheometric Scientific Inc., Piscataway, NJ, USA) equipped with a Couette cell at room temperature. The elastic modulus (G') shows a plateau at low frequencies for the soft gels (Fig. 2.13a), reflecting the formation of a percolating network. The plateau modulus increases with increasing concentration of the prepolymer mixture (c) following a power law[3]

$$G' = G'_0 (c - c^\star)^t, \tag{2.11}$$

where G'_0 is a prefactor, t is the critical exponent, and $c^\star$ is the percolation concentration. From this power law it is evident that the elastic modulus of the soft gels becomes very

sensitive to the concentration of the prepolymer mixture when the concentration of the prepolymer mixture is close to $c^\star$.

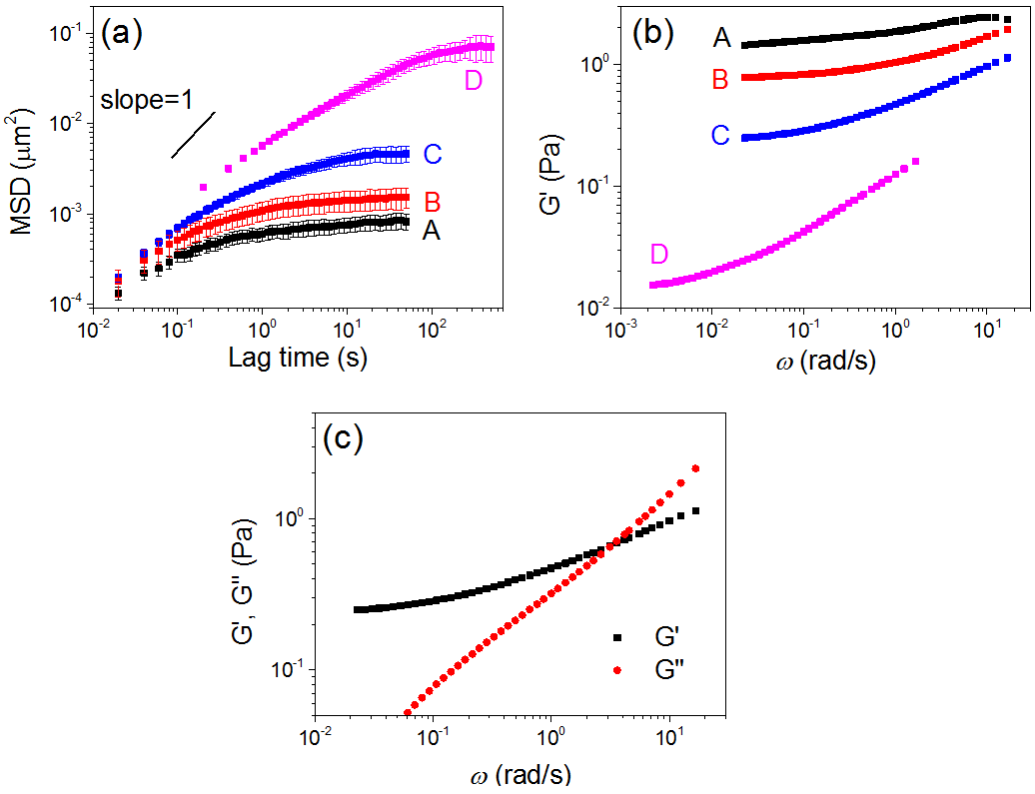

Figure 2.14 Probing the viscoelastic properties of the gels in the sample cells (containing the paramagnetic chains). (a) Mean-square displacement (MSD) of the particles in the gels as a function of lag time. The concentrations of the prepolymer mixture for the four samples A–D are 2.78 wt%, 2.77 wt%, 2.76 wt%, and 2.76 wt%, respectively. The slight changes of concentration can lead to significant differences in the MSD, because the concentration used here is close to the percolation threshold ($c^\star = 2.74\%$, see Fig. 2.13b).[3] It is the method of passive microrheology that makes it possible to measure the viscoelastic properties of the soft gels (containing the paramagnetic chains) directly within the sample cells. (b) Elastic modulus (G') calculated from the MSD. (c) Elastic modulus (G') and loss modulus (G'') plotted as functions of angular frequency (ω) for sample C. At low frequencies, the elastic character dominates.

As a result, we cannot directly use the elastic modulus obtained from macroscopic rheological measurements to characterize our soft gels in the sample cells ($\sim$160 μm thick), because a little change of the concentration of the prepolymer mixture during preparation of the gels can lead to a significant difference of the elastic modulus. In experiment, the concentration of the prepolymer mixture in the sample cells is difficult to control precisely, because the concentration can change slightly if some prepolymer molecules are adsorbed to the walls of the cell, to the pipette tips, or to the paramagnetic particles.

In order to solve this problem, we measured the elastic modulus of the soft gels directly

in the sample cells (containing the paramagnetic chains) by passive microrheology (i.e., particle tracking). About 15 single particles were used as the mechanical probes, and a fast camera (Photron, FASTCAM SA1) and a microscope (Leica DMI6000B) were used to detect the thermal fluctuations of the particles.[4,5] Fig. 2.14a shows the mean-square displacement (MSD) of the particles in the gels as a function of lag time. At long lag times the MSD levels off, indicating that the particles are confined in a network. The moduli of the gels can be calculated from the MSD of the particles based on the generalized Stokes-Einstein relation (GSER)[4,6]

$$G^*(\omega) = \frac{k_B T}{\pi R (i\omega) \mathscr{F}_u\{MSD(t)\}}, \tag{2.12}$$

where $G^*(\omega)$ is the complex shear modulus and $\mathscr{F}_u\{MSD(t)\}$ is the unilateral Fourier transform ($\mathscr{F}\{f(t)\} = \int_0^\infty e^{-i\omega\tau} f(\tau)\, d\tau$). Using the algorithm from Crocker and Weeks,[4,5] we calculated the shear moduli (Fig. 2.14b). Fig. 2.14c shows that at low frequencies (corresponding to long time scales) the gel is mainly elastic. In the main article we use the elastic modulus of the gels obtained from passive microrheology to characterize the gels.

2.8.2.4 Magnetic field of the Halbach magnetic array

We used permanent magnets to provide a homogeneous magnetic field.[7] The NdFeB permanent magnets were purchased from AR.ON GmbH. According to the manufacturer they have a remanence of 1.32 T. The magnets were arranged as shown in Fig. 2.1a. The magnets had dimensions of $8 \times 8 \times 15$ mm^3 and $14 \times 14 \times 15$ mm^3 for the inner and outer rings, respectively. The magnetic field at the center of this magnetic array was homogeneous (Fig. 2.15). This magnetic array was built around the objective of our home-built LSCM and it could be rotated by a motor. We put the samples in the middle of this array and used LSCM to observe the samples under the magnetic field. The typical observation area was in the central 2 mm^2, where the homogeneity of the magnetic field was $\sim 2\,000$ ppm (Fig. 2.15b).

The magnetic field of this magnetic array was simulated in Comsol Multiphysics (http://www.comsol.com). The parameters for the simulation were the same as in the experiments, such as the positions, the dimensions, and the remanence (1.32 T) of the magnets. The permanent magnets were modeled using Ampère's law. The influence of the housing (made of Aluminum) of the magnets was not considered. A detailed description of the simulation can be found in the model library of Comsol Multiphysics, "Static Field Modeling of a Halbach Rotor".

In some experiments we needed to change the magnetic field strength. This was realized by using a four-magnet Halbach array (Fig. 2.16, the magnets had dimensions of $14 \times 14 \times 15$ mm^3). By changing the distance between the magnets, the magnetic flux density in the center of this array could be changed from 0 mT to 101 mT. The homogeneity of this array in the central 2 mm^2 was $\sim 4\,000$ ppm.

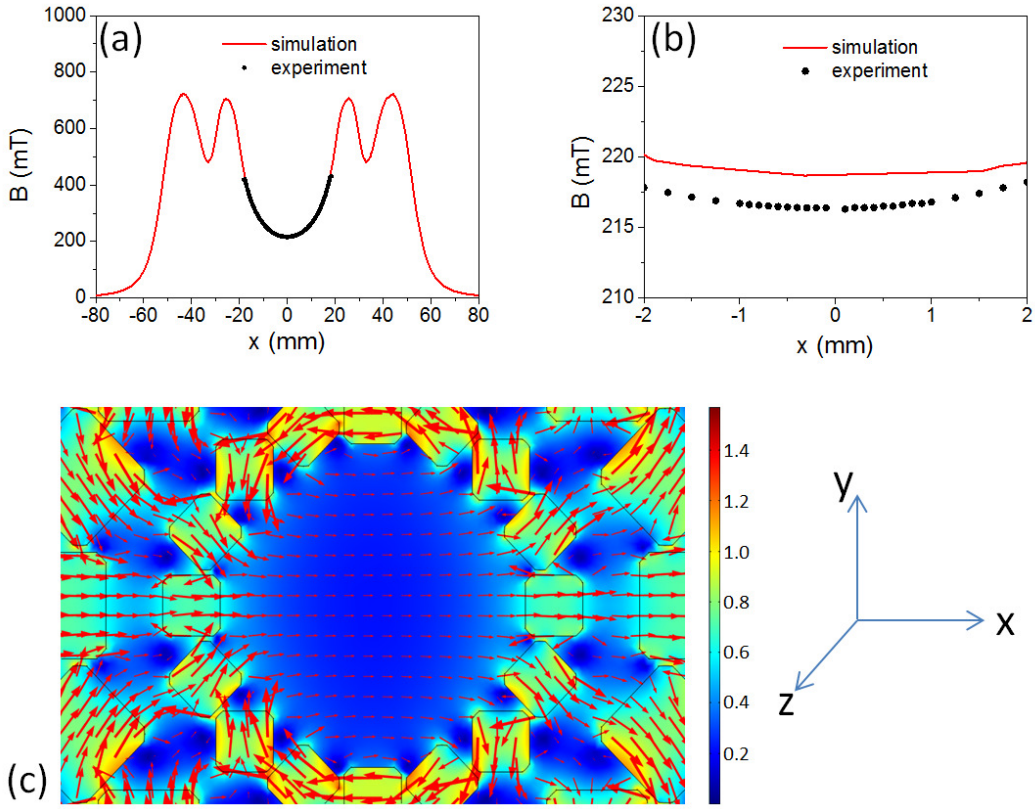

Figure 2.15 Comparison of measured and simulated magnetic flux density in the Halbach magnetic array. The arrangement of the 32 permanent magnets is shown in Fig. 2.1a. (a) Magnitude B of the magnetic flux density along the x-axis. The red solid curve shows simulation results using Comsol software. The solid black points are experimental data (measured by a Lake Shore Model 425 Gaussmeter with a transverse probe). The data for x around 0 are shown in (b). The homogeneity in the central 2 mm^2 is $\sim$ 2 000 ppm. (c) Simulated magnetic field in the magnetic array. The magnetic flux density is shown by color map and the direction of the magnetic field is shown by red arrows.

2.8.2.5 Bending rigidity of the paramagnetic particle chains

Here we provide experimental evidence that the paramagnetic particle chains already by themselves (i.e. without the embedding polymer matrix) feature a bending rigidity. For this purpose, instead of preparing a percolating polymer network (gel), we prepared a sol. We decreased the concentration of the prepolymer mixture to $c^\star/2$ ($c^\star$ is the critical concentration at which a percolating network can be formed, see Fig. 2.13b). The prepolymer mixture reacted and formed a sol after the catalyst was added. During the reaction a magnetic field of 100.8 mT was applied, thus the magnetic particles in the sol aligned into chains. If the particles had not been connected by the polymer, the linear particle chains would not have survived after the magnetic field was removed because of thermal agitation. However, we found that the linear particle chains were stable in the sol even for several days (Fig. 2.17a). Once more applying a magnetic field (18.7 mT)

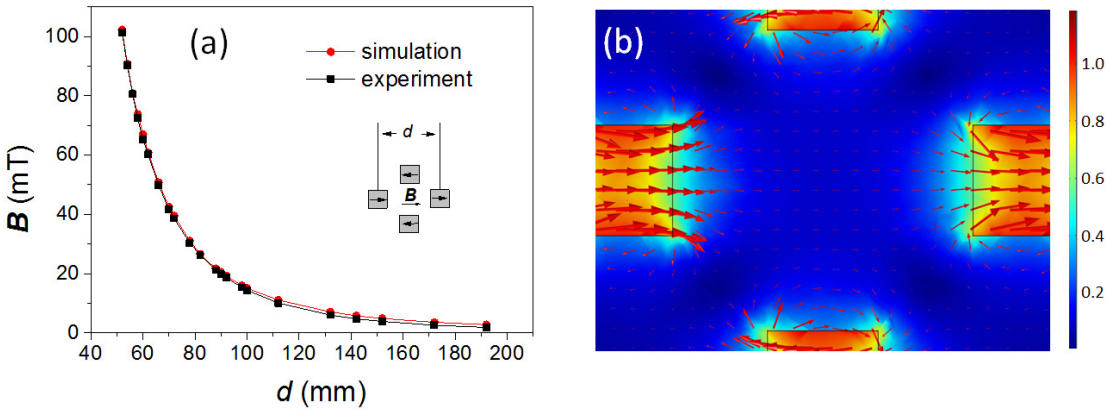

Figure 2.16 Magnetic field of the four-magnet Halbach array. (a) By changing the separation between the 4 magnets, the magnetic flux density at the center of the magnetic array can be changed. The red circle points are obtained from simulation using Comsol software, and the black square points are measured by a Lake Shore Model 425 Gaussmeter with a transverse probe. The homogeneity in the central 2 mm^2 is ~ 4000 ppm. (b) Simulated magnetic field in the four-magnet array. The magnetic flux density is shown by color map and the direction of the magnetic field is shown by red arrows.

most of the permanent paramagnetic chains in the sol aligned along the magnetic field direction (Fig. 2.17b). However, some of the chains bent and showed hairpin or "S"-shape morphologies (marked by the red arrows in Fig. 2.17b), indicating that the chains had a bending rigidity.[8]

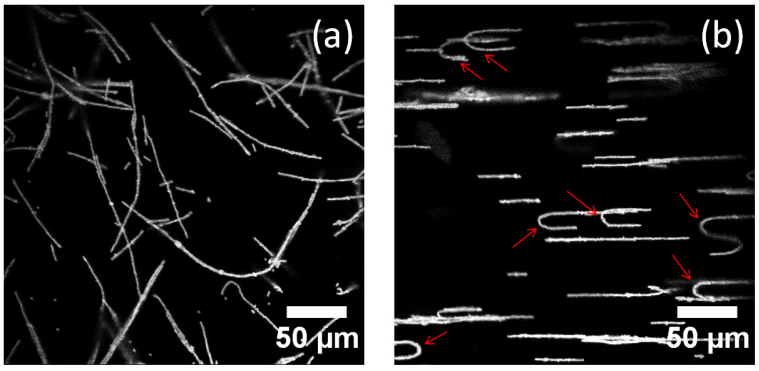

Figure 2.17 Typical chain morphologies in the sol (a) in the absence of a magnetic field and (b) under a magnetic field. The magnetic field of 18.7 mT was applied horizontally. Under the magnetic field most of the paramagnetic chains aligned along the magnetic field direction. Some of the chains bent and showed hairpin or "S"-shape morphologies (marked by the red arrows), indicating that they have a bending rigidity.[8] The scale bars are 50 μm.

We conjecture that some prepolymer molecules in the solution were adsorbed onto the surfaces of the paramagnetic particles. When the prepolymer cross-linked, a polymer layer on the surfaces of the particles was formed and connected the particles. This

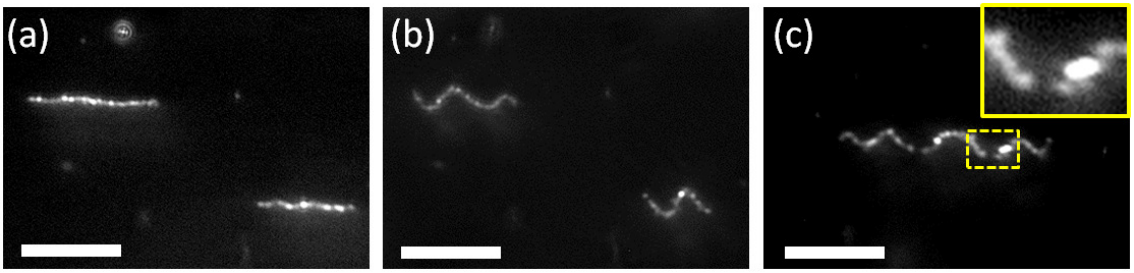

Figure 2.18 Magnetic chains formed by carbonyl iron particles in a gel with an elastic modulus of 170 Pa. (a) Without magnetic field, (b, c) under a magnetic field of 100.8 mT along the vertical direction. The inset in (c) shows an enlarged image of the fracture of the magnetic chain. The scale bars are 50 μm. These images were obtained using a 10$\times$ objective (NA=0.28, M Plan Apo) which collected the reflection light from the carbonyl iron particles.

polymer layer contributed to the bending rigidity. Only when the concentration of the pre-polymer mixture is higher than $c^\star$, a gel can be formed in the bulk. Apparently, already below this concentration, a connecting polymer layer can be formed on the surfaces of the paramagnetic particles. This suggests that a thin layer of polymer with a higher modulus compared to the bulk should be considered to understand the buckling behavior of the paramagnetic chains in the soft gels.

2.8.2.6 Buckling of magnetic particles in a "stiff" gel

In the main article, very soft gels (<1.5 Pa) were used as a matrix. If a stiffer gel was used, the paramagnetic particle chains could not deform the gel significantly under the magnetic field of 216 mT (maximum field in our set-up). Here we used carbonyl iron (CI, CC grade, BASF, Germany, d50 value=3.8-5.3 μm) as magnetic particles in order to increase the magnetic force between the magnetic particles. First, the saturation of magnetization of CI (~ 250 Am^2/kg) is significantly larger than that of our otherwise used paramagnetic particles (~ 20 Am^2/kg); second, the density of CI ($\sim 8\times10^3$ kg/m^3) is higher than that of our paramagnetic particles ($\sim 1.7\times10^3$ kg/m^3); last, the size of CI is about 3 times larger. According to $m = 4\pi R^3 \rho M/3$ (see Section 2.8.2.2), the magnetic moment can be 10^3 times larger compared to our paramagnetic case in the main article. As a result, even in a relatively "stiff" gel, the CI magnetic chains can deform the gel significantly. As shown in Fig. 2.18, in the gel with an elastic modulus of 170 Pa, the CI chains can buckle when a magnetic field of 100.8 mT is applied.

However, promoted by the polydispersity of the CI particles, the CI chains are not as smooth as the chains formed by the monodisperse paramagnetic particles (see Figs. 2.1 and 2.2 in the main article for comparison). In addition, we also observed fractures in some CI chains (Fig. 2.18c) probably due to the polydispersity of the particles. However, the chains do not break up into structures as shown in Fig. 2.9 of the main article (lower image), suggesting that there is still a relatively stiff polymer layer around the CI particles.

2.8.3 Supplementary information concerning the modeling

2.8.3.1 Magnetic interactions within the chain

In the following, we derive Eqs. (2.1) and (2.2) of the main article. We start from two neighboring particles on the chain. According to the assumptions made in the main article, each of them carries a magnetic moment $\mathbf{m}$ oriented in y-direction. They interact via the dipole-dipole magnetic interaction given by

$$V_{dd} = \frac{\mu_0}{4\pi}\left[\frac{\mathbf{m}\cdot\mathbf{m}}{r^3} - \frac{3\,(\mathbf{m}\cdot\mathbf{r})\,(\mathbf{m}\cdot\mathbf{r})}{r^5}\right], \tag{2.13}$$

where $\mathbf{r}$ is the vector joining the centers of the particles, $r = |\mathbf{r}|$, and μ_0 is the vacuum magnetic permeability. Since the particles on the chain are experimentally observed to remain in contact, we have $r = d$, with d the particle diameter. Furthermore, we ignore the first term in the square brackets because it is constant under the given assumptions. Indicating by α the angle between $\mathbf{r}$ and $\mathbf{m}$, we obtain

$$V_{dd} \sim -\frac{3\mu_0 m^2}{4\pi d^3}\cos^2\alpha. \tag{2.14}$$

Since $\mathbf{m}$ is oriented in the y-direction, $\psi = \pi/2 - \alpha$ is the angle between $\mathbf{r}$ and the x-axis. Skipping another constant term resulting from $\cos^2\alpha = 1 - \sin^2\alpha$, the non-constant part of the dipole-dipole interaction can thus be rewritten as

$$V_{dd} \sim \varepsilon_m \sin^2(\psi - \pi/2), \quad \text{with } \varepsilon_m = \frac{3\mu_0 m^2}{4\pi d^3}. \tag{2.15}$$

For an undeformed infinite straight chain oriented along the x-axis in the above set-up, the resulting expression for the total dipolar magnetic interaction energy per particle along the whole chain then reads

$$V_{dd}^{chain} \sim \varepsilon_m \sum_{n=1}^{\infty} \frac{1}{n^3} = \varepsilon_m \zeta(3), \tag{2.16}$$

where ζ is the Riemann Zeta function and $\zeta(3) \simeq 1.202$. Here, ε_m sets the scale of the nearest-neighbor dipolar interaction. In our minimal model the correction described by the factor $\zeta(3) \simeq 1.202$ due to higher-order neighbors is negligible. Since the contour lines of the magnetic chains preserve a smooth shape under the observed deformations, without any kinks, and as the chains do not fold back onto themselves, we thus confine ourselves to nearest-neighbor interactions.

For a large number of particles, the quantity ε_m sets the magnetic interaction energy per particle. Moreover, the total magnetic interaction energy scales approximately linearly with the number of particles and chain length.

We now switch to a continuum picture by specifying the line energy density along the magnetic chain. In our coordinate system, the angle ψ that the connecting vector $\mathbf{r}$ between two neighboring particles forms with the x-axis is locally given by $\psi \sim \arctan[y'(x)]$, where $y'(x) = dy/dx$. To obtain the resulting magnetic energy of the whole magnetic chain, we need to integrate the energy line density along the contour line. For simplicity, we transform this line integral to an integration along the x-axis. If we parameterize the contour line by the parameter s, the line element ds along the chain can be expressed as $ds = \sqrt{1+y'(x)^2}\,dx$. Therefore, the magnetic energy becomes

$$\begin{aligned} E_{magn}[y] &= W \int_{x_1}^{x_2} \sin^2\left\{\arctan\left[y'(x)\right] - \frac{\pi}{2}\right\}\sqrt{1+y'(x)^2}\,dx \\ &= W \int_{x_1}^{x_2} \frac{1}{\sqrt{1+y'(x)^2}}\,dx, \end{aligned} \tag{2.17}$$

where

$$W = \frac{\varepsilon_m}{d} = \frac{3\mu_0 m^2}{4\pi d^4} \tag{2.18}$$

is the magnetic energy per unit length and x_1, x_2 are the x-coordinates of the end points of the chain.

2.8.3.2 Elastic bending energy

Next, we briefly sketch the derivation of the elastic bending energy in Eq. (2.3) of the main article. For this purpose, we consider a parameterization $\mathbf{R}(s)$ of the contour line of the magnetic chain, where the positions $\mathbf{R}$ mark the points on the contour line and $s \in [s_1, s_2]$ with s_1 and s_2 labeling the end points of the chain. On this basis, the elastic bending energy is defined as[9]

$$E_{bend} = C_b \int_{s_1}^{s_2} \left|\frac{d^2\mathbf{R}(s)}{ds^2}\right|^2 ds. \tag{2.19}$$

Using the parameterization $\mathbf{R} = (x, y(x))$ and $ds = \sqrt{1+y'(x)^2}\,dx$, we obtain

$$\frac{d\mathbf{R}}{ds} = \left(1+y'(x)^2\right)^{-\frac{1}{2}} \begin{pmatrix} 1 \\ y'(x) \end{pmatrix} \tag{2.20}$$

and

$$\frac{d^2\mathbf{R}}{ds^2} = y''(x)\left(1+y'(x)^2\right)^{-2} \begin{pmatrix} -y'(x) \\ 1 \end{pmatrix}. \tag{2.21}$$

From this last expression, we obtain Eq. (2.3) in the main article when we again transform the line element ds to Cartesian coordinates, $ds = \sqrt{1+y'(x)^2}\,dx$.

2.8.3.3 Elastic displacement energy

Finally, we motivate the expression for the elastic displacement energy in Eq. (2.4) of the main article. The part $[y(x)]^2$ corresponds to a lowest order term in the displacement $y(x)$. We weight each of the two displacement factors $y(x)$ by the amount of chain material displaced per integration interval dx, given by the length of the chain per integration interval dx, i.e. $ds/dx = \sqrt{1+y'(x)^2}$. This leads to $[y(x)]^2\left[1+y'(x)^2\right]$. In addition to that, we have another factor $\sqrt{1+y'(x)^2}$, again from transforming the line element ds of the integration to Cartesian coordinates, $ds = \sqrt{1+y'(x)^2}\,dx$. In total, we obtain the expression in Eq. (2.4) of the main article.

We explain in the following why the experimental observations suggest this form as a lowest order term. In particular, we note that the experimental investigations suggest the form $[y(x)]^2$ rather than one containing the first derivative $[y'(x)]^2$. For this purpose, we consider the case of straight chains ($M = 0$) undergoing small rotations in a perpendicular magnetic field. This situation can be simply parameterized by $y(x) = Sx$, where $S = \tan\psi$ and ψ as introduced above giving the rotation angle. Furthermore $E_{bend} = 0$.

For $y(x) = Sx$, E_{magn} scales linearly with the chain length L. The same would apply for an energetic contribution $\sim \int_{x_1}^{x_2} [y'(x)]^2\left[1+y'(x)^2\right]^{3/2} dx$. Therefore, the latter expression inevitably leads to a rotation angle ψ that is independent of the chain length L. However, this contradicts the experimental results. In Fig. 2.19 we plot the rotation angle ψ as a function of chain length L measured in a gel of shear modulus $G' = 0.25$ Pa exposed to a perpendicular magnetic field of magnitude $B = 18.7$ mT. There is a clear dependency of the rotation angle on the chain length L. The energetic expression E_{displ} in Eq. (2.4) of the main article for rotations of straight chains $y(x) = Sx$ scales as $E_{displ} \sim L^3$ and thus leads to disproportionally higher energetic penalties for longer chains, reflecting the experimentally observed smaller rotation angles.

2.8.3.4 Discussion of resulting chain shapes

Now that our total model energy E_{tot} is set as the sum of Eqs. (2.1), (2.3), and (2.4) in the main article, a standard route to determine the shape $y(x)$ of the chain would be to find the extrema of the functional $E_{tot}[y(x)]$ with respect to the function $y(x)$. For this purpose, one calculates the functional derivative of $E_{tot}[y(x)]$ with respect to $y(x)$ and equates it with zero. The procedure is well known from the famous brachistochrone problem.[10] There one wishes to find the shape of a curve linking two end points such that a body moving between them under gravity passes the distance in the least possible amount of time.

However, there is a fundamental difference compared to the brachistochrone problem. While calculating the functional derivative, boundary terms appear that explicitly include contributions from the end points of the chain or trajectory $y(x)$. Technically, they result from partial integration. In the brachistochrone problem, one has sufficient information to handle these boundary terms: by construction of the problem, one knows that the end

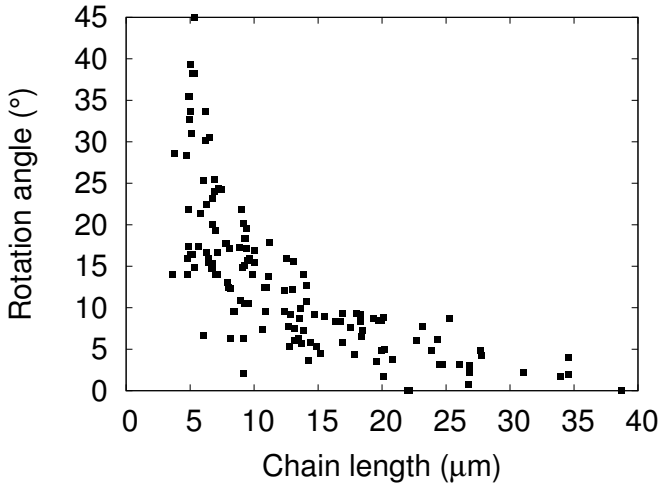

Figure 2.19 Experimentally observed rotation angles of magnetic chains in a gel of shear modulus $G' = 0.25$ Pa under a perpendicular magnetic field of magnitude $B = 18.7$ mT. To first approximation, a rigid rotation of straight chains occurs at small enough rotation angles. This is depicted, for instance, in Fig. 2.1c of the main article for small angles of the magnetic field.

points are fixed. Similarly, in other problems of infinitely extended elastic struts of periodic, periodically modulated, or localized deformations,[11–14] one can use the periodicity or localization to argue in favor of an evanescent influence of the boundary terms. This is very different from our present case, where the deflection encompasses the whole finite chain and in particular its end points. Unfortunately, acquiring sufficient knowledge of the associated boundary conditions would imply solving the whole complex three-dimensional nonlinear elasticity and magnetization problem, which is beyond the present scope and in fact was the reason to project to our reduced minimal model.

For completeness, however, we perform some additional variational analysis of our energy functional. We concentrate on possible solutions in the bulk that could be observed if boundary effects were absent (which is not the case for our experimentally investigated finitely-sized objects). Then, neglecting the boundary terms, the functional derivatives of Eqs. (2.1), (2.3), and (2.4) are calculated as follows (the dependencies of $y(x)$ and its derivatives on x is omitted for brevity on the right-hand sides):

$$\frac{\delta E_{magn}}{\delta y(x)} = W y'' \left(1 - 2y'^2\right) \left(1 + y'^2\right)^{-\frac{5}{2}}, \tag{2.22}$$

$$\frac{\delta E_{bend}}{\delta y(x)} = C_b \left[5y''^3 \left(6y'^2 - 1\right) - 20y'y''y''' \left(1 + y'^2\right) + 2y'''' \left(1 + y'^2\right)^2\right] \left(1 + y'^2\right)^{-\frac{9}{2}}, \tag{2.23}$$

and

$$\frac{\delta E_{displ}}{\delta y(x)} = C_d \left[2y - 2yy'^2 - 4yy'^4 - 3y^2y'' - 6y^2y'^2y''\right] \left(1 + y'^2\right)^{-\frac{1}{2}}. \tag{2.24}$$

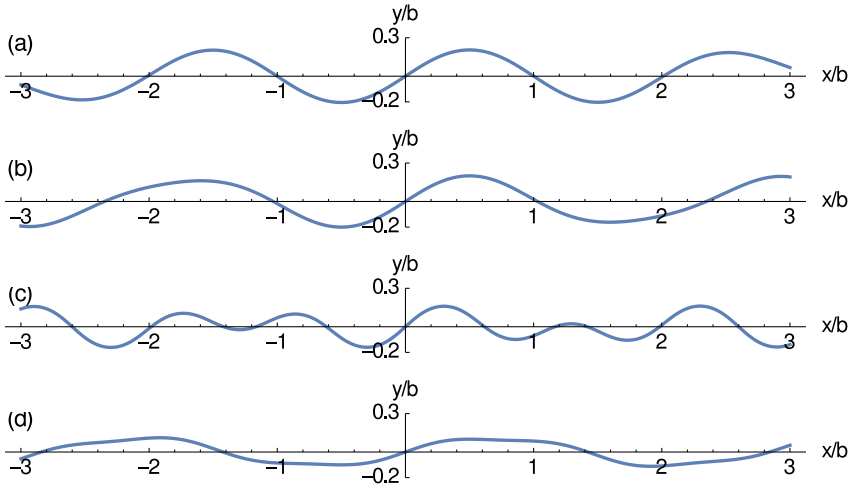

Figure 2.20 Numerical solutions of Eq. (2.25) for different imposed input conditions. In all cases we concentrate on uneven centro-symmetric solutions and thus prescribe $y(0) = y''(0) = 0$. As remaining necessary conditions, we specify the position of the first maximum: **(a)** $y'(0.5) = 0$, $y(0.5) = 0.205$; **(b)** $y'(0.5) = 0$, $y(0.5) = 0.2$; **(c)** $y'(0.3) = 0$, $y(0.3) = 0.16$; **(d)** $y'(0.5) = 0$, $y(0.5) = 0.1$.

Together, we obtain a nonlinear fourth-order differential equation for $y(x)$:

$$\begin{aligned}\frac{\delta E_{tot}}{\delta y(x)} = &\left(1+y'^2\right)^{-\frac{9}{2}} \Big[-\left(1+y'^2\right) y'' \left(W\left(-1+y'^2+2y'^4\right)+20C_b y' y'''\right) \\ &-3C_d y^2 \left(1+y'^2\right)^4 \left(1+2y'^2\right) y'' + 5C_b \left(-1+6y'^2\right) y''^3 \\ &-2C_d y \left(1+y'^2\right)^5 \left(-1+2y'^2\right) + 2C_b \left(1+y'^2\right)^2 y'''' \Big] = 0. \end{aligned} \tag{2.25}$$

Eq. (2.25) can in principle be solved numerically by integrating it outward from the center of the chain at $x = 0$. For this purpose, a sufficient amount of "initial conditions" (four in our case) for $y(x)$ and its derivatives needs to be provided. We concentrate on uneven centro-symmetric solutions, which directly prescribes two conditions: $y(0) = 0$ and $y''(0) = 0$. As was found before in a different context,[11] the solution is extremely sensitive to the two remaining imposed conditions. For illustration, we depict four examples in Fig. 2.20. There, we provide slightly varying positions of the first maximum $[y'(x) = 0]$ as the remaining two necessary conditions. Numerical integration shows that little variations in these conditions lead to qualitatively different oscillatory solutions.[15]

Altogether, we may conclude that the solutions resulting from Eq. (2.25) sensitively depend on the input conditions. As noted above, we do not have access to the appropriate conditions applying at the significantly displaced end points of the embedded chain. The strategy that we resorted to is therefore to use as an input directly the shapes of the chains suggested by the experiments. We found good representations of the experimental observations using the polynomial form suggested by Eq. (2.5) in the main article. In

particular, with regard to the pronounced displacements of the chain ends, this choice is preferred to, for instance, a sinusoidal ansatz. Then, instead of solving Eq. (2.25) explicitly, we minimize the energy functional $E_{tot}[y(x)]$ with respect to the remaining degrees of freedom of the chain deformation (M, S, x_1 and x_2 in the main article). Thus, even if we have used an ansatz for the chain deformation, this remains a nonlinear approach as we evaluate the nonlinear contributions to the energy functional $E_{tot}[y(x)]$.

2.8.3.5 Oscillatory solutions in the linear regime

In the previous part, we have demonstrated that various complex solutions can result from the nonlinear nature of Eq. (2.25). Here, we restrict ourselves to the situation in the inside of the magnetic chains for small amounts of deformation, i.e. at the onset of deformation. For this purpose, a linear stability analysis is performed by considering a linearized version of Eq. (2.25). As a result, we obtain a condition describing the onset of a linear deformational instability

$$W y''(x) + 2C_b y''''(x) + 2C_d y(x) = 0. \tag{2.26}$$

This equation has solutions of the kind $y(x) \sim \exp(\pm iqx)$, with wavenumber

$$q^2 = \frac{W \pm \sqrt{W^2 - 16C_bC_d}}{4C_b}. \tag{2.27}$$

The condition for the solutions to be purely oscillatory is $W^2/16C_bC_d > 1$ and defines an onset for this kind of deformation. It sets a threshold magnitude for the strength of the external magnetic field. Thus, for a perfectly oriented chain of identical particles in a spatially homogeneous elastic matrix, this linear stability analysis predicts a critical magnetic field amplitude above which an undulatory instability would arise in the inside of the chain. Our results are in agreement with the experimental observation of the wrinkles at onset in Fig. 2.1c and the final oscillatory shape in the inner part of the longer chains in Fig. 2.2a of the main article.

2.8.4 Technical description of the coarse-grained molecular dynamics simulations

2.8.4.1 Magnetic particles

In the molecular dynamics simulations, the centers of the magnetic particles and the nodes of the polymer mesh are treated as point particles in two-dimensional space. The magnetic particles additionally have one rotational degree of freedom, namely around the axis perpendicular to the model plane. As each magnetic particle is superparamagnetic, its magnetic moment is not affected by a rotation of the particle. Rather, the magnetic moment is determined by the magnetic field. Hence, we place the magnetic moment not

on the rotating center of the particle, but rather on a separate virtual site which does not rotate. It is placed at the same location as the center of the magnetic particle. Virtual sites are particles, whose position is not determined by integrating an equation of motion, rather their position is calculated from the position and orientation of other particles. In this way, they allow us to introduce rigid extended bodies into a molecular dynamics simulation.[16] Forces acting on any constituent of such a rigid body are transferred back to its center of mass, and thus included in the equation of motion of the rigid body.

Pairs of magnetic particles interact by the dipole-dipole interaction, Eq. (2.13). The dipole moment of the particles is assumed to be determined entirely by the external magnetic field, and its magnitude is deduced from the experimental magnetization curve (Fig. 2.11b). This assumption is valid as long as the external field is much stronger than the field created by the other magnetic particles. In other cases, a self-consistent approach has to be used to determine the local magnetic fields. In addition to the dipole-dipole interaction, the magnetic particles interact via a truncated and shifted, purely repulsive Lennard-Jones potential mimicking a rigid-sphere interaction. We use the Weeks-Chandler-Andersen potential[17] in the form

$$V_{WCA}\left(\frac{r}{\sigma}\right) = \begin{cases} 4\varepsilon\left[\left(\frac{r}{\sigma}\right)^{-12} - \left(\frac{r}{\sigma}\right)^{-6} + \frac{1}{4}\right] & \text{for } r \le r_c, \\ 0 & \text{otherwise,} \end{cases} \tag{2.28}$$

where r is the distance between the particle centers, $\varepsilon = 1000$ denotes the energy scale of the potential, and $r_c = 2^{1/6}\sigma$ is the cut-off distance, for which we use the experimental diameter of 1.48 μm. The parameter σ denotes the root of the non-shifted potential and is used in the visualizations in Figs. 2.9 and 2.10.

2.8.4.2 Polymer mesh

The polymer matrix is modeled as a bead-spring network based on a hexagonal lattice. We use a lattice constant a of one third of the experimentally observed particle diameter, i.e., $a \approx 0.49$ μm. Along the initial chain direction, we use 601 mesh points, along the perpendicular direction 301. The mesh points on the boundary of the system are fixed, all other mesh points can move in the x- and y-directions. Adjacent mesh points interact via a non-linear elastic spring based on the FENE-potential.[18] Here, we use a variant with different cut-off values for compression and expansion. It is given by

$$\begin{aligned} V(r) &= -\tfrac{1}{2} K (r_0 - r_{\min})^2 \ln\left[1 - \left(\tfrac{r - r_0}{r_0 - r_{\min}}\right)^2\right] \quad \text{for } r < r_0, \\ V(r) &= -\tfrac{1}{2} K (r_{\max} - r_0)^2 \ln\left[1 - \left(\tfrac{r - r_0}{r_{\max} - r_0}\right)^2\right] \quad \text{for } r > r_0. \end{aligned} \tag{2.29}$$

In these expressions, $K = 45$ controls the scale of the potential, the equilibrium distance $r_0 = a$ is equal to the lattice constant, while the minimum and maximum elongations, at

which the potential diverges, are $r_{\min} = 0.1a$ and $r_{\max} = 3a$, respectively. The potential, as well as its second derivative, are continuous at the equilibrium extension $r = r_0$. In order to prevent any volume element from shrinking to zero, angular potentials are used on all pairs of neighboring springs attached to the same mesh site, encompassing an angle of 60° in the unstrained mesh. The potential has the same functional form as the distance-based potential in Eq. (2.29), but with the values $K = 100$, $r_0 = \pi/3$, $r_{\min} = 0$, and $r_{\max} = \pi$. In the simulations both potentials are tabulated at 100 000 equally spaced intervals between the minimum and maximum extensions. Between those points, linear interpolation is used.

2.8.4.3 Particle-mesh coupling and boundary layer

The mesh spans the entire simulation area, including the area covered by the magnetic particles. In order to couple the polymer mesh to both, the translational and rotational motion of a magnetic particle, the seven mesh sites within the area of each magnetic particle are treated as virtual sites, rigidly following the motion of the magnetic particle. In other words, the mesh sites within the particle and the center of the magnetic particle form a rigid body. This additionally prevents a distortion of the gel matrix in the area occupied by the magnetic particles. Two variants of gel boundary layer around the particles are studied (Fig. 2.9 in the main article). In the case of a soft boundary layer, the mesh springs emerging from the mesh sites rigidly connected to the particle, are modeled as in Eq. (2.29) with the same parameters as for the bulk. In the case of a stiff boundary layer, a potential is used which is stiffer by three orders of magnitude. The following parameters are used in this case: $K = 45\,000$, $r_{\min} = -2a$, and $r_{\max} = 4a$.

2.8.5 Equation of motion and integration

The simulations are performed in the canonical ensemble at a temperature of 300 K. All particles except for the virtual sites are propagated according to a Langevin equation. For any component in a Cartesian coordinate system, it is given by

$$m_p \dot{v}(t) = -\gamma v(t) + F + F_r, \tag{2.30}$$

where m_p denotes the mass of the particle, v its velocity, F is the force due to the interaction with other particles, F_r denotes the random thermal noise, and γ is the friction coefficient. To maintain a temperature T, the thermal noise has to have a mean of zero and a variance of

$$\langle F_r^2 \rangle = 2 k_B T \gamma, \tag{2.31}$$

where $k_B T$ denotes the thermal energy. For the rotational degree of freedom of each magnetic particle, the same equation of motion is used, but mass, velocity, and forces are replaced by moment of inertia, angular velocity, and torques, respectively. The friction

coefficient, the thermal energy, and the mass of the mesh sites are all chosen to be unity, whereas the mass and rotational inertia of the centers of the magnetic particles are both 100. This slows down the relaxation time of the magnetic particles versus that of the polymer mesh and is helpful in stabilizing the simulation. The Langevin equation is integrated using a Velocity Verlet integrator. For the simulations with a stiff boundary layer, the time step is $dt = 0.001$, for a soft boundary layer it is $dt = 0.00004$. The simulations take approximately 100 000 time steps to converge.

Bibliography

[1] F. Ziemann, J. Rädler and E. Sackmann, *Biophys. J.*, 1994, **66**, 2210–2216.

[2] A. R. Bausch, W. Möller and E. Sackmann, *Biophys. J.*, 1999, **76**, 573–579.

[3] P. Tordjeman, C. Fargette and P. H. Mutin, *J. Rheol.*, 2001, **45**, 995–1006.

[4] T. G. Mason, T. Gisler, K. Kroy, E. Frey and D. A. Weitz, *J. Rheol.*, 2000, **44**, 917–928.

[5] http://www.physics.emory.edu/faculty/weeks//idl/index.html.

[6] T. G. Mason and D. Weitz, *Phys. Rev. Lett.*, 1995, **74**, 1250–1253.

[7] H. Raich and P. Blümler, *Concept. Magn. Reson. B*, 2004, **23B**, 16–25.

[8] C. Goubault, P. Jop, M. Fermigier, J. Baudry, E. Bertrand and J. Bibette, *Phys. Rev. Lett.*, 2003, **91**, 260802.

[9] L. Landau and E. Lifshitz, *Elasticity theory*, Pergamon Press, 1975.

[10] I. Gelfand and S. Fomin, *Calculus of variations*, Prentice-Hall Inc., Englewood Cliffs, NJ, 1963.

[11] G. W. Hunt, M. Wadee and N. Shiacolas, *J. Appl. Mech.*, 1993, **60**, 1033–1038.

[12] B. Audoly, *Phys. Rev. E*, 2011, **84**, 011605.

[13] H. Diamant and T. A. Witten, *arXiv preprint arXiv:1009.2487*, 2010.

[14] H. Diamant and T. A. Witten, *Phys. Rev. Lett.*, 2011, **107**, 164302.

[15] Wolfram Research, *Mathematica 10.0*, 2014.

[16] A. Arnold, O. Lenz, S. Kesselheim, R. Weeber, F. Fahrenberger, D. Röhm, P. Košovan and C. Holm, *Meshfree Methods for Partial Differential Equations VI*, 2013, pp. 1–23.

[17] J. D. Weeks, D. Chandler and H. C. Andersen, *J. Chem. Phys.*, 1971, **54**, 5237–5247.

[18] H. R. Warner Jr., *Ind. Eng. Chem. Fundam.*, 1972, **11**, 379–387.

3. Forces on rigid inclusions in elastic media and resulting matrix-mediated interactions

Mate Puljiz,[a] Shilin Huang,[b] Günter K. Auernhammer,[b] and Andreas M. Menzel[a]

[a] Institut für Theoretische Physik II: Weiche Materie, Heinrich-Heine-Universität Düsseldorf, 40225 Düsseldorf, Germany.
[b] Max Planck Institute for Polymer Research, Ackermannweg 10, 55128 Mainz, Germany.

Reprinted with permission from:
M. Puljiz, S. Huang, G. K. Auernhammer, A. M. Menzel. Phys. Rev. Lett. 117, 238003, 2016.

Statement of Contribution

In this paper, Shilin Huang contributes to the experiments. In more details, the contribution includes the following aspects:

(1) Using the Halbach magnetic setup for applying the homogeneous magnetic field.

(2) Setting up the optical parts for image recording.

(3) Preparing the gels with embedded paramagnetic particles (Fig. 3.3a).

(4) Performing experiments and image analysis, to obtain the displacement of the magnetic particles in the gel under the magnetic field (snapshots and experimental data points in Fig. 3.3, Fig. 3.4 and Fig. 3.5).

Abstract

To describe many-particle systems suspended in incompressible low-Reynolds-number *fluids*, effective hydrodynamic interactions can be introduced. Here, we consider particles embedded in *elastic* media. The effective elastic interactions between spherical particles are calculated analytically, inspired by the approach in the fluid case. Our experiments on interacting magnetic particles confirm the theory. In view of the huge success of the method in hydrodynamics, we similarly expect many future applications in the elastic case, e.g. for elastic composite materials.

3.1 Main text

Hydrodynamics determines our daily life. Examples are given by the flow of air into our lungs,[1] drinking of beverages and digestive processes,[2,3] technical applications such as microfluidic devices,[4] or shape optimization of planes, vehicles, ships, and propellers.[5–7] All these processes are described by the Navier-Stokes equations[8,9] or variants thereof. This set of equations typically poses significant challenges during evaluation due to a convective nonlinearity reflecting inertial effects. Basically, turbulence is driven by the inertial term. It often renders analytical solutions impossible.

The situation changes for small dimensions and velocities or high viscosity. Then, the relative strength of inertial effects, measured by the Reynolds number, is low. The nonlinearity can be neglected. A Green's function in terms of the so-called Oseen matrix is then available, which formally solves the problem analytically.[10,11] In this way, semi-dilute colloidal suspensions, i.e. the dispersion of nano- to micrometer-sized particles in a fluid,[11–18] or microswimmer suspensions[19–25] are described effectively. The explicit role of the fluid is eliminated and replaced by effective hydrodynamic interactions between the suspended particles.[10,11]

Despite the success of this theoretical approach for colloidal suspensions, hardly any investigations consider a surrounding elastic solid instead of a suspending fluid. This is surprising, since, as we show below, the formalism can be adopted straightforwardly to linearly elastic matrices and is confirmed by our experiments. Our approach will, for instance, facilitate describing the response of elastic composite materials to external stimuli. Such materials consist of more or less rigid inclusions embedded in an elastic matrix. They are of growing technological interest and may serve, e.g., as soft actuators or sound attenuation devices.[26–32]

In previous theoretical studies, the physics of one single rigid or deformable inclusion was addressed,[33–38] also under acoustic irradiation.[39–41] For more than a single inclusion, mainly the so-called load problem was analyzed theoretically for a pair of rigid inclusions: one prescribes displacements of two rigid inclusions in an elastic matrix, and then determines the forces necessary to achieve these given displacements.[42,43]

Here, we take the converse point of view, based on the cause-and-effect chain in our experiments: external forces are imposed onto the inclusions, or mutual forces between the inclusions are induced, for example to actuate the material or to tune its properties. In response to the forces, the inclusions displace. Since they cannot penetrate through the surrounding elastic matrix, they transmit the forces to the matrix and distort it. Such distortions lead to mutual long-ranged interactions between the inclusions, in analogy to hydrodynamic interactions in colloidal suspensions.[10,11,44]

We present a basic derivation of analytical expressions for these interactions from the underlying elasticity equations. Then, we confirm the theory by experiments on rigid paramagnetic particles embedded in soft elastic matrices. Mutual particle interactions are

induced by an external magnetic field. As we demonstrate, theory and experiment are in good agreement, and also allow for microrheological measurements.[45–48]

For simplicity, we assume a homogeneous, isotropic, infinitely extended elastic matrix, and low-amplitude deformations. Applying a bulk force density $\mathbf{f}_b(\mathbf{r})$ to the matrix, its equilibrated state satisfies the linear elastostatic Navier-Cauchy equations,[49]

$$\nabla^2\mathbf{u}(\mathbf{r}) + \frac{1}{1-2\nu}\nabla\nabla\cdot\mathbf{u}(\mathbf{r}) = -\frac{1}{\mu}\mathbf{f}_b(\mathbf{r}). \tag{3.1}$$

This is the elastic analogue to the linearized Stokes equation in low-Reynolds-number hydrodynamics.[11] Instead of velocities, $\mathbf{u}(\mathbf{r})$ here denotes the displacement field, describing the reversible relocations of the volume elements from their initial positions during deformations. μ is the shear modulus of the matrix and ν its Poisson ratio, connected to its compressibility.[50] We consider an incompressible matrix, i.e. $\nabla\cdot\mathbf{u}(\mathbf{r}) = 0$ along with $\nu = 0.5$. Yet, in contrast to the hydrodynamic case, also compressible elastic systems are readily addressed, and we present the corresponding expressions in the supplemental material.[51]

Importantly, for a point force density $\mathbf{f}_b(\mathbf{r}) = \mathbf{F}\delta(\mathbf{r})$ acting on the matrix, the resulting deformation field can be calculated analytically from Eq. (3.1) via Fourier transform as $\mathbf{u}(\mathbf{r}) = \underline{\mathbf{G}}(\mathbf{r})\cdot\mathbf{F}$. Here,

$$\underline{\mathbf{G}}(\mathbf{r}) = \frac{1}{8\pi\mu}\left[\frac{1}{r}\hat{\underline{\mathbf{I}}} + \frac{\mathbf{r}\mathbf{r}}{r^3}\right] \tag{3.2}$$

is the corresponding Green's function,[50] $\hat{\underline{\mathbf{I}}}$ the identity matrix, r=$|\mathbf{r}|$, and the underscore marks second-rank tensors and matrices. Still, it is practically impossible to explicitly solve Eq. (3.1) analytically in the presence of several rigid embedded particles of finite size. An iterative procedure resolves this problem, see Fig. 3.1.

We consider N rigid spherical particles of radius a, with no-slip boundary conditions on their surfaces. First we only address the ith particle at position $\mathbf{r}_i$, subject to an external force $\mathbf{F}_i$. The embedded particle transmits this force to the surrounding matrix and induces a displacement field

$$\mathbf{u}_i^{(0)}(\mathbf{r}) = \left(1 + \frac{a^2}{6}\nabla^2\right)\underline{\mathbf{G}}(\mathbf{r}-\mathbf{r}_i)\cdot\mathbf{F}_i. \tag{3.3}$$

This field is the elastic analogue of hydrodynamic Stokes flow,[10,11] for elastic media. Inserting Eq. (3.2) reproduces a corresponding expression in Ref. 38. Eq. (3.3) is confirmed as it satisfies Eq. (3.1), shows the correct limit $\mathbf{u}_i^{(0)}(\mathbf{r}) = \underline{\mathbf{G}}(\mathbf{r}-\mathbf{r}_i)\cdot\mathbf{F}_i$ for $|\mathbf{r}-\mathbf{r}_i| > a$ when $a \to 0$, and for $|\mathbf{r}-\mathbf{r}_i| = a$ is constant on the particle surface. Thus, Eq. (3.3) for $|\mathbf{r}-\mathbf{r}_i| = a$ reveals the rigid displacement

$$\mathbf{U}_i^{(0)} = \mathbf{u}_i^{(0)}(|\mathbf{r}-\mathbf{r}_i| = a) = \frac{1}{6\pi\mu a}\mathbf{F}_i \tag{3.4}$$

of the ith particle in response to $\mathbf{F}_i$ in accord with the no-slip conditions at $|\mathbf{r}-\mathbf{r}_i| = a$.

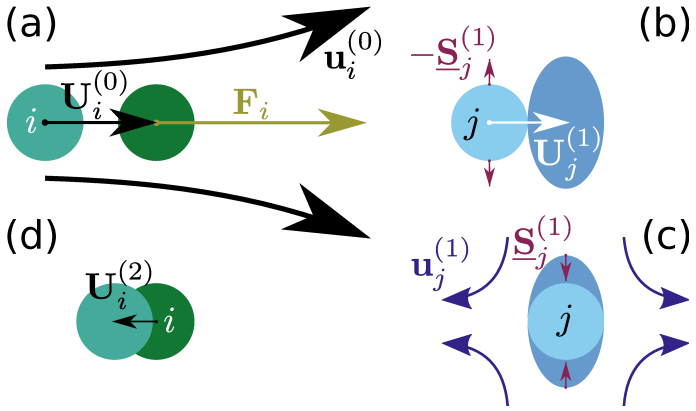

Figure 3.1 Illustration of the reflection of a displacement field $\mathbf{u}_i^{(0)}$ induced by (a) the force $\mathbf{F}_i$ that displaces particle i by $\mathbf{U}_i^{(0)}$. (b) Due to $\mathbf{u}_i^{(0)}$, particle j gets displaced by $\mathbf{U}_j^{(1)}$ and would be distorted as described by a stresslet $-\underline{\mathbf{S}}_j^{(1)}$ (rotations $\mathbf{\Omega}_j^{(1)}$ not depicted for simplicity). (c) However, particle j is rigid and resists to deformation, expressed by a counteracting stresslet $\underline{\mathbf{S}}_j^{(1)}$, which results in a displacement field $\mathbf{u}_j^{(1)}$. (d) The reflected $\mathbf{u}_i^{(0)}$, i.e. $\mathbf{u}_j^{(1)}$, displaces particle i by $\mathbf{U}_i^{(2)}$.

To find the effective elastic interactions between particles i and j ($j \neq i$), we take the induced displacement field $\mathbf{u}_i^{(0)}(\mathbf{r})$ as given. We need to determine how particle j reacts to the imposed field $\mathbf{u}_i^{(0)}(\mathbf{r})$. In general, particle j can be rigidly translated by a displacement vector $\mathbf{U}_j^{(1)}$ and rigidly rotated by a rotation vector $\mathbf{\Omega}_j^{(1)}$. Taking into account the no-slip conditions on the surface ∂V_j of the jth particle, the equality

$$\mathbf{U}_j^{(1)} + \mathbf{\Omega}_j^{(1)} \times (\mathbf{r} - \mathbf{r}_j) = \mathbf{u}_i^{(0)}(\mathbf{r}) + \int_{\partial V_j} \underline{\mathbf{G}}(\mathbf{r} - \mathbf{r}') \cdot \mathbf{f}(\mathbf{r}') \mathrm{d}S' \tag{3.5}$$

must hold for all $\mathbf{r} \in \partial V_j$. That is, the rigid displacement of each point on the surface shell of particle j (l.h.s.) must equal the displacement field in the matrix at the same point (r.h.s.). The latter is given by the imposed displacement field, here $\mathbf{u}_i^{(0)}(\mathbf{r})$, plus the deformation that the particle surface itself induces in the matrix, i.e. the integral term. Also an externally imposed global displacement field could be included (on the r.h.s.). $\mathbf{f}(\mathbf{r}')$ describes the surface force density exerted by the surface of particle j onto the matrix.

Such an embedded particle will translate and rotate as dictated by the surrounding matrix. We obtain the expression for $\mathbf{U}_j^{(1)}$ by integrating Eq. (3.5) over ∂V_j. Similarly, for $\mathbf{\Omega}_j^{(1)}$, Eq. (3.5) is multiplied dyadically by $\mathbf{r} - \mathbf{r}_j$, and after integration over ∂V_j the antisymmetric part is extracted. To perform the calculation, $\mathbf{u}_i^{(0)}(\mathbf{r})$ is Taylor expanded around $\mathbf{r}_j$. Moreover, we use that Eq. (3.1) for $\mathbf{r} \notin \partial V_i$ leads to $\nabla^4 \mathbf{u}_i^{(0)}(\mathbf{r}) = \mathbf{0}$ and $\nabla \times \nabla^2 \mathbf{u}_i^{(0)}(\mathbf{r}) = \mathbf{0}$. The last term in Eq. (3.5) vanishes at this stage as no total net external force or torque is applied to particle j at the present step of iteration. In the end, we

recover the elastic analogues of the hydrodynamic[10,11,52] Faxén laws

$$\mathbf{U}_j^{(1)} = \left(1+\frac{a^2}{6}\nabla^2\right)\mathbf{u}_i^{(0)}(\mathbf{r})\Big|_{\mathbf{r}=\mathbf{r}_j}, \tag{3.6}$$

$$\mathbf{\Omega}_j^{(1)} = \frac{1}{2}\nabla\times\mathbf{u}_i^{(0)}(\mathbf{r})\Big|_{\mathbf{r}=\mathbf{r}_j}. \tag{3.7}$$

This is how particle j is translated and rotated in the field $\mathbf{u}_i^{(0)}(\mathbf{r})$ induced by particle i. Yet, elastic retroaction occurs between the particles, as described in the following.

The force densities $\mathbf{f}(\mathbf{r}')$ in Eq. (3.5) that the particles exert on their environment in general will not vanish identically. Since the particles are rigid, they resist any deformation that $\mathbf{u}_i^{(0)}$ would imply. Thus, they exert counteracting stresses onto the deformed matrix. The stresslet exerted by particle j onto the matrix can be denoted as $\underline{\mathbf{S}}_j = \int_{\partial V_j} \mathrm{d}S'\{[\mathbf{f}(\mathbf{r}')\mathbf{r}' + (\mathbf{f}(\mathbf{r}')\mathbf{r}')^T]/2 - \hat{\underline{\mathbf{I}}}[\mathbf{f}(\mathbf{r}')\cdot\mathbf{r}']/3\}$, where $[\bullet]^T$ marks the transpose. In our case, we can directly calculate from Eq. (3.5) the stresslet $\underline{\mathbf{S}}_j^{(1)}$ that particle j exerts onto the matrix when it resists to the deformation described by $\mathbf{u}_i^{(0)}(\mathbf{r})$. To find the expression for $\underline{\mathbf{S}}_j^{(1)}$, one proceeds in the same way as described above for $\mathbf{\Omega}_j^{(1)}$ but eventually extracts the symmetric part. The latter contains the definition of $\underline{\mathbf{S}}_j^{(1)}$. We obtain

$$\underline{\mathbf{S}}_j^{(1)} = \frac{10\pi\mu a^3}{-3}\left(1+\frac{a^2}{10}\nabla^2\right)\left[\nabla\mathbf{u}_i^{(0)}(\mathbf{r}) + \left(\nabla\mathbf{u}_i^{(0)}(\mathbf{r})\right)^T\right]\Big|_{\mathbf{r}_j}. \tag{3.8}$$

This stresslet leads to additional distortions of the matrix, see Fig. 3.1, described by a displacement field $\mathbf{u}_j^{(1)}(\mathbf{r})$ that overlays $\mathbf{u}_i^{(0)}(\mathbf{r})$. We find $\mathbf{u}_j^{(1)}(\mathbf{r})$ from the general expression $\mathbf{u}_j(\mathbf{r}) = \int_{\partial V_j}\mathrm{d}S'\underline{\mathbf{G}}(\mathbf{r}-\mathbf{r}')\cdot\mathbf{f}(\mathbf{r}')$ by Taylor expanding the Green's function in $\mathbf{r}'$ around $\mathbf{r}' = \mathbf{r}_j$. The definition of $\underline{\mathbf{S}}_j$ shows up as the symmetric part of the second-order term of the series, similarly to the hydrodynamic case,[10,52] leading to

$$\mathbf{u}_j^{(1)}(\mathbf{r}) = -\left(\underline{\mathbf{S}}_j^{(1)}\cdot\nabla\right)\cdot\underline{\mathbf{G}}(\mathbf{r}-\mathbf{r}_j). \tag{3.9}$$

This expression completes our first step of iteration. In the second step, it is particle i that is exposed to the field $\mathbf{u}_j^{(1)}(\mathbf{r})$. Correspondingly, we find its reaction from Eqs. (3.6)–(3.9) by replacing $(\mathbf{u}_i^{(0)},\mathbf{U}_j^{(1)},\mathbf{\Omega}_j^{(1)},\underline{\mathbf{S}}_j^{(1)},\mathbf{u}_j^{(1)})$ with $(\mathbf{u}_j^{(1)},\mathbf{U}_i^{(2)},\mathbf{\Omega}_i^{(2)},\underline{\mathbf{S}}_i^{(2)},\mathbf{u}_i^{(2)})$. Particle i now feels the consequences of its self-generated field $\mathbf{u}_i^{(0)}(\mathbf{r})$ *reflected* by particle j in the form of $\mathbf{u}_j^{(1)}(\mathbf{r})$. Therefore, the procedure was termed *method of reflections* in hydrodynamics.[10,11] The displacement $\mathbf{U}_i^{(2)}$ in Fig. 3.1 results from this reflection. We have not found in the hydrodynamic derivation[11] the above reasoning of explicitly imposing on the matrix environment the rigidity-induced stress.

In principle, this refinement of the deformation field via back-and-forth reflections between the two particles can be continued, leading to increasingly-higher-order corrections in a/r_{ij}, where $r_{ij} = |\mathbf{r}_i - \mathbf{r}_j|$. For our example systems below, these iterations converge

quickly, see Fig. 3.3(c), so that it is sufficient to consider contributions up to (including) order r_{ij}^{-4}.

Due to the linearity of Eq. (3.1), we can sum up the particle displacements obtained from the different steps of iteration. Moreover, we can consider external forces $\mathbf{F}_i$ on *all* particles and calculate the resulting net displacements $\mathbf{U}_i$ due to the mutual elastic interactions ($i = 1,...,N$). These contributions superimpose. In analogy to the hydrodynamic[11] mobility matrix we express the result by an elastic *displaceability matrix* $\underline{\mathbf{M}}$:

$$\begin{pmatrix} \mathbf{U}_1 \\ \vdots \\ \mathbf{U}_N \end{pmatrix} = \begin{pmatrix} \underline{\mathbf{M}}_{11} & \dots & \underline{\mathbf{M}}_{1N} \\ \vdots & \vdots & \vdots \\ \underline{\mathbf{M}}_{N1} & \dots & \underline{\mathbf{M}}_{NN} \end{pmatrix} \cdot \begin{pmatrix} \mathbf{F}_1 \\ \vdots \\ \mathbf{F}_N \end{pmatrix}. \tag{3.10}$$

Limiting ourselves to contributions up to (including) order r_{ij}^{-4}, we find

$$\underline{\mathbf{M}}_{i=j} = M_0 \left[\hat{\underline{\mathbf{I}}} - \sum_{\substack{k=1 \\ k\neq i}}^{N} \frac{15}{4} \left(\frac{a}{r_{ik}} \right)^4 \hat{\mathbf{r}}_{ik} \hat{\mathbf{r}}_{ik} \right], \tag{3.11}$$

$$\underline{\mathbf{M}}_{i\neq j} = M_0 \frac{3}{4} \frac{a}{r_{ij}} \left[\left(\hat{\underline{\mathbf{I}}} + \hat{\mathbf{r}}_{ij} \hat{\mathbf{r}}_{ij} \right) + 2 \left(\frac{a}{r_{ij}} \right)^2 \left(\frac{1}{3} \hat{\underline{\mathbf{I}}} - \hat{\mathbf{r}}_{ij} \hat{\mathbf{r}}_{ij} \right) \right] + \underline{\mathbf{M}}^{(3)}_{i\neq j}, \tag{3.12}$$

where $M_0 = 1/6\pi\mu a$ and $\hat{\mathbf{r}}_{ij} = \mathbf{r}_{ij}/r_{ij}$ ($i, j = 1,2,...,N$).

In Eq. (3.11), $\hat{\underline{\mathbf{I}}}$ represents the immediate displacement of particle i due to the force $\mathbf{F}_i$ ($\mathbf{U}_i^{(0)}$ in Fig. 3.1). The second term $\sim r_{ik}^{-4}$ describes the rigidity-induced reflection from another particle ($\mathbf{U}_i^{(2)}$ in Fig. 3.1). It *counteracts* $\mathbf{U}_i^{(0)}$, or vanishes for $\mathbf{F}_i \perp \hat{\mathbf{r}}_{ik}$.

In Eq. (3.12), $\hat{\underline{\mathbf{I}}} + \hat{\mathbf{r}}_{ij}\hat{\mathbf{r}}_{ij}$ expresses the consequence of the force $\mathbf{F}_j$ acting on particle j: particle i is relocated in the induced displacement field ($\mathbf{U}_j^{(1)}$ in Fig. 3.1, for $i \leftrightarrow j$). The term $\sim r_{ij}^{-3}$ corrects this displacement field due to the finite size of particle j, in analogy to the Rodne-Prager formula in the fluid case.[11] $\underline{\mathbf{M}}^{(3)}_{i\neq j}$ describes additional three-body interactions $\sim r_{ij}^{-4}$ calculated in full analogy to the above procedure for the two-body interaction,

$$\underline{\mathbf{M}}^{(3)}_{i\neq j} = M_0 \frac{15}{8} \sum_{\substack{k=1 \\ k\neq i,j}}^{N} \left(\frac{a}{r_{ik}} \right)^2 \left(\frac{a}{r_{jk}} \right)^2 \left[1 - 3(\hat{\mathbf{r}}_{ik} \cdot \hat{\mathbf{r}}_{jk})^2 \right] \hat{\mathbf{r}}_{ik} \hat{\mathbf{r}}_{jk}. \tag{3.13}$$

That is, the deformation field induced by a force on a first particle j spreads to a second particle k, from where it is reflected towards the third particle i. The angular dependence allows for configuration-dependent attractive, repulsive, or bypass contributions, see Fig. 3.2.

Eqs. (3.10)–(3.13) represent the central theoretical result. Up to (including) order r_{ij}^{-4} it is exact, higher-body interactions for $N > 3$ do not enter (see Ref. 51 for $N = 4$). To confirm and illustrate the merit of the theory, we performed experiments on small groups

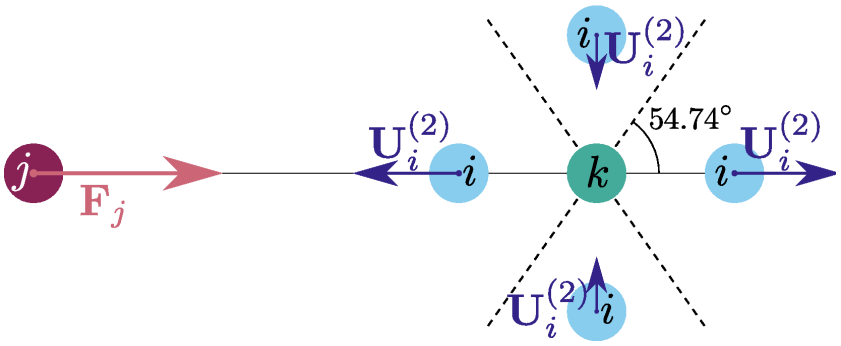

Figure 3.2 Illustration of example three-body contributions in Eq. (3.13). The force $\mathbf{F}_j$ on particle j induces a displacement field that is reflected from particle k due to its rigidity. Depending on its position, particle i is effectively attracted or repelled by particle j (strongest under coaxial alignment), pulled towards particle k (bypass), or not affected at all (dashed).

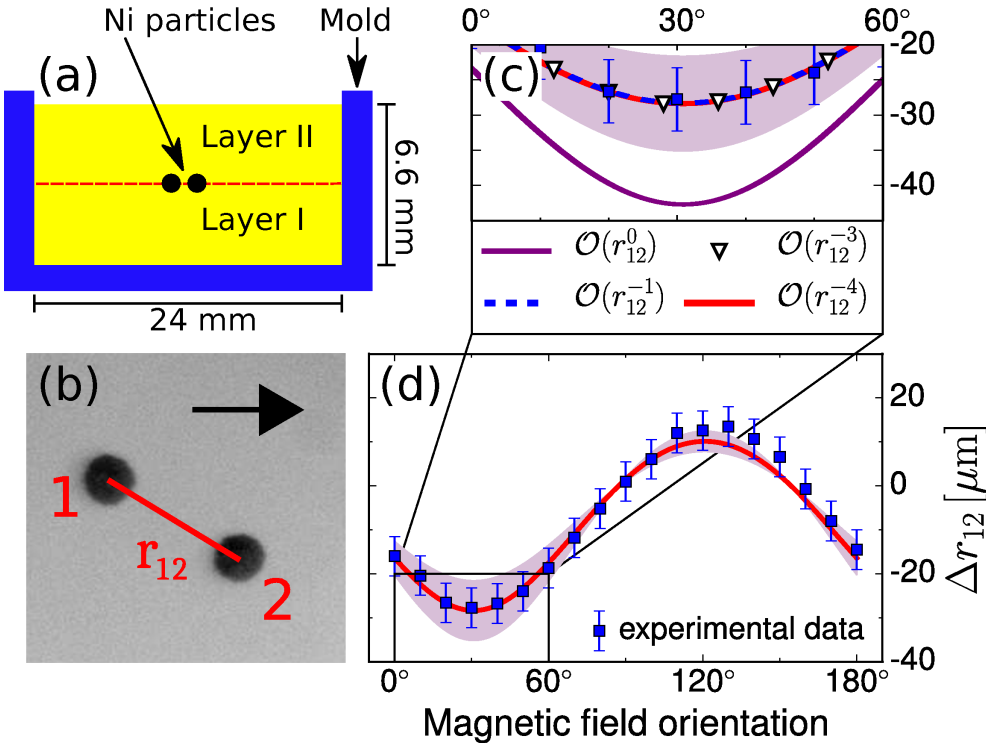

Figure 3.3 (a) Schematic of the samples. After fabrication of the bottom gel layer (I), the paramagnetic nickel (Ni) particles are placed into the center plane (dashed), before the top layer (II) is added. The enclosing plastic molds are open to the top for optical investigation. (b) Snapshot of a system of two Ni particles (diameters 150.6±1.9 μm) embedded in a soft elastic gel, here for vanishing external magnetic field. (c,d) Change in distance Δr_{12} between the two particles when applying an external magnetic field along different directions in the particle plane via clockwise rotation. The horizontal arrow in (b) defines the angle of 0°. Data points in (d) were measured experimentally. The line is calculated from the theory, where shaded areas arise from uncertainties in the experimental input values. An elastic modulus of $\mu = 83.0 \pm 14.3$ Pa is extracted. The "zoom" in (c) highlights the rapid convergence of the theory.

of paramagnetic particles embedded in a soft elastic gel matrix. Applying an external magnetic field induced mutual magnetic forces between the particles. Rotating the magnetic field tuned these forces. The resulting relative displacements of the particles were tracked by optical microscopy.

We used paramagnetic Nickel (Ni) particles obtained from Alfa Aesar ($-100+325$ mesh, purity 99.8%). The magnetic hysteresis curves (measured by a vibrating sample magnetometer, Lake Shore 7407) showed a low remanence of ~ 7.5 kA/m, a low coercive field of ~ 2.4 mT, and a volume magnetization of 291 ± 17 kA/m under an external magnetic field of ~ 216 mT. We carefully selected Ni particles of similar sizes (deviation less than 2% within each group) and a roundness $\gtrsim 0.91$ (measured by image analysis[53]). These particles were embedded in the middle plane of a soft elastic polydimethylsiloxane-based[54] gel, see Fig. 3.3(a). First, a bottom gel layer with a thickness of 3.3 mm and a diameter of 24 mm was prepared in a plastic mold. Second, after sufficient stiffening (~ 0.5 h), the Ni particles were carefully deposited on its top around the center. Third, a top gel layer with the same composition and size as the bottom layer was added. To ensure good connection between the two layers, at least 7 days of cross-linking were allowed.

Using a 32-magnet Halbach array to generate a homogeneous magnetic field,[54] we applied ~ 216 mT to the embedded Ni particles, which is close to saturation. Starting from the initial direction, the magnetic field was rotated clockwise for 180° in 18 steps within the plane containing the Ni particles. Their center-of-mass positions were tracked by a CCD camera (MATRIX VISION mvBlueCOUGAR-S) with the zoom macro lens (Navitar Zoom 7000) mounted above the samples and subsequent image analysis.[53]

We measured the changes in particle distance Δr_{ij} ($i \neq j$) for a two- and three-particle system, see Figs. 3.3 and 3.4, respectively, when rotating the external magnetic field. Forces $\mathbf{F}_i$ on the particles result from mutual magnetic interactions. Due to substantial particle separations, we approximate the induced magnetic moments as point dipoles.[55,56] Thus, we find [57]

$$\mathbf{F}_i = -\frac{3\mu_0 m^2}{4\pi} \sum_{\substack{j=1 \\ j\neq i}}^{N} \frac{5\hat{\mathbf{r}}_{ij}(\hat{\mathbf{m}}\cdot\hat{\mathbf{r}}_{ij})^2 - \hat{\mathbf{r}}_{ij} - 2\hat{\mathbf{m}}(\hat{\mathbf{m}}\cdot\hat{\mathbf{r}}_{ij})}{r_{ij}^4}, \tag{3.14}$$

with μ_0 the vacuum permeability and $\mathbf{m} = m\hat{\mathbf{m}}$ the induced magnetic moments, considered identical for all particles in the close-to-saturating homogeneous external magnetic field. Using as input parameters the experimentally determined particle positions, sizes, and magnetization, we extracted the elastic shear modulus and calculated all changes Δr_{ij} from Eqs. (3.10)–(3.14). The magnetic forces $\mathbf{F}_i$ after displacement are determined iteratively. Perfect agreement between theory and experiment in Figs. 3.3 and 3.4 supports the significance of the theoretical approach and highlights its potential for microrheological measurement of the shear modulus.

In summary, we considered rigid spherical particles displaced against a surrounding

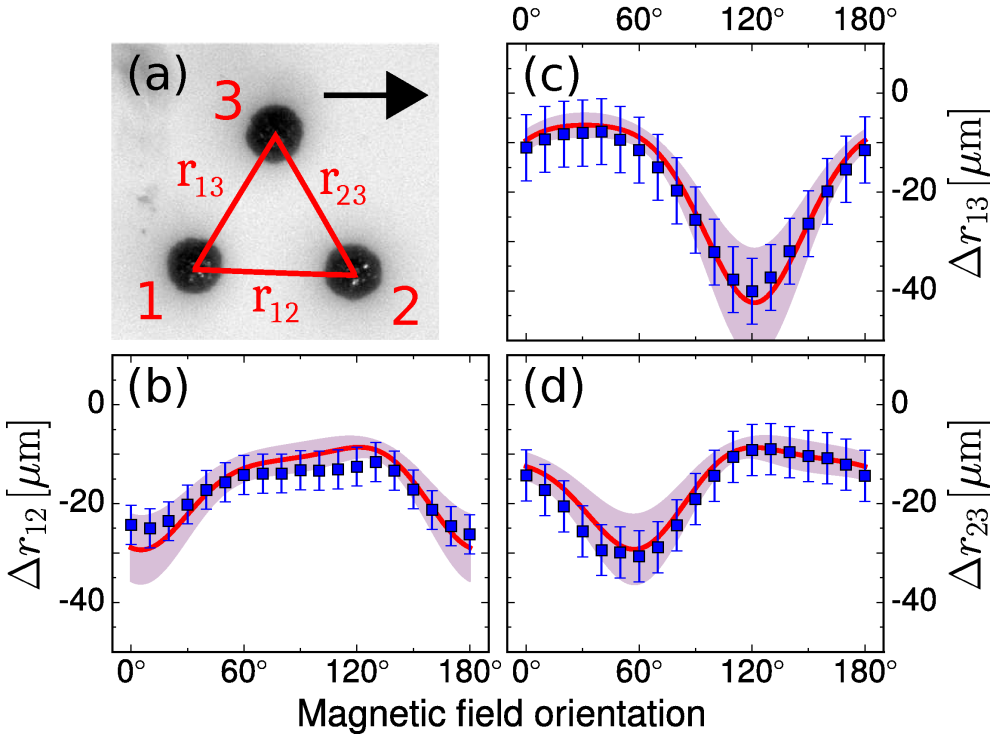

Figure 3.4 Same as in Fig. 3.3(b) and (d), now for a three-particle system. (a) The snapshot was taken for vanishing external magnetic field (particle diameters 208.5±2.3 μm). (b–d) Changes Δr_{ij} in all three distances ($i, j = 1,2,3$, $i \neq j$). The elastic modulus is $\mu = 76.3 \pm 11.7$ Pa.

elastic matrix by externally induced forces. We derived analytical expressions to calculate the resulting particle displacements. Mutual interactions due to induced matrix deformations are effectively included. This renders the procedure a promising tool to describe the behavior of elastic composite materials.[58–60] Our experiments on paramagnetic particles in a soft elastic gel matrix and subject to tunable magnetic interactions confirm the potential of the theory.

Upon dynamic extension, a prospective application concerns macroscopic rheology,[61] or nano- and microrheology,[45–48] where the matrix properties are tested by external agitation of embedded probe particles. Also biological and medical questions are addressable in this way, for instance cytoskeletal properties.[45–48,62] An extension of the theory to include imposed torques on the particles, e.g., due to magnetic anisotropy, is straightforward and will be presented in the near future.

The authors thank J. Nowak for measuring the magnetization curves and the Deutsche Forschungsgemeinschaft for support of this work through the priority program SPP 1681.

Bibliography

[1] Z. Zhang and C. Kleinstreuer, Phys. Fluids **14**, 862 (2002).

[2] Y. Meng, M. A. Rao, and A. K. Datta, Food Bioprod. Process. **83**, 297 (2005).

[3] M. J. Ferrua and R. P. Singh, J. Food. Sci. **75**, R151 (2010).

[4] T. M. Squires and S. R. Quake, Rev. Mod. Phys. **77**, 977 (2005).

[5] Q. R. Wald, Progr. Aerosp. Sci. **42**, 85 (2006).

[6] E. F. Campana, D. Peri, Y. Tahara, and F. Stern, Comput. Methods Appl. Mech. Engrg. **196**, 634 (2006).

[7] L. Müller, W. Heinze, D. Kožulović, M. Hepperle, and R. Radespiel, J. Aircraft **51**, 249 (2014).

[8] C. L. M. H. Navier, Mém. Acad. Sci. Inst. France **6**, 389 (1822).

[9] G. G. Stokes, Trans. Cambridge Philos. Soc. **8**, 287 (1845).

[10] S. Kim and S. J. Karrila, *Microhydrodynamics: principles and applications* (Butterworth-Heinemann, Boston, 1991).

[11] J. K. G. Dhont, *Introduction to dynamics of colloids* (Elsevier, Amsterdam, 1996).

[12] B. U. Felderhof, Phys. A **89**, 373 (1977).

[13] D. L. Ermak and J. A. McCammon, J. Chem. Phys. **69**, 1352 (1978).

[14] L. Durlofsky, J. F. Brady, and G. Bossis, J. Fluid Mech. **180**, 21 (1987).

[15] K. Zahn, J. M. Méndez-Alcaraz, and G. Maret, Phys. Rev. Lett. **79**, 175 (1997).

[16] J.-C. Meiners and S. R. Quake, Phys. Rev. Lett. **82**, 2211 (1999).

[17] J. K. G. Dhont, J. Chem. Phys. **120**, 1642 (2004).

[18] M. Rex and H. Löwen, Eur. Phys. J. E **26**, 143 (2008).

[19] C. M. Pooley, G. P. Alexander, and J. M. Yeomans, Phys. Rev. Lett. **99**, 228103 (2007).

[20] A. Baskaran and M. C. Marchetti, Proc. Natl. Acad. Sci. USA **106**, 15567 (2009).

[21] A. M. Menzel, A. Saha, C. Hoell, and H. Löwen, J. Chem. Phys. **144**, 024115 (2016).

[22] E. Lauga and T. R. Powers, Rep. Prog. Phys. **72**, 096601 (2009).

[23] K. Drescher, R. E. Goldstein, N. Michel, M. Polin, and I. Tuval, Phys. Rev. Lett. **105**, 168101 (2010).

[24] K. Drescher, J. Dunkel, L. H. Cisneros, S. Ganguly, and R. E. Goldstein, Proc. Natl. Acad. Sci. USA **108**, 10940 (2011).

[25] W. F. Paxton, K. C. Kistler, C. C. Olmeda, A. Sen, S. K. St. Angelo, Y. Cao, T. E. Mallouk, P. E. Lammert, and V. H. Crespi, J. Am. Chem. Soc. **126**, 13424 (2004).

[26] Y. An and M. T. Shaw, Smart Mater. Struct. **12**, 157 (2003).

[27] R. Fuhrer, E. K. Athanassiou, N. A. Luechinger, and W. J. Stark, Small **5**, 383 (2009).

[28] H. Böse, R. Rabindranath, and J. Ehrlich, J. Intell. Mater. Syst. Struct. **23**, 989 (2012).

[29] W. Cheng, J. Wang, U. Jonas, G. Fytas, and N. Stefanou, Nature Materials **5**, 830 (2006).

[30] T. Still, G. Gantzounis, D. Kiefer, G. Hellmann, R. Sainidou, G. Fytas, and N. Stefanou, Phys. Rev. Lett. **106**, 175505 (2011).

[31] J. Baumgartl, M. Zvyagolskaya, and C. Bechinger, Phys. Rev. Lett. **99**, 205503 (2007).

[32] J. Baumgartl, M. Zvyagolskaya, and C. Bechinger, Phys. Rev. Lett. **100**, 219903 (2008).

[33] J. D. Eshelby, Proc. R. Soc. A **241**, 376 (1957).

[34] J. D. Eshelby, Proc. R. Soc. A **252**, 561 (1959).

[35] L. J. Walpole, Proc. R. Soc. A **433**, 179 (1991).

[36] L. J. Walpole, Proc. R. Soc. A **434**, 571 (1991).

[37] L. J. Walpole, Q. J. Mech. Appl. Math. **58**, 129 (2005).

[38] N. Phan-Thien, J. Elasticity **32**, 243 (1993).

[39] H. L. Oestreicher, J. Acoust. Soc. Am. **23**, 707 (1951).

[40] A. N. Norris, J. Acoust. Soc. Am. **119**, 2062 (2006).

[41] A. N. Norris, J. Acoust. Soc. Am. **123**, 99 (2008).

[42] N. Phan-Thien and S. Kim, ZAMP **45**, 177 (1994).

[43] S. Kim and N. Phan-Thien, J. Elasticity **37**, 93 (1995).

[44] H. Tanaka and T. Araki, Phys. Rev. Lett. **85**, 1338 (2000).

[45] F. Ziemann, J. Rädler, and E. Sackmann, Biophys. J. **66**, 2210 (1994).

[46] A. R. Bausch, W. Möller, and E. Sackmann, Biophys. J. **76**, 573 (1999).

[47] T. A. Waigh, Rep. Prog. Phys. **68**, 685 (2005).

[48] C. Wilhelm, Phys. Rev. Lett. **101**, 028101 (2008).

[49] A.-L. Cauchy, *Exercices de mathématiques*, Vol. 3 (Bure frères, Paris, 1828) pp. 160–187.

[50] L. D. Landau and E. M. Lifshitz, *Theory of Elasticity* (Elsevier, Oxford, 1986).

[51] See Supplemental Material at *http://link.aps.org/supplemental/10.1103/PhysRevLett.117.238003* for the corresponding expressions in a compressible elastic matrix and for an analysis of experiments on a four-particle system.

[52] G. K. Batchelor and J. T. Green, J. Fluid Mech. **56**, 375 (1972).

[53] http://imagej.nih.gov/ij/.

[54] S. Huang, G. Pessot, P. Cremer, R. Weeber, C. Holm, J. Nowak, S. Odenbach, A. M. Menzel, and G. K. Auernhammer, Soft Matter **12**, 228 (2016).

[55] S. H. L. Klapp, J. Phys.: Condens. Matter **17**, R525 (2005).

[56] A. M. Biller, O. V. Stolbov, and Y. L. Raikher, Phys. Rev. E **92**, 023202 (2015).

[57] J. D. Jackson, *Classical Electrodynamics* (Wiley, New York, 1999).

[58] P. Ilg, Soft Matter **9**, 3465 (2013).

[59] S. Odenbach, Arch. Appl. Mech. **86**, 269 (2016).

[60] A. M. Menzel, Phys. Rev. E **94**, 023003 (2016).

[61] M. M. Denn and J. F. Morris, Annu. Rev. Chem. Biomol. Eng. **5**, 203 (2014).

[62] D. Mizuno, C. Tardin, C. F. Schmidt, and F. C. MacKintosh, Science **315**, 370 (2007).

3.2 Supplemental material

As stressed in the main text, the derivation of the displaceability matrix can likewise be performed for *compressible* systems. Following the same steps of derivation as in the main text, we present below the corresponding expressions for completeness. Apart from that, we add further experimental results and comparison with the theory for a four-particle system, in complete analogy to our presentation for the three-particle system in the main text.

3.2.1 Expressions for a compressible elastic matrix

For clarity and to facilitate the comparison with the hydrodynamic fluid case, we have presented in the main text the expressions for an *incompressible* elastic system. That is, the system tends to locally preserve the volume of all its volume elements during any type of elastic deformation. However, and in contrast to the hydrodynamic fluid case,[1–3] for elastic matrices it is straightforward to allow for *compressibility* in the derivation. This extended derivation proceeds in direct analogy to the one presented in the main text. Corresponding expressions are presented in the following using the same equation numbering as in the main text.

We again assume a homogeneous and isotropic elastic matrix of infinite extension. Once more, we start from the linear elastostatic Navier-Cauchy equations,[4]

$$\nabla^2\mathbf{u}(\mathbf{r})+\frac{1}{1-2\nu}\nabla\nabla\cdot\mathbf{u}(\mathbf{r})=-\frac{1}{\mu}\mathbf{f}_b(\mathbf{r}). \tag{3.15}$$

As in the main text, $\mathbf{u}(\mathbf{r})$ denotes the displacement field, μ the shear modulus of the matrix,[5] ν the Poisson ratio,[5] and $\mathbf{f}_b(\mathbf{r})$ the bulk force density. Now, we do not restrict our analysis to incompressible materials that locally adhere to $\nabla\cdot\mathbf{u}(\mathbf{r})=0$, and we do not assign a specific value to ν.

The resulting Green's function for a point force density $\mathbf{f}_b(\mathbf{r})=\mathbf{F}\delta(\mathbf{r})$ then reads[5]

$$\underline{\mathbf{G}}(\mathbf{r})=\frac{1}{16\pi(1-\nu)\mu}\left[\frac{3-4\nu}{r}\hat{\underline{\mathbf{I}}}+\frac{\mathbf{rr}}{r^3}\right]. \tag{3.16}$$

Using this expression, if an external force $\mathbf{F}_i$ is acting on a rigid spherical particle i of radius a embedded in the matrix with no-slip boundary conditions on its surface, a displacement field

$$\mathbf{u}_i^{(0)}(\mathbf{r})=\left(1+\frac{a^2}{6}\nabla^2\right)\underline{\mathbf{G}}(\mathbf{r}-\mathbf{r}_i)\cdot\mathbf{F}_i \tag{3.17}$$

is induced. Eq. (3.17) has the same form as in the main text, but $\underline{\mathbf{G}}$ is different, see Eq. (3.16). Again, the validity of Eq. (3.17) is confirmed as it satisfies Eq. (3.15), shows the correct limit $\mathbf{u}_i^{(0)}(\mathbf{r})=\underline{\mathbf{G}}(\mathbf{r}-\mathbf{r}_i)\cdot\mathbf{F}_i$ for $|\mathbf{r}-\mathbf{r}_i|>a$ when $a\to 0$, and for $|\mathbf{r}-\mathbf{r}_i|=a$ is

constant on the particle surface. For $|\mathbf{r}-\mathbf{r}_i| = a$, it reveals the rigid displacement

$$\mathbf{U}_i^{(0)} = \mathbf{u}_i^{(0)}(|\mathbf{r}-\mathbf{r}_i| = a) = \frac{5-6\nu}{24\pi(1-\nu)\mu a}\mathbf{F}_i \tag{3.18}$$

of the ith particle in response to $\mathbf{F}_i$.

The no-slip condition under our assumptions applies on the surface ∂V_j of a particle j also for compressible matrices. Thus Eq. (3.5) in the main text preserves its shape, i.e.

$$\mathbf{U}_j^{(1)} + \boldsymbol{\Omega}_j^{(1)} \times (\mathbf{r}-\mathbf{r}_j) = \mathbf{u}_i^{(0)}(\mathbf{r}) + \int_{\partial V_j} \underline{\mathbf{G}}(\mathbf{r}-\mathbf{r}') \cdot \mathbf{f}(\mathbf{r}') \mathrm{d}S', \tag{3.19}$$

where $\mathbf{U}_j^{(1)}$ denotes the translation of particle j, $\boldsymbol{\Omega}_j^{(1)}$ is its rotation, the displacement field $\mathbf{u}_i^{(0)}(\mathbf{r})$ is induced by particle i, and $\mathbf{f}(\mathbf{r}')$ denotes the surface force density that particle j exerts on the surrounding matrix. The derivation of expressions for $\mathbf{U}_j^{(1)}$ and $\boldsymbol{\Omega}_j^{(1)}$ in the form of the Faxén laws follows the same strategy as described in the main text and leads to

$$\mathbf{U}_j^{(1)} = \left(1 + \frac{a^2}{6}\nabla^2\right) \mathbf{u}_i^{(0)}(\mathbf{r})\Big|_{\mathbf{r}=\mathbf{r}_j}, \tag{3.20}$$

$$\boldsymbol{\Omega}_j^{(1)} = \frac{1}{2}\nabla \times \mathbf{u}_i^{(0)}(\mathbf{r})\Big|_{\mathbf{r}=\mathbf{r}_j}. \tag{3.21}$$

Also the stresslet $\underline{\mathbf{S}}_j$ exerted by particle j onto the matrix is derived in analogy to what is described in the main text. In general, for compressible systems, this stresslet is given by the expression $\underline{\mathbf{S}}_j = \int_{\partial V_j} \mathrm{d}S' [\mathbf{f}(\mathbf{r}')\mathbf{r}' + (\mathbf{f}(\mathbf{r}')\mathbf{r}')^T]/2$. This expression slightly differs from the one introduced below Eq. (3.7) in the main text for incompressible systems. There, a trace-free definition was used to exclude compressions and dilations of the matrix, which needs to be the case for volume-conserving systems. It can be seen from the main text that the difference in definitions plays no actual role for our derivation. The reason is Eq. (3.9), where the extra term $\sim \hat{\underline{\mathbf{I}}}$ in the incompressible case only leads to a contribution $\sim \nabla \cdot \underline{\mathbf{G}}$. Yet, $\nabla \cdot \underline{\mathbf{G}}$ vanishes in the incompressible case. Therefore, following the same strategy as described in the main text, we obtain

$$\begin{aligned}\underline{\mathbf{S}}_j^{(1)} = &-\frac{4\pi(1-\nu)\mu a^3}{4-5\nu}\left(1+\frac{a^2}{10}\nabla^2\right)\Bigg[\frac{1}{1-2\nu}\hat{\underline{\mathbf{I}}}\nabla\cdot\mathbf{u}_i^{(0)}(\mathbf{r}) \\ &+\frac{5}{2}\left(\nabla\mathbf{u}_i^{(0)}(\mathbf{r}) + \left(\nabla\mathbf{u}_i^{(0)}(\mathbf{r})\right)^T\right)\Bigg]\Bigg|_{\mathbf{r}=\mathbf{r}_j}.\end{aligned} \tag{3.22}$$

Likewise, the displacement field $\mathbf{u}_j^{(1)}(\mathbf{r})$ resulting from the rigidity of particle j and its resistance to deformation, expressed by the stresslet $\underline{\mathbf{S}}_j^{(1)}$, is calculated as described in the main text. Eq. (3.22) here contains a term $\sim 1/(1-2\nu)$, which would diverge for $\nu \to 0.5$. However, it gets canceled by a counter-factor $\sim (1-2\nu)$ in the calculation.

More precisely, upon inserting Eq. (3.17) into Eq. (3.22), the expression $\nabla\cdot\underline{\mathbf{G}}$ appears; straightforward calculation of $\nabla\cdot\underline{\mathbf{G}}$ via Eq. (3.16) leads to a factor $\sim(1-2\nu)$. In the end, $\mathbf{u}_j^{(1)}(\mathbf{r})$ has the same form as Eq. (3.9) in the main text,

$$\mathbf{u}_j^{(1)}(\mathbf{r}) = -\left(\underline{\mathbf{S}}_j^{(1)}\cdot\nabla\right)\cdot\underline{\mathbf{G}}(\mathbf{r}-\mathbf{r}_j). \tag{3.23}$$

In the next step, again, the reaction of particle i in response to the field $\mathbf{u}_j^{(1)}(\mathbf{r})$ is obtained from Eqs. (3.20)–(3.23) by replacing $(\mathbf{u}_i^{(0)}, \mathbf{U}_j^{(1)}, \boldsymbol{\Omega}_j^{(1)}, \underline{\mathbf{S}}_j^{(1)}, \mathbf{u}_j^{(1)})$ with $(\mathbf{u}_j^{(1)}, \mathbf{U}_i^{(2)}, \boldsymbol{\Omega}_i^{(2)}, \underline{\mathbf{S}}_i^{(2)}, \mathbf{u}_i^{(2)})$.

Summing up the contributions from the different steps of iteration and considering all N particles simultaneously leads to an expression in the form of an elastic displaceability matrix $\underline{\mathbf{M}}$ as given in the main text:

$$\begin{pmatrix}\mathbf{U}_1\\ \vdots\\ \mathbf{U}_N\end{pmatrix} = \begin{pmatrix}\underline{\mathbf{M}}_{11} & \cdots & \underline{\mathbf{M}}_{1N}\\ \vdots & \vdots & \vdots\\ \underline{\mathbf{M}}_{N1} & \cdots & \underline{\mathbf{M}}_{NN}\end{pmatrix}\cdot\begin{pmatrix}\mathbf{F}_1\\ \vdots\\ \mathbf{F}_N\end{pmatrix}. \tag{3.24}$$

Limiting ourselves to contributions up to (including) order r_{ij}^{-4}, we find for a *compressible* system the more general expressions

$$\begin{aligned}\underline{\mathbf{M}}_{i=j} &= M_0\Bigg\{\hat{\underline{\mathbf{I}}} - \sum_{\substack{k=1\\k\neq i}}^{N}\frac{3}{4(4-5\nu)(5-6\nu)}\left(\frac{a}{r_{ik}}\right)^4\\ &\quad\Big[\Big(37-44\nu+10(1-2\nu)^2\Big)\hat{\mathbf{r}}_{ik}\hat{\mathbf{r}}_{ik}\\ &\quad+5(1-2\nu)^2\left(\hat{\underline{\mathbf{I}}}-\hat{\mathbf{r}}_{ik}\hat{\mathbf{r}}_{ik}\right)\Big]\Bigg\},\end{aligned} \tag{3.25}$$

$$\begin{aligned}\underline{\mathbf{M}}_{i\neq j} &= M_0\frac{3}{2(5-6\nu)}\frac{a}{r_{ij}}\Bigg[\left(4(1-\nu)-\frac{4}{3}\left(\frac{a}{r_{ij}}\right)^2\right)\hat{\mathbf{r}}_{ij}\hat{\mathbf{r}}_{ij}\\ &\quad+\left(3-4\nu+\frac{2}{3}\left(\frac{a}{r_{ij}}\right)^2\right)\left(\hat{\underline{\mathbf{I}}}-\hat{\mathbf{r}}_{ij}\hat{\mathbf{r}}_{ij}\right)\Bigg]+\underline{\mathbf{M}}_{i\neq j}^{(3)},\end{aligned} \tag{3.26}$$

where $M_0=(5-6\nu)/24\pi(1-\nu)\mu a$ and $\hat{\mathbf{r}}_{ij}=\mathbf{r}_{ij}/r_{ij}$ $(i,j=1,2,...,N)$. Here, the three-body interactions contribute as given by $\underline{\mathbf{M}}_{i\neq j}^{(3)}$ in the form

$$\begin{aligned}\underline{\mathbf{M}}_{i\neq j}^{(3)} &= M_0\frac{3}{8(4-5\nu)(5-6\nu)}\sum_{\substack{k=1\\k\neq i,j}}^{N}\left(\frac{a}{r_{ik}}\right)^2\left(\frac{a}{r_{jk}}\right)^2\\ &\quad\Big[-10(1-2\nu)\Big((1-2\nu)\big((\hat{\mathbf{r}}_{ik}\cdot\hat{\mathbf{r}}_{jk})\hat{\underline{\mathbf{I}}}+\hat{\mathbf{r}}_{jk}\hat{\mathbf{r}}_{ik}\big)\\ &\quad+3(\hat{\mathbf{r}}_{ik}\cdot\hat{\mathbf{r}}_{jk})(\hat{\mathbf{r}}_{ik}\hat{\mathbf{r}}_{ik}+\hat{\mathbf{r}}_{jk}\hat{\mathbf{r}}_{jk})-\hat{\mathbf{r}}_{ik}\hat{\mathbf{r}}_{jk}\Big)\\ &\quad+3\left(7-4\nu-15(\hat{\mathbf{r}}_{ik}\cdot\hat{\mathbf{r}}_{jk})^2\right)\hat{\mathbf{r}}_{ik}\hat{\mathbf{r}}_{jk}\Big].\end{aligned} \tag{3.27}$$

The corresponding expressions for *incompressible* systems in the main text readily follow from Eqs. (3.24)–(3.27) by setting the Poisson ratio $\nu = 0.5$. Here, we derived and listed the more general expressions for *compressible* elastic matrices.

3.2.2 Four-particle system

In addition to the two- and three-particle samples described in the main text, we also generated and analyzed four-particle systems. Their preparation, experimental analysis, and the corresponding comparison with the theory are in complete analogy to the three-particle system described in the main text. We recall that our theoretical description in the main text *up to the investigated order* (including r_{ij}^{-4}) is exact for arbitrary particle numbers. No higher-body interactions appear to this order. Therefore, Eqs. (10)–(14) in the main text also apply to systems of particle numbers $N > 3$ up to (including) order r_{ij}^{-4}, i.e. if the particle separations are not significantly reduced.

Thus, our four-particle results predominantly provide a supplement to the results presented in the main text. Our experimental and theoretical results for the four-particle system are depicted in Fig. 3.5. One could continue to further increasing particle numbers in the same way.

Bibliography

[1] G. K. Batchelor and J. T. Green, J. Fluid Mech. **56**, 375 (1972).

[2] S. Kim and S. J. Karrila, *Microhydrodynamics: principles and applications* (Butterworth-Heinemann, Boston, 1991).

[3] J. K. G. Dhont, *Introduction to dynamics of colloids* (Elsevier, Amsterdam, 1996).

[4] A.-L. Cauchy, *Exercices de mathématiques*, Vol. 3 (Bure frères, Paris, 1828) pp. 160–187.

[5] L. D. Landau and E. M. Lifshitz, *Theory of Elasticity* (Elsevier, Oxford, 1986).

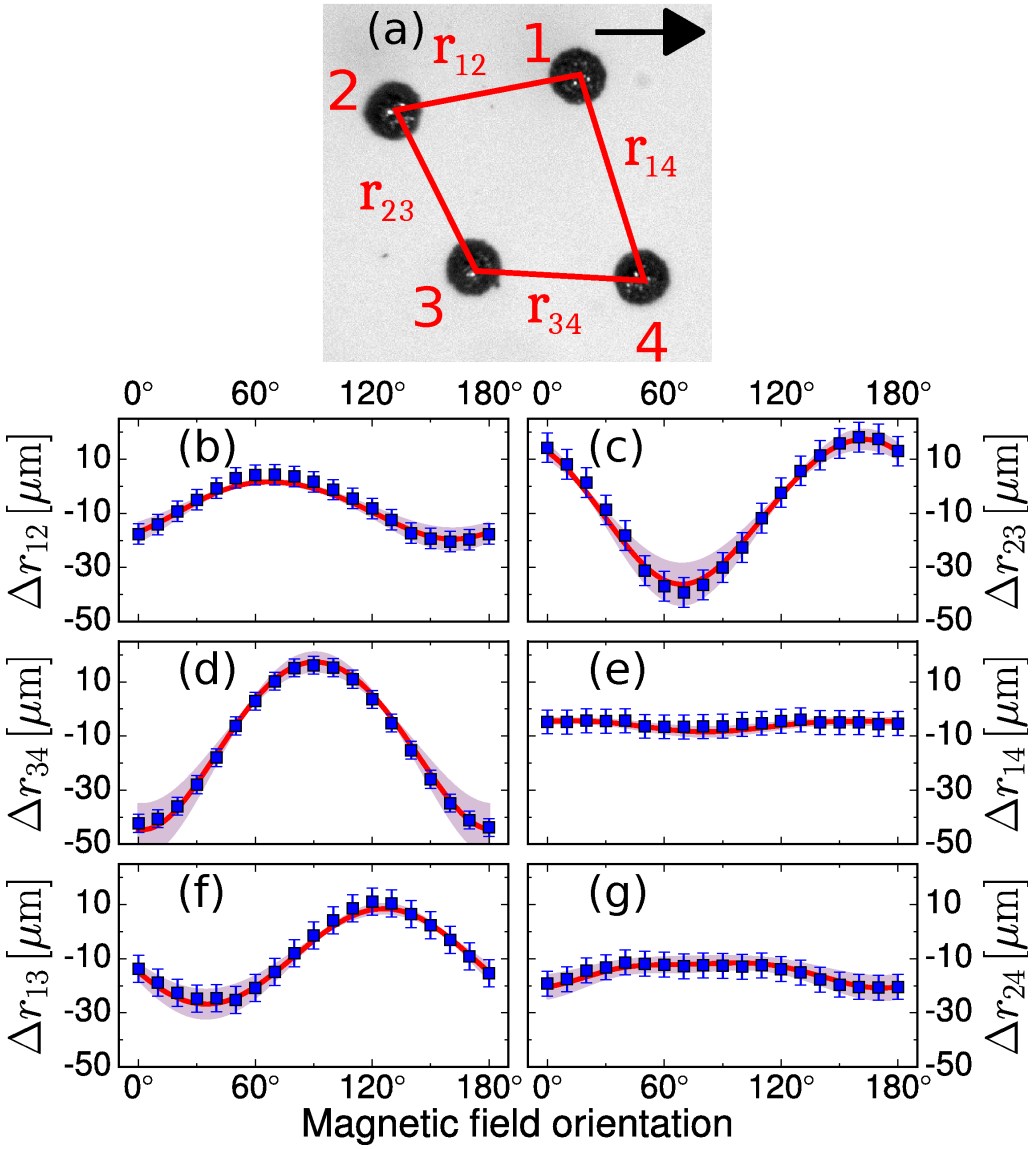

Figure 3.5 Same as in Figs. 3 and 4 in the main text, here for a four-particle system. (a) The snapshot was taken for vanishing external magnetic field (particle diameters 204.4±2.2 μm). (b–g) Changes Δr_{ij} in all six distances ($i, j = 1,2,3,4$, $i \neq j$). Good agreement between theory (red line) and experiments (blue squares) is observed, and the modulus of the gel matrix for this system is obtained as 85.7±12.6 Pa.

4. Microgels at the water/oil interface: In-situ observation of structural ageing and two dimensional magnetic bead microrheology

Shilin Huang,[a] Kornelia Gawlitza,[‡b] Regine von Klitzing,[b] Laurent Gilson,[a] Johannes Nowak,[c] Stefan Odenbach,[c] Werner Steffen,[a] and Günter K. Auernhammer[*a]

[a] Max Planck Institute for Polymer Research, Ackermannweg 10, 55128 Mainz, Germany.

[b] Stranski-Laboratorium für Physikalische und Theoretische Chemie, Technische Universität Berlin, Strasse des 17. Juni 124, 10623 Berlin, Germany.

[c] Chair of Magnetofluiddynamics, Measuring and Automation Technology, Institute of Fluid Mechanics, Technische Universität Dresden, 01069 Dresden, Germany.

[‡] Current address: Fachbereiche 1.9 Chemische und optische Sensorik, Bundesanstalt für Materialforschung und -prüfung (BAM), Richard-Willstätter-Str. 11, 12489 Berlin, Germany.

[*] Corresponding author. E-mail: auhammer@mpip-mainz.mpg.de

Reprinted with permission from:
S. Huang, K. Gawlitza, R. von Klitzing, L. Gilson, J. Nowak, S. Odenbach, W. Steffen, G. K. Auernhammer, Langmuir, 2016, 32 (3), 712–722.

Statement of Contribution

In this paper, Shilin Huang has the following contributions:

(1) Developing the experimental method to realize the in situ observation of the microgels at the water/oil interface (Fig. 4.1).

(2) Observing the behaviors of the microgels at the interface (Figs. 4.2– 4.7, Fig. 4.11, Fig. 4.15).

(3) Performing mechanical tests on the microgel aggregates at the water/oil interface using the magnetic particles (Fig. 4.8, Fig. 4.16).

(4) Calculating the magnetic force between the magnetic particles.

(5) Using the magnetic particles to shear the microgel-loaded interface (Fig. 4.9).

(6) Estimating the pair interaction potential for microgels at the interface (Figs. 4.12–4.14).

In addition, Shilin Huang contributes partially to writing the paper.

Abstract

Stimuli-responsive microgels can be used as stabilizer for emulsions. However, the details of structure and the viscoelastic property of the microgel-laden interface are still not well known. We synthesized fluorescently labeled microgels, and used confocal microscopy to observe their arrangement at the water/oil interface. The microgels aggregated spontaneously at the interface and the aggregated structure reorganized due to thermal motion. The structure of the interfacial layer formed by microgels depended on the microgel concentration at the interface. We suggest that the structure was controlled by the aggregation and adsorption of microgels at interface. The interparticle separation between microgels at the interface decreased over time, implying a slow ageing process of the microgels at the interface. Magnetic beads were introduced at the interface and used to trigger deformation of the microgel layer. Under compression and shear the microgels in the aggregated structure rearranged leading to plastic deformation, and some elastic responses were also observed.

4.1 Introduction

Solid colloidal particles can be used to provide long-term stability against coalescence in emulsions which are called (Ramsden)-Pickering emulsions.[1,2] In the last decade microgels have been explored to be used as Pickering emulsion stablilizers.[3–19] The most widely studied microgels are made of poly(N-isopropylacrylamide) (PNIPAM). The PNIPAM microgels are cross-linked soft particles swollen with water. PNIPAM microgels raise a lot of interest in basic research and applied science since they are responsive to external stimuli. PNIPAM has a lower critical solution temperature (LCST) of 32°C in aqueous solution. At room temperature the microgels are in the swollen state, and once heating above LCST they collapse. By introducing some other comonomers (e.g., acrylic acid and methacrylic acid) during synthesis they can be also sensitive to pH.[20–23] The mechanical properties of PNIPAM microgels can be controlled by the cross-linker density[24] and the comonomer content.[25] Typical elastic moduli of PNIPAM microgels range between several tens of kPa and several MPa. PNIPAM microgels are known to adsorb spontaneously and almost irreversible at the water/oil interface.[3,16,26] They can even stabilize emulsions similar to Pickering emulsions.

In contrast to non-deformable particles, microgels can deform at the interface adopting a "fried egg-like" structure,[27] with the "egg yolk" corresponding to the less deformable cores, and the "egg white" corresponding to the flattened shells (also called corona). The core-shell structure of microgels at the interface is caused by the fact that the cross-linker distribution in conventionally synthesized microgels is not homogeneous but decreases towards the periphery of the microgels.[17] This picture is supported by cryogenic scan-

ning electron microscopy (cryo-SEM) images.[27] Although Cryo-SEM can resolve the protrusion height of the microgels into the oil phase, the shape of the microgels in the water phase cannot be seen. Thus Geisel et al. used transmission x-ray microscopy to observe the 3-dimensional structure of microgels at the water/oil interface.[13] They found that the microgels deformed anisotropically and penetrated the oil droplets in the hydrated state. The protruded depth to the oil phase is about 20-30% of the size of microgels in water.[13,28] The shape of the microgels at the interface is suggested to be a balance of capillary force and the deformability of the microgels. The osmotic pressure in the microgel in the deformed state should also be taken into account.[29] The deformability of the microgels dominates the stability of the interface. The softer microgels are found to be more efficient to stabilize the interface.[27]

The interaction between microgels at the liquid interface is important for the interface property. Cryo-SEM images show that the microgels are in contact through their overlapping shells.[27] When the layer of adsorbed microgels on a Langmuir trough is compressed, the surface pressure shows a two-step increase,[3,7,30] reflecting that either the shells or the cores of the microgels are compressed. The microgels show soft repulsive behavior during compression.[7] The microgel-laden interface has a dilational elasticity maximum when the microgels have a flattened conformation at an intermediate surface pressure.[3]

Additionally, an attraction force between microgels at the interface has also been observed.[6,9] Cohin et al. reported that the microgels formed aggregates at the water/air interface at low microgel concentrations.[9] They suggested that the attraction was caused by the long-range capillary force. Moreover, the electrostatic forces between microgels do not play an important role in the interface property.[7,27,28,30] For example, Geisel et al. reported that for pH-sensitive microgels at the water/oil interface higher charge could lead to less repulsion. Thus, it is believed that the deformability of the microgels plays the dominating role in the interface property, and the other factors, such as charges/pH, temperature and crosslinking density, influence the interface property in an indirect way.[27,30] In addition, there are many similarities between microgels and linear polymers in their surface activity. For example, they can be easily adsorbed to interfaces. Interfaces laden with microgels and linear polymers show a maximum in the interfacial dilational elasticity at an intermediate surface pressure.[3,9] These similarities indicate that the polymer interaction between microgels is important for the interface property.

The packing of the microgels at the interface can also significantly influence interface properties. For example, if the emulsion droplets are not well covered by the microgels, the emulsion droplets will collapse until their surface is well covered.[27] However, it is also reported that it is not necessary to completely cover the interface in order to form a stable emulsion.[8] The spontaneous adsorption of microgels at the interface can form a hexagonal structure, though it cannot be easily controlled.[7] Some other two-dimensional (2D) arrangements as well as the coexistence of different structures are also observed.[3,31,32] A

highly ordered crystalline structure can be achieved by compression.[7]

In order to understand and control the stability of the microgel-laden interface in emulsions, the mechanical properties of the microgel-laden interface have to be studied. Macroscopic techniques can be used to study the interface properties, such as pendent drops and compression isotherm. A recent study by Geisel et al. was able to correlate the compression isotherms with the microscopic arrangement of the microgels.[7] The interface property can also be studied by 2D shear rheology using oscillatory shear rheometer, magnetic needle (or rod, disc) rheometer and passive microrheology.[33–35] For example, Brugger et al. used shear and dilatational rheology to study the viscoelastic property of poly-(N-isopropylacrylamide-co-methacrylicacid) (PNIPAM-co-MAA) microgels at a water/heptane interface.[31,32] They found that at low pH when the microgels were uncharged and densely packed at the interface, the interface lost its elasticity under small shear deformation (strain $< 10^{-3}$). At high pH when the microgels were charged and partially interconnected, the interface was soft-gel like. They proposed that the viscoelasticity of the interface was responsible for the emulsion stability. The interface at higher pH was more stable because of the higher elastic modulus.

To date there are still many open questions about the microgel-stabilized liquid interface.[6,29] The details of the structure and the corresponding viscoelastic property of the microgel-laden interface are still not well known. In this paper we use laser scanning confocal microscopy (LSCM) to study the adsorption, arrangement and rearrangement of microgels at the water/oil interface. For this purpose the microgels are fluorescently labeled so they are visible by LSCM. Our results on the ageing behavior of the microgels at the water/oil interface might have an implication on the long time stability of emulsions. Finally, by introducing magnetic beads, we are able to apply forces to the microgel layer at the interface. The study of interfacial microrheology contributes to understanding the interaction between the microgels at the water/oil interface.

4.2 Experimental section

4.2.1 Preparation of dye-labeled microgels

4.2.1.1 Materials

The monomer N-isopropylacrylamide (NIPAM; 97 %, Aldrich) was purified by recrystallization in n-hexane. The cross-linker N,N'-methylenebis(acrylamide) (MBA; $\geqslant$99.5 %, Fluka), potassium peroxodisulfate (KPS; $\geqslant$99 %, Fluka) and DL-2-allylglycine (AG; Aldrich) were used as received for microgel synthesis. Rhodamine B isothiocyanate (RITC; Aldrich) was used as received for labeling of the microgels. A low-molecular-weight trimethylsiloxy-terminated polydimethylsiloxane (PDMS, 770 g/mol, Alfa Aesar GmbH & Co. KG) was used as the oil phase as received. Superparamagnetic beads were pur-

chased from microParticles GmbH. They were labeled with fluorophores (visible in LSCM). According to the manufacturer these beads have a diameter of 4.7 ± 0.2 μm and are slightly negatively charged in water.

4.2.1.2 Synthesis of p-NIPAM-co-AG microgels

P-NIPAM-co-AG microgels with a crosslinker content of 5 mol% and a comonomer content of 25 mol% were synthesized by surfactant free emulsion polymerization via a temperature ramp.[36,37] Briefly, 2.26 g of the monomer NIPAM (0.02 mol), 0.15 g of the crosslinker MBA (0.005 mol) and 0.58 g of the comonomer AG (0.005 mol) were dissolved in 250 mL water followed by degassing for 1 h at 45°C. Afterwards, under continuous stirring a solution of 1 mL KPS (0.08 M) was added to the mixture to initiate the polymerization reaction. The temperature was slowly increased to 65°C at a rate of 1°C every 2 minutes. Finally, the polymerization was completed by stirring overnight at 65°C under N_2 atmosphere. The received microgels were purified by filtering over glass wool, dialysis for 2 weeks and finally freeze-drying at -85°C under 1×10^{-3} bar for 48 h.

4.2.1.3 Labeling of p-NIPAM-co-AG microgels with Rhodamine dye

The p-NIPAM-co-AG microgels were labeled with the dye RITC. Therefore, 100 mg of the dried microgels were diluted in 2 mL buffer (sodium hydrogencarbonate, pH 9.5). 300 μL of a RITC solution (1 mg/mL) was added and the mixture was stirred in the dark for 2 h. The labeled microgels were purified three times by centrifugation and washing with buffer solution. Finally, the sample was freeze dried at -85°C under 1×10^{-3} bar for 48 h.

4.2.1.4 Preparing microgel-water suspensions

The dry microgels were dispersed into Milli-Q water with a weight fraction of 1 wt% at room temperature for at least 48 h for rehydration. Then the temperature was increased to 60°C for 3 h. After shaking at 2500 r/min with a Reax Control (Heidolph, Schwabach, Germany) for 1 min and ultrasonication for 0.5 min (Transsonic 460/H, Elma), a suspension with good dispersion was obtained. We further diluted the suspension into different concentrations in order to form water/oil interfaces with different concentrations of microgels.

4.2.2 Methods

4.2.2.1 Light Scattering

The size of the microgels was determined by dynamic light scattering (DLS). An ALV goniometer setup with a Nd:YAG laser as light source (λ= 532 nm) and an ALV-6010/160E

digital full correlator (ALV, Langen, Germany) were used to obtain the correlation functions. These were recorded at a constant scattering angle of 90°. The DLS experiment was equipped with a thermostated toluene bath. The data analysis was performed with a Cumulant analysis. We measured three different concentrations between 0.0001 to 0.005 wt% and got consistent values for the hydrodynamic radius of 260 nm in the collapsed state and of 350 nm in the non-collapsed state at 45°C and 25°C respectively. We used rather low concentrations in order to eliminate possibility of interactions between the microgels which may hamper the free diffusion.

4.2.2.2 ζ potential

The ζ potential of the microgels was measured with a Zetasizer Nano ZS (Malvern Instruments Ltd.). Dynamic and electrophoretic light scattering measurements were performed at a fixed angle of 173°. The ζ potential of the microgels was about -20$\pm$4 mV at 25°C at a pH of about 6.

4.2.2.3 Confocal microscopy study

A home-built laser scanning confocal microscope was used to observe the water/oil interface.[38,39] The recording time for an image depended on the resolution of the image. We used three resolutions: 2048$\times$2048 pixels, 1024$\times$1024 pixels and 512$\times$512 pixels, and the corresponding recording time for each image was 51 s, 13 s and 3 s, respectively. An oil-immersion objective (PLAPON 60XO, 60$\times$, NA=1.42, working distance 150 μm, Olympus Deutschland GmbH, Germany) was used. MilliQ water was used to dilute the microgels, and PDMS was used as the oil phase. The experimental setup is shown in Fig. 4.1. A copper hole grid (diameter=1500 μm, height=20 μm) from Agar was used to hold the water phase, which contained different concentrations of microgels (0.01-0.3 wt%). After depositing a small drop of microgel/water suspension on the grid, PDMS oil (saturated by water before use) was carefully added until it covered the drop. The resulting water/oil interface was about 100-150 μm above the coverslip. For some samples fluorescently labeled superparamagnetic beads were introduced by adding 10 μL 1 wt% magnetic bead/PDMS suspension into the oil from the top. The magnetic beads were allowed to sediment to the water/oil interface and they stayed at the interface due to the capillary force. A homogeneous magnetic field was applied by using permanent magnets (Halbach array).[40,41] The magnetic field was aligned along the sample plane (perpendicular to the optical path of the microscope). The magnetic field was measured by a Lake Shore Model 425 Gaussmeter with a transverse probe. The magnetization curve of the superparamagnetic beads was measured with a vibrating sample magnetometer (VSM, Lake Shore 7407). The magnetization curve of the magnetic beads (Fig. 4.10, Supporting Information) showed a superparamagnetic behavior (remanence $\sim$0.2 Am^2/kg, saturation magnetization $\sim$16.6 Am^2/kg). These experiments were performed at room temperature.

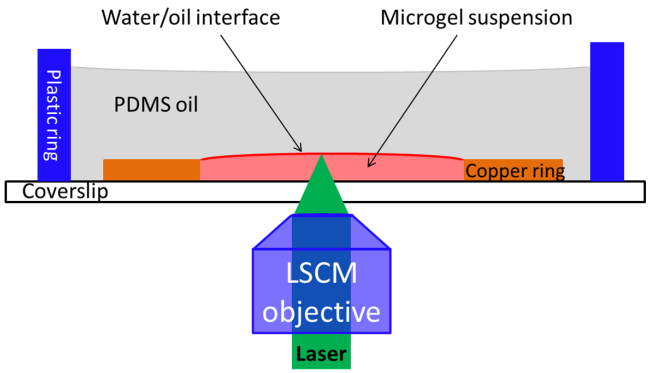

Figure 4.1 A sketch of the experimental setup.

4.2.2.4 Image analyse

The center positions of the microgels in the LSCM images were obtained by using the Particle Tracker plug-in of the ImageJ software.[42,43] The radial distribution function, also called pair correlation function $g(r)$,[44] was extracted from the position data by first calculating the distance for each possible particle pair. This set of distances was then transformed into a probability distribution normalized by the system density. Assuming hard sphere contacts, the first peak of $g(r)$ corresponds to particles in direct contact. The first peak was fitted using a Gaussian function to identify the peak position. We used IDL (Exelis Visual Information Solutions) for the calculation with a home-build algorithm (see Supporting Information for details). Due to the soft nature of the microgels,[7] we considered microgels to be in contact if the distance between the microgels was within 3 times of the standard deviation of the Gaussian fit to the first peak of $g(r)$. For determining the deformation field of the microgel layer at the interface triggered by the magnetic beads, we first tracked the displacement of every microgel in the images. The images were then divided into small areas (3×3 μm^2) and the deformation field was presented by the mean displacements in the small areas.

4.3 Results and discussion

4.3.1 Aggregation and self-assembly

When the concentration of the microgels at the water/oil interface was low, the microgels diffused along the interface (Movie S4-1 in Supporting Information). The image series in Fig. 4.2 shows how the microgels diffuse, aggregate and self-assemble at the interface. From Fig. 4.2a to Fig. 4.2b, the isolated single microgel (indicated by the red arrow) diffused before it met and connected to the 5-particle cluster. After the aggregation, the lower part of the cluster sensed the “newcomer”, and the cluster reorganized (see upper cluster in Fig. 4.2c, red dash circle). The aggregation and self-assembly were also be observed

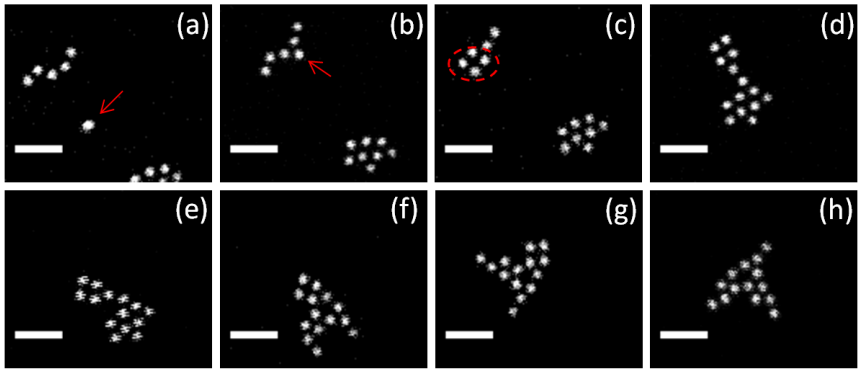

Figure 4.2 Aggregation and assembly of microgels at the water/oil interface. The images were taken (a) 8.6 min, (b) 9.4 min, (c) 10 min, (d) 17.5 min, (e) 30.7 min, (f) 33.9 min, (g) 38.5 min, and (h) 58.6 min after preparing the water/oil interface. All the images show the same set of microgels. The red arrow indicates an isolated single microgel that approached and connected to the 5-particle cluster. The interface concentration of microgels is 0.02 μm^{-2}. The scale bar is 5 μm.

when two larger clusters met, Fig. 4.2c-h. The aggregation was an irreversible process, and the microgels only reassembled within the clusters. These internal reorganizations in the clusters include local rearrangements of nearest neighbors and rearrangements of the entire cluster beyond the nearest neighbors. Note that in Fig. 4.2 the separation between nearest microgels in the clusters is about 1.5 μm, about twice the hydrodynamic diameter of the microgels in bulk water (700 nm).

These results indicate that there is a long-range attraction force between the microgels contributing to their aggregation and assembly. Below a distance of about 1.5 μm a repulsive force prevents the microgels from coming closer. We assume that the repulsive force is due to the overlap of microgel shells (weakly crosslinked polymer chains) at the interface.[7,45] Also an electrostatic repulsion could contribute to the repulsive force (see Sec. ζ potential above). Cohin et al. also observed clusters of microgels at the water/air interface.[9] They suggested that the capillary interaction as well as attractions between dangling polymer arms might be responsible for the formation of the clusters. The capillary force between microgels at interface was suggested to be due to the deformation of the interface close to the microgels. Although the weight of the microgels might not be enough to deform the interface, the interfacial deformations could be created if the contact line at the particle surface was undulated or irregularly shaped.[6,9]

In the Supporting Information (Figs. 4.12–4.14) we estimate the pair interaction potential between two microgels at the water/oil interface by using the particle tracking method. The pair interaction potential at a separation distance of 1.5 μm is $-220 \pm 130\ k_BT$ (k_BT is the thermal energy) and the corresponding attraction force is 2.4 ± 1.3 pN (Fig. 4.14, Supporting Information). The pair interaction potential drops off as $1/r^{(4\pm0.7)}$ (r is the center-to-center distance between the microgels). This scaling of the interaction potential

is in agreement with the capillary interaction due to undulation of contact line around the particles at interface.[46] In order to generate the attraction force found in our experiment, the contact line should have an undulation amplitude of ∼3 nm. The nanosize undulation of the contact line may be also supported by the cryo-SEM images which show digitations at the periphery of the microgels at the interface.[27] These digitations may reflect the undulation of the interface around the microgels. In the Supporting Information, we also discuss some other possible long-range attraction forces at interface.

4.3.2 Structure at the interface

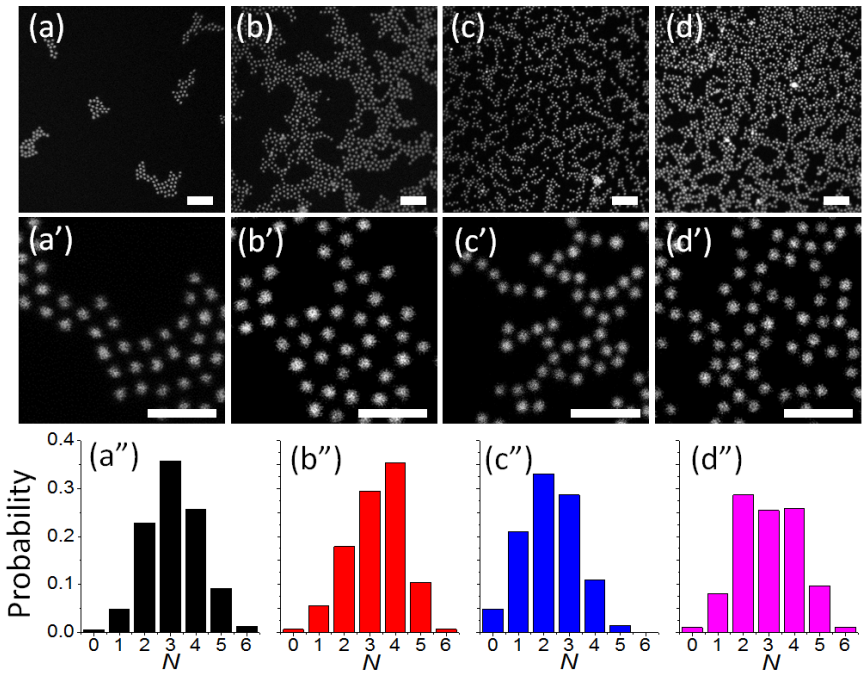

Figure 4.3 Structure of microgel assemblies at the water/oil interface. The interface concentrations of microgels are 0.03 μm^{-2}, 0.19 μm^{-2}, 0.26 μm^{-2} and 0.35 μm^{-2} for (a, a'), (b, b'), (c, c') and (d, d'), respectively. The different interface concentrations were obtained by changing the microgel concentration in the aqueous phase. The scale bars are 10 μm in (a, b, c, d) and 5 μm in (a', b', c', d'). All images were taken after waiting for 1 h after the interfaces were prepared. (a", b", c", d") show the probability for the number of nearest neighbors (N) in (a, b, c, d), respectively. 619, 1191, 1649 and 2236 microgels were used for the statistics in (a", b", c", d"), respectively.

Figure 4.3 shows the arrangement/topology of the microgels at the water/oil interface. At a low interface concentration, the microgels formed isolated domains (Fig. 4.3a). Within the domains, the microgels adopted local ordered structures (Fig. 4.3a'). Increasing the concentration of microgels led to a percolation of these domains (Fig. 4.3b, b'). Fig. 4.3a", b" show that the microgels tended to have more neighbors when the interface concentration was increased from 0.03 μm^{-2} to 0.19 μm^{-2}. However, this tendency was not observed when the concentration was further increased to 0.26 μm^{-2}. Fig. 4.3c, c'

show that at the concentration of 0.26 μm^{-2}, the interface had a ramified topology. The microgels tended to have only 2 neighbors (Fig. 4.3c"). The structure at this concentration (Fig. 4.3c) is reminiscent of the fractal structure formed by diffusion limited cluster aggregation.[47] When the concentration was further increased, a percolating microgel network with disordered microgels was observed (Fig. 4.3d).

The structure of microgels at the interface depends strongly on the preparation procedures. For example, in emulsions formed by limited coalescence process,[27,48] the microgels at the interface are compressed due to the decrease of interfacial area during coalescence. Thus, closely packing structures, e.g., hexagonal order (Fig. 4.11d, Supporting Information) can be observed at the emulsion interfaces. Large-scale hexagonal order can be obtained by using Langmuir trough where the compression can be well controlled.[7] For spontaneous adsorption of microgels at the interface, a highly compressed structure can be obtained if an excess of microgels in the aqueous phase is present.[3] In our experiment a thin layer of microgel dispersion was confined under the oil phase (Fig. 4.1), thus the interface area/volume ratio was much larger than in typical emulsions. This facilitated the adsorption of microgels to the interface. In addition, the absolute number of microgels was not enough to cover the entire interface. Consequently, the porous structures at the water/oil interface were formed (Fig. 4.3b-d). In the following we will show that the structure also depends strongly on the age of the interface.

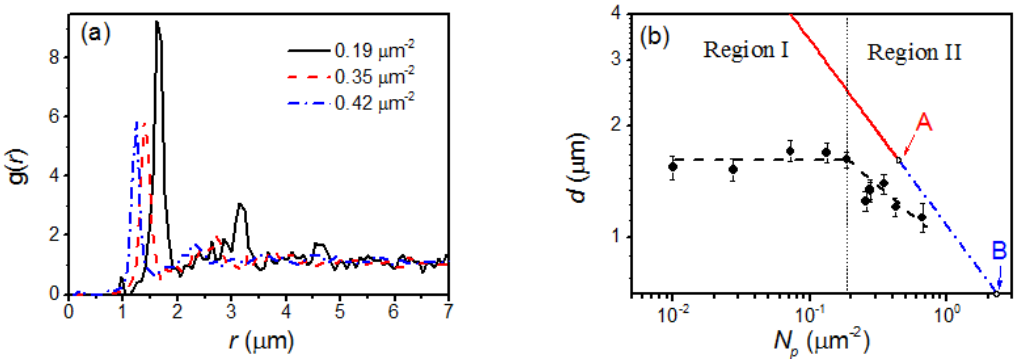

Figure 4.4 (a) The pair correlation function $g(r)$ of the microgels at the water/oil interface. $g(r)$ was calculated for $r \leqslant 11$ μm, and 1621, 5367 and 8050 pair distances were used for the calculation for the interfaces with microgel concentrations of 0.19 μm^{-2}, 0.35 μm^{-2} and 0.42 μm^{-2}, respectively. (b) Position of the first peak in $g(r)$ (mean nearest-neighbor distance, d) *vs.* the interface concentration of microgels (N_p). The red solid and blue dash-dotted curves show the inter-microgel distance when the microgels would be non-deformable and arranged in a hexagonal array. Points A and B represent the onset of an overlap of the shells according to the shell diameter of microgels at interface (A) and the hydrodynamic diameter in water (B).

We quantified the inter-microgel separation using the pair correlation function $g(r)$. $g(r)$ measures the probability of finding a microgel at a distance r from any given microgel at the interface. The first peak in $g(r)$ characterizes the mean nearest-neighbor dis-

tance. This mean nearest-neighbor distance was a function of microgel concentration at the interface (Fig. 4.4b). For low concentrations, the mean nearest-neighbor distance was almost independent of interface concentration of microgels (Region I in Fig. 4.4b). However, when the microgel concentration was high, the inter-microgel distance decreased with increasing concentration (Region II in Fig. 4.4b), even though the microgel concentration at the interface was still lower than expected from a hexagonal close-packed structure of flattened microgels at the interface (point A in Fig. 4.4b).

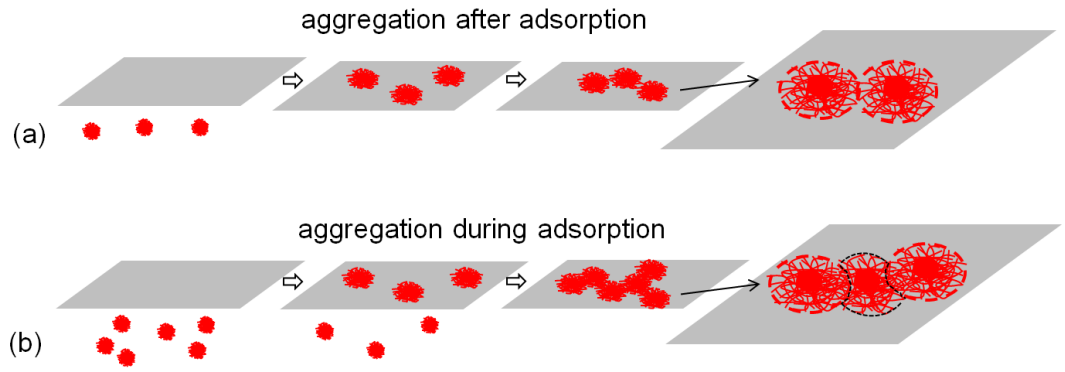

Figure 4.5 Scheme of aggregation of microgels at the interface. (a) At low microgel concentration, the microgels were first adsorbed onto the interface. The microgels had time to deform and spread at interface to form the core-shell structure before they aggregated. In the aggregation state, the inter-microgel distance was given by a balance between the attraction force (e.g., capillary force) and the repulsive force due to the overlap of the shells. The red dashed circles in the right (enlarged) scheme indicate the borders of the two completely spreading microgels. (b) At high microgel concentration, when the microgels were adsorbed onto the interface, the local interface could already be occupied by other microgels. The spread of polymer to form the shells was limited. For example, in the enlarged scheme the middle microgel only spread to the borders of its neighbors and did not spread completely, as indicated by the black dashed line.

We propose a mechanism as sketched in Fig. 4.5 to rationalize the two regions in Fig. 4.4b. In the low concentration region, the microgels were first adsorbed onto the interface and spread there to the assumed flattened shape. Thereafter they diffused at the 2D interface and the long-range attraction force (e.g., capillary force) drove them to aggregate. In the aggregation state, the inter-microgel distance was given by the balance between this attraction force and the repulsive force due to the overlap of polymer network in the shells of the microgels. However, at high concentration, when the microgels were adsorbed onto the interface, the local interface could already be occupied by other microgels. When adsorbing into holes of the existing structure, the spread of the freshly adsorbed microgels could be hindered by the limited space in between the already adsorbed microgels. This would lead to a decreased spread of the freshly adsorbed microgels and consequently to a lower mean inter-microgel distance (region II of Fig. 4.4b). In the following part we will show that a shorter inter-microgel distance is actually energetically

preferable.

4.3.3 Ageing of the structure formed at the interface

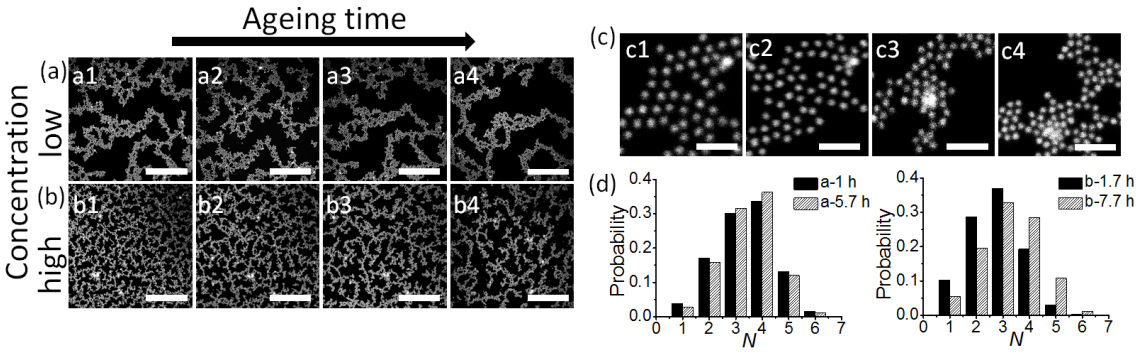

Figure 4.6 Microgels at the water/oil interface after different ageing times. The microgel concentrations at the interface were (a) 0.13–0.14 μm^{-2} and (b) 0.26–0.29 μm^{-2}. During ageing some additional microgels were adsorbed at the interface, increasing slightly the interface concentration. The ageing time for (a1, a2, a3, a4) is 1 h, 2 h, 2.7 h and 5.7 h, respectively. The ageing time for (b1, b2, b3, b4) is 1.7 h, 2.7 h, 3.9 h and 7.7 h, respectively. (c1, c2, c3, c4) show the detailed microgel arrangement for (a1, a4, b1, b4). The same positions of the interfaces are shown as indicated by the brighter microgels. (d) gives the probability for the number of nearest neighbors. More than 1700 microgels were used for the statistics. The scale bars are 50 μm in (a, b) and 5 μm in (c).

The structure of microgels at the water/oil interface evolved over time (Fig. 4.6). The topology became denser (less ramified) and the voids between the microgel network grew larger during ageing. In Fig. 4.6b some of the clusters disconnected from the system spanning network with increasing ageing time. The microstructures in Fig. 4.6c show that the local order stayed at a similar level during ageing. Fig. 4.6d reveals that after ageing, the microgels were on average surrounded by more neighbors. For both concentrations in Fig. 4.6, the inter-microgel separation decreased during ageing (Fig. 4.7). These results imply that the structure formed by the microgels at the interface evolved spontaneously during ageing.

The ageing behavior of the microgel-laden interface has been studied by using pendant drop tensiometry.[11] Deshmukh et al. suggested that at short times, the adsorption process is controlled by the diffusion of the microgels from bulk to the interface. At long times, the interface gets filled with microgels and thereby a barrier for further microgel adsorption at the interface is created. Li et al. suggested that after the microgels are adsorbed onto the interface, the deformation and spread of the microgels at the interface is a slow process.[14] Here, we resolve single microgels at the interface. We find that even without external compression or significant addition of microgels to the interface, the microgels approach on average spontaneously during ageing. Note that this ageing phenomenon is

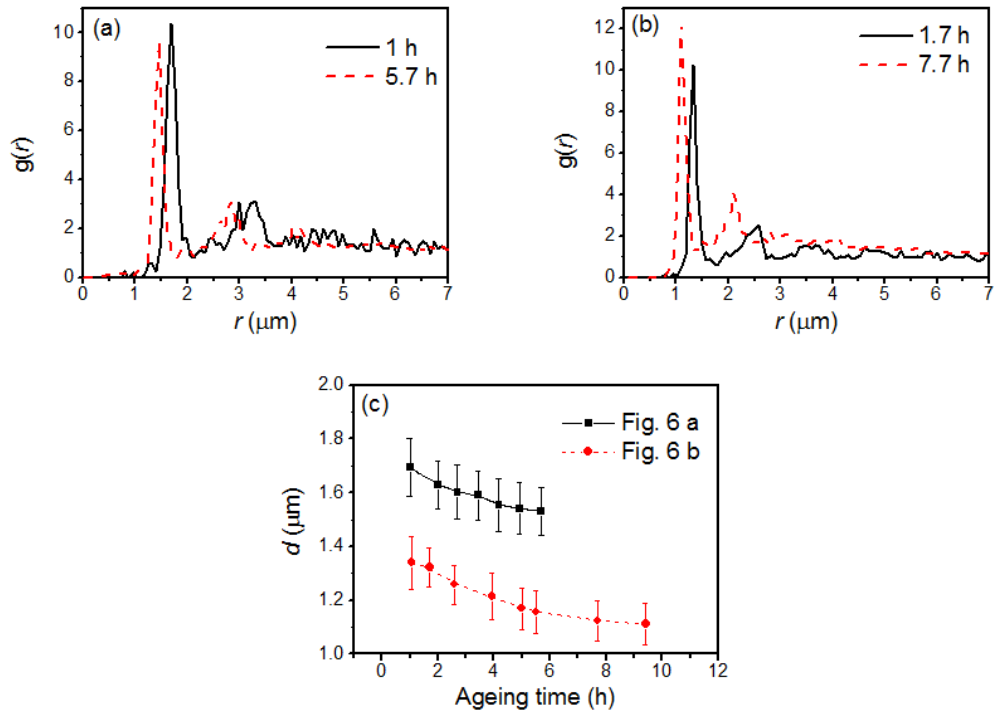

Figure 4.7 (a, b) Pair correlation function $g(r)$ of the microgels at water/oil interface during ageing. More than 6000 pair distances were used to calculate $g(r)$ for $r \leqslant 11$ μm. (a, b) correspond to Fig. 4.6a, b. (c) The mean nearest-neighbor distance (d) *vs*. ageing time.

rather general for microgels at interfaces and not specific to our water/oil interface, e.g., it is also observed at the water/air interface (Fig. 4.15, Supporting Information).

The origin of the ageing behavior of the microgels at water/oil (or water/air) interface is still unclear. On the one hand, the decrease of the inter-microgel separation may result from the change of morphology (i.e., spreading at the interface, protruding into the oil phase) of the microgels at the interface. For solid particles, Kaz et al. have reported that the adsorption of polystyrene microspheres from water to a water/oil interface is very slow (complete equilibration may take months).[49] The slow dynamics is ascribed to activated hopping of the contact line over nanoscale surface heterogeneities on the particle. Compared to solid particles at interface, the dynamic wetting behavior of soft particles at interface is even more complicated due to their deformability and structural complexity.[14] In addition, recent experimental results show that the microgels and their constituting polymer (e.g., PNIPAM) have similar surface activity.[3,9] For linear PNIPAM adsorbed at the water/air interface, a thin layer of polymer with a thickness of 1.5 nm is formed. This layer has a low water content which approximately equal to phase-separated PNIPAM above the LCST.[50] A collapsed PNIPAM layer (e.g., above LCST) can behave like soft glassy material, slowly evolving with time.[51] For the microgels at the interface, a similar polymer layer formed by PNIPAM with slower dynamics may exist and contribute to the slow ageing behavior. According to a recent theoretical study by Mehrabian et.

al.,[52] the thin polymer layer around the microgels is probably due to the adsorption of free polymer chains (i.e., the chains that are not cross-linked) inside the microgels to the interface.

On the other hand, the fact that the interparticle separation between microgels at interface decreases over time may result from the interaction between neighboring microgels. As the driving force for spreading/deforming the microgels at the interface is the interfacial tension,[14] it should depend strongly on the local polymer concentration at the interface. If a microgel at the interface is surrounded by other microgels, and the shells of the microgels can interpenetrate,[3] this driving force to spread may decrease. As a result, the deformed crosslinked polymer network in the microgels may shrink accordingly, leading to the decrease of inter-microgel separation.

4.3.4 Response to lateral forces

By introducing superparamagnetic beads at the water/oil interface, lateral forces can be applied on the microgel assemblies at the interface (see the sketch in Fig. 4.8a; here the overall interface concentration of microgels is lower than 0.2 μm^{-2}). Without a magnetic field, the magnetic beads have no magnetic interaction. Under a magnetic field, the magnetic beads can be polarized along the magnetic direction and act approximately as magnetic dipoles.[53] When the magnetic beads align along the external magnetic field direction (e.g., the configuration shown in Fig. 4.8a), the resulting magnetic dipoles are attractive. This magnetic attraction force between the magnetic beads can compress the microgels between them laterally. We focused on the magnetic bead pairs (with microgels between the beads) with a typical center-to-center distance of 6-18 μm. We first increased the magnetic field from 0 mT to 100.8 mT in 5 steps ($\sim$ 10 min/step, quasi-static), and recorded images containing the magnetic beads and the microgels for each step, see Fig. 4.8b. The magnetic attraction force (F_{mag}) between the two magnetic beads was calculated based on the magnetization curve and the center positions of the beads (Eq. (4.2) and Fig. 4.3, see Supporting Information). At equilibrium F_{mag} was balanced by the repulsive force from the microgels (e.g., a soft repulsive force due to overlap of the shells of the microgels).[7,54] The calculated F_{mag} for the sample shown in Fig. 4.8b is plotted in Fig. 4.8c as a function of center-to-center distance (L) between the two magnetic beads. When the magnetic field was increased, the magnetic attraction between the magnetic beads (i.e., the compression force acting on the microgels between the beads) became stronger. This led to the decrease of L (see Fig. 4.8b, and Points A $\rightarrow$ F in Fig. 4.8c). The force-displacement response was nonlinear (detailed discussion is given in Fig. 4.18, see Supporting Information). Meanwhile, under compression, the microgels were squeezed and expelled out from the space between the magnetic beads (one example of the displacements of the microgels during compression is shown in Fig. 4.16, see Supporting Information). After increasing the magnetic field to 100.8 mT, we removed

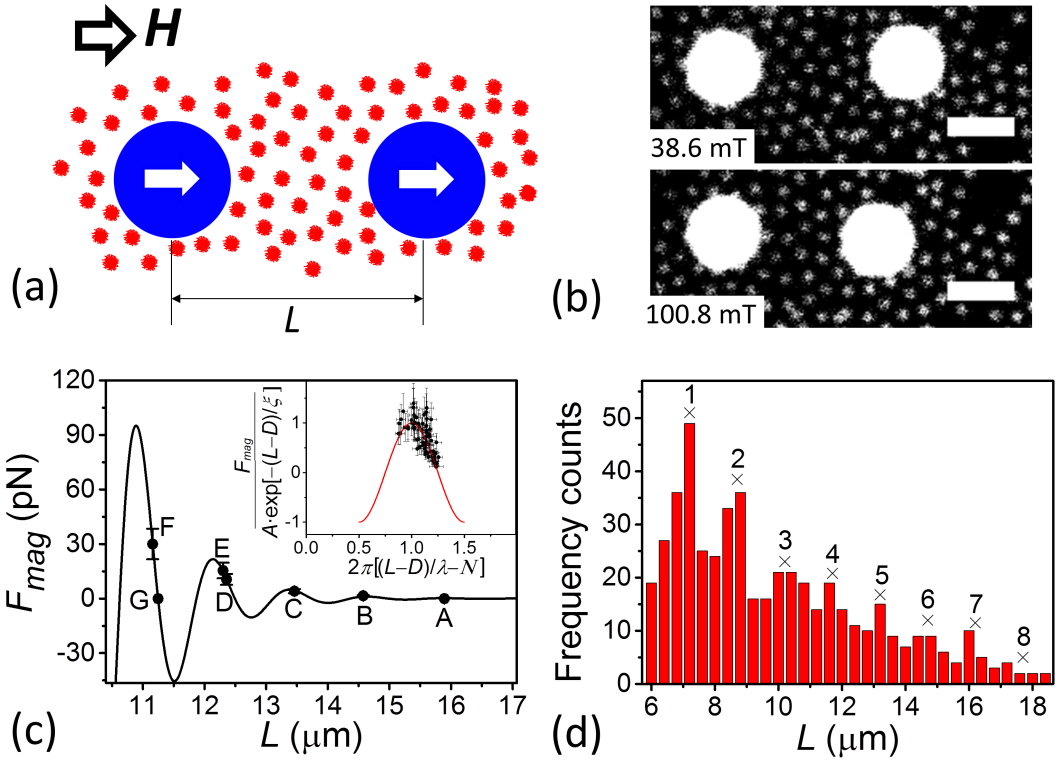

Figure 4.8 (a) Lateral compression of microgel assembly (red particles) at the water/oil interface by magnetic beads (blue particles). Under a horizontal magnetic field (***H***), the magnetic beads act as magnetic dipoles (indicated by the white arrows). The resulting attraction force between the magnetic beads can compress the microgels between them. L is the center-to-center distance between the magnetic beads. (b) LSCM images of magnetic beads (large white spots) and microgels (small white spots) at the water/oil interface, showing that L decreases when the magnetic field is increased. The scale bar is 5 μm. The corresponding magnetic attraction force (F_{mag}) is plotted (black circles with error bars) as a function of L in (c). The magnetic field was changed stepwise ($\sim$ 10 min/step) following the sequence: 0 mT (Point A), 26.4 mT (Point B), 38.6 mT (Point C), 60.2 mT (Point D), 80.5 mT (Point E), 100.8 mT (Point F), and 0 mT (Point G). The solid curve represents an oscillatory force profile using Eq. (4.1) with $A = 1.5\times10^5$ pN, $\xi = 0.84$ μm, $\lambda = 1.25$ μm and $D = 4.7$ μm. The inset shows $F_{mag}/[A\cdot e^{-(L-D)/\xi)}]$ *vs.* $2\pi[(L-D)/\lambda - N]$ for 20 different compression measurements, where the integer N is a shift factor to shift all the oscillations into a single sinusoidal cycle. (d) Histogram showing the distribution of center-to-center distances for 477 arbitrarily selected magnetic bead pairs under zero magnetic fields. The cross points indicate the positions where $L = (5.7 + n\cdot 1.5)$ μm, where n is an integer given on top of the cross points.

the magnetic field (Points F $\rightarrow$ G in Fig. 4.8c). L only slightly increased and it was significantly smaller than its original value before compression (Point A in Fig. 4.8c). Qualitatively, it can be concluded that the deformation of the microgel assemblies under lateral compression by magnetic beads is plastic, and some elastic recovery can also be observed during unloading.

In order to better understand the force response of the microgel assemblies under compression by magnetic beads, we examined the center-to-center distances of 477 arbitrarily selected magnetic bead pairs (with microgels between the beads) under zero magnetic field. The distribution of the center-to-center distances of the magnetic bead pairs is shown in Fig. 4.8d. Interestingly, the histogram shows discrete peaks with peak-to-peak separation close to the typical inter-microgel spacing (i.e., 1.5 μm, see Fig. 4.4b). This phenomenon is reminiscent of stratification (i.e., step-wise thinning) of thin liquid films.[55–58] For example, Nikolov et. al. reported that a thinning film of aqueous dispersion of polystyrene latex nanoparticles changed its thickness with regular step-wise jump transitions, with the average jump of a step equal to the particle diameter.[58] The stratification can be understood by a layer-by-layer thinning of ordered structures of colloidal particles formed inside the film.[55,58] For microgel assemblies at the water/oil interface between the magnetic beads, the layer-by-layer thinning behavior can be observed directly in experiment (e.g., Fig. 4.16), and it is also demonstrated by the discrete peaks in the histogram of center-to-center distances of magnetic beads (confining the microgels) in Fig. 4.8d.

It is well known that a thin film of molecules (or colloidal particles) under confinement by two surfaces can show oscillatory forces when the two surfaces approach, reflecting the oscillatory density profile, that is, the formation of layers of molecules (or colloidal particles) parallel to the surfaces.[55–57] With the decrease of film thickness, the layers of molecules (or colloidal particles) are pressed out one after another, leading to alternating repulsion and attraction.[59] According to the step-wise thinning behavior of the microgels between the magnetic beads, an oscillatory force F from the microgels (at equilibrium this force is balanced by F_{mag}) can be expected during the approach of the magnetic beads:[55]

$$F_{(L-D)} = A \cdot e^{-\frac{L-D}{\xi}} \cos(2\pi \frac{L-D}{\lambda}), \tag{4.1}$$

where A is the amplitude, ξ the decay length and λ the period of the force oscillation. $(L-D)$ is the surface-to-surface distance between the magnetic beads, where $D \sim 4.7$ μm (mean diameter of the magnetic beads). An oscillatory force profile which fits the experimental data well is shown in Fig. 4.8c. It shows that when two magnetic beads approach and compress the microgels between them, F_{mag} should overcome the local maximum of the oscillatory forces. After approaching, if the magnetic field is removed, the magnetic beads will go to the local equilibrium position (e.g., from Point F to Point G) instead of recovering to the original position (point A). Note that using the experimental configuration illustrated in Fig. 4.8a, we can only apply compression force to the microgel assemblies, thus only the repulsive force from the microgels (balanced by the attractive magnetic force between the magnetic beads) can be detected. For similar compression measurements, the $F_{mag}(L)$ curves can collapse on a single master curve in the plot of $F_{mag}/[A \cdot e^{-(L-D)/\xi}]$ *vs.* $2\pi[(L-D)/\lambda - N]$, where the integer N (N = 0, 1, 2...) is used to shift the oscillations into a single sinusoidal cycle, see the inset of Fig. 4.8c. The parameters of Eq. (4.1)

have the typical values: $A = 1.5 \times 10^5$ pN, $\xi = 0.66 \pm 0.29$ μm, $\lambda = 1.55 \pm 0.41$ μm and $D = 4.61 \pm 0.46$ μm (the least-squares method was used for fitting Eq. (4.1) to the experimental results, and the deviations were obtained from 20 compression measurements). The period of the force oscillation λ is close to the inter-microgel spacing and it is also consistent with the peak-to-peak separation shown in Fig. 4.8d. The amplitude A is related to the interaction between the microgels, and the decay length ξ reflects how far the ordering of microgels correlates.[56] Even thought a systematic study of these parameters is outside the scope of this paper, they might be useful for studying the interaction and ordering of microgels at interfaces.

In addition, from the images in Fig. 4.8b (also Fig. 4.16, see Supporting Information) it is clear that the shells of the microgels (dark regions around the white cores of the microgels) can transmit the stress. This is due to the fact that the shells of microgels at the interface consist of weakly cross-linked polymer chains which can show an elastic response to a certain degree. The morphology (i.e., the "fried egg-like" structure) of the microgels at the interface may also change under compression.[3] However, within our optical resolution we cannot resolve this morphology change due to the compression force by the magnetic beads.

We also used magnetic beads to shear the microgel layer at the water/oil interface (Fig. 4.9, Movies S4-2–S4-4 in the Supporting Information). Fig. 4.9a shows that a magnetic dumbbell (formed by two beads) at the interface was oriented horizontally. After the magnetic field was rotated counterclockwise by 25°, the magnetic dumbbell followed the rotation (Fig. 4.9b, Movie S4-2 in the Supporting Information). The resulting deformation field in the microgel layer is displayed in Fig. 4.9c. It is evident that the microgels around the magnetic dumbbell followed its rotation (the left lower part in Fig. 4.9c shows a different deformation due to the presence of other magnetic beads at the interface out of the view field).

The deformation of the microgel layer in the vicinity of the magnetic dumbbell propagated over a distance of about 15 μm (Fig. 4.9c), indicating that the microgel-microgel bonds was able to transmit the shear stress. From a microscopic point of view, the microgels tended to be connected to the neighboring microgels and move cooperatively. During deformation the microgel-microgel bonds were not permanently connected. Instead, some bonds were broken and new bonds were formed. This structural rearrangement would lead to a plastic deformation of the microgel layer. Another example where the microgels show cooperative motion and structural rearrangement is a porous microgel layer under shear (Movie S4-3 in the Supporting Information).

The responses of microgels at the water/oil interface under shear should result from the inter-microgel interactions. Due to the attraction force between microgels, the microgel-microgel bonds can withstand a stretching force up to about 2 pN (Fig.4.14, Supporting Information), and an even higher compression force (Fig. 4.8c). These bonds connect the

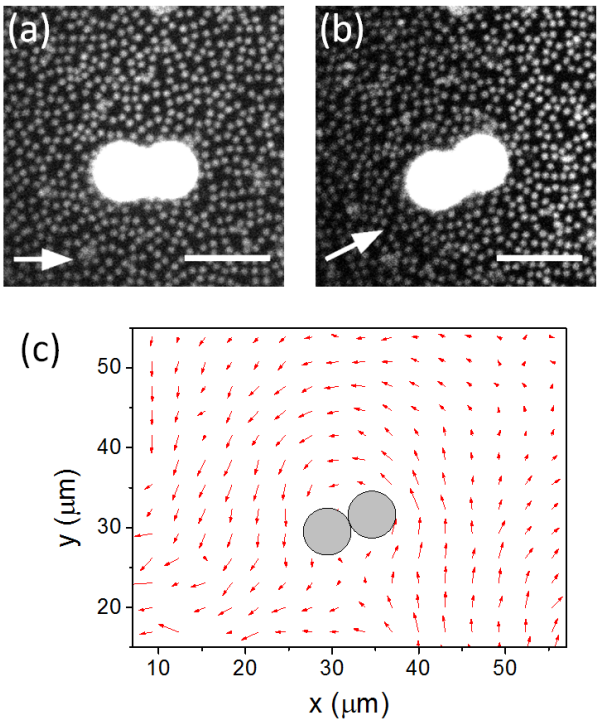

Figure 4.9 (a, b) Shearing the microgel-loaded interface by a magnetic dumbbell. A magnetic field (indicated by the arrow) of 216 mT was applied along the interface and rotated counterclockwise (stepwise, 2.5°/step, 3.5 min/step). The microgel concentration at the interface is 0.58 μm^{-2}. The scale bar is 10 μm. (c) The deformation field in the microgel layer triggered by the rotated magnetic dumbbell (a $\rightarrow$ b, 25°). The top-bottom asymmetry in the deformation field is due to neighboring magnetic beads out of the view field. The full movie can be found in the Supporting Information (Movie S4-2).

microgels, leading to the cooperative motion of the microgels under shear. Additionally, as shown in Fig. 4.2 and Movie S4-1 in the Supporting Information, the microgels in the aggregated structures can rearrange even without external excitation. Such an easy rearrangement of microgels in the aggregated structure is probably due to the fact that by rearrangement the microgels only change neighbors, i.e., the old bonds are replaced by the new ones, therefore the total energy of the aggregated structure does not change significantly by rearrangement. For these reasons the microgel layer can significantly rearrange under shear (e.g., Movie S4-3 in the Supporting Information). From these microscopic studies, we expect that the microgel layer at the water/oil interface should have viscoelastic properties, i.e., the rearrangement of microgels contributes to the viscous property, while the deformation of the microgel-microgel bonds contributes to the elastic property. Indeed, in experiment we also observed some elastic responses. For example, after shearing the microgel layer by the magnetic beads, if the magnetic field was removed, some short magnetic chains rotated back for a certain angle (see Movie S4-4 in the Supporting Information).

4.4 Conclusion

We followed the temporal evolution of microgels at the water/oil interface using confocal microscopy. Microgels at the water/oil interface have a tendency to aggregate. Their interaction is weak enough that the formed cluster are able to reorganize. As the interaction between the microgels at the interface is long-range and the pair interaction potential drops off as $1/r^{(4.0\pm0.7)}$ (r is the inter-microgel separation), we suggest that the capillary force dominates the aggregation. The inter-microgel distance after aggregation is suggested to be a balance of this attraction force and the repulsive force due to the overlap of the shells of microgels at the interface. The microgels at the water/oil interface can form different structures depending on the local microgel concentration. At low concentration they form isolated domains, while at high concentration they form fractal-like percolated structures. From studies on Pickering foams stabilized with non-deformable silica particles it is known that those fractal-like percolated networks can increase the stability of the interface enormously.[60]

Different to the widely accepted picture that the microgels tend to form hexagonal structure at the interface, our results point out that the structure of the microgel layer at the interface is strongly dependent on the adsorption kinetics and the history of the interface. The inter-microgel distance in the aggregated structure is dependent on the local microgel concentration at the interface. We propose that this dependency is due to different aggregation processes: aggregation after adsorption at the interface (at low microgel concentrations) and aggregation during adsorption (at high microgel concentrations). Without external compression or an excess of microgels in the aqueous phase, the aggregated structure of the microgels at the interface becomes denser and the inter-microgel distance decreases over time. This ageing behavior might have an implication on the long time stability of emulsions stabilized by microgels. Using superparamagnetic beads we can compress and shear the microgel layer at the interface. Under compression, the deformation of the microgel layer is mainly plastic due to the rearrangement of the microgels. However, some elastic recovery can also be observed after unloading. Our results also indicate that the microgel assemblies at the interface show the step-wise thinning behavior (stratification) under the lateral compression by magnetic beads. Under shear, the microgels move cooperatively and structural rearrangement is present. These microrheological studies may help to understand the macroscopic viscoelastic property and stability of the microgel-laden interfaces.

4.5 Acknowledgement

The authors acknowledge the Deutsche Forschungsgemeinschaft (DFG) via the priority program SPP 1681 "Feldgesteuerte Partikel-Matrix-Wechselwirkungen" (SH and GKA

acknowledge the project AU321/3-1; KG and RvK acknowledge the project KL1165/16; JN and SO acknowledge the project OD18/21). LG acknowledges financial support by the DFG via the priority program SPP 1486 "Particles in Contact". JN and SO acknowledge support by the DFG in the framework of the Research Training Group 1865 “Hydrogel-based Microsystems”. Judith Witte is acknowledged for ζ potential measurements of the p-NIPAM-co-AG microgels.

Bibliography

[1] Ramsden, W. Separation of Solids in the Surface-Layers of Solutions and ‘Suspensions’ (Observations on Surface-Membranes, Bubbles, Emulsions, and Mechanical Coagulation).–Preliminary Account. *Proc. R. Soc. London* **1903**, *72*, 156–164.

[2] Pickering, S. U. CXCVI. Emulsions. *J. Chem. Soc. Trans.* **1907**, *91*, 2001.

[3] Pinaud, F.; Geisel, K.; Masse, P.; Catargi, B.; Isa, L.; Richtering, W.; Ravaine, V.; Schmitt, V. Adsorption of Microgels at an Oil-Water Interface: Correlation between Packing and 2D Elasticity. *Soft Matter* **2014**, *10*, 6963–6974.

[4] Noskov, B. A.; Latnikova, A. V.; Lin, S. Y.; Loglio, G.; Miller, R. Dynamic Surface Elasticity of Beta-casein Solutions during Adsorption. *J. Phys. Chem. C* **2007**, *111*, 16895–16901.

[5] Noskov, B. A.; Akentiev, A. V.; Bilibin, A. Y.; Grigoriev, D. O.; Loglio, G.; Zorin, I. M.; Miller, R. Dynamic Surface Properties of Poly(N-isopropylacrylamide) Solutions. *Langmuir* **2004**, *20*, 9669–9676.

[6] Deshmukh, O. S.; van den Ende, D.; Cohen Stuart, M.; Mugele, F.; Duits, M. H. G. Hard and Soft Colloids at Fluid Interfaces: Adsorption, Interactions, Assembly and Rheology. *Adv. Colloid Interface Sci.* **2014**, *in press*.

[7] Geisel, K.; Richtering, W.; Isa, L. Highly Ordered 2D Microgel Arrays: Compression versus Self-assembly. *Soft Matter* **2014**, *10*, 7968–7976.

[8] Geisel, K.; Henzler, K.; Guttmann, P.; Richtering, W. New Insight into Microgel-Stabilized Emulsions Using Transmission X-ray Microscopy: Nonuniform Deformation and Arrangement of Microgels at Liquid Interfaces. *Langmuir* **2015**, *31*, 83–89.

[9] Cohin, Y.; Fisson, M.; Jourde, K.; Fuller, G. G.; Sanson, N.; Talini, L.; Monteux, C. Tracking the Interfacial Dynamics of PNiPAM Soft Microgels Particles Adsorbed at the Air-Water Interface and in Thin Liquid Films. *Rheol. Acta* **2013**, *52*, 445–454.

[10] Ngai, T.; Auweter, H.; Behrens, S. H. Environmental Responsiveness of Microgel Particles and Particle-stabilized Emulsions. *Macromolecules* **2006**, *39*, 8171–8177.

[11] Deshmukh, O. S.; Maestro, A.; Duits, M. H. G.; van den Ende, D.; Cohen Stuart, M.; Mugele, F. Equation of State and Adsorption Dynamics of Soft Microgel Particles at an Air-Water Interface. *Soft Matter* **2014**, *10*, 7045–7050.

[12] Destribats, M.; Eyharts, M.; Lapeyre, V.; Sellier, E.; Varga, I.; Ravaine, V.; Schmitt, V. Impact of PNIPAM Microgel Size on Its Ability to Stabilize Pickering Emulsions. *Langmuir* **2014**, *30*, 1768–1777.

[13] Geisel, K.; Henzler, K.; Guttmann, P.; Richtering, W. New Insight into Microgel-Stabilized Emulsions Using Transmission X-ray Microscopy: Nonuniform Deformation and Arrangement of Microgels at Liquid Interfaces. *Langmuir* **2014**, *31*, 83–89.

[14] Li, Z. F.; Geisel, K.; Richtering, W.; Ngai, T. Poly(N-isopropylacrylamide) Microgels at the Oil-Water Interface: Adsorption Kinetics. *Soft Matter* **2013**, *9*, 9939–9946.

[15] Monteux, C.; Marliere, C.; Paris, P.; Pantoustier, N.; Sanson, N.; Perrin, P. Poly(N-isopropylacrylamide) Microgels at the Oil-Water Interface: Interfacial Properties as a Function of Temperature. *Langmuir* **2010**, *26*, 13839–13846.

[16] Li, Z. F.; Richtering, W.; Ngai, T. Poly(N-isopropylacrylamide) Microgels at the Oil-Water Interface: Temperature Effect. *Soft Matter* **2014**, *10*, 6182–6191.

[17] Richtering, W. Responsive Emulsions Stabilized by Stimuli-Sensitive Microgels: Emulsions with Special Non-Pickering Properties. *Langmuir* **2012**, *28*, 17218–17229.

[18] Wiese, S.; Spiess, A.; Richtering, W. Microgel-Stabilized Smart Emulsions for Biocatalysis. *Angew. Chem.* **2013**, *125*, 604–607.

[19] Dickinson, E. Microgels-An Alternative Colloidal Ingredient for Stabilization of Food Emulsions. *Trends Food Sci. Technol.* **2015**, *43*, 178–188.

[20] Kratz, K.; Eimer, W. Swelling Properties of Colloidal Poly(N-Isopropylacrylamide) Microgels in Solution. *Ber. Bunsenges. Phys. Chem.* **1998**, *102*, 848–854.

[21] Dingenouts, N.; Norhausen, C.; Ballauff, M. Observation of the Volume Transition in Thermosensitive Core-Shell Latex Particles by Small-Angle X-ray Scattering. *Macromolecules* **1998**, *31*, 8912–8917.

[22] Senff, H.; Richtering, W. Temperature Sensitive Microgel Suspensions: Colloidal Phase Behavior and Rheology of Soft Spheres. *J. Chem. Phys.* **1999**, *111*, 1705–1711.

[23] Robert, P. Temperature-sensitive Aqueous Microgels. *Adv. Colloid Interface Sci.* **2000**, *85*, 1–33.

[24] Burmistrova, A.; Richter, M.; Uzum, C.; von Klitzing, R. Effect of Cross-linker Density of P(NIPAM-co-AAc) Microgels at Solid Surfaces on the Swelling/shrinking Behaviour and the Young's Modulus. *Colloid Polym. Sci.* **2011**, *289*, 613–624.

[25] Burmistrova, A.; Richter, M.; Eisele, M.; Üzüm, C.; von Klitzing, R. The Effect of Co-monomer Content on the Swelling/shrinking and Mechanical Behaviour of Individually Adsorbed PNIPAM Microgel Particles. *Polymers* **2011**, *3*, 1575–1590.

[26] Massé, P.; Sellier, E.; Schmitt, V.; Ravaine, V. Impact of Electrostatics on the Adsorption of Microgels at the Interface of Pickering Emulsions. *Langmuir* **2014**, *30*, 14745–14756.

[27] Destribats, M.; Lapeyre, V.; Wolfs, M.; Sellier, E.; Leal-Calderon, F.; Ravaine, V.; Schmitt, V. Soft Microgels as Pickering Emulsion Stabilisers: Role of Particle Deformability. *Soft Matter* **2011**, *7*, 7689–7698.

[28] Geisel, K.; Isa, L.; Richtering, W. Unraveling the 3D Localization and Deformation of Responsive Microgels at Oil/Water Interfaces: A Step Forward in Understanding Soft Emulsion Stabilizers. *Langmuir* **2012**, *28*, 15770–15776.

[29] Monteillet, H.; Workamp, M.; Appel, J.; Kleijn, J. M.; Leermakers, F. A. M.; Sprakel, J. Ultrastrong Anchoring Yet Barrier-Free Adsorption of Composite Microgels at Liquid Interfaces. *Adv. Mater. Interfaces* **2014**, *1*, 1300121.

[30] Geisel, K.; Isa, L.; Richtering, W. The Compressibility of pH-Sensitive Microgels at the Oil-Water Interface: Higher Charge Leads to Less Repulsion. *Angew. Chem.* **2014**, *126*, 5005–5009.

[31] Brugger, B.; Rütten, S.; Phan, K.; Möller, M.; Richtering, W. The Colloidal Suprastructure of Smart Microgels at Oil-Water Interfaces. *Angew. Chem., Int. Ed.* **2009**, *48*, 3978–3981.

[32] Brugger, B.; Vermant, J.; Richtering, W. Interfacial Layers of Stimuli-responsive Poly-(N-isopropylacrylamide-co-methacrylicacid)(PNIPAM-co-MAA) Microgels Characterized by Interfacial Rheology and Compression Isotherms. *Phys. Chem. Chem. Phys.* **2010**, *12*, 14573–14578.

[33] Mendoza, A. J.; Guzmán, E.; Martínez-Pedrero, F.; Ritacco, H.; Rubio, R. G.; Ortega, F.; Starov, V. M.; Miller, R. Particle Laden Fluid Interfaces: Dynamics and Interfacial Rheology. *Adv. Colloid Interface Sci.* **2014**, *206*, 303–319.

[34] Bouchama, F.; Di Meglio, J. Two-dimensional Rheology of Soap Films. *J. Phys.: Condens. Matter* **1996**, *8*, 9525–9529.

[35] Reynaert, S.; Brooks, C. F.; Moldenaers, P.; Vermant, J.; Fuller, G. G. Analysis of the Magnetic Rod Interfacial Stress Rheometer. *J. Rheol.* **2008**, *52*, 261–285.

[36] Meng, Z.; Smith, M.; Lyon, L. Temperature-programmed Synthesis of Micron-sized Multi-responsive Microgels. *Colloid Polym. Sci.* **2009**, *287*, 277–285.

[37] Gawlitza, K.; Georgieva, R.; Tavraz, N.; Keller, J.; von Klitzing, R. Immobilization of Water-Soluble HRP within Poly-N-isopropylacrylamide Microgel Particles for Use in Organic Media. *Langmuir* **2013**, *29*, 16002–16009.

[38] Roth, M.; Franzmann, M.; D'Acunzi, M.; Kreiter, M.; Auernhammer, G. Experimental Analysis of Single Particle Deformations and Rotations in Colloidal and Granular Systems. *arXiv preprint, arXiv:1106.3623* **2011**.

[39] Roth, M.; Schilde, C.; Lellig, P.; Kwade, A.; Auernhammer, G. K. Colloidal Aggregates Tested via Nanoindentation and Quasi-simultaneous 3D Imaging. *Eur. Phys. J. E.* **2012**, *35*, 124.

[40] Raich, H.; Blümler, P. Design and Construction of a Dipolar Halbach Array with a Homogeneous Field from Identical Bar Magnets: NMR Mandhalas. *Concepts Magn. Reson., Part B* **2004**, *23*, 16–25.

[41] Huang, S.; Pessot, G.; Cremer, P.; Weeber, R.; Holm, C.; Nowak, J.; Odenbach, S.; Menzel, A. M.; Auernhammer, G. K. Buckling of paramagnetic chains in soft gels. *Soft Matter* **2015**, DOI 10.1039/C5SM01814E.

[42] Sbalzarini, I. F.; Koumoutsakos, P. Feature Point Tracking and Trajectory Analysis for Video Imaging in Cell Biology. *J. Struct. Biol.* **2005**, *151*, 182–195.

[43] ImageJ, *http://imagej.nih.gov/ij/*.

[44] Ohtsuka, T.; Royall, C. P.; Tanaka, H. Local Structure and Dynamics in Colloidal Fluids and Gels. *Europhys. Lett.* **2008**, *84*, 46002.

[45] Nakahama, K.; Fujimoto, K. Thermosensitive Two-dimensional Arrays of Hydrogel Particles. *Langmuir* **2002**, *18*, 10095–10099.

[46] Stamou, D.; Duschl, C.; Johannsmann, D. Long-range Attraction between Colloidal Spheres at the Air-water Interface: The Consequence of an Irregular Meniscus. *Phys. Rev. E* **2000**, *62*, 5263.

[47] Lin, M. Y.; Lindsay, H. M.; Weitz, D. A.; Ball, R. C.; Klein, R.; Meakin, P. Universality in Colloid Aggregation. *Nature* **1989**, *339*, 360–362.

[48] Destribats, M.; Wolfs, M.; Pinaud, F.; Lapeyre, V.; Sellier, E.; Schmitt, V.; Ravaine, V. Pickering Emulsions Stabilized by Soft Microgels: Influence of the Emulsification Process on Particle Interfacial Organization and Emulsion Properties. *Langmuir* **2013**, *29*, 12367–12374.

[49] Kaz, D. M.; McGorty, R.; Mani, M.; Brenner, M.; Manoharan, V. N. Physical Ageing of the Contact Line on Colloidal Particles at Liquid Interfaces. *Nat. Mater.* **2012**, *11*, 138–142.

[50] Richardson, R. M.; Pelton, R.; Cosgrove, T.; Zhang, J. A Neutron Reflectivity Study of Poly (N-isopropylacrylamide) at the Air-water Interface with and without Sodium Dodecyl Sulfate. *Macromolecules* **2000**, *33*, 6269–6274.

[51] Guillermic, R.; Saint-Jalmes, A. Dynamics of Poly-nipam Chains in Competition with Surfactants at Liquid Interfaces: from Thermoresponsive Interfacial Rheology to Foams. *Soft Matter* **2013**, *9*, 1344–1353.

[52] Mehrabian, H.; Harting, J.; Snoeijer, J. H. Soft particles at a fluid interface. *arXiv preprint arXiv:1507.07540* **2015**.

[53] Wilhelm, C.; Browaeys, J.; Ponton, A.; Bacri, J. C. Rotational Magnetic Particles Microrheology: the Maxwellian Case. *Phys. Rev. E* **2003**, *67*, 011504.

[54] Garbin, V.; Jenkins, I.; Sinno, T.; Crocker, J. C.; Stebe, K. J. Interactions and Stress Relaxation in Monolayers of Soft Nanoparticles at Fluid-Fluid Interfaces. *Phys. Rev. Lett.* **2015**, *114*, 108301.

[55] Kind, M.; Peukert, W.; Rehage, H.; Schuchmann, H. P. *Colloid Process Engineering*; Springer, 2014.

[56] Zeng, Y.; Grandner, S.; Oliveira, C. L.; Thünemann, A. F.; Paris, O.; Pedersen, J. S.; Klapp, S. H.; von Klitzing, R. Effect of particle size and Debye length on order parameters of colloidal silica suspensions under confinement. *Soft Matter* **2011**, *7*, 10899–10909.

[57] Grandner, S.; Zeng, Y.; Klitzing, R. v.; Klapp, S. H. Impact of surface charges on the solvation forces in confined colloidal solutions. *J. Chem. Phys.* **2009**, *131*, 154702.

[58] Nikolov, A. D.; Wasan, D. T. Ordered micelle structuring in thin films formed from anionic surfactant solutions: I. Experimental. *J. Colloid Interface Sci.* **1989**, *133*, 1–12.

[59] Christov, N. C.; Danov, K. D.; Zeng, Y.; Kralchevsky, P. A.; von Klitzing, R. Oscillatory Structural Forces Due to Nonionic Surfactant Micelles: Data by Colloidal-Probe AFM vs Theory. *Langmuir* **2009**, *26*, 915–923.

[60] Carl, A.; Bannuscher, A.; von Klitzing, R. Particle Stabilized Aqueous Foams at Different Length Scales-Synergy between Silica Particles and Alkylamines. *Langmuir* **2015**, *31*, 1615–1622.

4.6 Supporting Information

4.6.1 Experimental section

4.6.1.1 Fabrication of oil-in-water emulsions

The oil-in-water emulsions were obtained by mixing 0.4 mL microgel/water suspension (0.1 wt%) and 0.1 mL low-molecular weight (770 g/mol) polydimethylsiloxane (PDMS, Alfa Aesar GmbH & Co. KG) with a Reax Control (Heidolph, Schwabach, Germany) at 2500 r/min for 1 min. Due to the fact that the oil had a lower density (0.92 g/cm^3) compared to water (1.00 g/cm^3), the oil droplets were accumulated at the top of the water phase. The emulsions were transferred onto a coverslip (thickness of $\sim$160 μm, Menzel-Gläser, Germany) and the internal structure of the emulsions was observed using a home-built laser scanning confocal microscope (LSCM).[1,2] The emulsion droplets were sticky to the coverslip, thus we could not resolve the interface structure of the emulsion droplets without optical disturbance close to the coverslip surface. We used the stickiness of the emulsion droplets to image them in a micro-fluidic channel. We allowed the emulsion droplets to immobilize on a coverslip and used this coverslip to cover a micro-fluidic channel. The height of the channel was set by spacer to $\sim$160 μm and the channel was filled with water. In this configuration, the bottom part of the emulsion droplets which were attached to the top of the channel could be imaged without optical disturbances.

In order to fabricate emulsion droplets with a high particle density at the interface, we first deposited the emulsion on top of a coverslip and allowed them to coalesce for about 1h in a sealed environment in order to limit evaporation. The total interfacial area of the emulsion droplets decreased and the microgel concentration at the interface increased. After this process we used the above-mentioned method to observe the surface structure of the emulsion droplets.

4.6.1.2 Tracking particle aggregation and diffusion at water/oil interface

A microgel/water suspension with a microgel concentration of 0.02 wt% was used. The sample configuration was the same with Fig. 4.1 of the main article. In order to have a fast recording speed, we used a microscope (Leica DMI6000B) combined with a high-speed camera (Photron, FASTCAM SA1). The videos were recorded with a recording rate of 500 frames per second at a resolution of 512$\times$512 pixels (0.2 μm/pixel). We used the 100$\times$/0.75 objective (LEICA). The phase contrast mode of the microscope was used in order to increase the contrast between the microgels and the water/oil interface. The trajectories of the microgels were then extracted using the IDL algorithm from Crocker, Grier, and Weeks.[3] For studying the aggregation kinetics, the inter-microgel separation (r) between two aggregating microgels (single before aggregation) was calculated based on the positions of the microgels. For studying the diffusive behavior of single microgels

at the water/oil interface, the trajectories (typically within 16 s) of single microgels were extracted and the mean square displacement (MSD) of the diffusing particles was calculated using the IDL algorithm from Crocker, Grier, and Weeks.[3] The background drift due to large-scale flow or microscope stage movement was eliminated before the calculation of MSD. Because in long experimental times the microgels formed clusters, the time for observing the aggregation and diffusion was typically within 40 min after preparation of the interface.

4.6.1.3 Ageing of microgels at water/air interface

The sample cell was fabricated by gluing a Teflon ring (inner diameter = 15 mm) to a microscope slide using a transparent mounting wax (Gatan GmbH, Germany). 200 μL microgel/water suspension (0.05 wt%) was added to the sample cell. The cell was covered with another microscope slide on top and sealed with grease (Glisseal ® N, Borer Chemie, Solothurn, Switzerland). The microgels at the water/air interface were observed using the microscope (Leica DMI6000B) and the images were recorded using the high-speed camera (Photron, FASTCAM SA1).

4.6.1.4 Algorithm for calculating the pair correlation function g(r)

The algorithm for calculating the pair correlation function g(r) from the confocal images includes the following steps: (1) The position data of the microgels can be obtained by using ImageJ software with a particle tracker plugin.[4,5] (2) Choose a distance range $[0, L]$ where the g(r) is calculated. (3) Divide $[0, L]$ into N equidistant bins (N is an integer). The distance step is $\Delta r = L/N$. (4) Loop over all the positions of the microgels, select the microgel pairs with an inter-microgel separation within $[0, L]$. (5) Count for each bin n (corresponding to an inter-microgel distance between $(n-1)\Delta r$ and $n\Delta r$) the number of microgel pairs that have the right inter-microgel distance. (6) Divide this particle count by the area $(2n-1)\pi\Delta r^2$. (7) Divide the calculated value by the number density of the microgels. The number density is calculated by dividing the count of microgel pairs within a separation of L by the area πL^2.

4.6.1.5 Calculation of the magnetic force

Without a magnetic field, the magnetic moment for the superparamagnetic beads is 0. However, when an external magnetic field is applied, the magnetic beads are magnetized along the external magnetic field direction. The magnetization (M) per unit mass of the magnetic beads under a certain magnetic field can be obtained from the magnetization curve (Fig. 4.10). The magnetic moment (m) for every bead is

$$m = \rho V M, \tag{4.2}$$

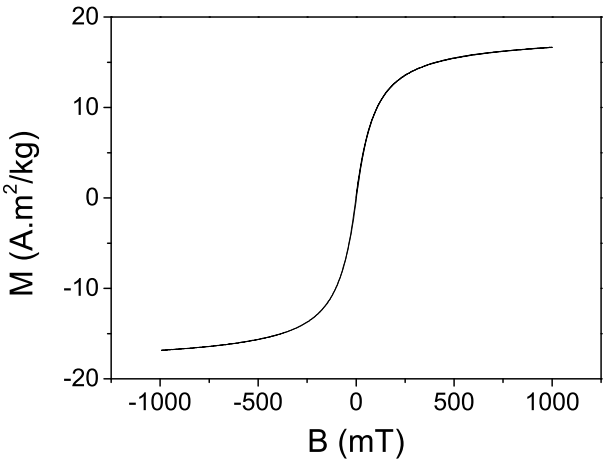

Figure 4.10 Magnetization curve of the magnetic beads showing a superparamagnetic behavior.

where ρ is the mass density (1.7 g/cm^3) and V is the volume of the bead (diameter = 4.7 $\pm$ 0.2 μm, according to manufacturer). The magnetic force ($\vec{F}_{mag}$) between two superparamagnetic beads is calculated using a dipole-dipole approximation[6]

$$\vec{F}_{mag} = \frac{3\mu_0 m^2}{4\pi R^4}[(3\cos^2\alpha - 1)\vec{r} + \sin(2\alpha)\vec{\theta}], \tag{4.3}$$

where R is the separation between two magnetic dipoles, m is the dipole moment for the two magnetic beads and μ_0 is the permeability of vaccum. α is the angle between the magnetic field and the vector connecting the two bead centers. $\vec{r}$ and $\vec{\theta}$ are the radial and tangential vectors.

4.6.2 Results and discussion

4.6.2.1 Assembly of microgels at the interface of emulsion droplets

Because the microgels were fluorescently labeled, they appeared bright in the LSCM image (Fig. 4.11a). It is evident that the microgels were located at the oil/water interface. The microgels were not closely packed at the interface of emulsion droplets (Fig. 4.11b). However, after the emulsion droplets coalesced, closely packed structures at the interface were formed (Fig. 4.11c), and some local ordered structures (e.g., hexagonal array) were observed (Fig. 4.11d).

4.6.2.2 Pair interaction potential

Fig. 4.12a shows the inter-microgel separation (r) of the aggregating microgel pairs as a function of time. The three curves present three different pairs. It can be seen that at large inter-microgel separation ($r > 3.2$ μm), even though the inter-microgel separation tends to decrease with time, it shows significant fluctuation. However, when the inter-microgel

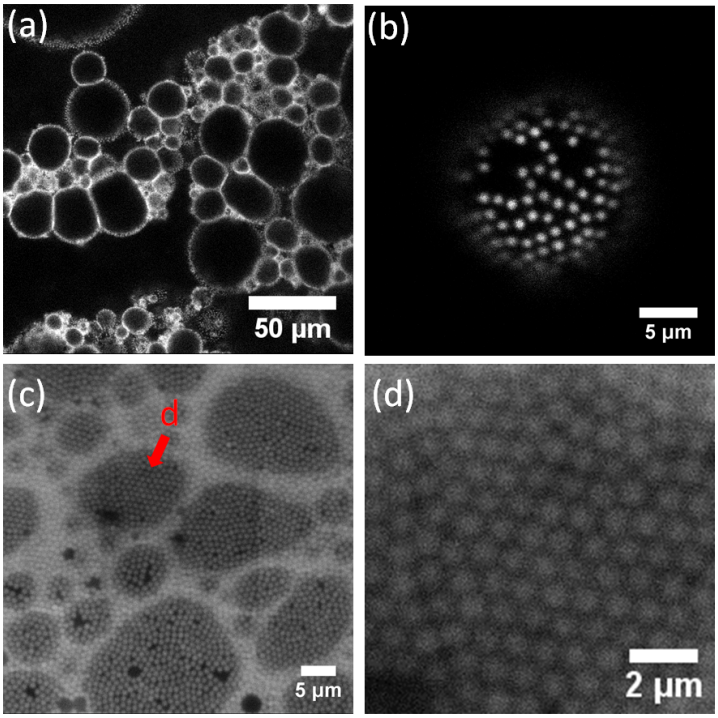

Figure 4.11 (a) LSCM image of oil-in-water emulsion droplets stabilized by microgels. The fluorescently labeled microgels appear bright in the LSCM image. (b) Typical interface structure of oil-in-water emulsion droplets stabilized by microgels. The diameter of this droplet is about 20 μm and this image shows the lower part of the droplet. (c) Interface structure of emulsion droplets after letting them coalesce for 1 h. The red arrow indicates the structure which is enlarged in (d).

separation is small ($r < 3.2$ μm), the inter-microgel separation decreases abruptly, indicating an strong attraction force (significantly larger than the thermal fluctuation). As shown in Fig. 4.12b, the inter-microgel separation can be approximately described as

$$r = A(t - t_{max})^B, \tag{4.4}$$

where A and B are the fitting parameters. In the following we will estimate the pair interaction potential based on Eq. (4.4).

The equation of motion for a microgel of mass m at the water/oil interface is[7]:

$$m\frac{d^2r}{dt^2} = F_{drag} + F_{inter} + F_{stoch}, \tag{4.5}$$

where F_{stoch} is the stochastic thermal force, F_{inter} is the interaction force and F_{drag} is the viscous drag force. Assuming that the microgel has a density of ~ 1000 kg/m^3, a diameter of ~ 1 μm and a typical $\frac{d^2r}{dt^2}$ of $\sim 5 \times 10^{-3}$ m/s^2 (the typical acceleration just before contact), the inertial term is in the order of 10^{-18} N, which is 6 order smaller than the interaction force (Fig. 4.14b). Thus the inertia term can be neglected. The F_{stoch} can also be neglected when the thermal fluctuation is small compared to the interaction force, i.e., when the inter-microgel separation is smaller than 3.2 μm. Thus the equation of

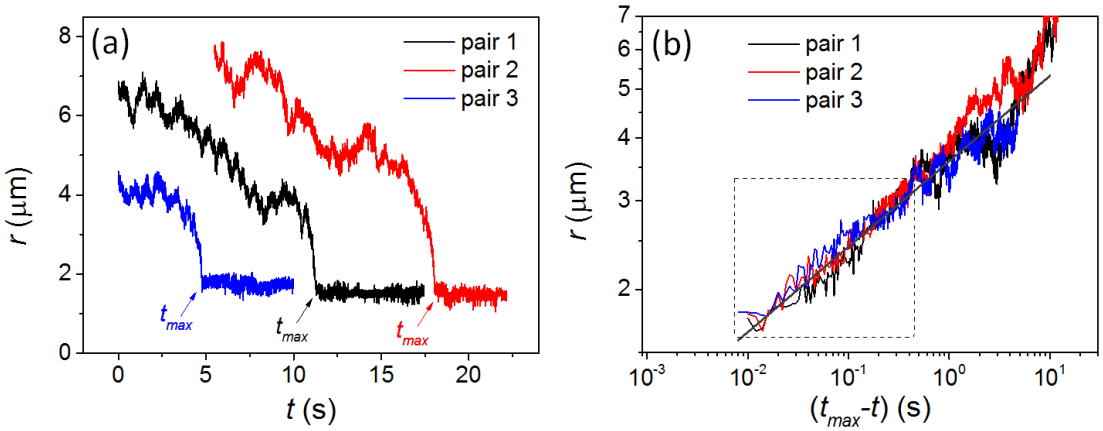

Figure 4.12 (a) Inter-microgel separation (r) as a function of time (t). The results for three different pairs of aggregating microgels are shown with different colours. t_{max} is the time when two microgels contact. (b) Log-log plot of inter-microgel separation as a function of relative time ($t_{max}-t$). The dash square indicates the data ($r < 3.2$ μm) used for fitting using Eq. (4.4). The straight solid line represents an example of the fit to Eq. (4.4).

motion becomes:

$$F_{inter} = -F_{drag}. \tag{4.6}$$

At the interface the drag force acting on a micrometer-sized particle is proportional to velocity (v)[7,8]

$$F_{drag} = -\xi v, \tag{4.7}$$

where ξ is the friction coefficient and v is the velocity. Because the morphology (i.e., the "fried egg-like" structure) of the microgel at the interface is unclear, we cannot compute the friction coefficient directly according to the geometry and the equilibrium wetting state.[7,8] Instead, we tracked the Brownian motion of about 100 single microgels at the interface (Fig. 4.13). As the Brownian motion is driven by the thermal energy k_BT and the thermal force is stochastic, the resulting mean displacement of the microgels over time is 0. However, the mean square displacement MSD ($\langle \Delta x^2(t) \rangle$) is proportional to the lag time (t):[9]

$$\langle \Delta x^2(t) \rangle = \langle x(t) - x(0) \rangle^2 = 2dDt, \tag{4.8}$$

where D is the diffusion coefficient and d is the dimension (here $d = 2$). The Einstein relation (or Einstein-Smoluchowski relation) relates this diffusive behavior to the friction coefficient[9–11]

$$D = \frac{k_BT}{\xi}. \tag{4.9}$$

Using Eq. (4.8) and the data shown in Fig. 4.13 we obtain $D = 0.08 \pm 0.02$ μm^2/s. In addition, using Eqs. (4.6, 4.7) the pair interaction potential as a function of inter-microgel separation r can be calculated:

$$U(r) = -\int_{\infty}^{r} F_{inter}\, dr = \xi \int_{\infty}^{r} v(r')\, dr'. \tag{4.10}$$

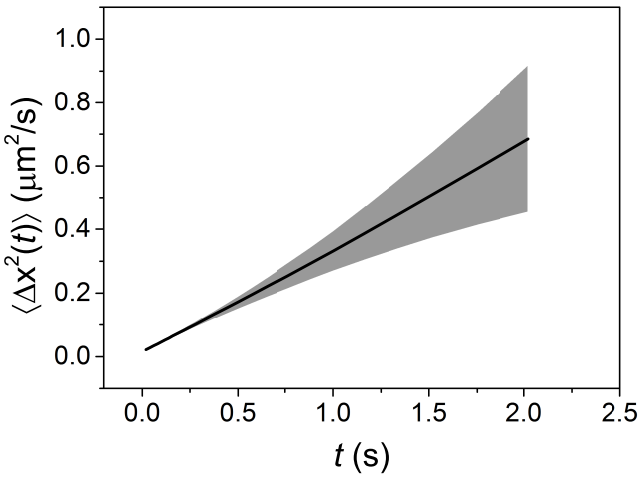

Figure 4.13 The mean square displacement ($\langle \Delta x^2(t) \rangle$) of microgels at the water/oil interface as a function of lag time (t). The solid line represents the mean values and the shaded area represents the error bars. About 100 single microgels were used for the statistics.

According to Eq. (4.4), $v = AB(\frac{r}{A})^{\frac{B-1}{B}}$, thus Eq. (4.10) becomes

$$U(r) = \frac{A^{1/B}B^2}{2B-1}\,\frac{k_BT}{D}\,r^{2-1/B}. \tag{4.11}$$

The interaction force is

$$F_{inter}(r) = -\frac{dU(r)}{dr} = -A^{1/B}\,B\,\frac{k_BT}{D}\,r^{1-1/B}. \tag{4.12}$$

A and B can be determined by fitting the experimental data to Eq. (4.4) (see Fig. 4.12b) for every aggregating microgel pair. Thus, the pair interaction potential as well as the interaction force can be estimated for every microgel pair. Fig. 4.14 shows the results for 20 aggregating microgel pairs. The interaction potential for two microgels at the equilibrium separation ($\sim 1.5\ \mu$m) is $-220 \pm 130\ k_BT$. This interaction potential explains why the microgels aggregate spontaneously and the microgels cannot leave the clusters by thermal fluctuation. The corresponding attraction force at this distance is 2.4 ± 1.3 pN (Fig. 4.14b). The mean interaction potential is equal to 1 k_BT when the inter-microgel separation is 6.3 μm, and it is 12 k_BT when the inter-microgel separation is 3.2 μm. That is the reason why the attraction force significantly dominates the movement of the microgels when they are closer than 3.2 μm.

From the fittings we obtain $B = 0.167 \pm 0.018$. According to Eqs. (4.11, 4.12) the following scaling relations can be deduced: $U(r) \propto r^{-4.0\pm0.7}$ and $F_{inter}(r) \propto r^{-5.0\pm0.7}$. These scaling relations help to understand the origin of the long-range interaction between microgels at water/oil interface. First, this attraction force is not van der Waals force, because van der Waals force only becomes significant when the inter-microgel separation is tens of nanometer.[12] Secondly, the attraction force may arise from the dipolar interaction,

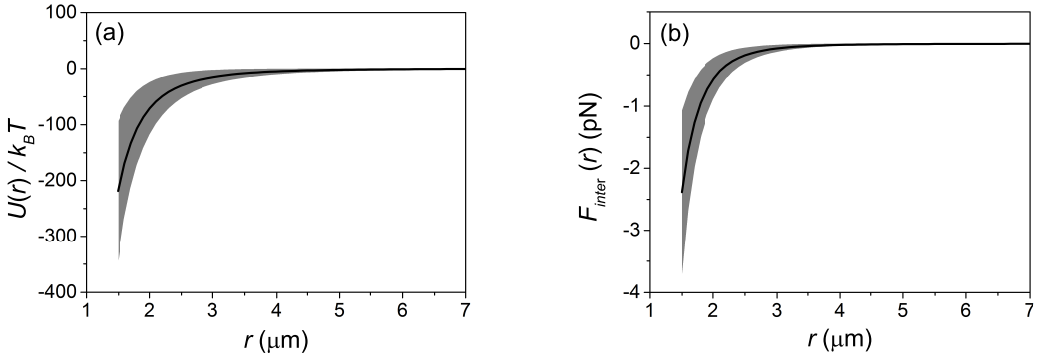

Figure 4.14 (a) The pair interaction potential $U(r)$ (normalized by thermal energy k_BT) of microgels at water/oil interface as a function of inter-microgel separation r, estimated using Eq. (4.11). (b) The interaction force $F_{inter}(r)$ between two microgels at water/oil interface, estimated using Eq. (4.12). 20 aggregating microgel pairs were used to determine $U(r)$ and F_{inter}. The solid lines represent the mean values and the shaded areas represent the error bars.

which is due to the surface charge heterogeneity.[13] Such surface heterogeneity can introduce in-plane dipoles leading to the attraction force. This dipolar interaction potential, $U(r) \propto r^{-3}$, is not consistent with our experimental results.

The capillary forces, which are caused by the deformation of the interface, are long-range and may be the origin of the interaction between microgels at interface. As microgels are swollen in water (containing more than 95% water in the swollen state),[14] their density is comparable to the water phase. Consequently, the weight of the microgels is probably unable to deform the interface. However, the deformation of interface may arise if the contact line on the particle surface is irregular.[15] For solid particle, the undulation of contact line is due to the chemical or topographical heterogeneities of the particle surface. The undulation of contact line leads to a quadrupolar interaction, and the resulting interaction potential is

$$U(r) = -12\pi\,\gamma\,h_c^2\,\cos(2\varphi_A + 2\varphi_B)\,\frac{r_c^4}{r^4}, \tag{4.13}$$

where h_c is the amplitude of the undulation of the contact line. The particle and the water/oil interface intersect at the contact radius r_c. γ is the water-oil interfacial tension. The angles φ_A and φ_B measure the orientation of the diagonals of the respective quadrupoles relative to the line connecting the centres of the two particles. When two particles approach they will first rotate relative to each other until the angle-dependent prefactor is a minimum and then be attracted to each other.[15]

The scaling with separation distance of the capillary interaction $U(r) \propto r^{-4}$ is consistent with our estimated interaction potential $U(r) \propto r^{-4.0\pm0.7}$. The necessary undulation amplitude can be estimated assuming $\cos(2\varphi_A + 2\varphi_B) = 1$, $\gamma \sim 42$ mN/m, and $r_c \sim 1.5$ μm. With Eqs. (4.11, 4.13) the necessary undulation amplitude amounts to $h_c = 3 \pm 1$ nm. This result implies that a nanometer-sized undulation of the contact line around the microgels

is able to explain the attraction force as observed in the experiment. The undulation of the contact line may be also supported by the fact that the interface between microgels is not flat as shown by cryo-SEM images.[16,17] At the periphery of microgels digitation structures are present. These digitation structures may reflect the undulation of the interface around the microgels.

We also note that the $U(r) \propto r^{-4.0\pm0.7}$ relation is reminiscent of the fluctuation-induced capillary interactions.[18–20] The origin of this interaction is that the presence of inclusions in an interface change the thermal fluctuations of this interface leading to a Casimir-type interaction. The far field calculations[18,20] show that the fluctuation-induced interaction potential is significantly smaller than our experimental value. There are, however, additional contributions at short distances, that may significantly increase this interaction.[19] In our future study we will focus more intently on the origin of the attraction force between microgels at interfaces.

4.6.2.3 Ageing of microgels at water/air interface

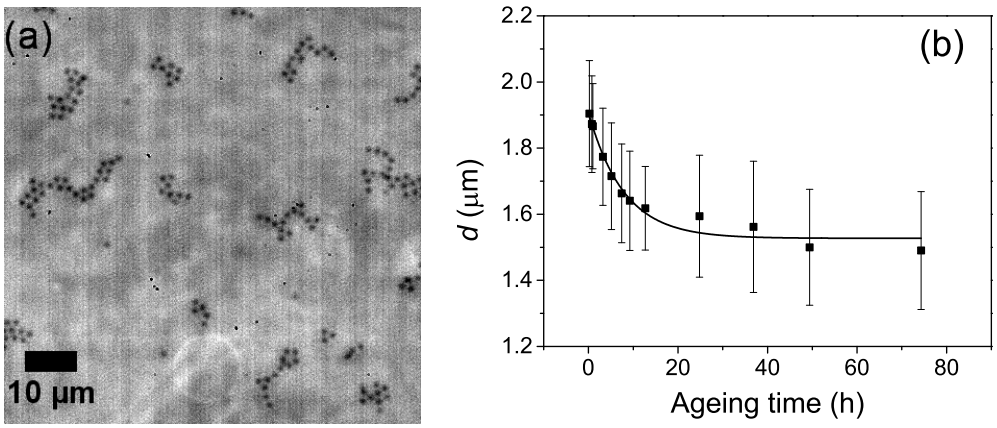

Figure 4.15 (a) Microgels at water/air interface as imaged by phase contrast microscopy. The scale bar is 10 μm. (b) The mean nearest-neighbor distance (d) *vs*. ageing time (t) for microgels at water/air interface. The microgel concentration at the interface is 0.04 μm^{-2}. The solid line shows the best fit using an exponential decay function: $d = A_0 e^{-t/\tau} + d_0$ where A_0, τ, d_0 are the fitting parameters.

The ageing behavior of microgel aggregates was also observed at the water/air interface (Fig. 4.15a). The mean nearest-neighbor distance decreased over time following an exponential decay function. The exponential time constant τ was found to be 8 h (Fig. 4.15b).

4.6.2.4 Displacement of microgels under lateral compression

By introducing superparamagnetic beads at the water/oil interface, lateral forces can be applied on the microgel layer at the interface. As shown in Fig. 4.8a, the structure of the

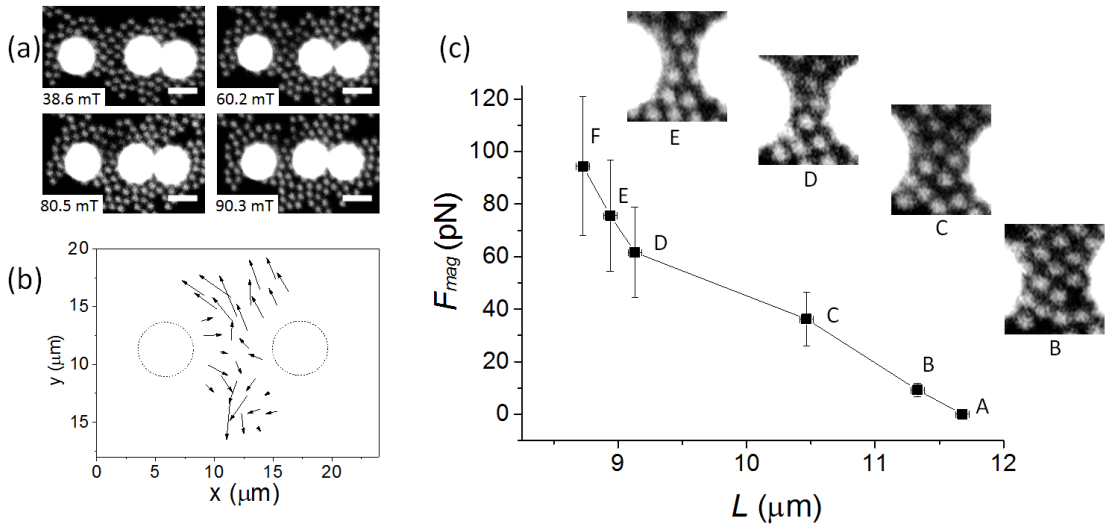

Figure 4.16 (a) Using magnetic beads to compress the microgels at the water/oil interface. The magnetic field was applied along the horizontal direction, creating an attraction force between the magnetic beads (large white spots). The magnetic field strength was increased stepwise from 0 mT, 38.6 mT, 60.2 mT, 80.5 mT, 90.3 mT to 100.8 mT (∼10 min/step). The scale bar is 5 μm. (b) The displacements of the microgels between the magnetic beads when the magnetic field was increased from 38.6 mT to 90.3 mT. The dotted circles indicate the positions of the magnetic beads, and the arrows show the displacements of the microgels. (c) The compression force (equal to the magnetic attraction force F_{mag}) as a function of center-to-center distance (L) of the magnetic beads (between the two magnetic beads on the left-hand side in (a)). Points A-F correspond to magnetic fields of 0 mT, 38.6 mT, 60.2 mT, 80.5 mT, 90.3 mT and 100.8 mT. The structure of the microgel layer between the magnetic beads is shown by the enlarged images.

microgel layer between the two magnetic beads (on the left-hand side; larger field of view is shown in Fig. 4.17) changed when a horizontal magnetic field was applied. The attraction force between the magnetic beads increased with increasing magnetic field strength. For example, when the magnetic field was increased from 38.6 mT to 90.3 mT, the attraction force between the two magnetic beads increased from $\sim$ 9 pN to $\sim$ 76 pN. Due to the attractive magnetic force, the magnetic beads compressed the microgel layer between them. Under compression, the microgels were squeezed and expelled out from the space between the magnetic beads (Fig. 4.8b). In Fig. 4.8c the compression force acting on the microgel layer (due to the magnetic attraction between the magnetic beads) is plotted as a function of the center-to-center distance of the magnetic beads. A non-linear response was observed. From zero field (Point A) up to Point C, the slope was almost constant, while from Point C to Point D the slope (absolute value) decreased. The corresponding structure of the microgel layer between the magnetic beads changed significantly from Point C to Point D–some microgels were expelled out (see Fig. 4.8a and the enlarged images in Fig. 4.8c). The slope (absolute value) of the force-displacement curve increased after Point D. Apparently the barrier to expel the remaining layers of microgels was higher than

the applied force.

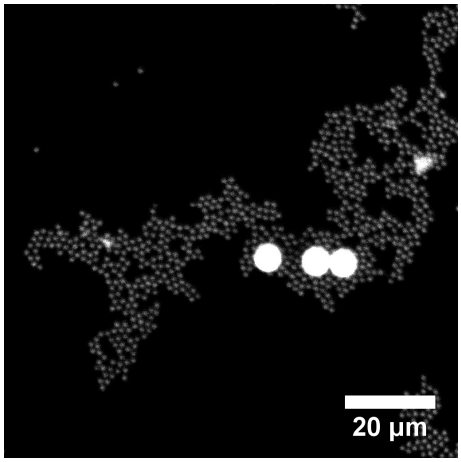

Figure 4.17 Structure of microgels at the water/oil interface with magnetic beads. Fig. 4.8 shows the region close to the magnetic beads (brightest spots).

In order to explore the nonlinear response of the deformation of microgel assemblies on compression force, we fit the results of the compression measurements to the nonlinear formula

$$F_{mag} = C(L_0 - L)^{\alpha}, \tag{4.14}$$

where C is a prefactor, L_0 the initial center-to-center distance between the magnetic beads before compression, and α the nonlinear factor. This equation is able to describe the (overall) increasing tendency of F_{mag} (i.e., the compression force acting on the microgels between the magnetic beads which is balanced by the repulsive force from the microgels) when L decreases (e.g., Fig. 4.8c). We find that α is not correlated with L_0 (Fig. 4.18a), while C decreases with increasing L_0 approximately following $C \propto 10^{-\beta L_0}$, where β is a positive parameter (Fig. 4.18b). This result indicates that F_{mag} decays exponentially with increasing center-to-center distance of the magnetic beads, consistent with Eq. (4.1) in the main article.

4.6.2.5 Movies

Movie S4-1: Diffusion and aggregation of microgels at water/oil interface.

Movie S4-2: Shearing microgel-loaded interface by magnetic beads. A magnetic field of 216 mT was applied along the sample plane and rotated quasi-statically counterclockwise. The large particles are 4.7 ± 0.2 μm magnetic beads and the small particles are microgels. This movie corresponds to Fig. 4.9 of the main article where the magnetic field is only rotated by 25°.

Movie S4-3: Shearing microgel-loaded interface with a porous structure by magnetic beads. A magnetic field of 216 mT was applied along the sample plane and rotated quasi-

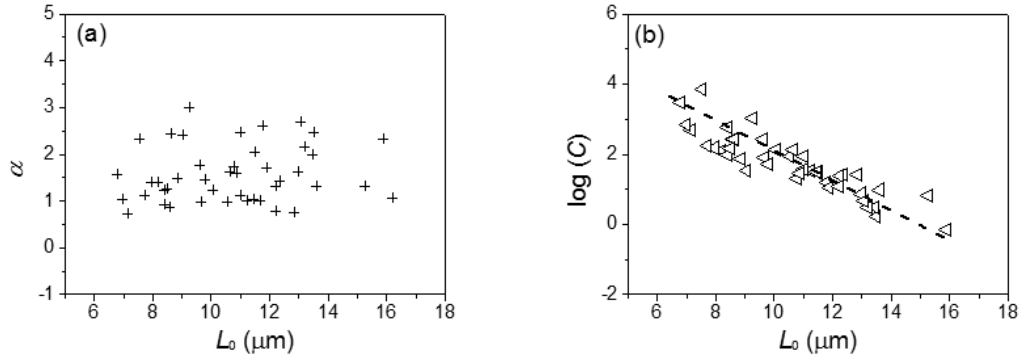

Figure 4.18 Fitting parameters α (a) and C (b) of Eq. (4.14) as functions of the initial center-to-center distance (L_0) between the magnetic beads (with microgels between the beads). The dash line in (b) is guide to the eye, showing $C \propto 10^{-\beta L_0}$, where β is a positive parameter. The results from 45 compression measurements are shown here.

statically counterclockwise. The large particles are 4.7 ± 0.2 μm magnetic beads and the small particles are microgels.

Movie S4-4: Shearing microgel-loaded interface by magnetic beads. Firstly, there was no magnetic field; secondly a magnetic field (64 mT) along the interface pointing to the vertical direction was applied; thirdly, we changed the field to the horizontal direction. At last, the magnetic field was removed. The large particles are 4.7 ± 0.2 μm magnetic beads and the small particles are microgels.

Bibliography

[1] Roth, M.; Franzmann, M.; D'Acunzi, M.; Kreiter, M.; Auernhammer, G. Experimental Analysis of Single Particle Deformations and Rotations in Colloidal and Granular Systems. *arXiv preprint, arXiv:1106.3623* **2011**.

[2] Roth, M.; Schilde, C.; Lellig, P.; Kwade, A.; Auernhammer, G. K. Colloidal Aggregates Tested via Nanoindentation and Quasi-simultaneous 3D Imaging. *Eur. Phys. J. E.* **2012**, *35*, 124.

[3] http://www.physics.emory.edu/faculty/weeks//idl/index.html.

[4] Sbalzarini, I. F.; Koumoutsakos, P. Feature Point Tracking and Trajectory Analysis for Video Imaging in Cell Biology. *J. Struct. Biol.* **2005**, *151*, 182–195.

[5] http://imagej.nih.gov/ij/.

[6] Martin, J. E. Theory of Strong Intrinsic Mixing of Particle Suspensions in Vortex Magnetic Fields. *Phys. Rev. E* **2009**, *79*, 011503.

[7] Loudet, J. C.; Alsayed, A. M.; Zhang, J.; Yodh, A. G. Capillary Interactions between Anisotropic Colloidal Particles. *Phys. Rev. Lett.* **2005**, *94*, 018301.

[8] Park, B. J.; Pantina, J. P.; Furst, E. M.; Oettel, M.; Reynaert, S.; Vermant, J. Direct Measurements of the Effects of Salt and Surfactant on Interaction Forces between Colloidal Particles at Water-oil Interfaces. *Langmuir* **2008**, *24*, 1686–1694.

[9] Ortega, F.; Ritacco, H.; Rubio, R. G. Interfacial Microrheology: Particle Tracking and Related Techniques. *Curr. Opin. Colloid Interface Sci.* **2010**, *15*, 237–245.

[10] Einstein, A. Über die von der Molekularkinetischen Theorie der Wärme Geforderte Bewegung von in Ruhenden Flüssigkeiten Suspendierten Teilchen. *Ann. Phys.* **1905**, *4*, 549–560.

[11] Von Smoluchowski, M. Zur kinetischen Theorie der Brownschen Molekularbewegung und der Suspensionen. *Ann. phys.* **1906**, *326*, 756–780.

[12] Park, B. J.; Furst, E. M. Attractive Interactions between Colloids at the Oil-Water Interface. *Soft Matter* **2011**, *7*, 7676–7682.

[13] Chen, W.; Tan, S.; Ng, T. K.; Ford, W. T.; Tong, P. Long-ranged Attraction between Charged Polystyrene Spheres at Aqueous Interfaces. *Phys. Rev. Lett.* **2005**, *95*, 218301.

[14] Gao, J.; Hu, Z. Optical Properties of N-isopropylacrylamide Microgel Spheres in Water. *Langmuir* **2002**, *18*, 1360–1367.

[15] Stamou, D.; Duschl, C.; Johannsmann, D. Long-range Attraction between Colloidal Spheres at the Air-water Interface: The Consequence of an Irregular Meniscus. *Phys. Rev. E* **2000**, *62*, 5263.

[16] Pinaud, F.; Geisel, K.; Masse, P.; Catargi, B.; Isa, L.; Richtering, W.; Ravaine, V.; Schmitt, V. Adsorption of Microgels at an Oil-Water Interface: Correlation between Packing and 2D Elasticity. *Soft Matter* **2014**, *10*, 6963–6974.

[17] Destribats, M.; Lapeyre, V.; Wolfs, M.; Sellier, E.; Leal-Calderon, F.; Ravaine, V.; Schmitt, V. Soft Microgels as Pickering Emulsion Stabilisers: Role of Particle Deformability. *Soft Matter* **2011**, *7*, 7689–7698.

[18] Goulian, M.; Bruinsma, R.; Pincus, P. Long-range Forces in Heterogeneous Fluid Membranes. *Europhys. Lett.* **1993**, *22*, 145.

[19] Lehle, H.; Oettel, M. Importance of Boundary Conditions for Fluctuation-induced Forces between Colloids at Interfaces. *Phys. Rev. E* **2007**, *75*, 011602.

[20] Yolcu, C.; Haussman, R. C.; Deserno, M. The Effective Field Theory Approach towards Membrane-mediated Interactions between Particles. *Adv. Colloid Interface Sci.* **2014**, *208*, 89–109.

5. Structure and rheology of microgel monolayers at the water/oil interface

Shilin Huang,[a] **Kornelia Gawlitza,**[‡b] **Regine von Klitzing,**[b] **Werner Steffen,**[a] **and Günter K. Auernhammer**[*a]

[a] Max Planck Institute for Polymer Research, Ackermannweg 10, 55128 Mainz, Germany.
[b] Stranski-Laboratorium für Physikalische und Theoretische Chemie, Technische Universität Berlin, Strasse des 17. Juni 124, 10623 Berlin, Germany.
[‡] Current address: Fachbereiche 1.9 Chemische und optische Sensorik, Bundesanstalt für Materialforschung und -prüfung (BAM), Richard-Willstätter-Str. 11, 12489 Berlin, Germany.
[*] Corresponding author. E-mail: auhammer@mpip-mainz.mpg.de

To submit.

Statement of Contribution

In this paper, Shilin Huang has the following contributions:

(1) Developing the methods to prepare the Gibbs and Langmuir monolayers whose structures can be observed under inverted microscope (Fig. 5.1a).

(2) Designing and calibrating the magnetic setup for the oscillating magnetic field (Fig. 5.1c, d).

(3) Performing the experiments on passive microrheology (Figs. 5.2–5.4) and active microrheology (Fig. 5.6, Fig. 5.12).

(4) Writing the algorithms to analyze the vibration modes of the microgel aggregates (Fig. 5.3b, c).

(5) Writing the algorithms to calculate the shear moduli based on the oscillation of the magnetic dimers.

(6) Analyzing the structures of the microgel monolayers (Fig. 5.5, Fig. 5.8, Fig. 5.9, Fig. 5.10).

(7) Exploring the mechanisms for the elasticity of microgel monolayers at the interface (Fig. 5.7).

(8) Measuring the hydrodynamic diameter of the microgels in water using particle tracking method.

(9) Performing simulation to obtain the geometry factor in Eqs. (5.3–5.4) (Fig. 5.11).

In addition, Shilin Huang contributes partially to writing the paper.

Abstract

We investigate the rheological property of microgel monolayers at the water/oil interface using passive and active microrheological methods. At low surface coverage, the microgels at the water/oil interface have a tendency to form aggregated structures (networks) with dominating elasticity. At high surface coverage the microgels form densely packed monolayers. Using microsized magnetic particles as the local rheological probes in the dense microgel monolayers, we perform in situ study of their rheological properties and structures. We observe four regimes where the elasticity of the microgel monolayer has different dependence on the microgel concentration at the interface. The rheological properties of the microgel monolayers are not only dependent on the concentration, but also strongly correlated with the inter-microgel distance and spacial arrangement of the microgels at the interface. Our results also show that the microgel monolayers act similar to soft glassy materials.

5.1 Introduction

Colloids are used to stabilize emulsions which find wide applications in food industry, cosmetics, paints, medicine, et al.[1,2] Thanks to their strong detachment energy,[3] colloids can be irreversibly trapped at the water/oil interface. The colloids create a steric barrier at the interface that imparts stability to emulsions.[1] The rheological properties of the colloidal monolayers at the water/oil interfaces influence the droplet deformation, coalescence, breakup and thus also the stability of emulsions.[1,2,4] The rheological properties of these colloidal monolayers are dominated by the interparticle interactions and the resulting structures at the interface.[5,6] For charged particles at the water/oil interface, the electrostatic repulsion is enhanced due to the strongly reduced electrostatic screening in the oil phase (compared to that in the aqueous phase).[7–11] Attractive forces are also present for particles at the water/oil interface. Except for the van der Waals interactions which become significant when the particles are close to contact (in the range of tens of nanometer for microsized particles),[12] long-range attractions between the microsized particles at the water/oil interfaces are also widely observed.[13,14] These long-range attractions are capillary interactions induced by local deformations of the water/oil interface surrounding the particles. For small enough particles, when gravitational effects can be neglected, the deformations of the water/oil interface around the particles can be caused by the undulated contact lines on the particle surfaces.[14] By tailoring the interparticle interactions, the particles can form different monolayer structures at the water/oil interface, from crystals to aggregated structures.[5,6,15] Compared to repulsive crystals, the shear moduli of the solid particle monolayers with aggregated structures increase faster with increasing surface coverage.[5] The shear moduli of the solid particle monolayers tend to diverge (e.g.,

up to $\sim$10 N/m)[15] when the particles become densely packed at the interface.[5,16]

Soft particles, e.g., the poly(N-isopropylacrylamide) (PNIPAM) based microgels, have been used as stabilizers in emulsions in order to fabricate stimulus-responsive emulsions.[17–20] Similar to solid particles, the microgels at the interface have a large detachment energy; similar to linear amphiphilic polymers, the microgels in the aqueous phase can be spontaneously adsorbed onto the water/oil interface.[21,22] Because of the interplay of surface tension and deformability, a microgel adsorbed at the water/oil interface stretches and deforms, adopting the so-called "fried-egg" like structure, with the egg-yolk as the dense core while the egg-white as the spreading polymer layer (shell) around the core.[18,19] The interfacial properties of the microgel monolayers and the emulsion stability are dominated by the deformability of the microgels.[18] Whereas, the contribution from the electrostatic repulsive force between microgels at the interface is rather small.[23] Microgels form aggregated structures even at low concentrations, probably driven by the long-range capillary attractive forces.[24,25] Different to solid particle monolayers at the water/oil interface which show a divergence of rheological property when the particles are densely packed,[26] microgel monolayers can be further deformed under the lateral compression.[27] Even under high compression, the shear moduli of the microgel monolayers are relatively small (only up to $\sim 10^{-3}$ N/m) .[28,29] It has been reported that the microgels and their constituting polymers (linear PNIPAM) at the water/oil interface have very similar dilational elasticity.[27] Recently, Zielińska et al. used neutron reflectivity to study the PNIPAM-based nanogel (small microgels with size less than 50 nm[30]) at the water/air interface.[31] They found that the nanogels at the interface have a collapsed polymer layer in contact with air. This collapsed polymer layer has a low water content (similar to that for a collapsed microgel at temperature above the lower critical solution temperature (LCST)) and have a thickness in the range of 1-2 nm depending on the crosslinking density. The collapsed polymer layer is also present for linear PNIPAM at the water/air interface.[31,32] It is still an open question how this collapsed polymer layer influences the rheological properties of the microgel monolayers.

The structure-rheology relationship for microgel monolayers at the water/oil interface is an essential topic for microgel-stabilized emulsions. However, it has not been widely explored yet. Recently, Rey et al.[28] performed a detailed study. They measured the shear moduli of the microgel monolayers at the water/air interface as a function of surface pressure using the microdisk rheometer. Additionally, they performed *ex situ* characterizations of the structure of the microgel monolayers in a similar system (microgels at the water/oil interface).[28,33] Although the *ex situ* study has gained new insights to structure-rheology relationship for microgel monolayers, it has some disadvantages due to the following facts. Firstly, the structure of colloidal monolayers at the water/oil interface is very sensitive to preparation details and it is not always reproducible.[6,33] Secondly, mesoscopic heterogeneity may occur in microgel monolayers.[27] At last, the mechanical probe (e.g.,

the Wilhelmy plate or microdisk) may locally change the structures of the microgel monolayers. For solid particle monolayers, simultaneous visualization of the structure and measurement of the rheological property have been realized and this method provides deep understanding on the rheology-structure relationship.[2,34,35] However, similar method has not been used for microgel monolayers. The primary difficulty is to realize the sub-micron resolution for *in situ* visualization of the structure of the microgel monolayers.

In this work, using microrheological methods, we study the rheological property of the microgel monolayers at the water/oil interface with simultaneous *in situ* visualization of the structures. Resolving single microgels, we explore *in situ* the interplay between microgel interaction, structure, and rheology of the microgel monolayers over a wide range of microgel concentration at the interface. At low microgel concentrations, the microgels at the interface form open networks which show obvious thermal fluctuations. This allows us to obtain the apparent shear moduli of the microgel networks by analyzing these thermal fluctuations. At high concentrations, microsized magnetic particles are used as local rheological probes to detect the rheological properties of the densely packed microgel monolayers. We find that under different compression states, the microgel monolayers show elasticity arising from different mechanisms. In addition, the frequency dependence of the rheological property reveals that the microgel monolayers behave like two-dimensional (2D) soft glassy materials.

5.2 Materials and methods

In this study we used PNIPAM-based microgels, cross-linked with 5 mol% of (N,N'-methylenebis-(acrylamide)) and 25 mol% of comonomer (DL-2-allylglycine). The microgels were synthesized by surfactant-free emulsion polymerization in a temperature ramp (see Ref. 36 for details). The microgels were swollen by Milli-Q water and stored at a concentration of 1 wt%. At ambient temperature the hydrodynamic diameter of the microgels is 970 ± 60 nm with a polydispersity index of 0.6, determined by dynamic light scattering (DLS, details see Supporting Information).

In this work we prepared both Gibbs and Langmuir monolayers. We either relied on spontaneous adsorption of the microgels from the aqueous phase onto the water/oil interface (Gibbs), or we spread the microgels at the interface using a volatile solvent (Langmuir). For Gibbs monolayers, we used diluted microgel suspensions with microgel concentrations of 0.07-0.1wt%. A thin layer (< 170 μm) of the diluted microgel suspension was deposited on top of a coverslip with the three phase contact line pinned by a copper ring (1.5 mm hole, ~ 40 μm thick, Agar Scientific). This aqueous layer was covered by water-saturated polydimethylsiloxane oil (PDMS, 770 g/mol, Alfa Aesar GmbH & Co. KG). The microgels spontaneously adsorbed onto the water/oil interface. This method could be used to prepare monolayers with microgel concentration up to $\sim$0.57

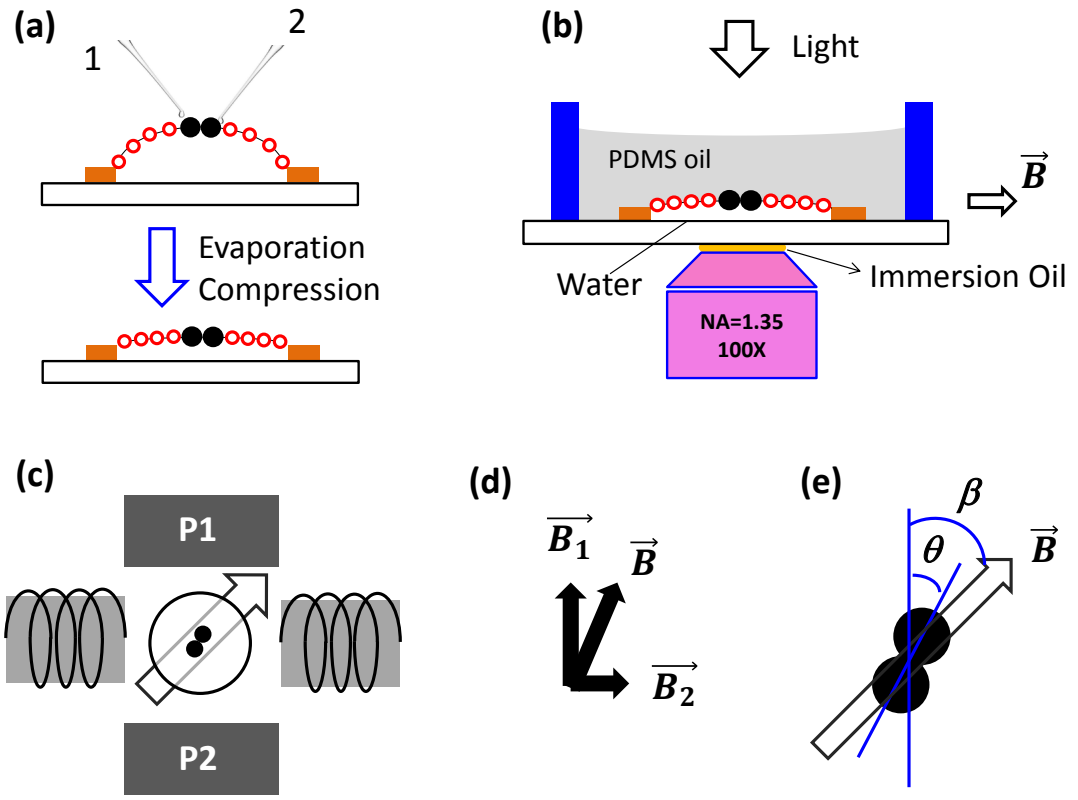

Figure 5.1 (a) Preparation of a dense microgel monolayer with a small amount of magnetic particles. The microgels (indicated as small red particles, introduced by liquid 1) and very small amount of magnetic particles (indicated as large dark particles, introduced by liquid 2) are spread onto the water surface at the same time. Evaporation is used to reduce the surface area of the water drop, leading to the compression of the microgel monolayer at the interface. The use of the magnetic particles is only necessary for the active microrheology. (b) After evaporation the water layer was covered with water-saturated PDMS oil. An oil-immersion objective with high numerical aperture (NA = 1.35, working distance = 170 μm) is used to observed the microgels at the water/oil interface. (c) An oscillating magnetic field is applied in the plane of the water/oil interface. A set of permanent magnets (P1 and P2) provide a permanent magnetic field of $\vec{B}_1$ (52.7 mT) shown in (d), while a pair of coils (with pure iron cores) provide a dynamic magnetic field $\vec{B}_2$ ($B_2 = 24.5\sin(\omega t)$ mT, where ω is the angular frequency). The summation of $\vec{B}_1$ and $\vec{B}_2$ is an oscillatorily rotating magnetic field of $\vec{B}$ with an rotation angle of $\beta = \beta_0 \sin(\omega t)$. (e) We focus on isolated magnetic dimers aligned along $\vec{B}_1$ in the microgel monolayers. A magnetic dimer oscillates in the oscillating field $\vec{B}$ with a smaller rotation angle θ and a phase lag ϕ ($\theta = \theta_0 \sin(\omega t - \phi)$, $\theta_0 < \beta_0$).

μm^{-2}. The Langmuir monolayers were prepared by using aqueous microgel suspensions with 0.1 wt% microgels and 8 wt% isopropyl alcohol (IPA). Different amounts (0.5-1.5 μL) of this suspension were spread onto the surfaces of water drops (0.5-1 μL) sitting in the copper rings on the coverslips (see Fig. 5.1a). After spreading of the microgels, the

drops were allowed to evaporate to form thin liquid layers. Because of the evaporation of water, the surfaces of the drops shrank and the microgels at the surfaces were laterally compressed.[37] After the thickness of the aqueous layers became smaller than $\sim$170 μm, they were covered with PDMS oil. The Langmuir monolayers had a higher degree of order compared to the Gibbs monolayers at high concentrations. This was probably caused by the in-plane shear flows when the microgels were introduced onto the drop surfaces. The Langmuir method was used to prepare the monolayers with concentration up to $\sim$1.34 μm^{-2}. After preparation of the monolayers, the samples were allowed to equilibrate for at least 1 h before the measurements. We used an inverted microscope (Leica, DMI6000B) in bright-field mode to observe the microscopic structure of the microgel monolayers at the water/oil interface. Some images in the following text are inverted in order to highlight the microgels. An oil-immersion objective (UPlanApo PH3, 100×, NA=1.35, working distance 170 μm, Olympus Deutschland GmbH, Germany) was used in order to have sub-micron resolution. A high-speed camera (Photron, FASTCAM SA1) was used to record the images and videos. The details of the image analysis can be found in Ref. 36.

At low microgel concentration, the thermal fluctuations in the microgel monolayers were pronounced. We used the high-speed camera to record the thermal motion of the microgels at the water/oil interface (frame rate 60 Hz and shutter speed 1/1000 s). The trajectories of the microgels were then extracted using the IDL algorithm from Crocker, Grier, and Weeks.[38] The positioning accuracy was typically better than 10 nm as deduced from the dried microgels on the coverslip. When the concentration of microgels at the water/oil interface was high, the thermal fluctuation became too weak for optical detection. In this case, we used an active microrheological method. We spread very small amount of magnetic particles to the Langmuir monolayers (together with the microgels), see Fig.5.1a. The magnetic particles were either superparamagnetic particles purchased from microParticles GmbH (diameter=4.4 ± 0.3 μm), or carbonyl iron particles from BASF (CC grade, d_{50}=3.8-5.3 μm). In the microgel monolayers the magnetic particles formed monomers, dimers, trimers, et al.. For the active microrheological measurements we only used the isolated dimers (see Fig. 5.9 for an example, Supporting Information), because they had the simplest shape with magnetic anisotropy.

The magnetic setup used to provide the oscillating magnetic field was shown in Fig. 5.1 (c, d). Two permanent magnets (P1 and P2) provided the static field of $\vec{B}_1$ (52.7 mT), while the dynamic field $\vec{B}_2$ following a sinusoidal waveform ($B_2 = 24.5\sin(\omega t)$ mT) was provided by the coils (with ARMCO pure iron as the core material). The current going through the coils was controlled using a waveform generator (33220A, Agilent), a custom-built amplifier and a power supply (TTi EX354D). The sum $\vec{B} = \vec{B}_1 + \vec{B}_2$ was an oscillating magnetic field with an oscillating angle $\beta = \beta_0 \sin(\omega t)$. Here β_0 is 24.9°. Before applying the oscillating magnetic field, the samples were manually rotated to orient the magnetic

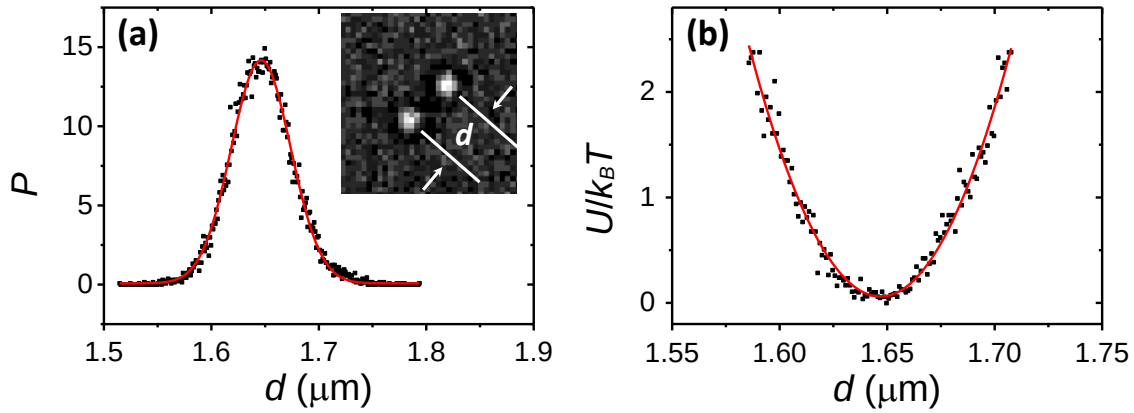

Figure 5.2 (a) The probability distribution of the inter-microgel distance d for the microgel dimer shown in the inset. The red line shows the fitting to the Gaussian distribution. (b) Inter-microgel interaction potential (U) estimated by inverting the Boltzmann distribution ($P(d) \propto \mathrm{e}^{-U(d)/k_BT}$ where k_BT is the thermal energy). The red line is the fit to harmonic potential $U = k(d-d_0)^2/2$, where k is the spring constant and d_0 is the mean inter-microgel distance.

dimers along the $\vec{B}_1$ direction. A magnetic dimer in the dense microgel monolayer was driven to oscillate with a small oscillation angle ($\theta = \theta_0 \sin(\omega t - \phi)$, $\theta_0 < \beta_0$) and a phase lag (ϕ). Typically, θ_0 was smaller than 4° (corresponding to a strain smaller than 4×10^{-4}). We used this small rotation amplitude to avoid structural change and yielding of the microgel monolayers. The fast camera was used to record the oscillation of the magnetic dimers. The synchronization between the fast camera and the applied voltage to the coil was realized using the trigger signal from the waveform generator. We measured θ and ϕ based on the recorded videos. Similar active microrheological methods have been used to measure the local viscoelasticity of three dimensional (3D) systems, e.g., living cells.[39,40]

5.3 Results and discussion

5.3.1 Inter-microgel interactions and finite-size aggregates

Single microgels at the water/oil interface have a tendency to form aggregated structures. The driving force for aggregation is significant when the inter-microgel distance is smaller than ~ 3.2 μm (about 2 times of the diameter of microgel shells at the water/oil interface).[36] This attraction is probably driven by capillary interaction between microgels due to undulation of the contact line (with an undulation amplitude of ~ 3 nm on the periphery).[24,36] For aggregated pairs of microgels, the measured probability distribution of the center-to-center distance $P(d)$ follows a Gaussian distribution (Fig. 5.2a). Accordingly, the inter-microgel interaction potential $U(d)$ can be estimated by inverting the Boltzmann

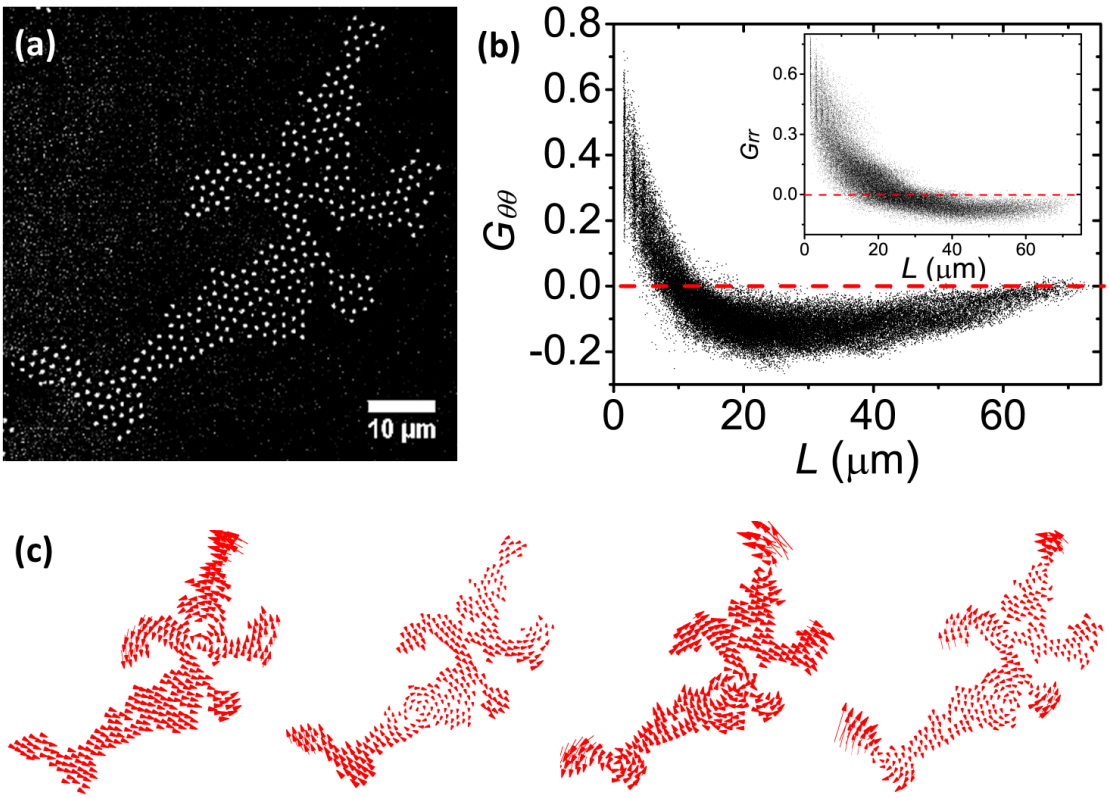

Figure 5.3 (a) An aggregate consisting of 332 microgels at the water/oil interface. The scale bar is 10 μm. (b) Velocity correlation function of microgel pairs in the aggregate shown in (a). $G_{\theta\theta}$ and G_{rr} represent the correlation function along the tangential and longitudinal directions, respectively. (c) The four lowest vibration modes of the same aggregate in (a).

distribution:[13,41]

$$P(d) \propto \mathrm{e}^{-\frac{U(d)}{k_B T}}, \tag{5.1}$$

where k_B is the Boltzmann constant and T is the absolute temperature. Following the good Gaussian fit in Fig. 5.2a, $U(d)$ has a parabolic shape and can be fitted to the potential of a harmonic oscillator (Fig. 5.2b). The extracted effective spring constant is 2150 ± 850 $k_B T/\mu\mathrm{m}^2$ based on 31 arbitrary selected aggregated microgel pairs (the variation between pairs is the main source of the uncertainty).

Fig. 5.3a shows a large aggregate of microgels which is fluctuating at the water/oil interface. The aggregate does not rearrange internally in the observation time of 4 min. Following the thermal motion of all the microgels in this aggregate, we calculate the velocity correlation function: $G^{ij}_{\theta,r} = \langle v^i_{\theta,r}(t) v^j_{\theta,r}(t)\rangle_t$, where $i, j = 1, ..., N$ ($N = 332$) runs over all particles and $\langle\cdot\rangle_t$ means the average over time. θ and r represent the tangential and longitudinal directions relative to the vector connecting the two microgel centers. If two microgels move exactly along the same direction with the same speed, the velocity correlation function will have a value of unity; if they move along opposite direction, the

correlation will be negative. If their motion is not correlated, $G^{ij}_{\theta,r} = 0$. We find that the correlation value for most of the microgel pairs in the aggregate is non-zero (Fig. 5.3b), implying that the motions of the microgels in the aggregate are correlated. This correlation arises from the interactions between the microgels.

The correlation matrix (see Supporting Information) reveals the vibration eigenmodes of this microgel aggregate.[42,43] The four lowest-frequency eigenmodes given in Fig. 5.3c show long-distance cooperative motion of the microgels in the aggregate. These modes include also shear deformations in the aggregate. This implies that microgels cannot slide or roll freely over each other. We attribute this phenomenon to two possible effects: firstly, the capillary interaction between the microgels, i.e., the forces between the capillary multipoles,[6,14,44] are orientation dependent. This orientation-dependent interaction provides the microgel aggregates certain resistance to shear.[45,46] Secondly, according to recent study using neutron reflectivity, for a microgel adsorbed at the interface, the polymer layer in direct contact with the non-aqueous phase is collapsed and has a low water content, approximately equal to phase-separated PNIPAM above LCST.[31,32] The thickness of this collapsed layer is in the range of 1-2 nm. For microgels in water at room temperature, the hydrogen bonding between PNIPAM (amide groups) and water dominates, leading to the highly swollen state; however, the collapsed PNIPAM layer at the interface should have a dominating inter- and intra-polymer hydrogen bonding and polymer-polymer hydrophobic interactions, as for microgels at temperature higher than LCST.[30] These molecular forces can also interact between neighboring microgel shells, imparting the stickiness between the neighboring microgels at the interface. This effect may partially contribute to the bending rigidity of the microgel aggregates at the interface.

5.3.2 Fluctuating system-spanning networks

With increasing the microgel concentration at the water/oil interface, the microgels can form a percolating system-spanning network (Fig. 5.4a). At microgel concentrations below $\sim 0.37\ \mu\mathrm{m}^{-2}$, obvious thermal fluctuation can be observed in the microgel networks. For example, we tracked the motion of the microgels in the network in Fig. 5.4a and measured the mean squared displacement (MSD) $\langle \Delta r^2 \rangle$ as a function of lag time (τ) (Fig. 5.4b). According to Einstein equation, particles diffusing in a Newtonian liquid follow $\langle \Delta r^2 \rangle = 2dD_T t$, where d is the dimensionality and D_T is the translational diffusion coefficient.[47–49] However, the MSD of the microgels in the network shows a sub-diffusive behavior ($\langle \Delta r^2 \rangle \sim t^{\alpha}$ with α smaller than unity) up to the lag time of several tens of seconds. This is due to the fact that the movement of the microgels in the network is confined by their neighbors through the inter-microgel interactions (as discussed above). For longer times, α tends to increase because of some structural rearrangement in the network. Even though the inter-microgel interaction is much stronger compared to the thermal energy, we occasionally observe the structural rearrangement (e.g., exchanging neighbors) in the

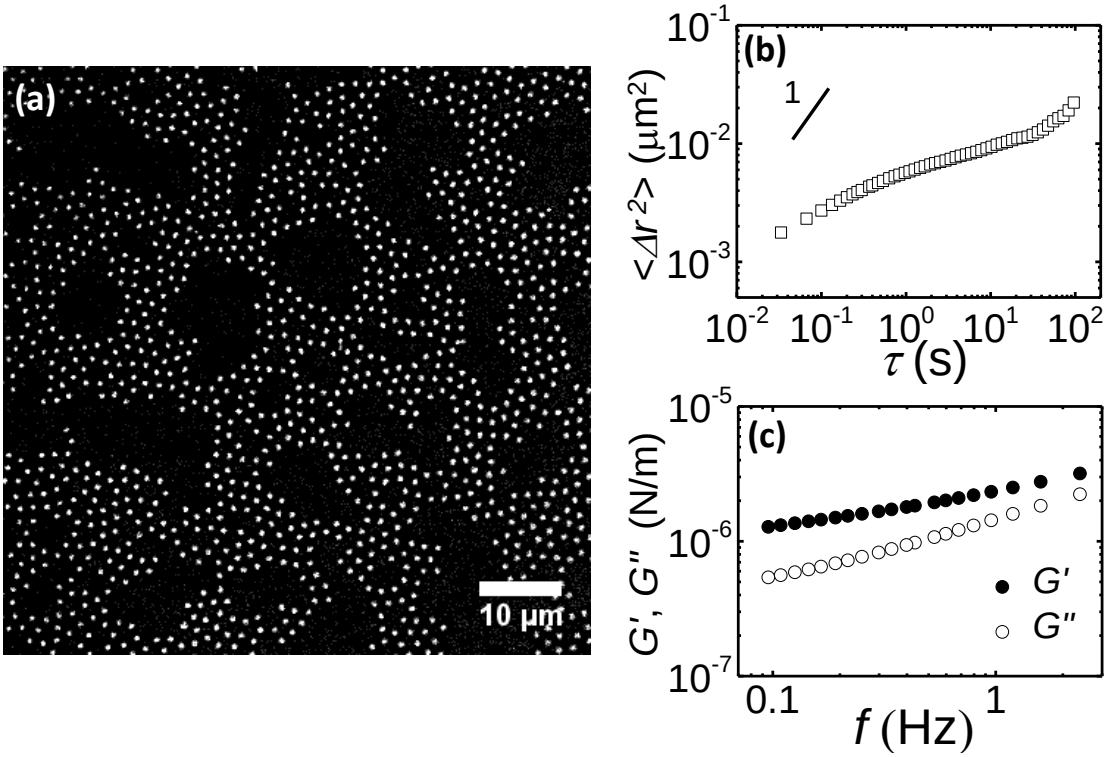

Figure 5.4 (a) An percolating network of microgels at the water/oil interface (Gibbs monolayer). The microgel concentration is $\sim 0.25\ \mu\mathrm{m}^{-2}$. (b) Mean squared displacement (MSD, $\langle \Delta r^2 \rangle$) as a function of lag time for the microgel network. (g) The storage modulus (G') and loss modulus (G'') of the same microgel network.

microgel network at the water/oil interface. These rearrangements seem to be driven by long range capillary forces at the interface (see Supporting Information, Fig. 5.10). This structural relaxation also implies that the aggregated structures (microgel networks) are not in a thermodynamic equilibrium. Through the rearrangement of the microgels the system tends to form a structure with lower free energy (e.g., a less deformed water/oil interface). For the microgel networks at the water/oil interface, the MSD mainly reflects the interaction between the microgels, because the viscous drag from the subphases on the microgels is relatively small (e.g., the MSD for isolated microgels diffusing at the water/oil interface is ∼50 times larger compared to the sample in Fig. 5.4 at 1 s). Thus, in the following we directly use the MSD of the microgels to obtain the apparent viscoelasticity of the microgel networks at the interface without considering the drag from the subphases (see Supporting Information).

In a three-dimensional (3D) system, one can deduce the shear moduli of the system based on the thermal fluctuations of the embedded tracer particles, given that the tracers are large enough compared to the building blocks of the systems. This method is called passive microrheology. The complex shear modulus G^* is related to the MSD through the

generalized Stokes-Einstein (GSE) equation:[50,51]

$$G^*(\omega) = \frac{k_B T}{\pi a i \omega \mathscr{F}\{\Delta r^2(t)\}}, \tag{5.2}$$

where $k_B T$ is the thermal energy, a is the particle radius and $\mathscr{F}$ represents the Fourier transform. For a 2D system like ours, we cannot use eq. (5.2) directly. The reason for this lies in the translational diffusion coefficient D_T. For a particle in a 3D Newtonian liquid, $D_T^{3D} = (6\pi\eta a)^{-1}$. For a thin particle (cylinder) in a finite-size membrane, the translational diffusion coefficient is $D_T^{2D} = [\ln(R/a') - 0.5](4\pi\eta_{2D})^{-1}$, where R is the finite size of the 2D membrane, η_{2D} is the 2D viscosity and a' is the radius of the thin cylinder.[52] Thus, in order to obtain the 2D shear moduli of the microgel monolayer using the thermal fluctuation (Fig. 5.4b), we replace a in eq. (5.2) with an apparent size factor: $[\ln(R/a') - 0.5]^{-1}$, where R is the (macroscopic) radius of the microgel monolayer (0.75 mm, radius of the copper ring, see *Materials and methods*) and a' is the radius of the microgel shells at the water/oil interface. Consequently, the apparent 2D shear moduli for the microgel monolayer can be obtained based on the measured MSD.[38,50] As shown in Fig. 5.4c, the obtained apparent storage modulus of the microgel network at the interface in Fig. 5.4a is higher than the apparent loss modulus in the frequency range of 0.1-2.4 Hz, indicating that the microgel network is essentially elastic.

At low concentrations ($c_p < 0.40\ \mu\text{m}^{-2}$), for the Gibbs and Langmuir monolayers, the microgels at the water/oil interface form aggregated structures while keeping the inter-microgel distance constant ($d = 1.63 \pm 0.07\ \mu$m), see Fig. 5.5c. This gives the measure of the mean diameter of the microgel shells (spreading layer of polymer) at the interface. In other words, each microgel occupies a circular area at the interface with a diameter of $1.63 \pm 0.07\ \mu$m. The constant inter-microgel distance at low concentration is due to the fact that the microgels at the interface have enough space to deform and adopt the "fried-egg" like structure. They are in the minimum of their interaction potential (Fig. 5.2b). For area fractions of the microgel shells at the interface above the 2D dense random packing, i.e., area fraction ≈ 0.84,[53] corresponding to a microgel number density of $c_p \approx 0.40\ \mu\text{m}^{-2}$, the inter-microgel distance in the Langmuir monolayers decreases with increasing the microgel concentration following $d \propto c^{-0.5}$. This reveals the fact that the Langmuir microgels at the interface are laterally compressed when the microgel concentration is higher than c_p, which can also be visualized in the images shown in Fig. 5.5a. For $c > 0.4\ \mu\text{m}^{-2}$ the Gibbs monolayers differ in several aspects from Langmuir monolayers: (i) The inter-microgel distances are more scattered for the Gibbs monolayers (crosses in Fig. 5.5c). This is because the Gibbs monolayers were formed by random adsorption of microgels from the aqueous phase onto the water/oil interface (i.e., the structures cannot be well controlled). (ii) The inter-microgel distances of Gibbs monolayers tend to be smaller compared to Langmuir monolayers at the same concentration. (iii) The Gibbs monolayers are less ordered. The latter is shown by their smaller ψ_6—

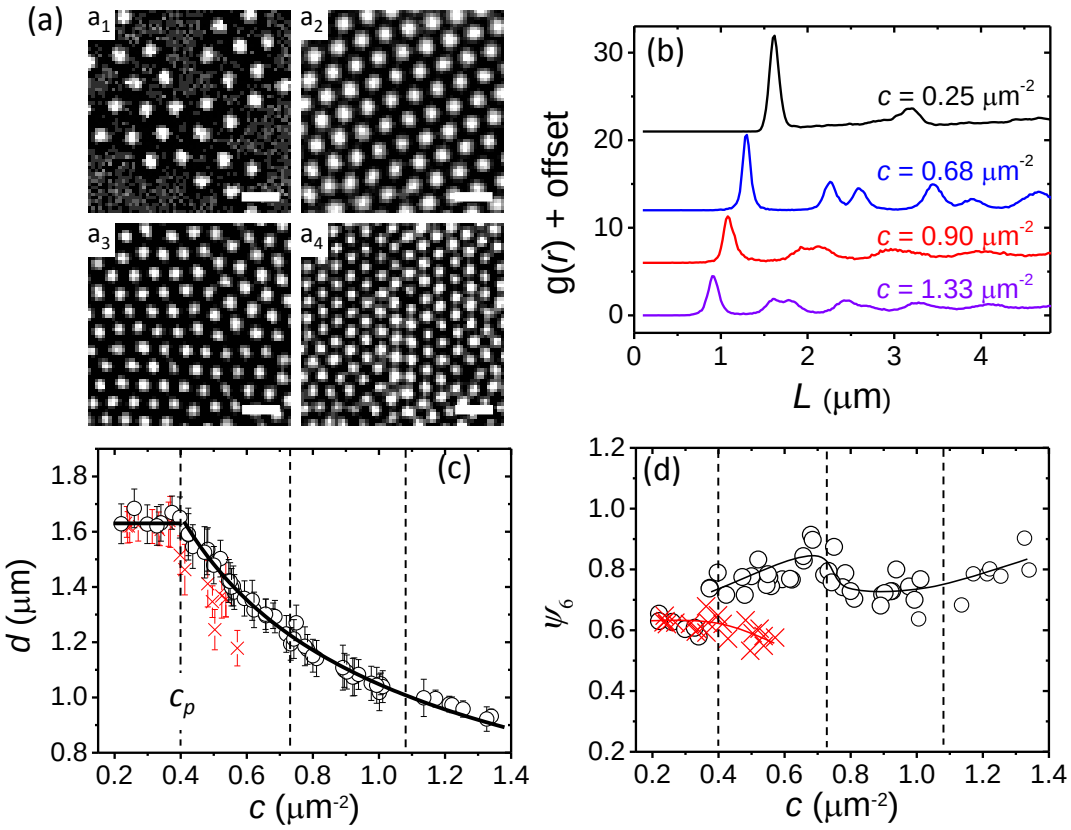

Figure 5.5 (a) Images for microgel monolayers with different concentrations (c). The scale bars represent 2 μm. The concentrations of microgels at the water/oil interface for a_1, a_2, a_3 and a_4 are 0.25 μm^{-2}, 0.68 μm^{-2}, 0.90 μm^{-2}, 1.33 μm^{-2} , respectively. (b) Pair correlation function $g(r)$ for the four samples in (a). (c) Inter-microgel distance (d) for microgel monolayers at the water/oil interface as a function of microgel concentration. The first peak in $g(r)$ is used to obtain d. The inter-microgel distance keeps constant at low concentrations, as indicated by the horizontal solid line for $c < c_p$ (c_p represents the concentration for dense random packing of the microgel shells at the interface). At high concentrations ($c > c_p$), the inter-microgel distance decreases with increasing concentration following $d \propto c^{-0.5}$ (indicated by the solid curve for $c > c_p$). The data points are for Langmuir monolayers (open circles) and Gibbs monolayers (crosses). (d) The 2D orientational order parameters for sixfold symmetry (ψ_6) as a function of microgel concentration. The lines are guides to the eye, and the data points are for Langmuir monolayers (open circles) and Gibbs monolayers (crosses). At low concentration the Langmuir monolayers and Gibbs monolayers have similar inter-microgel distance (c) and ψ_6 (d). However, at high concentration ($c > c_p$), the Gibbs monolayers are more disordered and the inter-microgel distances are smaller compared to the Langmuir monolayers.

the 2D orientational order parameter for sixfold symmetry (Fig. 5.5d). ψ_6 is obtained by $\psi_6 = \langle | \sum_{k=1}^{NN} e^{i6\theta_{jk}}/NN | \rangle$, where θ_{jk} represents the orientation (relative to a fixed axis) of the connecting vector between the centers of particle j and its neighbor k, and NN is the number of nearest neighbors.[54,55]

5.3.3 Dense systems

When the microgels become closely packed at the water/oil interface, the thermal fluctuations of the microgels drop below the detection limit of our image analysis, i.e., the shear modulus of the microgel monolayer is beyond the upper detection limit of the passive microrheology (in the order of 10^{-5} N/m). Consequently, in order to measure the rheological property of the microgel monolayers with high microgel concentrations, external stimuli are necessary to trigger the deformation of the microgel monolayers and measure their shear moduli. We introduced magnetic particles into the closely packed microgel monolayers, and used an oscillating magnetic field (Fig. 5.1) to weakly deform/shear the microgel monolayers.

For a microsized magnetic dimer oscillating in the microgel monolayer, neglecting the inertia effect, the magnetic toque acting on the magnetic dimer $\Gamma_{\mathrm{m}} = \Gamma_0 \sin[2(\beta-\theta)]/2$ is balanced by the viscoelastic torque from the microgel monolayer: $\Gamma_{\mathrm{ve}} = \kappa G^* \theta$, where G^* is the complex shear modulus of the microgel monolayer.[39,40] In our system the viscous drag from the adjacent phases on the magnetic dimer can be neglected because of their small contribution (see Supporting Information for details). The prefactor for the magnetic torque Γ_0 is calibrated by studying the magnetic dimer oscillating in a soft gel with a known storage modulus and a vanishing loss modulus. The geometry factor κ is obtained by simulation of a particle dimer rotating in an elastic membrane using COMSOL Multiphysics software (see Supporting Information, Fig. 5.11). We find $\kappa \approx 33.6R^2$, where R is the radius of the magnetic particle (κ is about 2.7 times of the geometry factor for a single sphere rotating in the membrane $\kappa_s = 4\pi R^2$).[52] The storage and loss moduli for the microgel monolayers are obtained by:[40]

$$G' = \frac{\Gamma_0}{\kappa}\left(\frac{\beta_0}{\theta_0}\cos\phi - 1\right), \tag{5.3}$$

$$G'' = \frac{\Gamma_0}{\kappa}\frac{\beta_0}{\theta_0}\sin\phi, \tag{5.4}$$

respectively (see Supporting Information for more details), where β_0, θ_0 and ϕ are measured from experiments. The results for the microgel monolayer in Fig. 5.6a are given in Fig. 5.6b. It shows that the storage modulus of the closely-packed microgel monolayer is higher than the loss modulus. The storage modulus of the microgel monolayer is weakly dependent on frequency. This weak frequency dependence of modulus is reminiscent of soft glassy rheology,[56] which will be discussed in more detail in the following sections.

5.3.4 Concentration dependent elasticity

The storage moduli (G' at 1 Hz) for the microgel monolayers at the water/oil interface with different microgel concentrations (c) are shown in Fig. 5.7a. There are four regimes observed for the Langmuir monolayers. In the first regime (c $< 0.40\ \mu\mathrm{m}^{-2}$), the storage

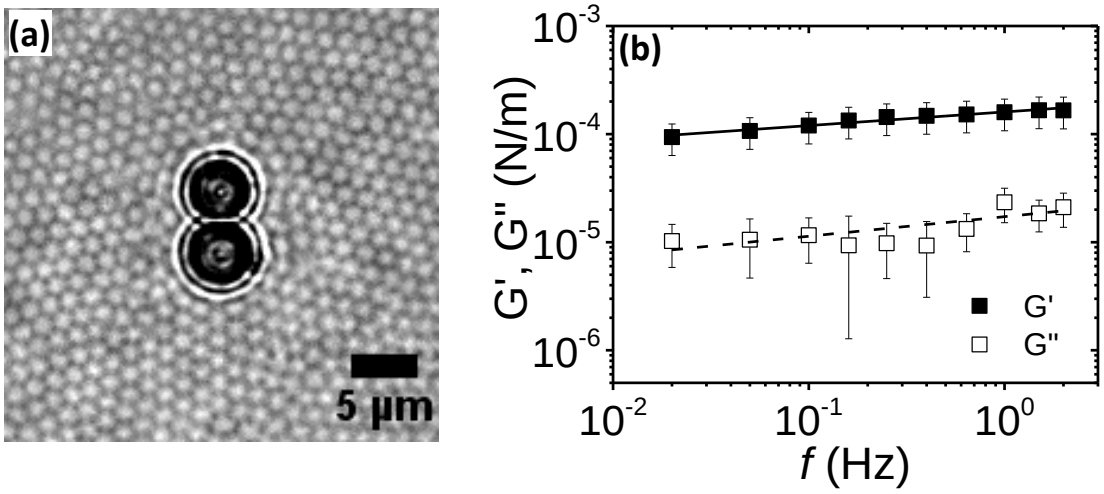

Figure 5.6 (a) A magnetic dimer sitting in the microgel monolayer at the water/oil interface. This microgel monolayer has a microgel concentration of 0.47 μm^2, a degree of local order ψ_6=0.78, and a mean inter-microgel distance of 1.52$\pm$0.09 μm. The two big particles at the center of this image are the magnetic particles, while the white particles are the microgels. The scale bar is 5 μm. (b) Storage modulus (G') and loss modulus (G'') of the microgel monolayer shown in (a) as functions of frequency (f). The lines represent linear fits to the data.

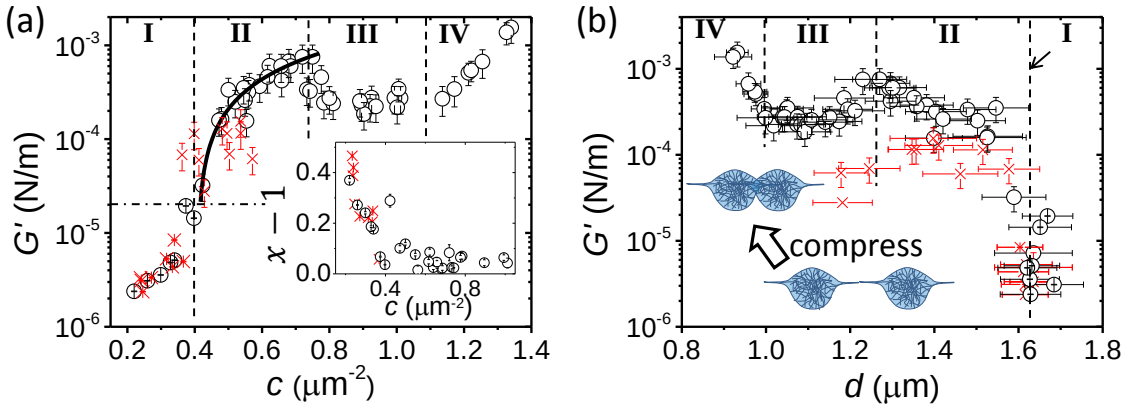

Figure 5.7 Storage moduli (G' at 1 Hz) of the microgel monolayers at the water/oil interface as functions of microgel concentration c (a) and inter-microgel distance d (b). The inset in (a) shows the frequency dependence of storage modulus ($G' \propto f^{x-1}$) of the microgel monolayer as a function of c. The solid line represents $G' \propto (c - c_p)^{\mu}$, where $c_p = 0.40$ μm^{-2} and $\mu = 1$. The black circles in (a, b) are for the Langmuir monolayers, while the red crosses are for the Gibbs monolayers. The inset in (b) gives a sketch of the microgels with the "fried-egg" morphology under lateral compression. The vertical dashed lines separate the concentration range into 4 regimes, while the horizontal dash-dotted line in (a) indicates the storage modulus below which passive microrheology is used to determine the storage modulus.

modulus increases with c, up to $\sim 2\times10^{-5}$ N/m. As discussed above, at low concentration the microgels form aggregated networks driven by the capillary forces. Indeed, it has been predicted that the monolayer from capillary multipoles exhibits considerable shear elasticity.[45,46] For monolayers from capillary hexapoles in contact (in 2D hexagonal lattice), the storage modulus is predicted to be $G'_h = 64\sigma(H/r_c)^2$; while for the monolayers from capillary quadrupoles in contact (in 2D square lattice), $G'_q = 23\sigma(H/r_c)^2$, where H is the amplitude of the undulation of the contact line whose average radius is r_c, and σ is the interfacial tension. Using the experimental parameters, $H = 3$ nm,[36] $\sigma = 42.6$ mN/m[57] and $r_c = 0.82$ μm, we obtain $G'_h = 3.7\times10^{-5}$ N/m and $G'_q = 1.3\times10^{-5}$ N/m. These resulting values are in good agreement with the measured shear modulus ($\sim 2\times10^{-5}$ N/m) of the microgel monolayers at $c \sim 0.40$ μm^{-2} (corresponding to the random close packing of the microgel shells at the water/oil interface). This further supports the fact that at low concentrations (when the microgels are not compressed at the interface), the capillary interactions between the microgels dominate the elasticity of the microgel monolayers.

In the second regime, the storage moduli of the Langmuir monolayers follow another increasing tendency, $G' \propto (c - c_p)^{\mu}$, where $c_p = 0.40$ μm^{-2} and $\mu = 1$ (see the solid line in Fig. 5.7a). This indicates that the storage moduli of the microgel monolayers are determined by another mechanism. As shown in Fig. 5.5c, the inter-microgel distance decreases with increasing concentration in the second region, meaning that the shells of the microgels are under lateral compression (overlapping). Compressing the shells of the microgels is like compressing deformable 2D disks (the stress should mainly be transmitted through the nanosized, collapsed interfacial polymer layers[31] in the shells). The quasilinear increase of G' with $c - c_p$ for 2D and 3D deformable particle systems has been observed in experiments and simulations.[16,58,59] For example, Mason et al. showed that for a model system of disordered (monodispersed) deformable particles which interact through an effective repulsive anharmonic potential, G' and $c - c_p$ have a quasilinear relationship.[58,59] We expect that similar effects, i.e., the disordered arrangement of the microgels and their anharmonic interaction potential under compression, would lead to the quasilinear increase of G' with $c - c_p$ as observed in the second regime. The former effect (disordered arrangement) is reflected by the degree of order, ψ_6. As shown in Fig. 5.5d, for the Langmuir monolayers, ψ_6 increases with increasing concentration in this regime. The increase of ordering under compression is also observed in simulations of 2D and 3D deformable particles.[53,59,60] The latter effect (repulsive anharmonic potential) is related to the core-shell morphology of the microgels and the collapsed polymer layer at the interface. Because of the low water content and the strong inter- and intra-polymer interactions,[30–32] the collapsed polymer layers at the interface should have a higher elastic modulus compared to the swollen part of the microgels. Probably, this thin interfacial polymer layer determines the repulsive potential when the shells of the microgels start to overlap (i.e., in the second regime).

In the third regime, G' of the microgel monolayer decreases and becomes insensitive to microgel concentration. The decrease of interfacial elasticity of microgel monolayers under lateral compression has been reported, and there exist two explanations.[27,28] The first explanation is based on the behavior of the constituting polymers (PNIPAM).[27] At low surface coverage, the PNIPAM polymers are lying at the interface. However, when they are lack of space at the interface (e.g., when the expanded shells of the microgels strongly overlap), the PNIPAM polymers may fold into multilayers. The formation of these folds leads to the loss of elasticity of the interfacial polymer layer, because the stress can be easily relaxed. This effect is also generic for other linear polymer/protein monolayers at interface.[26,61] Alternatively, the second explanation is based on the packing states of the microgels at the interface.[28,62] Under low compression the microgels form shell-shell contacts, while under high compression the shell-shell contacts change into core-core contacts. In the transition region, as suggested by Rey et al., the partial lose of the stress-bearing network of microgels in shell-shell contacts leads to the decrease of elasticity.[28]

In our experiments, we also observe that the degree of order decreases in the third regime (see Fig. 5.5d). This implies that the shells of the microgels at the interface are frustrated, which also supports that the polymer layers in the shells fold out of interface and lose their resistance to lateral compression.

In the fourth region, G' increases with increasing concentration. In the plot of G' vs d (Fig. 5.7b), the fourth region takes place only when the inter-microgel distances become smaller than $\sim$1 μm, which is close to the hydrodynamic diameter of the microgels in water. This means that in the fourth region the main bodies of the microgels are in direct contact (overlapping, see sketch in Fig. 5.7b), leading to the increased elasticity of the microgel monolayers. It has been suggested that the Hertzian model would be able to describe the interaction potential between microgels for this contact mechanism.[62]

The storage moduli of the Gibbs monolayers are also given in Fig. 5.7. At low concentrations ($c < c_p$) the elastic moduli of the microgel monolayers are independent of the preparation methods. However, when the concentration is close to c_p, the Gibbs monolayers tend to have a higher storage modulus. This is because at concentrations around c_p, the microgels in the Gibbs monolayers are under stronger compression compared to the Langmuir monolayers (as indicated by the smaller inter-microgel distance, see Fig. 5.5c). However, at high concentrations ($c > c_p$), the storage moduli of the Gibbs monolayers are smaller compared to the Langmuir monolayers due to their more disordered structures (Fig. 5.5d). These results highlight that the rheological properties of the microgel monolayers are not only dependent on the concentration, but also on the inter-microgel distance (compression states) and the structural ordering.

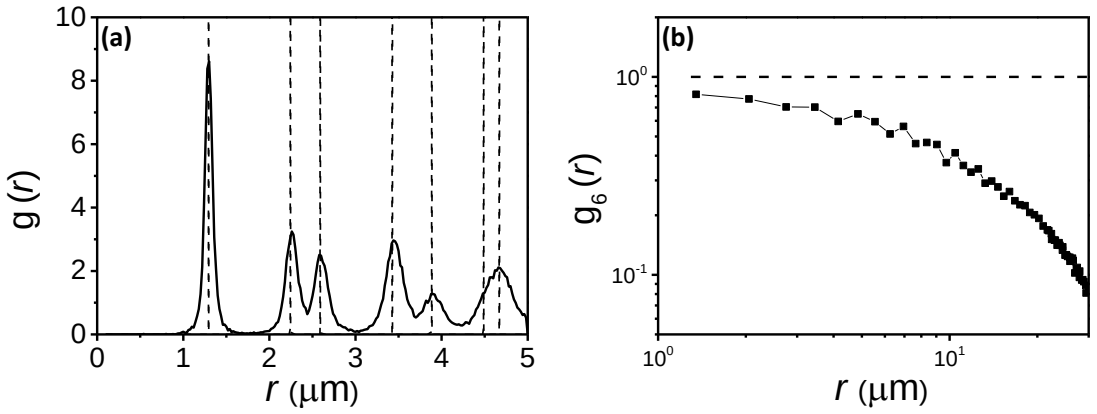

Figure 5.8 (a) Pair correlation function $g(r)$ of a microgel monolayer with high local order ($\psi_6 = 0.91$, see Fig. 5.9 for the image of the sample). (b) Orientational correlation function $g_6(r)$ for the same microgel monolayer. The dash lines in (a) and (b) represent the results from an ideal hexagonal array generated numerically.

5.3.5 Frequency dependent rheology

The storage moduli of the microgel monolayers have a weak power-law dependence on frequency, $G' \propto f^{x-1}$ with $x-1 \to 0$ for dense microgel monolayers (see inset in Fig. 5.7a). This rheological behavior is reminiscent of soft glassy materials (SGMs).[56] For SGMs, the frequency dependence of G' is either a weak power law or negligible.[56] There are a wide range of materials belonging to SGMs, including foams, emulsions, pastes, and slurries.[56] Glassy dynamics is a natural consequence of structural disorder and metastability.[56] Even though the state of least free energy would be ordered, a SGM is not able to achieve this state by thermal motion alone because the system has to cross energy barriers that are very large compared to thermal energy.[63] The rheology of SGMs reflects this structural relaxation in which the elements have to cross these large energy barriers.

The structural disorder of the microgel monolayers is reflected by the relatively small order parameter ψ_6 (typically smaller than 0.9, see Fig. 5.5d). Moreover, even though some local ordered structures can be observed in the dense microgel monolayers (e.g., Fig. 5.5a (a_2)), the orientational correlation function ($g_6(r) = \langle \psi_6(\vec{r})\psi_6^*(\vec{0})\rangle$) decays quickly with increasing distance (see Fig. 5.8b), indicating the absence of long-range order.[64] Thus, the microgel monolayers are in fact disordered in long range. The metastability of the microgel monolayers is evident at low concentrations: the microgel networks show structural rearrangement (Fig. 5.10 in Supporting Information). At high concentrations, the structural rearrangement is not obvious during our observation times because the microgels are quenched by mutual compression between neighbors. The rearrangement of the structures in the microgel monolayers requires an activation energy which is compa-

rable to the inter-microgel interaction potential. This activation energy is significantly higher than the thermal energy, especially when the microgels are under lateral compression. Thus, the dense microgel monolayers retain the metastable state. As a result of the structural disorder and metastability, microgel monolayers act as SGMs.

5.4 Conclusions

In conclusion, we have explored the inter-microgel interactions as well as the rheology-structure relationship of microgel monolayers at the water/oil interface. We find that the microgels at the water/oil interface have an attraction potential which drives the microgels to aggregate. The percolating microgel networks show dominating elasticity. When the microgel concentration at the interface is beyond c_p (dense random packing for the microgel shells), the inter-microgel distance decreases following $d \propto c^{-0.5}$ for a large range of concentration, reflecting the fact that the soft microgels at the interface can be strongly deformed under lateral compression.

We find four regimes for the microgels under lateral compression. In the first regime ($c < c_p$), the microgels have a constant excluded area at the interface ($d = 1.63 \pm 0.07\ \mu$m). They can be regarded as soft disks floating at the water/oil interface which are connected into networks by the capillary interactions. After the microgel concentration reaches c_p, in the second regime, the microgel shells start to overlap, showing a linear increase of storage modulus upon concentration (similar to compressing soft disks). Under lateral compression, the interfacial polymer layers (i.e., the collapsed polymer layers in contact with oil) in the shells may dominate the elasticity of the microgel monolayers in this region. In the third regime, however, the storage modulus decreases probably due to the escape of polymer segments in the interfacial polymer layers out from the interface under compression. In the fourth regime, when the inter-microgel distances become smaller than the hydrodynamic diameter of microgels in water, the storage moduli of the microgel monolayers increase due to the overlapping of the main bodies of the microgels. Our results thus provide a framework for modeling the rheological properties of the microgel monolayers at the water/oil interface. On the one hand, the different inter-microgel interaction potentials in different compression states should be taken into account. On the other hand, the arrangement of the microgels at the interface is also important as it determines how the microgels interact with their neighbors (e.g., in which compression state).

In addition, the frequency dependence of the rheological property of the microgel monolayers at the water/oil interface indicates that the microgel monolayers act as soft glassy materials. This is because of their structural disorder and metastability. Microgels at the interface can be a good experimental model system for soft glassy materials. As shown in this work, the detailed structural information is accessible during rheological

measurement. This may make it possible to perform simulations with the similar local structure using active microrheology. Another advantage of using microgels as the model system for soft glassy materials is that the softness, size and the structural order can be readily tuned.

5.5 Acknowledgements

The authors acknowledge the Deutsche Forschungsgemeinschaft for support of this work through the priority program SPP 1681 (No. AU 321/3-2).

Bibliography

[1] Hunter, T. N.; Pugh, R. J.; Franks, G. V.; Jameson, G. J. The role of particles in stabilising foams and emulsions. *Advances in Colloid and Interface Science* **2008**, *137*, 57–81.

[2] Barman, S.; Christopher, G. F. Simultaneous interfacial rheology and microstructure measurement of densely aggregated particle laden interfaces using a modified double wall ring interfacial rheometer. *Langmuir* **2014**, *30*, 9752–9760.

[3] Binks, B.; Lumsdon, S. Influence of particle wettability on the type and stability of surfactant-free emulsions. *Langmuir* **2000**, *16*, 8622–8631.

[4] Pawar, A. B.; Caggioni, M.; Ergun, R.; Hartel, R. W.; Spicer, P. T. Arrested coalescence in Pickering emulsions. *Soft Matter* **2011**, *7*, 7710–7716.

[5] Reynaert, S.; Moldenaers, P.; Vermant, J. Interfacial rheology of stable and weakly aggregated two-dimensional suspensions. *Physical Chemistry Chemical Physics* **2007**, *9*, 6463–6475.

[6] Reynaert, S.; Moldenaers, P.; Vermant, J. Control over colloidal aggregation in monolayers of latex particles at the oil-water interface. *Langmuir* **2006**, *22*, 4936–4945.

[7] Pieranski, P. Two-dimensional interfacial colloidal crystals. *Physical Review Letters* **1980**, *45*, 569.

[8] Hurd, A. J. The electrostatic interaction between interfacial colloidal particles. *Journal of Physics A: Mathematical and General* **1985**, *18*, L1055.

[9] Aveyard, R.; Binks, B. P.; Clint, J. H.; Fletcher, P. D. I.; Horozov, T. S.; Neumann, B.; Paunov, V. N.; Annesley, J.; Botchway, S. W.; Nees, D.; Parker, A. W.;

Ward, A. D.; Burgess, A. N. Measurement of long-range repulsive forces between charged particles at an oil-water interface. *Physical review letters* **2002**, *88*, 246102.

[10] Oettel, M.; Dietrich, S. Colloidal interactions at fluid interfaces. *Langmuir* **2008**, *24*, 1425–1441.

[11] Park, B. J.; Pantina, J. P.; Furst, E. M.; Oettel, M.; Reynaert, S.; Vermant, J. Direct measurements of the effects of salt and surfactant on interaction forces between colloidal particles at water-oil interfaces. *Langmuir* **2008**, *24*, 1686–1694.

[12] Park, B. J.; Furst, E. M. Attractive interactions between colloids at the oil–water interface. *Soft Matter* **2011**, *7*, 7676–7682.

[13] Nikolaides, M.; Bausch, A.; Hsu, M.; Dinsmore, A.; Brenner, M.; Gay, C.; Weitz, D. Electric-field-induced capillary attraction between like-charged particles at liquid interfaces. *Nature* **2002**, *420*, 299–301.

[14] Stamou, D.; Duschl, C.; Johannsmann, D. Long-range attraction between colloidal spheres at the air-water interface: The consequence of an irregular meniscus. *Physical Review E* **2000**, *62*, 5263.

[15] Barman, S.; Christopher, G. F. Role of capillarity and microstructure on interfacial viscoelasticity of particle laden interfaces. *Journal of Rheology (1978-present)* **2016**, *60*, 35–45.

[16] Cicuta, P.; Stancik, E. J.; Fuller, G. G. Shearing or compressing a soft glass in 2D: time-concentration superposition. *Physical review letters* **2003**, *90*, 236101.

[17] Ngai, T.; Auweter, H.; Behrens, S. H. Environmental responsiveness of microgel particles and particle-stabilized emulsions. *Macromolecules* **2006**, *39*, 8171–8177.

[18] Destribats, M.; Lapeyre, V.; Wolfs, M.; Sellier, E.; Leal-Calderon, F.; Ravaine, V.; Schmitt, V. Soft microgels as Pickering emulsion stabilisers: role of particle deformability. *Soft Matter* **2011**, *7*, 7689–7698.

[19] Richtering, W. Responsive emulsions stabilized by stimuli-sensitive microgels: emulsions with special non-Pickering properties. *Langmuir* **2012**, *28*, 17218–17229.

[20] Monteux, C.; Marliere, C.; Paris, P.; Pantoustier, N.; Sanson, N.; Perrin, P. Poly (N-isopropylacrylamide) microgels at the oil- water interface: Interfacial properties as a function of temperature. *Langmuir* **2010**, *26*, 13839–13846.

[21] Deshmukh, O. S.; Maestro, A.; Duits, M. H.; van den Ende, D.; Stuart, M. C.; Mugele, F. Equation of state and adsorption dynamics of soft microgel particles at an air–water interface. *Soft matter* **2014**, *10*, 7045–7050.

[22] Li, Z.; Geisel, K.; Richtering, W.; Ngai, T. Poly (N-isopropylacrylamide) microgels at the oil–water interface: adsorption kinetics. *Soft Matter* **2013**, *9*, 9939–9946.

[23] Geisel, K.; Isa, L.; Richtering, W. The Compressibility of pH-Sensitive Microgels at the Oil–Water Interface: Higher Charge Leads to Less Repulsion. *Angewandte Chemie International Edition* **2014**, *53*, 4905–4909.

[24] Cohin, Y.; Fisson, M.; Jourde, K.; Fuller, G. G.; Sanson, N.; Talini, L.; Monteux, C. Tracking the interfacial dynamics of PNiPAM soft microgels particles adsorbed at the air–water interface and in thin liquid films. *Rheologica Acta* **2013**, *52*, 445–454.

[25] Huang, S.; Gawlitza, K.; von Klitzing, R.; Gilson, L.; Nowak, J.; Odenbach, S.; Steffen, W.; Auernhammer, G. K. Microgels at the Water/Oil Interface: In Situ Observation of Structural Aging and Two-Dimensional Magnetic Bead Microrheology. *Langmuir* **2016**, *32*, 712–722.

[26] Monroy, F.; Ortega, F.; Rubio, R. G.; Ritacco, H.; Langevin, D. Surface rheology of two-dimensional percolating networks: Langmuir films of polymer pancakes. *Physical review letters* **2005**, *95*, 056103.

[27] Pinaud, F.; Geisel, K.; Massé, P.; Catargi, B.; Isa, L.; Richtering, W.; Ravaine, V.; Schmitt, V. Adsorption of microgels at an oil–water interface: correlation between packing and 2D elasticity. *Soft Matter* **2014**, *10*, 6963–6974.

[28] Rey, M.; Fernández-Rodríguez, M. Á.; Steinacher, M.; Scheidegger, L.; Geisel, K.; Richtering, W.; Squires, T. M.; Isa, L. Isostructural solid–solid phase transition in monolayers of soft core–shell particles at fluid interfaces: structure and mechanics. *Soft Matter* **2016**, *12*, 3545–3557.

[29] Brugger, B.; Vermant, J.; Richtering, W. Interfacial layers of stimuli-responsive poly-(N-isopropylacrylamide-co-methacrylicacid)(PNIPAM-co-MAA) microgels characterized by interfacial rheology and compression isotherms. *Physical Chemistry Chemical Physics* **2010**, *12*, 14573–14578.

[30] Saunders, B. R.; Vincent, B. Microgel particles as model colloids: theory, properties and applications. *Advances in colloid and interface science* **1999**, *80*, 1–25.

[31] Zielińska, K.; Sun, H.; Campbell, R. A.; Zarbakhsh, A.; Resmini, M. Smart nanogels at the air/water interface: structural studies by neutron reflectivity. *Nanoscale* **2016**, *8*, 4951–4960.

[32] Richardson, R. M.; Pelton, R.; Cosgrove, T.; Zhang, J. A neutron reflectivity study of poly (N-isopropylacrylamide) at the air-water interface with and without sodium dodecyl sulfate. *Macromolecules* **2000**, *33*, 6269–6274.

[33] Geisel, K.; Richtering, W.; Isa, L. Highly ordered 2D microgel arrays: compression versus self-assembly. *Soft Matter* **2014**, *10*, 7968–7976.

[34] Keim, N. C.; Arratia, P. E. Mechanical and microscopic properties of the reversible plastic regime in a 2D jammed material. *Physical review letters* **2014**, *112*, 028302.

[35] Keim, N. C.; Arratia, P. E. Yielding and microstructure in a 2D jammed material under shear deformation. *Soft Matter* **2013**, *9*, 6222–6225.

[36] Huang, S.; Gawlitza, K.; von Klitzing, R.; Gilson, L.; Nowak, J.; Odenbach, S.; Steffen, W.; Auernhammer, G. K. Microgels at the Water/Oil Interface: In Situ Observation of Structural Aging and Two-Dimensional Magnetic Bead Microrheology. *Langmuir* **2016**, *32*, 712–722.

[37] Horigome, K.; Suzuki, D. Drying Mechanism of Poly (N-isopropylacrylamide) Microgel Dispersions. *Langmuir* **2012**, *28*, 12962–12970.

[38] http://www.physics.emory.edu/faculty/weeks//idl/index.html.

[39] Wilhelm, C.; Browaeys, J.; Ponton, A.; Bacri, J.-C. Rotational magnetic particles microrheology: the Maxwellian case. *Physical Review E* **2003**, *67*, 011504.

[40] Wilhelm, C. Out-of-equilibrium microrheology inside living cells. *Physical review letters* **2008**, *101*, 028101.

[41] Ershov, D.; Sprakel, J.; Appel, J.; Stuart, M. A. C.; van der Gucht, J. Capillarity-induced ordering of spherical colloids on an interface with anisotropic curvature. *Proceedings of the National Academy of Sciences* **2013**, *110*, 9220–9224.

[42] Kaya, D.; Green, N.; Maloney, C.; Islam, M. Normal modes and density of states of disordered colloidal solids. *Science* **2010**, *329*, 656–658.

[43] Chen, K.; Ellenbroek, W. G.; Zhang, Z.; Chen, D. T. N.; Yunker, P. J.; Henkes, S.; Brito, C.; Dauchot, O.; van Saarloos, W.; Liu, A. J.; Yodh, A. G. Low-frequency vibrations of soft colloidal glasses. *Physical review letters* **2010**, *105*, 025501.

[44] Danov, K. D.; Kralchevsky, P. A. Capillary forces between particles at a liquid interface: General theoretical approach and interactions between capillary multipoles. *Advances in colloid and interface science* **2010**, *154*, 91–103.

[45] Danov, K. D.; Kralchevsky, P. A.; Naydenov, B. N.; Brenn, G. Interactions between particles with an undulated contact line at a fluid interface: Capillary multipoles of arbitrary order. *Journal of colloid and interface science* **2005**, *287*, 121–134.

[46] Kralchevsky, P. A.; Denkov, N. D.; Danov, K. D. Particles with an undulated contact line at a fluid interface: interaction between capillary quadrupoles and rheology of particulate monolayers. *Langmuir* **2001**, *17*, 7694–7705.

[47] Ortega, F.; Ritacco, H.; Rubio, R. G. Interfacial Microrheology: Particle Tracking and Related Techniques. *Curr. Opin. Colloid Interface Sci.* **2010**, *15*, 237–245.

[48] Einstein, A. Über die von der Molekularkinetischen Theorie der Wärme Geforderte Bewegung von in Ruhenden Flüssigkeiten Suspendierten Teilchen. *Ann. Phys.* **1905**, *4*, 549–560.

[49] Von Smoluchowski, M. Zur kinetischen Theorie der Brownschen Molekularbewegung und der Suspensionen. *Ann. phys.* **1906**, *326*, 756–780.

[50] Mason, T. G. Estimating the viscoelastic moduli of complex fluids using the generalized Stokes–Einstein equation. *Rheologica Acta* **2000**, *39*, 371–378.

[51] Mason, T. G.; Weitz, D. Optical measurements of frequency-dependent linear viscoelastic moduli of complex fluids. *Physical review letters* **1995**, *74*, 1250.

[52] Saffman, P.; Delbrück, M. Brownian motion in biological membranes. *Proceedings of the National Academy of Sciences* **1975**, *72*, 3111–3113.

[53] Bolton, F.; Weaire, D. Rigidity loss transition in a disordered 2D froth. *Physical review letters* **1990**, *65*, 3449.

[54] Halperin, B.; Nelson, D. R. Theory of two-dimensional melting. *Physical Review Letters* **1978**, *41*, 121.

[55] Peng, Y.; Wang, Z.; Alsayed, A. M.; Yodh, A. G.; Han, Y. Melting of colloidal crystal films. *Physical review letters* **2010**, *104*, 205703.

[56] Sollich, P.; Lequeux, F.; Hébraud, P.; Cates, M. E. Rheology of soft glassy materials. *Physical review letters* **1997**, *78*, 2020.

[57] Rehfeld, S. J. Adsorption of sodium dodecyl sulfate at various hydrocarbon-water interfaces. *The Journal of Physical Chemistry* **1967**, *71*, 738–745.

[58] Mason, T.; Bibette, J.; Weitz, D. Elasticity of compressed emulsions. *Physical review letters* **1995**, *75*, 2051.

[59] Mason, T.; Lacasse, M.-D.; Grest, G. S.; Levine, D.; Bibette, J.; Weitz, D. Osmotic pressure and viscoelastic shear moduli of concentrated emulsions. *Physical Review E* **1997**, *56*, 3150.

[60] Hutzler, S.; Weaire, D. The osmotic pressure of a two-dimensional disordered foam. *Journal of Physics: Condensed Matter* **1995**, *7*, L657.

[61] Langevin, D.; Monroy, F. Interfacial rheology of polyelectrolytes and polymer monolayers at the air–water interface. *Current opinion in colloid & interface science* **2010**, *15*, 283–293.

[62] Maldonado-Valderrama, J.; del Castillo-Santaella, T.; Adroher-Benítez, I.; Moncho-Jordá, A.; Martín-Molina, A. Thermoresponsive microgels at the air–water interface: the impact of the swelling state on interfacial conformation. *Soft Matter* **2016**,

[63] Sollich, P. Rheological constitutive equation for a model of soft glassy materials. *Physical Review E* **1998**, *58*, 738.

[64] Keim, P.; Maret, G.; von Grünberg, H.-H. Frank's constant in the hexatic phase. *Physical Review E* **2007**, *75*, 031402.

5.6 Supporting Information

5.6.1 Dynamic light scattering

We used dynamic light scattering (DLS) to measure the size of the microgels in water. An ALV goniometer setup with a Nd:YAG laser (λ= 532 nm) and an ALV-6010/160E digital full correlator (ALV, Langen, Germany) were used to obtain the correlation functions. The scattered light was recorded at a constant scattering angle of 90°. The DLS experiment was equipped with a thermostated toluene bath. All experiments were performed at ambient temperature. The microgel concentration was 2.5×10^{-4} wt%. Before the DLS measurement, the solution was filtered using a 5 μm disposable filter. The cumulant analysis was used to obtain the size of the microgels. At ambient temperature the measured hydrodynamic diameter of the microgels is 970±60 nm with a polydispersity index of 0.6.

We also used the particle tracking method to determine the mean squared displacement ($\langle \Delta x^2(t) \rangle$) of the microgels in water. Based on the Stokes-Einstein equation, the hydrodynamic diameter D of the microgels in water can be deduced by [1]

$$D/2 = \frac{k_B T}{\pi \eta \langle \Delta x^2(t) \rangle} t, \tag{5.5}$$

where η is the viscosity of water. The deduced hydrodynamic diameter of microgels in water was ~ 1 μm, which is in good agreement with the result from DLS.

5.6.2 Magnetic dimer in highly ordered monolayer

Fig. 5.9 shows a microgel monolayer with a magnetic dimer. The degree of local order for this monolayer is high ($\psi = 0.91$). However, as discussed in the main text, this microgel monolayer lacks long-range orientational order, due to defects. That is, the order can only retain for a short distance. For most microgel monolayers in the main text, the degree of order is lower than this sample.

5.6.3 Vibration eigenmodes

In order to analyze the vibration property of the microgel aggregate shown in Fig. 5.3 of the main text, we use the covariance matrix analysis.[2–4] We consider a system of particles with the exact same interactions and geometry as the microgel aggregate and neglect damping. We tracked the motion of all the microgels in the aggregate for 241 s with a frame rate of 30 Hz, thus we obtain 7230 position data for each microgel. After removing a potential drift, we determine the time-averaged position for each microgel. Relative to the time-averaged positions, a displacement vector $\mathbf{U}(t)$ can be obtained. It contains the displacements in 2D for all times t for all the microgels in the aggregate. A covariance

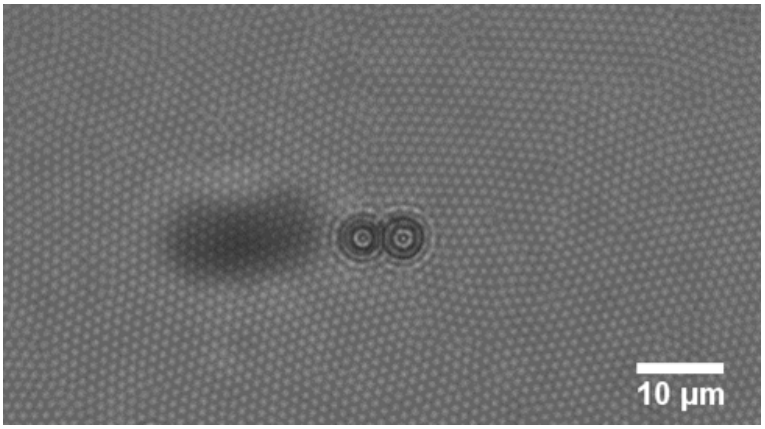

Figure 5.9 A microgel monolayer with a magnetic dimer. This microgel monolayer has a microgel concentration of 0.68 μm^{-2}, a high degree of local order ψ_6=0.91, and a mean inter-microgel distance of 1.3±0.05 μm. The two big particles at the center of this image are the magnetic particles, while the white particles occupying the whole area are the microgels. The scare bar is 10 μm.

matrix $\underline{C}$ is constructed with $C_{ij} = \langle U_i U_j \rangle_t$, where i and j run through all microgels and coordination directions (i.e., x and y). Here $\langle \bullet \rangle_t$ represents the time average. The stiffness matrix $\underline{K}$, which contains the effective spring constants between the microgels, is proportional to the inverse of $\underline{C}$ with $\underline{K} = k_B T \underline{C}^{-1}$. Finally, the dynamic matrix $\underline{D}$ can be obtained:

$$\underline{D} = \frac{K}{m} = \frac{k_B T \underline{C}^{-1}}{m}, \tag{5.6}$$

where m is the mass of a microgel. This dynamic matrix yields the eigenfrequencies and eigenvectors of the microgel aggregate. The calculations are performed using the matlab software.

5.6.4 Structural rearrangement

At low surface coverage, the microgels at the interfaces form aggregated structures, probably driven by the long-range capillary force.[5,6] The microgels have a strong inter-microgel interaction potential (e.g., the estimated depth of the potential is about 200 $k_B T$, and the effective spring constant is about 2150 $k_B T/\mu$m^2). This interaction potential leads to the fact that the microgels cannot be separated by thermal energy after they aggregate. However, we observed that structural rearrangement can take place. For example, in Fig. 5.10a, the five-microgel aggregate reorganizes and change its shape with time. In Fig. 5.10b, the indicated particle in an open microgel network changes its neighbors. In a dense region, the rearrangement of microgels involves with the rearrangments of the neighboring microgels. These structural rearrangement events imply that for the microgels at the interface (when the microgels are not laterally compressed), the capillary forces

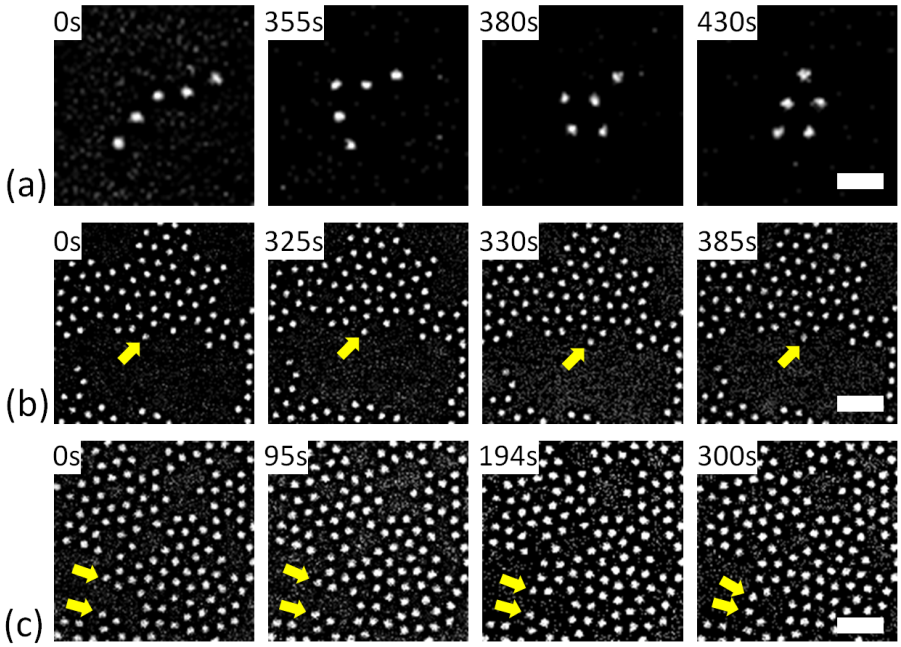

Figure 5.10 Structural rearrangements of microgels at the water/oil interface. (a) A five-microgel aggregate changes its shape spontaneously. (b) A microgel in a percolating network changes its neighbors spontaneously. (c) A rearrangement event can involve several microgels. The scale bars are 2.5 μm and 5 μm in (a) and (b, c), respectively. The time at the upper left corner of each image is the waiting time.

dominate other attractive forces (e.g., hydrophobic interactions and hydrogen bonding). In this case, the bonds between microgels are not irreversible (even though the strength is high). Old bonds can be replaced by the new bonds if the capillary force from other neighboring microgels becomes more significant. These results indicate that the microgel networks are in the metastable state. Through rearrangement of the microgels, the system approaches a more energetically favorable state.

5.6.5 Neglecting the drag from subphases in passive microrheology for simplification

A spherical particle moving in a viscous fluid with a velocity of $\mathbf{v}$ feels a frictional force $\mathbf{F_b}$, called "Stokes' drag":[7]

$$\mathbf{F_b} = -\xi_b \mathbf{v} \tag{5.7}$$

The friction coefficient ξ_b, first deviated by G. G. Stokes (for small Reynolds numbers, e. g., for small particles or highly viscous liquid), is related to the radius of the particle (R) and the dynamic viscosity of the liquid (η):

$$\xi_b = 6\pi\eta R. \tag{5.8}$$

Small spherical particles (e.g., several micrometers or less in diameter) in a purely viscous liquid undergo Brownian motion driven by the thermal energy (k_BT). As the thermal forces are stochastic, the resulting mean displacement of the diffusing particles over time is zero, while the mean squared displacement MSD ($\langle \Delta x^2(t) \rangle$) changes over time ($t$):[8]

$$\langle \Delta x^2(t) \rangle = \langle x(t) - x(0) \rangle^2 = 2dDt, \tag{5.9}$$

where D is the diffusion coefficient and d is the dimensionality. The diffusion coefficient can be obtained by Einstein relation (or Einstein–Smoluchowski relation):[9,10]

$$D = \frac{k_BT}{\xi_b} \tag{5.10}$$

Combining Eqs. (5.8-5.10) results in the Stokes–Einstein equation (for $d = 2$):

$$\langle \Delta x^2(t) \rangle = \frac{4k_BT}{\xi_b} t. \tag{5.11}$$

For particles at the interface, the interfacial drag is related to the interfacial drag coefficient (ξ_i):

$$\mathbf{F_i} = -\xi_i \mathbf{v} \tag{5.12}$$

As the Einstein relation also applies for 2D system, the MSD at the interface is

$$\langle \Delta x^2(t) \rangle = \frac{4k_BT}{\xi_i} t. \tag{5.13}$$

In the experiments for the microgel networks at the interface (e.g., Fig. 5.4 in the main text), $\langle \Delta x^2(t) \rangle$ is measured. Thus, ξ_i can be obtained from eq. (5.13). For the sample shown in Fig. 5.4b in the main text (one of the weakest networks in our study), we obtain $\xi_i \approx (10 - 100)\xi_b$ (in the interesting time window of 0.07-1.7 s, corresponding to 0.1-2.4 Hz). Here, for calculating the ξ_b, we use $R = 0.5$ μm (hydrodynamic radius of microgels in water) and $\eta_b = 4 \times 10^{-3}$ Pa.s (mean viscosity of water and oil). Thus, the drag force acting on the microgels in the network at the interface is typically dominated by the interactions between the microgels. The drag force from the subphases plays a less important role. Thus, in our present study, for simplification, we neglect the drag from the subphases, and refer the measured moduli as "apparent" moduli.

5.6.6 Drag from subphases is negligible for active microrheology

Except for the forces from the microgel monolayer, the water and oil phases can also have some drag forces on the rotating magnetic dimers. Here we estimate the order of this viscous torque from the water and oil phases. We consider a dimer rotating in a viscous liquid with a viscosity (η) of 4 mPa.s (for water it is about 1 mPa.s and for our

PDMS oil it is about 7 mPa.s; here we assume halves of the particles are located in water and oil). The viscous toque can be calculated by

$$\Gamma_{\mathrm{v}} = \kappa \mathrm{V} \mathrm{G}_{\mathrm{v}} \theta, \tag{5.14}$$

where V is the volume of the magnetic dimer and $\mathrm{G_v}$ is shear modulus for the viscous liquid. We find κ=11.5 through simulation. The maximal frequency (f) in our study (active microrheology) is 2 Hz, thus we can expect the loss modulus at 2 Hz is $\sim$50 mPa ($G'' = 2\pi f \eta$). Using the typical rotation angle of $< 10°$, we obtain the upper limit of the viscous torque is $\sim 9 \times 10^{-18}$ Nm. On the other hand, the applied magnetic torque is typically larger than $\sim 2 \times 10^{-16}$ Nm. Thus the contribution of the viscous drag from the water/oil phase to the rotation of the magnetic dimer is smaller than 5%.

For interfacial rheometer, the dimensionless ratio between the drag from the interface and the drag from the subphases is called Boussinesq number:

$$B_0 = \eta_s / (\eta_b L), \tag{5.15}$$

with L the characteristic length of the system. When $B_0 \gg 1$, the subphase drag is negligible.[11] For viscoelastic interfaces, the Boussinesq number is frequency dependent,

$$B_0(\omega) = \frac{G_s''(\omega) - iG_s'(\omega)}{\omega L \eta_b}. \tag{5.16}$$

In our system, the probed frequency range is 0.02-2 Hz, using $G_s' = 2 \times 10^{-5}$ N/m ($G_s' \gg G_s''$), $\eta_b \approx 4 \times 10^{-3}$ Pa.s (mean viscosity of water and oil), $L \approx 9$ μm (length of a dimer), we obtain $44 < |B_0(\omega)| < 4.4 \times 10^3$.

For the dense microgel monolayers which are measured using active microrheology, as $G_s' > 2 \times 10^{-5}$ N/m, the Boussinesq number (absolute value) at different frequencies should be significantly larger than unity. Based on this fact, we neglect the drag from the subphases on the rotation of the magnetic dimers in the dense microgel monolayers.

5.6.7 Rotation of a dimer in an elastic membrane

In order to obtain the geometry factor κ for a particle dimer (see main text, e.g., κ in eqs. (5.3) and (5.4), we performed simulations using COMSOL Multiphysics software with the Solid Mechanics Module (linear solid mechanics). In the simulation, the elastic membrane has a thickness of 0.5 μm and a radius of 80 μm, a Young's modulus of 2×10^5 Pa (this value is chosen arbitrarily, because in the framework of linear mechanics, it does not influence the obtained κ), and a Poisson's ratio of 0.49 (nearly incompressible). A rigid particle dimer is put at the middle of the circular membrane. The two rigid particles in the dimer have the same diameter of 4.4 μm. An toque (Γ) of 1.3×10^{-13} Nm is applied at the particle dimer (the direction of the torque is normal to the membrane surface). This torque leads to an small rotation angle as observed in our experiment. A snapshot of

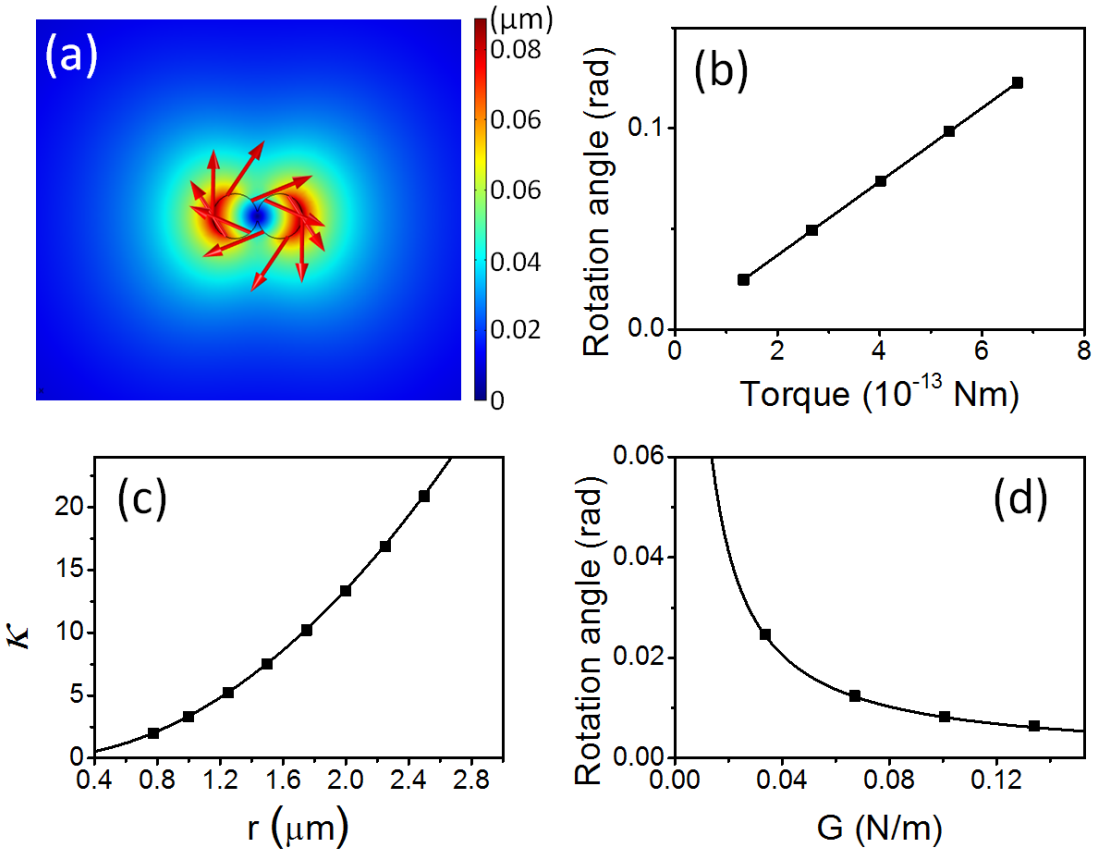

Figure 5.11 (a) Simulation of a particle dimer rotating in an elastic membrane using COMSOL Multiphysics software (linear solid mechanics). Here the elastic membrane has a thickness of 0.5 μm, a Young's modulus of 2×10^5 Pa and a Poisson's ratio of 0.49. The particle dimer consists of two particles with the same diameter of 4.4 μm. The applied toque (Γ) is 1.3×10^{-13} Nm. The color map shows the total displacement in μm. The arrows show the displacement vectors (not to scale). (b) Based on the similar setup in (a), the rotation angle (θ) increases linearly with the applied torque. The solid line shows the linear fit. (c) The geometry factor κ ($\kappa = \Gamma/(G\theta)$ where G is the membrane modulus: shear modulus$\times$thickness) as a function of radius (r) of the particles in the dimer. The solid line represents $\kappa = 33.6r^2$. (d) Rotation angle as a function of G. The applied toque is fixed at 1.3×10^{-13} Nm. The solid line represents $\theta = \Gamma/(G\kappa)$ with $\kappa = 33.6r^2$. The thickness of the membrane is changed between 0.5-2 μm in order to obtain the different G. The results show that $\kappa = 33.6r^2$ applies for membranes with different thickness.

the simulation result is shown in Fig. 5.11a. As shown in Fig. 5.11b, the rotation angle increases linearly with increasing the torque. We also change the size of the particle dimer, and calculate the geometry factor κ ($\kappa = \Gamma/(G\theta)$, where G is the membrane modulus: shear modulus$\times$thickness). In Fig. 5.11c it shows that $\kappa \approx 33.6r^2$ (unit: m^2/rad). In Fig. 5.11d, we check the effect of the thickness of the membrane on this geometry factor. It shows that $\kappa \approx 33.6r^2$ applies for membranes with different thickness.

5.6.8 Details about eqs. (5.3) and (5.4) in the main text

Consider the experimental setup shown in Fig. 5.1e in the main text, the magnetic torque on the magnetic dimer is

$$\Gamma_{\mathrm{m}} = \Gamma_0 \sin[2(\beta-\theta)]/2. \tag{5.17}$$

For $(\beta-\theta) \to 0$, $\sin[2(\beta-\theta)]/2 \approx \beta-\theta$, thus eq. (5.17) becomes

$$\Gamma_{\mathrm{m}} \approx \Gamma_0(\beta-\theta). \tag{5.18}$$

The viscoelastic torque by the microgel monolayer is

$$\Gamma_{\mathrm{ve}} = \kappa G^* \theta. \tag{5.19}$$

The magnetic torque should be balanced by the viscoelastic torque for the micro-sized magnetic dimer rotating in the microgel monolayers, $\Gamma_{\mathrm{m}} = \Gamma_{\mathrm{ve}}$. Thus, based on eq. (5.18) and eq. (5.19), the modulus of the microgel monolayer can be obtained by

$$G^* = \frac{\Gamma_0(\beta-\theta)}{\kappa\theta}. \tag{5.20}$$

We apply a magnetic field with rotation angle $\beta = \beta_0 e^{i\omega t}$ to the magnetic dimer. The magnetic dimer in the microgel monolayer rotates with an rotation angle $\theta = \theta_0 e^{i(\omega t-\phi)}$. Thus eq. (5.20) becomes

$$G^* = \frac{\Gamma_0}{\kappa}\frac{\beta_0 e^{i\omega t} - \theta_0 e^{i(\omega t-\phi)}}{\theta_0 e^{i(\omega t-\phi)}}. \tag{5.21}$$

Using $e^{i\phi} = \cos\phi + i\sin\phi$, eq. (5.21) can be simplified into

$$G^* = \frac{\Gamma_0}{\kappa}[(\frac{\beta_0}{\theta_0}\cos\phi - 1) + i\frac{\beta_0}{\theta_0}\sin\phi]. \tag{5.22}$$

This means that the complex modulus of the microgel monolayer has a real part (G') and an image part (G''). They are given in eqs. (5.3) and (5.4) in the main text.

5.6.9 Passive microrheology *vs* active microrheology

In the main text, we use the active microrheological method for the microgel monolayers with an elastic modulus higher than 2×10^{-5} N/m (see Fig. 5.7). In this case, the rotation of the magnetic dimer is smaller than 4°(corresponding to a strain smaller than 4×10^{-4}). The resulting maximal displacement of the microgels is smaller than their radius. This guarantees that there are no structural changes or yielding induced by the oscillatory rotation of the magnetic dimers.

In the experiments, we did observe that the active microrheological method (with the same configuration shown in Fig. 5.1c, d) was not well suitable to measure weak microgel monolayers. For example, Fig. 5.12 shows the shear moduli for a sample with low

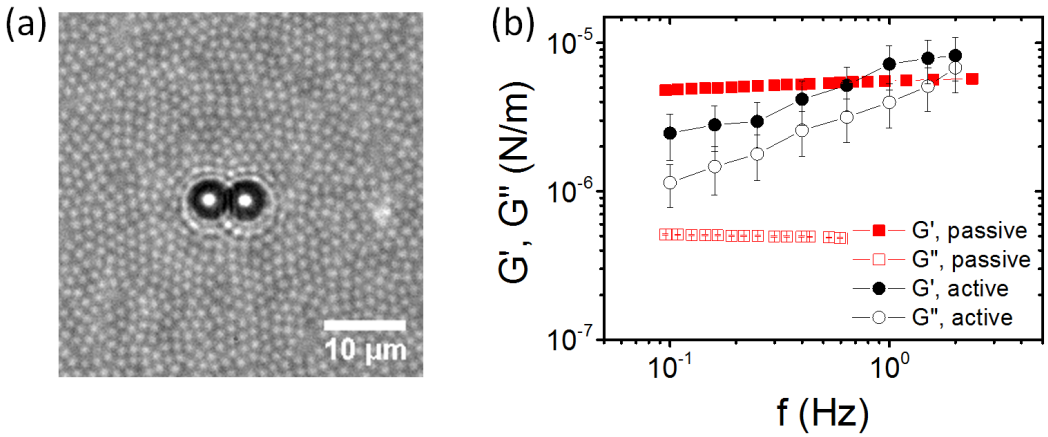

Figure 5.12 Comparing the results obtained from the passive and active microrheological methods for a relatively weak microgel monolayer. (a) The local structure of the microgel monolayer with the magnetic dimer. This microgel monolayer has a microgel concentration of 0.37 μm^{-2}, a degree of local order ψ_6=0.59, and a mean inter-microgel distance of 1.64$\pm$0.09 μm. The two big particles at the center of this image are the magnetic particles, while the white particles in the whole area are the microgels. The scale bar is 10 μm. (b) The storage modulus (G') and loss modulus (G'') obtained from passive (red squares) and active (black circles) microrheological methods. For this weak microgel monolayer, the applied magnetic force in the active microrheology can cause yielding (non-linear effects), leading to higher dissipations (larger G'') and a larger frequency dependence of G'. In the main text, we only use the active microrheological method for the microgel monolayers with an elastic modulus higher than 2×10^{-5} N/m (see Fig. 5.7), in order to avoid possible structural changes and yielding during measurements.

concentration (0.37 μm^{-2}) probed by the passive and active microrheological methods. For high frequencies (0.6-2 Hz), both methods lead to comparable storage moduli (the difference is within the experimental uncertainty). However, there exist two major differences. Firstly, the frequency dependence of the storage modulus measured by the active microrheological method is larger compared to that measured by passive microrheological method. Secondly, the loss moduli measured by active microrheology are higher at all frequencies. We believe that the applied magnetic force caused yielding (non-linear effects) in the relatively weak microgel monolayer, leading to higher dissipations (larger loss moduli).

Bibliography

[1] Waigh, T. A. Microrheology of complex fluids. *Reports on Progress in Physics* **2005**, *68*, 685.

[2] Kaya, D.; Green, N.; Maloney, C.; Islam, M. Normal modes and density of states of disordered colloidal solids. *Science* **2010**, *329*, 656–658.

[3] Chen, K.; Ellenbroek, W. G.; Zhang, Z.; Chen, D. T. N.; Yunker, P. J.; Henkes, S.; Brito, C.; Dauchot, O.; van Saarloos, W.; Liu, A. J.; Yodh, A. G. Low-frequency vibrations of soft colloidal glasses. *Physical review letters* **2010**, *105*, 025501.

[4] Chen, K.; Still, T.; Schoenholz, S.; Aptowicz, K. B.; Schindler, M.; Maggs, A.; Liu, A. J.; Yodh, A. Phonons in two-dimensional soft colloidal crystals. *Physical Review E* **2013**, *88*, 022315.

[5] Huang, S.; Gawlitza, K.; von Klitzing, R.; Gilson, L.; Nowak, J.; Odenbach, S.; Steffen, W.; Auernhammer, G. K. Microgels at the Water/Oil Interface: In Situ Observation of Structural Aging and Two-Dimensional Magnetic Bead Microrheology. *Langmuir* **2016**, *32*, 712–722.

[6] Cohin, Y.; Fisson, M.; Jourde, K.; Fuller, G. G.; Sanson, N.; Talini, L.; Monteux, C. Tracking the interfacial dynamics of PNiPAM soft microgels particles adsorbed at the air–water interface and in thin liquid films. *Rheologica Acta* **2013**, *52*, 445–454.

[7] Stokes, G. G. *On the effect of the internal friction of fluids on the motion of pendulums*; Pitt Press, 1851; Vol. 9; p 38.

[8] Waigh, T. A. Microrheology of complex fluids. *Rep. Prog. Phys.* **2005**, *68*, 685.

[9] Einstein, A. Über die von der Molekularkinetischen Theorie der Wärme Geforderte Bewegung von in Ruhenden Flüssigkeiten Suspendierten Teilchen. *Ann. Phys.* **1905**, *4*, 549–560.

[10] Von Smoluchowski, M. Zur kinetischen Theorie der Brownschen Molekularbewegung und der Suspensionen. *Ann. phys.* **1906**, *326*, 756–780.

[11] Fuller, G. G.; Vermant, J. Complex fluid-fluid interfaces: rheology and structure. *Annual review of chemical and biomolecular engineering* **2012**, *3*, 519–543.

Acknowledgements

[In der elektronischen Fassung aus Datenschutzgründen entfernt]

Curriculum vitae

[In der elektronischen Fassung aus Datenschutzgründen entfernt]

Affidavit

I hereby declare that I wrote the dissertation submitted without any unauthorized external assistance and used only sources acknowledged in the work. All textual passages which are appropriated verbatim or paraphrased from published and unpublished texts as well as all information obtained from oral sources are duly indicated and listed in accordance with bibliographical rules. In carrying out this research, I complied with the rules of standard scientific practice as formulated in the statutes of Johannes Gutenberg-University Mainz to insure standard scientific practice.

(Place, Date)	(Signature)